The Structure and Development of Magmatic Plumbing Systems at Spreading Centres in the Afar Rift

Christopher Moore

Submitted in accordance with the requirements for the degree of
Doctor of Philosophy

The University of Leeds
School of Earth and Environment

March 2021

The candidate confirms that the work submitted is their own, except where work which has formed part of jointly authored publications has been included. The contribution of the candidate and the other authors to this work has been explicitly indicated below. The candidate confirms that appropriate credit has been given within the thesis where reference has been made to the work of others.

The work in Chapter 2 of this thesis has appeared in publication as follows:
Moore, C., Wright, T., Hooper, A., & Biggs, J. (2019). The 2019 eruption of Erta 'Ale volcano, Ethiopia: Insights into the shallow plumbing system of an incipient mid-ocean ridge. *Geochemistry, Geophysics, Geosystems*, **20**(12). `https://doi.org/10.1029/2019GC008692`
The concept and scope of this paper was developed by myself and the co-authors. I performed the data processing and analysis based on published literature, and wrote and produced all the figures in the paper and supplementary materials. The paper was then improved by comments from the co-authors and journal reviewers. The processed data used in this paper can be found here: `https://dx.doi.org/10.5285/da9725f0-8a25-489a-b1fa-ee445b8fe5d3`

The work in Chapter 3 of this thesis is in peer-review with the journal *Journal of Geophysical Research: Solid Earth* following an invitation to re-submit the manuscript, and appears in an online pre-print archive as follows:
Moore, C., Wright, T., & Hooper, A. (2020). Rift Focusing and Magmatism During Late-Stage Rifting in Afar, Ethiopia. *Earth and Space Science Open Archive*, **19**. `https://doi.org/10.1002/essoar.10503895.1`
The concept and scope of this paper was developed by myself and the co-authors. I performed the data processing and analysis based on published literature, and wrote and produced all the figures in the paper and supplementary materials. The processed data used in this paper can be found here: `https://407data.ceda.ac.uk/neodc/comet/data/licsarproducts`

The work in Chapter 4 of this thesis is a manuscript to be submitted to the journal *Geophysical Research Letters* as follows:
Moore, C., Wright, T., & Hooper, A. (in prep.). Post-Rift Relaxation at the Dabbahu-Manda-Hararo Segment in Afar, Ethiopia.
The concept and scope of this paper was developed by myself and the co-authors. I used a legacy dataset processed by Carolina Pagli alongside data processed by myself. I performed analysis based on published literature, and wrote and produced all the figures in the paper and supplementary materials.

Acknowledgements

Well this was tough! I admit that I was warned many times about the perils of doing, and in particular writing up, a PhD thesis but nothing really prepares you for the persistence and sacrifice that's required. Despite all that, I would absolutely have done it again if given the chance. The opportunity to be able to spend your time exploring a subject you find fascinating and challenging is one that I will always remember fondly. That being said, I would not have reached this point if it weren't for the patience, support, and guidance from not a small number of people.

Firstly I'd like to thank my main supervisor Tim Wright, who has reliably been there to answer questions, provide ideas, and read everything I've shown him; as well as providing the opportunity to do fieldwork in Ethiopia and actually visit the volcanoes I was looking at through my computer! I'd also like to thank my other supervisors Andy Hooper and Juliet Biggs who were always happy to contribute ideas and provide much appreciated support.

Thanks to my friends and colleagues who have been there for chats, stupid questions, football, lunch, and beers - all undervalued components of completing a PhD! In particular I'd like to thank Sam and Dinko who put up with living with me for two years. Thanks of course also go to all my family for providing unwavering encouragement and to my Dad for proofreading with a much appreciated experienced eye!

Last, but definitely not least, to Annie; who I met at the start of this PhD and has reminded me every day since that there are things in life worth more than work! In recent months I may have tested her patience to the limit by spending evenings and weekends writing, but she has been an inexhaustible source of love, support, and motivation, for which I am forever thankful.

To everyone mentioned above, and many more besides, with full sincerity and from the bottom of my heart,

Ta.

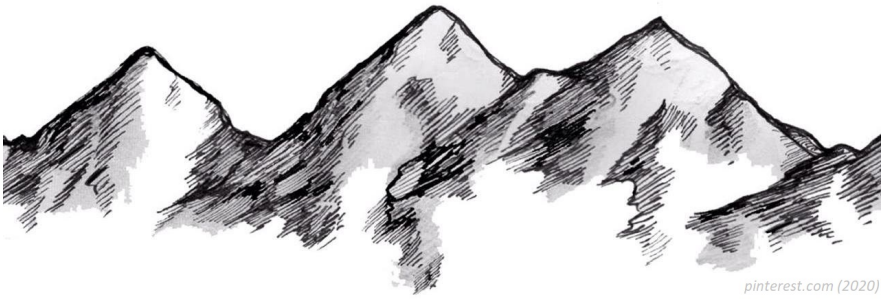

"If you trust in yourself... and believe in your dreams... and follow your star... you'll still get beaten by people who spent their time working hard and learning things and weren't so lazy."

- Terry Pratchett

Abstract

The Afar region of Ethiopia provides a unique example of a sub-aerial volcanic dominated rift in a transitional phase between continental and oceanic style rifting. Within volcanic spreading segments in Afar, the role of shallow magmatic intrusions and the rheological structure of the sub-surface in accommodating long-term extensional strain is not well understood. In this thesis, I aim to investigate these processes using satellite-borne interferometric synthetic aperture radar (InSAR) observations of surface deformation to target the simple questions of "Where is the magma?", "Where is the strain?", and "What is the rheological structure of the crust?". Using Sentinel-1 InSAR observations from 2014-2019 I develop an up-to-date map of average surface velocities across the whole Afar rift at a high spatial resolution. To achieve this, I refine an atmospheric time series filtering technique, using a weighting system to reduce the influence of noisy pixels and epochs. I also develop a novel methodology to reference InSAR derived velocities to regional Global Navigation Satellite Systems (GNSS) observations of plate motions in remote environments where the spatial distribution of GNSS data is limited.

Using this dataset, I apply numerical models of sub-surface deformation sources to assess the shallow magmatic plumbing systems at several volcanic centres throughout Afar. In particular, the deformation signal in the build-up to and during the 2017-2019 eruption at Erta 'Ale volcano in northern Afar highlights the complexity of these plumbing systems with shallow magma bodies at $\sim$ 1 km depth being fed by a deeper network of dykes and sills to magma reservoirs at the base of the crust. By monitoring the level of the long-lived lava lake in the Erta 'Ale summit caldera throughout the eruption, I also show that the shallow sources involved are hydraulically connected, indicating a similar interaction between the summit caldera and a local rift zone as previously established at Kilauea volcano, Hawaii. I also observe this linkage between shallow magma bodies within the crust and deeper magma bodies at the base of the crust at the Dabbahu-Manda-Hararo volcanic segment (DMHVS) in central Afar.

By combining 2014-2019 Sentinel-1 and 2006-10 Envisat time series of ground motions at the DMHVS, I model the $\sim$ 14 year post-rifting response to the large 2005-2010 rifting episode, combining both the viscoelastic relaxation of the upper mantle with continued

magma movement within the segment. I find that the optimal sub-surface structure below the DMHVS consists of a 17-22 km thick elastic lid which overlies a viscoelastic half-space with a viscosity of 0.6-1.8 $\times$ 10^{18} Pa s. I also show that sustained activity at volcanic centres is necessary to replicate the post-rifting deformation signal, and is indicative of a connection to a deeper reservoir beneath the DMHVS, as inferred by previous geophysical studies.

From mapping the spatial distribution of surface extension within the Afar rift, I also establish how extension is focussed within $\sim$ 10-15 km of volcanic segments in northern Afar, while extension is distributed over $\sim$ 80-160 km in south and central Afar with amagmatic faulting accommodating the strain. I infer that this change is indicative of the temporal evolution of the rift, with segments in northern Afar more closely resembling incipient mid-ocean ridges (MORs), in keeping with strain localisation facilitating the transition between continental and oceanic rifting. My findings further the understanding of the architecture of shallow magmatic plumbing systems at rift volcanoes, the state of the crust beneath spreading segments, and the spatial distribution of strain between segments. This provides a basis to incorporate more complexity in models of post-rift relaxation, and to develop thermal models to assess the similarity of sub-aerial spreading ridges in Afar to MORs.

Contents

List of Figures **xi**

List of Tables **xiii**

Nomenclature **xv**

1 Introduction **1**
1.1 Afar Tectonic Setting 2
1.2 Magma Plumbing Systems in Extensional Settings 6
1.3 InSAR Observations and Modelling 10
1.4 Aims & Objectives 15
1.5 Thesis Roadmap 16

2 The 2017 Eruption of Erta 'Ale Volcano, Ethiopia: Insights into the Shallow Axial Plumbing System of an Incipient Mid-Ocean Ridge **29**
2.1 Abstract 29
2.2 Introduction 30
2.2.1 Tectonic Setting 31
2.2.2 2017 Erta 'Ale Eruption 32
2.3 InSAR Data 33
2.4 Analysis 35
2.4.1 Ground Deformation 35
2.4.2 Lava Lake Level & Pressure Changes 41
2.4.3 Lava Flow Extent & Effusion Rate 45
2.5 Discussion 47
2.6 Conclusions 49
2.7 Acknowledgements 50

3 Rift Focussing and Magmatism During Late-Stage Rifting in Afar, Ethiopia **59**
3.1 Abstract 59
3.2 Introduction 60

3.2.1 Regional Setting 60
3.2.2 InSAR Velocity Methods & Applications in Afar 62
3.3 Data Processing and Time Series Methods 64
3.3.1 Sentinel-1 Data 64
3.3.2 Time Series 64
3.3.3 3D Velocities 66
3.4 Key Findings & Discussion 68
3.4.1 Plate Motions & Uncertainties 68
3.4.2 Rift Extension & Focussing 70
3.4.3 Magmatic Deformation 74
3.5 Conclusions 76
3.6 Acknowledgements 77

4 Post-Rift Relaxation at the Dabbahu-Manda-Hararo Segment in Afar, Ethiopia 87
4.1 Abstract 87
4.2 Introduction 88
4.2.1 Afar Tectonic Setting 88
4.2.2 Major Rifting Events 89
4.2.3 Post-Intrusion Deformation Modelling 91
4.3 Time Series & Modelling Methodology 92
4.3.1 InSAR Time Series 92
4.3.2 Viscoelastic Model 92
4.4 Analysis & Discussion 96
4.5 Conclusions 99
4.6 Acknowledgements 100

5 Discussion & Conclusions 107
5.1 Magma Plumbing Systems at Rift Volcanoes 107
5.2 Sub-Surface Structure below Volcanic Rift Segments 110
5.3 Strain Localisation & Rift Development 112
5.4 Limitations & Future Work 113
5.4.1 Afar Surface Velocity Map 113
5.4.2 Post-Rift Relaxation Model 114
5.4.3 Shallow Axial Magma Bodies 116
5.5 Concluding Remarks 116

A Supplementary Materials for Chapter 2 125
A.1 Time Series Methods 125
A.2 Supplementary Figures & Tables 127

B Supplementary Materials for Chapter 3 **135**
B.1 Time Series Methodology 135
B.2 Supplementary Tables & Figures 138

C Supplementary Materials for Chapter 4 **153**

List of Figures

1.1 Evolution of the Afar rift from 11Ma 2
1.2 GNSS vectors and focal mechanisms in the Afar rift 3
1.3 Stages of continental rifting 4
1.4 Mechanisms of continental rifting 5
1.5 Depth of melt inclusions and melt lenses at MORs 7
1.6 Schematic cross-section of the magma plumbing system at Kilauea, Hawaii 8
1.7 Map of the volcanic segments, Sentinel-1 InSAR coverage, and long-term GNSS velocities in the Afar Rift. 10
1.8 Sketch of Sentinel-1 TOPS mode SAR acquisitions 12
1.9 Examples of PS and small baseline interferogram networks 13
1.10 Example interferogram network 14

2.1 Maps of the Danakil Depression and Erta 'Ale volcano. 31
2.2 Maps of surface deformation at Erta 'Ale volcano. 36
2.3 Time series of surface deformation at Erta 'Ale volcano. 37
2.4 Time series of rift extension at Erta 'Ale volcano 38
2.5 Co-intrusive interferograms, best-fit models, and a cross-section of model sources for Erta 'Ale volcano 39
2.6 Sketch of SAR lava lake shadows 42
2.7 Erta 'Ale lava lake depths and edifice deformation from 2014-19 43
2.8 Cumulative lava flow area from the 2017-19 Erta 'Ale eruption 46

3.1 Map of the volcanic segments, Sentinel-1 InSAR coverage, and long-term GNSS velocities in the Afar Rift. 61
3.2 Line of sight velocities for each track over Afar for 2014-19. 67
3.3 3D surface velocities and errors over Afar for 2014-19 69
3.4 2014-19 rift-perpendicular and vertical velocities for four cross-rift profiles and four volcanic regions in Afar. 71
3.5 2014-19 rift-perpendicular velocities for 21 cross-rift profiles in Afar. . . 72
3.6 2014-19 time series of vertical displacements at five volcanic centres in Afar. 74

4.1 Map of the Afar rift and sketch of viscoelastic model setup 90
4.2 Overall model RMSE for each model setup 94
4.3 Map and time series of data, model, and residual displacements 96
4.4 Cross-rift profiles of data and model displacements 97

5.1 Depth of magma lenses at MORs and in Afar 115

A.1 Comparison of atmospheric corrections at Erta 'Ale volcano. 128
A.2 Interferograms and modelled phase for pre-eruptive deformation at Erta 'Ale. 129
A.3 Interferograms and modelled phase for post-intrusive deformation at Erta 'Ale. 129
A.4 RSLC images of the Erta 'Ale lava lake. 130
A.5 Time series of Erta 'Ale lava lake depths. 131
A.6 Time Series of Erta 'Ale north pit depths. 132

B.1 Change in LOS RMSE following atmospheric corrections for all frames over Afar 140
B.2 Spatial and temporal variation in LOS residual displacements for all frames over Afar 144
B.3 Test of the influence of a time series phase-bias on cumulative LOS displacements 144
B.4 GNSS derived horizontal surface velocity fields over Afar 145
B.5 Track LOS standard deviation over Afar 146
B.6 Cross-validation test of LOS displacements in the track overlap regions . 147
B.7 Contributions of InSAR and GNSS to horizontal velocity maps 148
B.8 LOS surface deformation at Dallol with elastic model and residual displacements 149
B.9 LOS surface deformation at Nabro with elastic model and residual displacements 150

C.1 Green's function responses at magmatic sources within the Dabbahu segment 155
C.2 Temporal and spatial variation in model RMSE at the Dabbahu segment 156
C.3 Magmatic source time series at the Dabbahu segment 157
C.4 Range of models fits to LOS displacement time series at various points . 159

List of Tables

2.1 Optimal pre-eruptive and co-intrusive model geometries for Erta 'Ale . . 41

A.1 Photos and field reports of the Erta 'Ale lava lake. 127

B.1 Details of the 12 Sentinel-1 frames used for processing over Afar. 138

C.1 Magmatic source volume changes at the Dabbahu segment 154

Nomenclature

List of acronyms

2D	2 Dimensional
3D	3 Dimensional
AFVS	Afdera Volcanic Segment
AGVS	Asal-Ghoubbet Volcanic Segment
ALVS	Alayta Volcanic Segment
APS	Atmospheric Phase Screen
BLUE	Best Linear Unbiased Estimator
CEDA	Centre for Environmental Data Analysis
CMER	Central Main Ethiopian Rift
COMET	Centre for Observation and Modelling of Earthquakes, Volcanoes and Tectonics
DEM	Digital Elevation Model
DMHVS	Dabbahu-Manda-Hararo Volcanic Segment
E	East
EAR	East African Rift
EAVS	Erta 'Ale Volcanic Segment
ECMWF	European Centre for Medium-Range Weather Forecasts
ERS	European Remote Sensing
ESA	European Space Agency
GACOS	Generic Atmospheric Correction Online Service

GAR	Gulf of Aden Rift
GBIS	Geodetic Bayesian Inversion Software
GMT	Generic Mapping Tools
GNSS	Global Navigation Satellite Systems
InSAR	Interferometric Synthetic Aperture Radar
ITRF	International Terrestrial Reference Frame
LiCSAR	Looking into Continents from Space with Synthetic Aperture Radar
LOS	Line Of Sight
MCMC	Markov Chain Monte Carlo
MER	Main Ethiopian Rift
MIVS	Manda-Inakir Volcanic Segment
MODIS	Moderate Resolution Imaging Spectroradiometer
MOR	Mid-Ocean Ridge
N	North
NASA	National Aeronautics and Space Administration
NE	North-East
NERC	Natural Environment Research Council
NMER	Northern Main Ethiopian Rift
NVR	Nabro Volcanic Range
NW	North-West
PDF	Probability Density Function
PSI	Persistent Scatterer Interferometry
RMS	Root Mean Square
RMSE	Root Mean Square Error
RSLC	Re-sampled Single Look Complex
RSR	Red Sea Rift

S	South
SAR	Synthetic Aperture Radar
SBAS	Small Baseline Subset
SE	South-East
SLC	Single Look Complex
SMER	Southern Main Ethiopian Rift
SRTM	Shuttle Radar Topography Mission
SW	South-West
TAVS	Tat 'Ale Volcanic Segment
TOPS	Terrain Observation with Progressive Scans
VCM	Variance-Covariance Matrix
W	West

List of symbols

α	Satellite Heading	[°]
$\Delta\rho$	Satellite Range Change	[rad]
Δh	Change in Lava Lake Height	[m]
ΔP	Pressure Change	[Pa]
η	Viscosity	[Pa s]
λ	Lamé's First Parameter / Elastic Modulus	[Pa]
μ	Lamé's Second Parameter / Shear Modulus	[Pa]
ν	Poisson's Ratio	
ϕ	Rift Axis Angle	[°]
ρ	Density	[kg m^{-3}]
σ^2	Variance	[m^2]
σ_1	Direction of Maximum Compressive Stress	[Pa]
σ_3	Direction of Minimum Compressive Stress	[Pa]

θ	Satellite Incidence Angle	[°]
c	Constant Displacement Offset	[m]
d	Data Vector	
d_x	Total Displacement at Epoch x	[m]
E	East Horizontal Displacement	[m]
G	Decision Matrix	
g	Gravitational Acceleration	[m s^{-2}]
h	Elastic Lid Thickness	[km]
$H1$	Rift-perpendicular Horizontal Displacement	[m]
$H2$	Rift-parallel Horizontal Displacement	[m]
i_{xy}	Displacement between Epochs x and y	[m]
K	Laplacian Scale Factor	
L	Line of Sight Displacement	[m]
M	Number of Pixels	
m	Model Vector	
N	North Horizontal Displacement	[m]
Q_{dd}	Data Variance-Covariance Matrix	
Q_{mm}	Model Variance-Covariance Matrix	
r_{xy}	Displacement Residual at Pixel x and Epoch y	[m]
t_x	Time at Epoch x	[s]
v	Velocity	[m s^{-1}]
w	Lava Lake Pit Shadow Width	[m]
Z	Vertical Displacement	[m]

Chapter 1

Introduction

Continental rifting and sea floor spreading form an integral part of global plate tectonics. As continental rifts develop, lithospheric thinning may facilitate the production of magma through decompression melting (McKenzie, 1978). Where rifts are assisted by mantle plumes, additional heating of the lithosphere of 100-200°C is sufficient to produce enough magmatic material to account for the large igneous provinces associated with the onset of oceanic rifting (White and McKenzie, 1989). Flood basalts in Ethiopia, Saudi Arabia, and Yemen are attributed to the onset of rifting in East Africa $\sim$ 30 Ma, initiated by a mantle plume below the Afar region of Ethiopia (Furman et al., 2006). Active rifting in East Africa and the Afar region is on-going, with development of the rift providing a unique example of on-land incipient sea floor spreading in northern Afar.

During the transition from continental rifting to sea floor spreading, the role of shallow magmatic intrusions in accommodating the spatial and temporal distribution of extensional strain is still poorly understood. In extremely remote settings such as Afar, satellite remote sensing provides the opportunity to observe both long-term and short-term surface processes over wide spatial scales. In this thesis, I use satellite-borne interferometric synthetic aperture radar (InSAR) observations of ground motions in the Afar rift to map and model the localisation of extensional strain, the role of magmatic intrusions in accommodating this strain, and the structure of shallow magmatic plumbing systems at spreading centres. In this chapter I will introduce the state of rifting in Afar, summarise the present understanding of magma plumbing systems in extensional settings, and provide an overview of the uses of InSAR observations and modelling for investigating volcanic systems. I will also define the primary aims and objectives of this thesis, and provide a roadmap through the works displayed in Chapters 2-5.

1.1 Afar Tectonic Setting

The Afar triangle lies at the northern-most tip of the East African Rift (EAR) in Ethiopia, Djibouti, and Eritrea. Rifting in this region initiated $\sim$ 30 Ma with voluminous flood basalts associated with a large mantle upwelling (Wolfenden et al., 2004, Furman et al., 2006, Rooney et al., 2012). This mantle plume is observable in the present day as a region of low seismic velocities in the upper-mantle below the Afar region (Ritsema et al., 1999, Chang et al., 2011, Civiero et al., 2015). Since the initiation of continental rifting, the Afar region has developed into a rift-rift-rift triple junction between the NW-SE trending Red Sea Rift (RSR) and Gulf of Aden Rift (GAR), and the NE-SW trending Main Ethiopian Rift (MER); accommodating the divergence of the Arabian Plate, the Nubian Plate, and the Somalian Plate (e.g. Corti, 2009). The evolution of the triple junction from 11 Ma to the present day is shown in Figure 1.1 with the initiation and propagation of the MER southwards from Afar, combined with

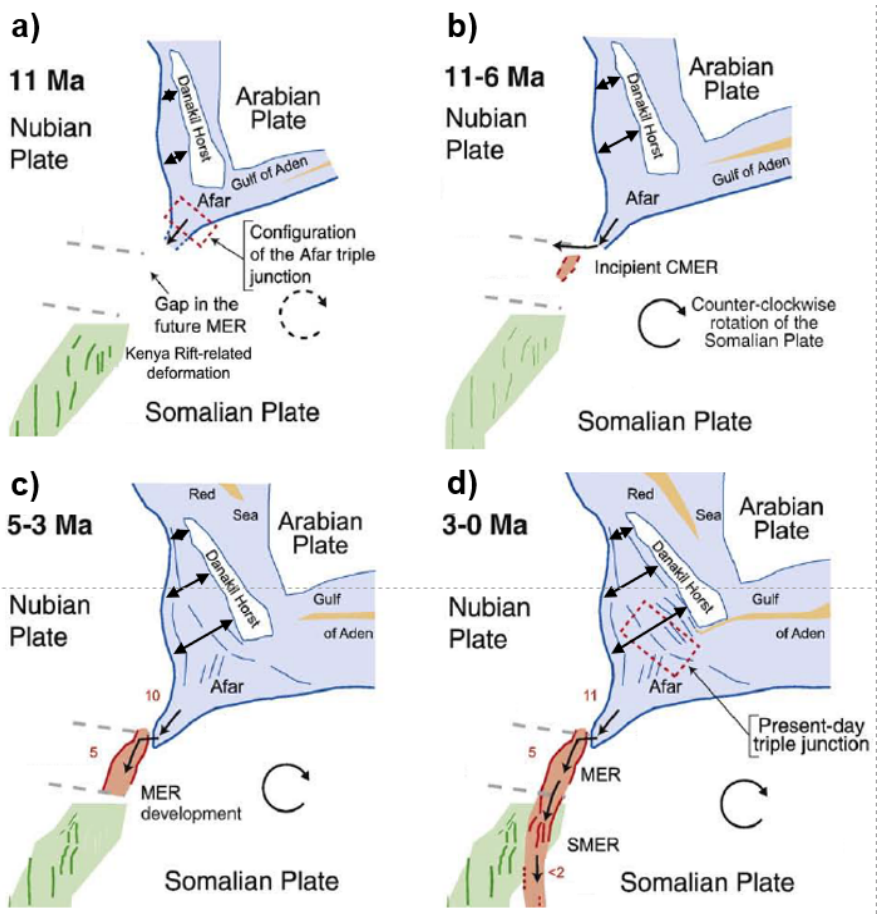

Figure 1.1: Evolution of the Afar rift from 11Ma to present from Bonini et al. (2005). Arrows in Afar highlight the 'saloon-door' opening of the Afar triangle with rotation of the Danakil Horst (Kidane, 2016), with red numbers on the Main Ethiopian Rift (MER) showing the estimated age of the onset of rifting (Ma) in the Central MER (CMER) and Southern MER (SMER). *Figure modified from Corti (2009), based on Bonini et al. (2005).*

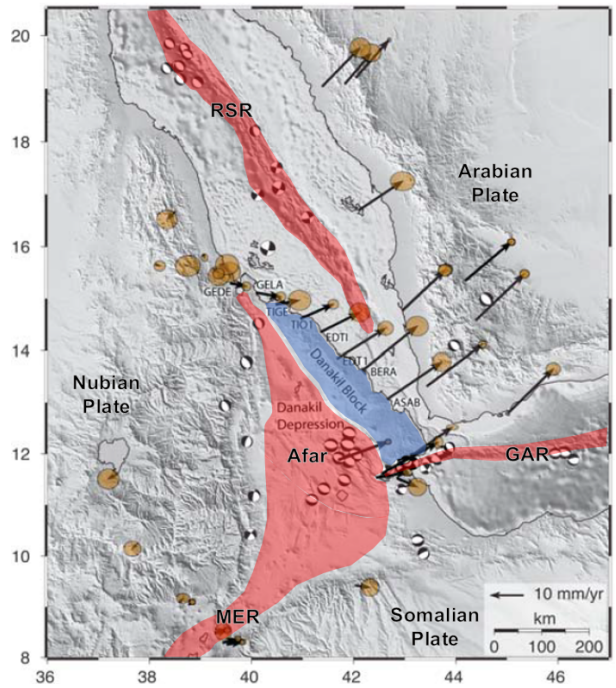

Figure 1.2: Magmatic rifts (red) in the Afar region, with the Danakil block (blue), GNSS vectors (with 95% error ellipses) showing plate motions relative to the Nubian Plate, and earthquake focal mechanisms (Havard catalogue 1976-2009). RSR - Red Sea Rift, GAR - Gulf of Aden Rift, MER - Main Ethiopian Rift. *Figure modified from McClusky et al. (2010).*

the opening of the Afar triangle with the motion of the Arabian plate (Wolfenden et al., 2004, Corti, 2009).

Observations of current plate motions using Global Navigation Satellite Systems (GNSS) show that, relative to a stable Nubian Plate, the Somalian Plate is moving towards the SE at a rate of 4-6 mm/yr (McClusky et al., 2010, Saria et al., 2014), while the Arabian plate is moving towards the NE at a rate of 18-20 mm/yr (McClusky et al., 2010, ArRajehi et al., 2010). The extension of 18-20 mm/yr over the RSR is transferred gradually onto on-land RSR segments in northern and central Afar from $\sim$ 13-16 °N, producing the anti-clockwise motion of the Danakil Horst micro-plate (Kidane, 2016, Viltres et al., 2020), as shown in Figures 1.1 and 1.2. As the triple junction develops, the on-land portions of the RSR in northern and central Afar and the GAR in southern Afar are predicted to connect in $\sim$ 5 Ma (Doubre et al., 2017, Eagles et al., 2002).

The spatial variation in rifting styles from the MER, the Afar Rift, and the oceanic RSR can be thought of as an analogue to the development of a continental rift through time. Figure 1.3 shows a schematic of rift development from flood basalts to oceanic rifting, where the Afar rift lies between the stages shown in Figures 1.3d-e. Magmatism is thought to play a crucial role in assisting continental break-up, by reducing the stress required to rupture the lithosphere (Buck, 2006). As shown in Figure 1.4, melt

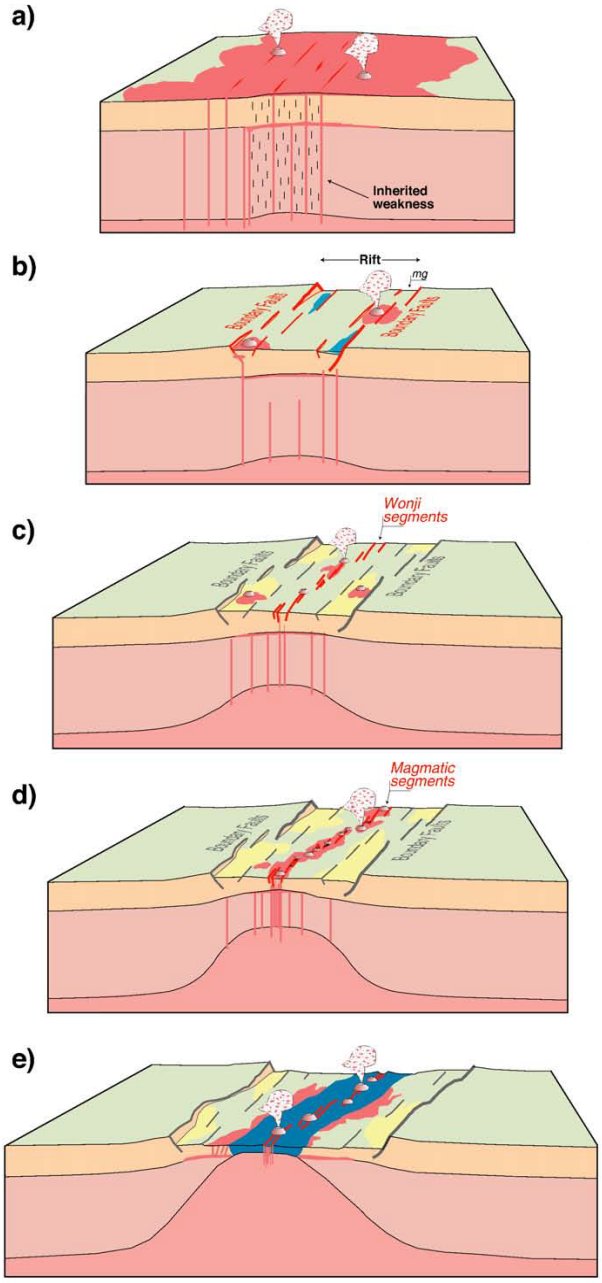

Figure 1.3: The stages of continental rifting in East Africa: (a) Flood basalts where inherited lithospheric weaknesses help to localise the onset of rifting. (b) Extension is largely accommodated by boundary faults with the creation of a rift valley. (c) Deformation becomes focussed within the rift valley (e.g. Wonji fault segments in the Main Ethiopian Rift). (d) Increased magmatism in the rift valley helps to further localise extension into discrete magmatic rift segments (Ebinger, 2005). (e) Further magmatism, rift localisation, and lithospheric thinning assists the transition into oceanic spreading centres, with erupted and intruded lavas forming seaward-dipping reflectors observed at passive margins. The northwards trend of rift maturity in East Africa may be represented by current rifting styles in the Kenyan rift (b), the Southern Main Ethiopian Rift (c), the Northern Main Ehtiopian Rift (d), and the oceanic Red Sea Rift (e). *Figure from Corti (2009), based on Ebinger (2005).*

intrusions in the lithosphere may also contribute to the localisation of extensional strain, further promoting the development of the rift (Corti, 2009, Ebinger, 2005).

The Afar rift is indicative of a late-stage continental rift in the transitional phase between continental and oceanic style rifting (e.g. Hayward and Ebinger, 1996). Seismic reflection and receiver function studies indicate that the crust below Afar is extensively thinned and altered compared to the surrounding Ethiopian highlands. Crustal thicknesses range from 20-45 km below the Ethiopian highlands, which thins abruptly to $\sim$ 15-30 km in the MER and central Afar, and $\sim$ 15-20 km in northern Afar (Lavayssière et al., 2018, Hammond et al., 2011, Bastow and Keir, 2011, Tiberi et al., 2005). The crust thins further to $\sim$ 10 km in the submarine oceanic portions of the RSR and GAR (Hammond et al., 2011, Maguire et al., 2006). Seismic anisotropy also indicates a high proportion of melt within the Afar crust (Gallacher et al., 2016), particularly below spreading segments in Afar (Hammond and Kendall, 2016, Hammond, 2014, Stork et al., 2013). This is in agreement with observations of shallow seismicity attributed to the movement of melt within the crust (Illsley-Kemp et al., 2018b). Petrological studies of erupted deposits also indicate that the temperature of the upper mantle below Afar is elevated (Ferguson et al., 2013), allowing the production of large quantities of melt (Armitage et al., 2015). Gallacher et al. (2016) observe an along-rift thinning of the lithosphere-asthenosphere boundary (LAB) from 120 $\pm$ 55 km depth below the MER to $<$ 81 km depth below Afar, which is consistent with petrological estimates of maximum

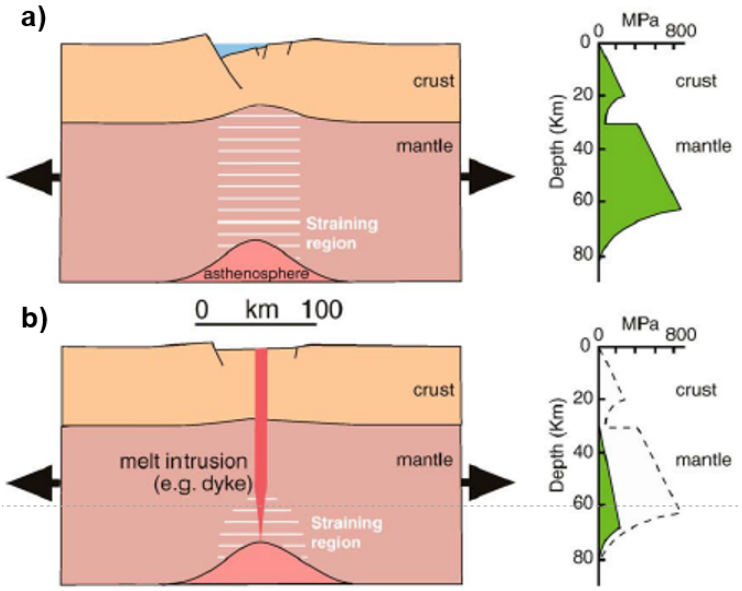

Figure 1.4: First-order mechanisms of continental rifting from tectonic (a) and magmatic (b) accommodated extension. Crustal strength profiles highlight the lower yield stress required to separate two lithospheric blocks with magmatic intrusions. *Figure from Corti (2009), based on Buck (2006) and Ebinger (2005).*

melting depths of 53-88 km for the CMER (Rooney et al., 2005), and 80 ± 45 km for Afar (Ferguson et al., 2013).

The development of discrete rifting segments is a key feature in the evolution of the rift (Hayward and Ebinger, 1996, Ebinger and Casey, 2001, Keir et al., 2015), as shown in Figure 1.3. With rift development, magmatism and extension are expected to concentrate into these segments which eventually form into Mid-Ocean Ridge (MOR) spreading centres (Makris and Ginzburg, 1987). Further indicators of the development of oceanic-style rifting include seismicity between segments in Afar that suggest the formation of a proto-transform fault (Illsley-Kemp et al., 2018a), gravity profiles showing that high density crust being formed at the centre of rift segments (Lewi et al., 2016), the observation of symmetrical magnetic reversals about rift segments (Bridges et al., 2012), and the presence of shallow magma bodies beneath spreading centres (Pagli et al., 2012, Xu et al., 2017). While these observations suggest that the Afar rift is in a transitional state between continental and oceanic style rifting, it is not well established how far spreading segments in Afar are through this process.

1.2 Magma Plumbing Systems in Extensional Settings

Magmatism in extensional settings is assisted by the orientation of minimum compressive stress (σ_3), perpendicular to the rift zone, promoting shallow vertical intrusions such as dykes (e.g. Tibaldi et al., 2014). These settings include continental rifts, such as the MER, mid-ocean ridges (MORs), such as the East Pacific Rise (EPR), and volcano flank rifts, such as the East rift-zone (ERZ) at Kilauea, Hawaii. In settings with thinned crust ($\lesssim$ 15 km), such as MORs (Phipps Morgan et al., 1987, Bown and White, 1994, Carbotte and Scheirer, 2004), Afar (Hammond et al., 2011, Bastow and Keir, 2011, Tiberi et al., 2005), and the Kilauea ERZ (Ryall and Bennett, 1968, Hill and Zucca, 1987), the composition of magmatism is predominately basaltic (e.g. Kay et al., 1970, Macdonald, 1949, Barberi et al., 1972) with relatively quick transport of melt from depth to the shallow plumbing systems giving little time for fractional alteration or crustal assimilation in the melt. In rift settings with thicker crust ($\gtrsim$ 15 km), such as the MER (Dugda et al., 2005, Chambers et al., 2019) and in Iceland (Darbyshire et al., 2000, Kumar et al., 2007), magmatism can be more explosive with both basaltic and rhyolitic melts being produced (e.g. Jakobsson, 1972, Self and Sparks, 1978, Fontijn et al., 2018, Iddon et al., 2019).

At MORs, the depth of a persistent magma lens below the rift axis is dependant, to the first order, on the spreading rate and the crustal thickness (e.g. Phipps Morgan and Chen, 1993). Slow and ultra-slow spreading ridges such as the Mid-Atlantic Ridge (MAR) are defined by a full spreading rate of $\lesssim$ 40 mm/yr (Wanless and Behn, 2017,

Dick et al., 2003). These rifts are typically host to axial grabens (Dick et al., 2003, Buck et al., 2005, Cannat et al., 2019), with spatially (along-axis) and temporally intermittent magma lenses where melt is distributed throughout the crust up to ~ 8 km depth (see Figure 1.5; Wanless and Behn, 2017, Dunn et al., 2005). In contrast, fast spreading ridges with full spreading rates of $\gtrsim 80$ mm/yr, such as the EPR, show a consistent magma lens at 1-3 km depth below an axial rise (Wanless and Behn, 2017, Marjanović et al., 2014, Carbotte et al., 2013, Sinton and Detrick, 1992). Dick et al. (2003) show how the rift spreading rate and crustal thickness largely define whether the MOR develops either an axial ridge and shallow magma lens for faster spreading rates and a thin crust, or an axial graben and distributed melt for slower spreading rates and a thicker crust. Outliers in this trend include MORs with additional supply of melt at hot-spots, such as at the Galápagos Spreading Centre (GSC; Chen and Lin, 2004, White et al., 2008, Boddupalli and Canales, 2019), Axial Seamount on the Juan de Fuca Ridge (Sigmundsson, 2016, Nooner and Chadwick, 2009), and the Reykjanes Ridge, offshore Iceland (Chen, 2000, Phipps Morgan et al., 1987). Elevated mantle temperatures and additional melt supply mean that spreading centres with slower spreading rates may exhibit similar features to a fast-spreading ridge, such as an axial rise and a shallow magma lens (Chen and Lin, 2004, Chen and Morgan, 1996). The magma plumbing system at Axial Seamount shows similarities to sub-aerial rift volcanoes (Sigmundsson, 2016), where repeated dyke intrusions are sourced from a magma reservoir beneath the central caldera (Hefner et al., 2020, Nooner and Chadwick, 2009).

Shallow magma reservoirs ($\lesssim 5$ km depth) have also been observed at several sub-aerial volcanoes and rift zones (e.g. Jerram and Bryan, 2015). The ERZ at the Kilauea volcano, Hawaii, is formed from the ocean-ward slip of the island along basal décollement to the S/SE of Kilauea (e.g. Denlinger and Okubo, 1995, Liu et al., 2018). Persistent activity since the 1800s at the summit caldera and ERZ vents including Pu'u'Ō'ō since 1983 (Patrick et al., 2020; and references therein), is sourced from a central magma reservoir at 3-5 km depth below and ~ 2 km south of the Kilauea summit caldera (Anderson et al., 2015, Poland et al., 2014). This reservoir is hydraulically connected to

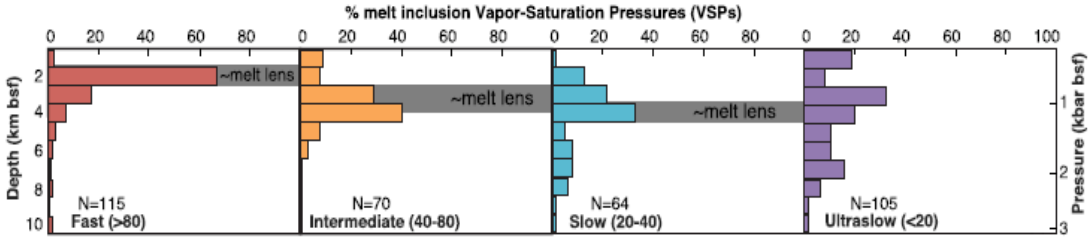

Figure 1.5: Histograms of the percentage melt inclusion Vapour Saturation Pressures at four classes of mid-ocean ridge, based on the full spreading rate in mm/yr. Grey bars indicate the approximate depth of seismically imaged melt lenses. *Figure from Wanless and Behn (2017).*

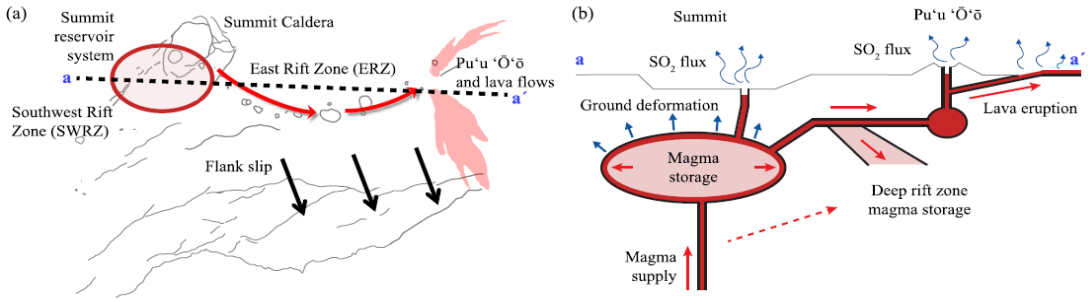

Figure 1.6: (a) Map of the Kilauea volcano and East Rift Zone (ERZ), Hawaii, with (b) physics-based schematic cross-section along profile a-a' showing the routes of magma supply and storage between the Kilauea summit and ERZ. *Figure from Anderson and Poland (2016).*

both the shallow reservoir at 1-2 km depth below the summit Halema'uma'u crater and lava lake (Poland et al., 2014, Bagnardi et al., 2014, Anderson et al., 2015), and the ERZ plumbing system which maintains a smaller reservoir below Pu'u'Ō'ō, 15-20 km down-rift from the summit caldera (see Figure 1.6; Patrick et al., 2019, 2015, Anderson and Poland, 2016). Similar shallow rift plumbing systems, fed from central magma reservoirs, are also present on the flanks of volcanoes such as Piton de la Fournaise, Réunion (e.g. Michon et al., 2015, Peltier et al., 2005); Ambryn, Vanuatu (Shreve et al., 2019, Hamling et al., 2019); and Etna, Italy (e.g. Froger et al., 2001, Harris et al., 2000, Chauhan et al., 2020). In contrast to rift zones formed from far-field stresses, such as plate motions, these volcano flank rift zones are formed from near-field stresses, often due to the gravitational collapse of the edifice, which may not be persistent over long time scales. As such, these rift plumbing systems have much smaller spatial extents than the rift zones in Iceland, and in Afar.

Sub-aerial sea-floor spreading of the MAR in Iceland is caused by the presence of a mantle plume (e.g. Wolfe et al., 1997, Ito et al., 1999) resulting in anomalously thick (up to ~ 40 km) oceanic crust (Darbyshire et al., 2000, Jenkins et al., 2018). Plate extension of ~ 20 mm/yr (DeMets et al., 1994) is accommodated within broad rift zones in Iceland (Karson, 2017), producing both effusive and explosive volcanism (Gudmundsson, 2000). Major rifting events in Iceland include Laki-Grímsvötn, 1783-85 (e.g. Thordarson and Self, 1993), Askja, 1874-76 (e.g. Sigurdsson and Sparks, 1978b), Krafla, 1975-84 (e.g. Buck, 2006), and Bárdarbunga, 2014-15 (e.g. Sigmundsson et al., 2014). These effusive fissure swarms and dyke intrusions are fed by the shallow lateral flow of melt into the rift zones from magma reservoirs below central volcanoes (Sigurdsson and Sparks, 1978a, Gudmundsson et al., 2016). Smaller rifting events have also been shown to have the potential to trigger larger eruptions at central volcanoes, such as the effusive flank dyke intrusion which preceded the explosive 2010 Eyjafjallajökull eruption (Sigmundsson et al., 2010). This interaction between rift zone and central volcano shows similarities to the plumbing systems found at other hot-spot rift locations such as Kilauea (Poland

et al., 2014), Axial Seamount (Sigmundsson, 2016), and Afar (Wright et al., 2006).

Spreading centres in Afar are perhaps the closest sub-aerial analogy for the magmatic plumbing systems at MORs, due to the thinned crust, especially in northern Afar, and high melt flux from the presence of the Afar plume (Hayward and Ebinger, 1996, Pagli et al., 2012, Wright et al., 2012). The on-land portion of the RSR is expressed in northern Afar by the Erta 'Ale volcanic segment (EAVS), and in central Afar by the Dabbahu-Manda-Hararo volcanic segment (DMHVS). As shown in Figure 1.7, the Tat 'Ale, Afdera, and Alayta volcanic segments (TAVS, AFVS, and ALVS respectively) accommodate the strain in the region between the EAVS and the DMHVS (Pagli et al., 2014), with the early-stages of transform faults forming between these segments (Illsley-Kemp et al., 2018a). Recent volcanism is abundant in Afar with several eruptions at volcanic centres on the EAVS being sourced from shallow magma reservoirs (Amelung et al., 2000, Nobile et al., 2012, Pagli et al., 2012, Field et al., 2012a, Xu et al., 2017), with an axial sill at $\sim$ 1 km depth at the Alu-Dalafilla volcanic centre (Pagli et al., 2012). The presence of shallow melt bodies on the slow-spreading segment raises questions on the first order controls on MOR plumbing systems and how these controls may be affected by additional melt flux at hot-spots. While spreading centres in Afar raise key issues in the structure of rift-zone plumbing systems, and their evolution with rift development, they are relatively under-studied in comparison to rift zones in Iceland, and plumbing systems such as at Kilauea. In Chapter 2 of this thesis, I provide an in-depth analysis of a long-lived plumbing system at the Erta 'Ale volcano, while in Chapter 3 I investigate the localisation of extension over the rift and the related magmatic deformation at spreading centres in Afar.

A major rifting event on the DMHVS from 2005-10 sourced melt both from depth and from the nearby Dabbahu and Gabho volcanic centres (Wright et al., 2006, Ayele et al., 2009, Hamling et al., 2010, Barnie et al., 2016). The interaction of multiple sources and the total magnitude of the eruption is comparable to the 1975-84 Krafla rifting episode in Iceland, as well as the 1978 Asal-Ghoubbet volcanic segment (AGVS) eruption in southern Afar (Wright et al., 2012). Major rifting events such as these play a crucial role in accommodating long-term plate motions; despite this, the dynamics of the plumbing systems involved throughout the rifting cycle are still poorly understood (Ebinger et al., 2010, Barnie et al., 2016). Spatial and temporal limitations hinder our ability to study this further as Iceland and Afar are the only locations where large scale rifts are observable sub-aerially, and these large rifting events are rarer than smaller eruptions and intrusions. Wright et al. (2012) suggest that future models of the rifting cycle should include both realistic crustal structure at spreading segments, which is likely to be thermally weakened than the surrounding crust, and the movement of magma within the rift zone. I address this in Chapter 4 by making use of a $\sim$ 15 year

time series to constrain a new model of the long-term post-rifting response to the 2005 DMHVS rifting episode.

1.3 InSAR Observations and Modelling

In the following section I will outline the justification for using InSAR to study volcanic processes in the Afar rift, provide a brief overview of InSAR processing and time series analysis, and describe some of the common modelling practices used to interpret surface deformation at volcanic centres. Comprehensive descriptions of InSAR processing and time series analysis can be found in works such as Hanssen (2001), Ferretti et al. (2007), and Hooper et al. (2012), while overviews of geodetic modelling

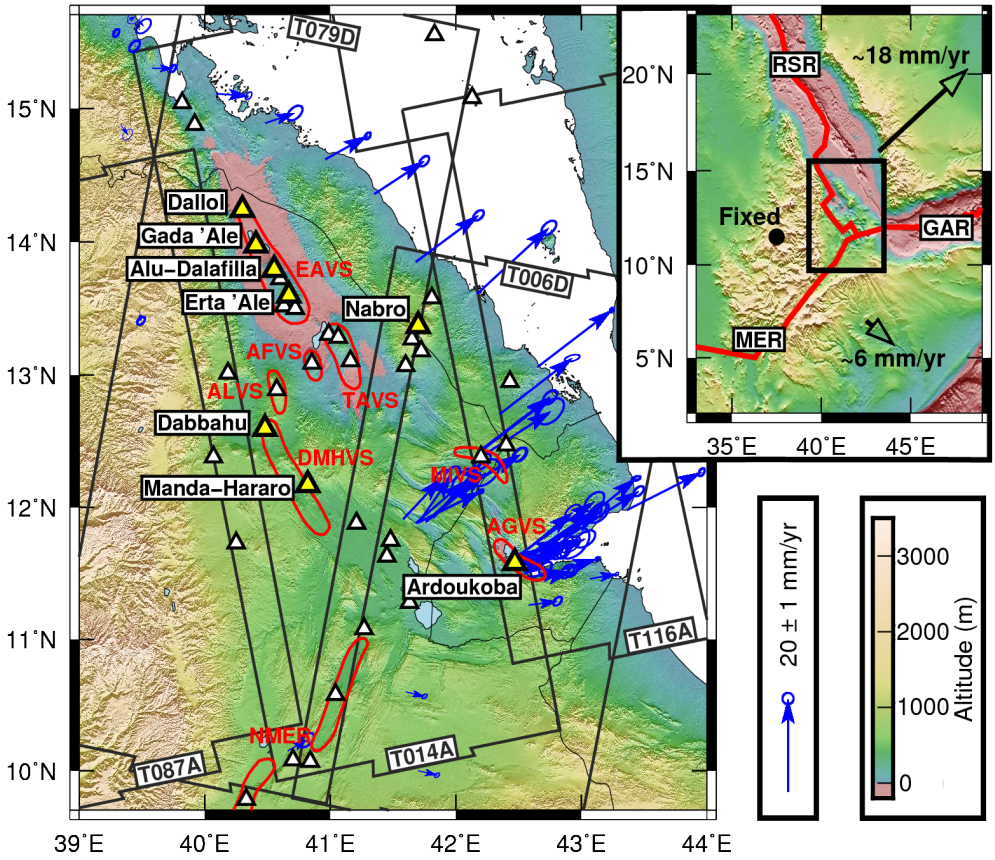

Figure 1.7: The Afar Rift with white triangles indicating Holocene volcanoes and key volcanoes highlighted in yellow. Simplified volcanic segments (VS) are shown in red: AFVS - Afdera, ALVS - Alayta, AGVS - Asal-Ghoubbet, DMHVS - Dabbahu-Manda-Hararo, EAVS - Erta 'Ale, MI - Manda-Inakir, NMER - Northern Main Ethiopian Rift, TAVS - Tat 'Ale. A subset of GNSS velocity vectors with 95% confidence error ellipses (blue arrows) from (King et al., 2019) show the long-term plate motions relative to the Nubian plate. Grey box outlines show the Sentinel-1 coverage from three ascending (T014A, T087A, T116A) and two descending (T006D, T079D) tracks. Inset map shows the relative movement of the Arabian and Somalian plates to the Nubian plate, with plate boundaries from Bird (2003). RSR - Red Sea Rift, GAR - Gulf of Aden Rift, MER - Main Ethiopian Rift. *Figure and caption from Moore et al. (in review).*

practices in volcanic settings can be found in works such as Segall (2010).

The extreme remote environment of Afar, combined with recent geopolitical instability in the region, means that volcanic centres in Afar are poorly monitored, with ground observations generally limited to location specific field surveys. Sparse networks of continuous seismic and GNSS stations offer monitoring of large events and the regional tectonics (e.g. Pagli et al., 2014, Chambers et al., 2019; and references therein), while observations of local events at volcanic centres are limited to temporary networks (e.g. Jones et al., 2012, Illsley-Kemp et al., 2018b). Satellite remote sensing provides the opportunity to regularly monitor surface processes across wide spatial scales. Synthetic Aperture Radar (SAR) holds an advantage over other remote sensing techniques, such as optical and thermal imaging, in that observations can be made regardless of time of day or weather conditions. InSAR has been used to detect ground motions at volcanic centres in Afar since the launch of the European Space Agency's (ESA) European Remote Sensing (ERS) satellites in 1992, and later several other missions (e.g. Atzori et al., 1996, Amelung et al., 2000). The ESA Sentinel-1 satellites (A and B) have been in operation since 2014 and offer free data usage, with 12-24 day track repeat times over Afar and up to $\sim$ 20×5 m spatial resolution. Figure 1.7 shows the coverage of ascending (South-North flight direction) and descending (North-South flight direction) Sentinel-1A/B tracks over Afar. In this thesis I make use of the new Sentinel-1 observations to develop maps and time series of surface displacements with significantly improved spatial and temporal resolution to previous InSAR studies in Afar.

SAR interferometry differences the phase component of two radar acquisitions in order to resolve the change in range ($\Delta\rho$) from the satellite to the surface between the two epochs. By accounting for contributing factors such as the topography ($\Delta\rho_{topo}$), differences in the satellite orbits ($\Delta\rho_{orbit}$), tropospheric ($\Delta\rho_{tropos}$) and ionospheric ($\Delta\rho_{ionos}$) signals, and other sources of noise ($\Delta\rho_{noise}$), a map of surface displacements ($\Delta\rho_{def}$) between the two epochs can be resolved (Equation 1.1).

$$\Delta\rho = \Delta\rho_{topo} + \Delta\rho_{orbit} + \Delta\rho_{atmos} + \Delta\rho_{ionos} + \Delta\rho_{noise} + \Delta\rho_{def} \tag{1.1}$$

The automated LiCSAR (Looking into Continents from Space with SAR) tool is specialised for batch Sentinel-1 TOPS (Terrain Observation with Progressive Scans) mode data processing (Lazeckỳ et al., 2020, González et al., 2016) which utilises GAMMA software (Werner et al., 2000). All Sentinel-1 data used in this thesis is processed using LiCSAR. Lazeckỳ et al. (2020) provide an in depth LiCSAR processing description, with more general InSAR processing practices outlined by works such as Hanssen (2001) and Ferretti et al. (2007). Briefly, single look complex images (SLCs) are formed from merging bursts and swaths within a single track (see Figure 1.8). LiCSAR defines a

system of track frames such that the resulting SLCs have broadly consistent dimensions ($\sim$ 250×250 km). SLCs are then resampled to a reference image to produce resampled SLCs (RSLCs), which can then be differenced in the phase domain to produce wrapped interferograms (values between 0-2π) between any two RSLCs. Phase coherence maps show the change in surface properties within a group of pixels. Incoherence between two epochs can be produced by variations in surface scattering such as from water or vegetation. Coherent interferograms are then filtered to remove short-wavelength noise signals, and unwrapped to resolve the cumulative phase range change in the satellite line of sight (LOS).

Long-term trends in surface deformation can be resolved by developing a time series of displacements from a network or sequence of interferograms. Stacking is the simplest method of resolving time series, where several interferograms are averaged to resolve displacement rates whilst reducing background noise. Using stacking, the sequence is vulnerable to interferograms that are incoherent or particularly noisy. Persistent scatter interferometry (PSI) utilises pixels which are dominated by a single scatterer in a sequence of interferograms, reducing the noise associated with varying phase reflections from several distributed scatterers within a pixel (Hooper et al., 2012). Using only PS pixels, PSI is then able to construct a network of interferograms with respect to a single "primary" acquisition as shown in Figure 1.9a. Small baseline methods use connections between epochs with relatively short temporal baselines to minimise pixel decorrelation often seen in long interferograms. By utilising multiple connections over

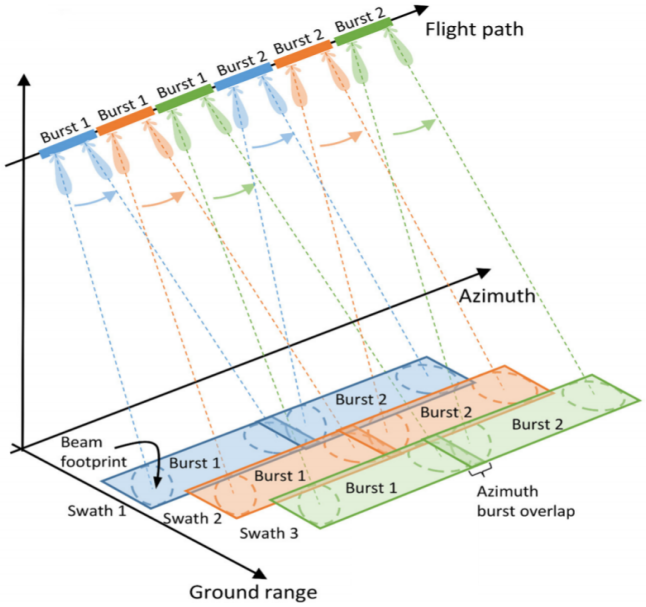

Figure 1.8: Sketch of Sentinel-1 TOPS mode SAR acquisitions with sequential bursts being imaged along track in the azimuth direction consisting of three swaths in the range direction. *Figure modified from Merryman Boncori (2019).*

the same time period (see Figure 1.9b), small baseline approaches are able to produce a robust estimate of the displacement time series (Berardino et al., 2002, Lanari et al., 2007). In this thesis, I make use of the short-baseline approach to extract time series of surface deformation at volcanic centres in Afar.

Figure 1.10 shows an example interferogram network for four acquisition dates, with unknown cumulative displacement values d_1, d_2, and d_3 at epochs 1, 2, and 3 respectively. Using all available interferograms, the SBAS network shown in Figure 1.10 can be formulated as shown in Equation 1.2 and solved using a linear least squares inversion. This small-baseline style methodology is well established in extracting time series of displacements and long-term displacement rates from large networks of interferograms, and has been automated by several software packages including Π-RATE (Wang et al., 2012; and references therein), StaMPS (Hooper et al., 2012), GIAnT (Agram et al., 2013), and LiCSBAS (Morishita et al., 2020).

$$\begin{bmatrix} 1 & 0 & 0 \\ 0 & 1 & 0 \\ -1 & 1 & 0 \\ -1 & 0 & 1 \\ 0 & -1 & 1 \end{bmatrix} \begin{bmatrix} d_1 \\ d_2 \\ d_3 \end{bmatrix} = \begin{bmatrix} i_{01} \\ i_{02} \\ i_{12} \\ i_{13} \\ i_{23} \end{bmatrix} \tag{1.2}$$

Phase delays due to variations in atmospheric water vapour, pressure, and temperature, can produce significant errors in InSAR displacement time series. Methods to mitigate this effect include calculating and removing a linear trend of phase with elevation, removing an atmospheric model, and time series filtering to calculate and remove an atmospheric phase screen (APS). A linear trend of phase with elevation can occur

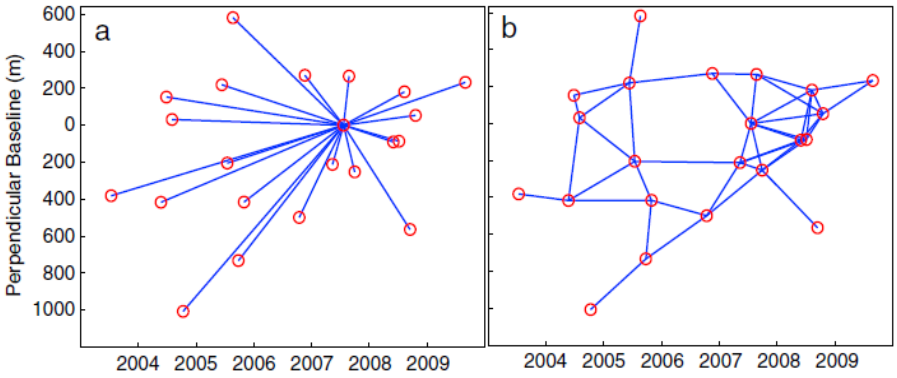

Figure 1.9: Example interferogram networks for the persistent scatterer (a) and small baseline (b) time series approaches. Red circles show SAR acquisition dates, with blue connecting lines representing interferograms. The perpendicular baseline is the distance between the satellite positions at each acquisition perpendicular to the look direction. *Figure modified from Hooper et al. (2012).*

due to an extended travel time within a stable atmosphere for pixels at lower altitudes, and may be corrected by solving for and removing this linear trend from the whole image, or spatial subsets within an image (e.g. Elliott et al., 2008, Bekaert et al., 2016). Atmospheric models, which attempt to replicate phase delays at the time of acquisition, are also widely used as they are independent of the InSAR data (e.g. Yu et al., 2017, 2018, Weiss et al., 2020, Morishita et al., 2020). In cases where these models are poorly constrained, it can be necessary to include a scaling factor to avoid introducing additional error to the dataset (e.g. Shen et al., 2019).

After these corrections have been applied to individual interferograms or epochs, time series filtering may also be required to remove residual turbulent atmospheric delays and extract long-term trends. If we assume that atmospheric noise is not temporally correlated, an APS for each epoch is calculated by applying a high-pass filter in time and a low-pass filter in space, to extract any residual atmospheric signals in the data, which is then removed from the time series (e.g. Sousa et al., 2011). APS methods generally utilise uniform filters, based on the assumption that atmospheric delays are not temporally correlated. Proposed improvements to the APS correction include incorporating global weather models (e.g. Jung et al., 2013), and the temporal variance of a pixel (e.g. Liu et al., 2011, Refice et al., 2011). In Chapter 3, I demonstrate how weighting pixels based on their spatial and temporal variance can produce an effective APS filter to extract long-term trends in surface displacements.

The modelling of InSAR and GNSS deformation signals is crucial to understanding the dynamics of local volcanic plumbing systems and regional rifting processes. Simple source solutions including planar dislocations (Okada, 1985) and point pressure sources (Mogi, 1958) within an elastic half-space are able to accurately reproduce many surface deformation signals (e.g. Amelung et al., 2000, Pagli et al., 2012, Field et al., 2012b,

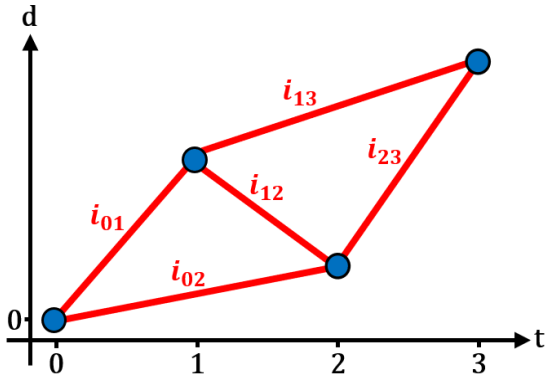

Figure 1.10: Sketch of an example interferogram network for four epochs (0, 1, 2, 3) and five connecting interferograms (i_{01}, i_{02}, i_{12}, i_{13}, i_{23}), to resolve cumulative surface displacements (d).

Hamlyn et al., 2014, Temtime et al., 2018). Limitations in these simple elastic models may arise from assuming that magma is incompressible, producing a deficit between the modelled change in volume and the observed erupted volume (Rivalta and Segall, 2008). Due to thermal alteration from magma reservoirs, pathways, and mush zones, the host rock close to magma plumbing systems is also not likely to behave elastically. While the addition of a viscoelastic "shell" around a spherical magma chamber can produce a similar deformation signal to an elastic point source, it may provide a more realistic mechanism for the temporal evolution in surface deformation (e.g. Segall, 2010, Hamlyn et al., 2014).

When modelling long-term rifting processes, it is also necessary to consider the time-dependant viscous response of the lower crust, as well as the instantaneous elastic response, to any deformation sources. Models of post-rift relaxation following Krafla 1975-84 rifting episode (Einarsson and Sigmundsson, 2006, Drouin, 2016), and the background deformation during the DMH 2005-10 rifting episode (Nooner and Chadwick, 2009, Hamling et al., 2014), find that a viscous layer is necessary below an elastic lid to reproduce the observed deformation. In Chapter 4, I expand on the work of Hamling et al. (2014) to account for the role of ongoing active magmatism in the rift zone during post-rifting viscous relaxation. While these long-term processes associated with the rifting cycle operate at depth ($\sim$ 15-30 km), InSAR and GNSS can struggle to constrain these sources as the observations are made at the surface. It is therefore vital when modelling deformation signals from InSAR and GNSS, to incorporate results from other methods such as petrology, seismicity, and magnetotellurics where possible.

1.4 Aims & Objectives

The principle aim of this thesis is to make use of new InSAR observations of ground motions to further the understanding of how far along the Afar Rift is in its transition from continental to oceanic rifting. This may be broken down into the following simple questions:

1) Where is the magma?
   Is magma being stored at shallow depths below spreading ridges, and how does the plumbing system required to sustain it compare to MORs and other rift zones?

2) Where is the strain?
   Is extension largely accommodated within spreading segments or is it more distributed across the rift zone, and does this change as the rift develops?

3) What is the rheological structure of the crust?
   How do the materials below spreading segments react to large rifting events, and does the strength vary throughout the rifting cycle?

I aim to answer these questions by completing the following key objectives, as described in detail in Section 1.5:

1) Produce InSAR observations and models of shallow sources associated with surface deformation at spreading centres in Afar.

2) Build a coherent map of surface velocities using Sentinel-1 observations, and develop improvements to APS filtering and GNSS referencing in remote regions.

3) Develop new models of viscoelastic post-rifting relaxation using longer time series that are now available, accounting for on-going magma movement at volcanic centres throughout the rifting cycle.

1.5 Thesis Roadmap

The next three chapters of this thesis consist of journal articles with the purpose of attempting to answer each of the three principle objectives outlined previously. Chapter 2, "The 2017 Eruption of Erta 'Ale Volcano, Ethiopia: Insights in the Shallow Axial Plumbing System of an Incipient Mid-Ocean Ridge", explores the deformation sources and pressure state within the shallow plumbing system below the Erta 'Ale volcano in the build-up to, and during the 2017-19 flank eruption. These observations and models provide a novel insight into the shallow and deep magma storage and magma pathways on the EAVS which has previously been shown to be capable of hosting shallow axial magma lenses (Pagli et al., 2012). The work in this chapter has been reviewed and published in the journal *Geochemistry, Geophysics, Geosystems*, **20**(12).

Chapter 3, "Rift Focussing and Magmatism During Late-Stage Rifting in Afar, Ethiopia", widens the scale of observations to cover the whole of Afar in order to observe how extension across the whole region is accommodated. Identifying differences between spreading segments in Afar is also crucial in understanding the varying rifting styles in Afar, as outlined by the axial ridge at the EAVS and axial graben at the DMHVS. I also identify ongoing deformation at several volcanic centres including Dallol and Erta 'Ale (as shown in Chaper 2) on the EAVS, the off-axis Nabro volcano, and large-scale deformation at the DMHVS. The work in this chapter is in revision with the journal *Journal of Geophysical Research: Solid Earth.*

Chapter 4, "Post-Rifting Relaxation at the Dabbahu-Manda-Hararo Segment in Afar, Ethiopia", focusses on the post-rifting relaxation deformation at the DMHVS identified in Chaper 3, from the initial 2005 rifting event. By combining the Sentinel-1 time series with Envisat data from Pagli et al. (2014), I am able to provide new constraints on the crustal structure at the DMHVS whilst accounting for ongoing magma movement through the system, providing insight into the rifting cycle at spreading segments. The

work in this chapter is in a form ready to be submitted to the journal *Geophysical Research Letters*.

In Chapter 5, "Discussion & Conclusions", I relate the results from Chapters 2, 3, and 4 to each other, and to previous multidisciplinary findings to set the results from this thesis in a wider context. I also discuss the limitations of the work in this thesis, and the future challenges that remain to overcome these limitations.

References

Agram, P., Jolivet, R., Riel, B., Lin, Y., Simons, M., Hetland, E., Doin, M.-P. and Lasserre, C. (2013). New radar interferometric time series analysis toolbox released. *Eos, Transactions American Geophysical Union*, **94**(7), pp. 69–70. 1.3

Amelung, F., Oppenheimer, C., Segall, P. and Zebker, H. (2000). Ground deformation near Gada 'Ale volcano, Afar, observed by radar interferometry. *Geophysical Research Letters*, **27**(19), pp. 3093–3096. doi:10.1029/2000GL008497. 1.2, 1.3, 1.3

Anderson, K. R. and Poland, M. P. (2016). Bayesian estimation of magma supply, storage, and eruption rates using a multiphysical volcano model: Kīlauea Volcano, 2000-2012. *Earth and Planetary Science Letters*, **447**, pp. 161–171. doi:10.1016/j.epsl.2016.04.029. 1.6, 1.2

Anderson, K. R., Poland, M. P., Johnson, J. H. and Miklius, A. (2015). Episodic deflation-inflation events at Kīlauea Volcano and implications for the shallow magma system. *Hawaiian Volcanoes: From Source to Surface*, **208**, p. 229. 1.2

Armitage, J. J., Ferguson, D. J., Goes, S., Hammond, J. O., Calais, E., Rychert, C. A. and Harmon, N. (2015). Upper mantle temperature and the onset of extension and break-up in Afar, Africa. *Earth and Planetary Science Letters*, **418**, pp. 78–90. doi:10.1016/j.epsl.2015.02.039. 1.1

ArRajehi, A., McClusky, S., Reilinger, R., Daoud, M., Alchalbi, A., Ergintav, S., Gomez, F., Sholan, J., Bou-Rabee, F., Ogubazghi, G., Haileab, B., Fisseha, S., Asfaw, L., Mahmoud, S., Rayan, A., Bendik, R. and Kogan, L. (2010). Geodetic constraints on present-day motion of the Arabian Plate: Implications for Red Sea and Gulf of Aden rifting. *Tectonics*, **29**(TC3011). doi:10.1029/2009TC002482. 1.1

Atzori, S., Coltelli, M., Marsella, M. and Puglisi, G. (1996). ERS1/2 interferometry on Erta Ale volcano: the study of a proto-ocean ridge using SAR. *Orbit*, **25087**(05414), p. 12929. 1.3

Ayele, A., Keir, D., Ebinger, C., Wright, T. J., Stuart, G. W., Buck, W. R., Jacques, E., Ogubazghi, G. and Sholan, J. (2009). September 2005 mega-dike emplacement in the Manda-Harraro nascent oceanic rift (Afar depression). *Geophysical Research Letters*, **36**(L20306). doi:10.1029/2009GL039605. 1.2

Bagnardi, M., Poland, M. P., Carbone, D., Baker, S., Battaglia, M. and Amelung, F. (2014). Gravity changes and deformation at Kilauea Volcano, Hawaii, associated with summit eruptive activity, 2009-2012. *Journal of Geophysical Research: Solid Earth*, **119**, pp. 7288–7305. doi:10.1002/2014JB011506. 1.2

Barberi, F., Tazieff, H. and Varet, J. (1972). Volcanism in the Afar Depression: Its Tectonic and Magmatic Significance. *Tectonophysics*, **15**(1-2), pp. 19–29. doi:10.1016/B978-0-444-41087-0.50007-5. 1.2

Barnie, T. D., Keir, D., Hamling, I., Hofmann, B., Belachew, M., Carn, S., Eastwell, D., Hammond, J. O. S., Ayele, A., Oppenheimer, C. and Wright, T. (2016). A multidisciplinary study of the final episode of the Manda Hararo dyke sequence, Ethiopia, and implications for trends in volcanism during the rifting cycle. *Geological Society, London, Special Publications*, **420**, pp. 149–163. doi:10.1144/SP420.6. 1.2

Bastow, I. D. and Keir, D. (2011). The protracted development of the continent-ocean transition in Afar. *Nature Geoscience*, **4**(4), pp. 248–250. doi:10.1038/ngeo1095. 1.1, 1.2

Bekaert, D., Segall, P., Wright, T. J. and Hooper, A. J. (2016). A network inversion filter combining GNSS and InSAR for tectonic slip modeling. *Journal of Geophysical Research: Solid Earth*, **121**(3), pp. 2069–2086. 1.3

Berardino, P., Fornaro, G., Lanari, R. and Sansosti, E. (2002). A new algorithm for surface deformation monitoring based on small baseline differential SAR interferograms. *IEEE Transactions on Geoscience and Remote Sensing*, **40**(11), pp. 2375–2383. doi:10.1109/TGRS.2002.803792. 1.3

Bird, P. (2003). An updated digital model of plate boundaries. *Geochemistry, Geophysics, Geosystems*, **4**(3). doi:10.1029/2001GC000252. 1.7

Boddupalli, B. and Canales, J. P. (2019). Distribution of crustal melt bodies at the hotspot-influenced section of the Galápagos Spreading Centre from seismic reflection images. *Geophysical Research Letters*, **46**(9), pp. 4664–4673. doi:10.1029/2019GL082201. 1.2

Bonini, M., Corti, G., Innocenti, F., Manetti, P., Mazzarini, F., Abebe, T. and Pecskay, Z. (2005). Evolution of the Main Ethiopian Rift in the frame of Afar and Kenya rifts propagation. *Tectonics*, **24**(1). 1.1

Bown, J. W. and White, R. S. (1994). Variation with spreading rate of oceanic crustal thickness and geochemistry. *Earth and Planetary Science Letters*, **121**, pp. 435–449. doi:10.1016/0012-821X(94)90082-5. 1.2

Bridges, D. L., Mickus, K., Gao, S. S., Abdelsalam, M. G. and Alemu, A. (2012). Magnetic stripes of a transitional continental rift in Afar. *Geology*, **40**(3), pp. 203–206. doi:10.1130/G32697.1. 1.1

Buck, W. R. (2006). The role of magma in the development of the Afro-Arabian Rift System. *Geological Society, London, Special Publications*, **259**, pp. 43–54. doi:10.1144/GSL.SP.2006.259.01.05. 1.1, 1.4, 1.2

Buck, W. R., Lavier, L. L. and Poliakov, A. N. (2005). Modes of faulting at mid-ocean ridges. *Nature*, **434**(7034), pp. 719–723. doi:10.1038/nature03358. 1.2

Cannat, M., Sauter, D., Lavier, L., Bickert, M., Momoh, E. and Leroy, S. (2019). On spreading modes and magma supply at slow and ultraslow mid-ocean ridges. *Earth and Planetary Science Letters*, **519**, pp. 223–233. 1.2

Carbotte, S. M., Marjanović, M., Carton, H., Mutter, J. C., Canales, J. P., Nedimović, M. R., Han, S. and Perfit, M. R. (2013). Fine-scale segmentation of the crustal magma reservoir beneath the East Pacific Rise. *Nature Geoscience*, **6**(10), pp. 866–870. doi:10.1038/ngeo1933. 1.2

Carbotte, S. M. and Scheirer, D. S. (2004). Variability of ocean crustal structure created along the global mid-ocean ridge. *Hydrogeology of the oceanic lithosphere*, pp. 59–107. 1.2

Chambers, E. L., Harmon, N., Keir, D. and Rychert, C. A. (2019). Using ambient noise to image the Northern East African Rift. *Geochemistry, Geophysics, Geosystems*. 1.2, 1.3

Chang, S. J., Merino, M., Van Der Lee, S., Stein, S. and Stein, C. A. (2011). Mantle flow beneath Arabia offset from the opening Red Sea. *Geophysical Research Letters*, **38**(L04301). doi:10.1029/2010GL045852. 1.1

Chauhan, M. S., Cannavò, F., Carbone, D. and Greco, F. (2020). Insights into Mt Etna December 2018 eruption from joint inversion of deformation and gravity data. *Geophysical Research Letters*, **47**(16), p. e2020GL087786. 1.2

Chen, Y. J. (2000). Dependence of crustal accretion and ridge-axis topography on spreading rate, mantle temperature, and hydrothermal cooling. *Geological Society of America Special Papers*, **349**, pp. 161–179. doi:10.1130/0-8137-2349-3.161. 1.2

Chen, Y. J. and Lin, J. (2004). High sensitivity of ocean ridge thermal structure to changes in magma supply: The Galápagos Spreading Center. *Earth and Planetary Science Letters*, **221**(1-4), pp. 263–273. doi:10.1016/S0012-821X(04)00099-8. 1.2

Chen, Y. J. and Morgan, J. P. (1996). The effects of spreading rate, the magma budget, and the geometry of magma emplacement on the axial heat flux at mid-ocean ridges. *Journal of Geophysical Research-Solid Earth*, **101**(B5), pp. 11475–11482. doi:10.1029/96JB00330. 1.2

Civiero, C., Hammond, J. O., Goes, S., Fishwick, S., Ahmed, A., Ayele, A., Doubre, C., Goitom, B., Keir, D., Kendall, J. M., Leroy, S., Ogubazghi, G., Rümpker, G. and Stuart, G. W. (2015). Multiple mantle upwellings in the transition zone beneath the northern East-African Rift system from relative P-wave travel-time tomography. *Geochemistry, Geophysics, Geosystems*, **16**(9), pp. 2949–2968. doi:10.1002/2015GC005948. 1.1

Corti, G. (2009). Continental rift evolution: From rift initiation to incipient break-up in the Main Ethiopian Rift, East Africa. *Earth-Science Reviews*, **96**(1-2), pp. 1–53. doi:10.1016/j.earscirev.2009.06.005. 1.1, 1.1, 1.3, 1.1, 1.4

Darbyshire, F. A., White, R. S. and Priestley, K. F. (2000). Structure of the crust and uppermost mantle of Iceland from a combined seismic and gravity study. *Earth and Planetary Science Letters*, **181**(3), pp. 409–428. 1.2, 1.2

DeMets, C., Gordon, R. G., Argus, D. F. and Stein, S. (1994). Effects of recent revision to the geomagnetic reversal timescale on estimates of current plate motion. *Geophysical Research Letters*, **21**(20), pp. 2191–2194. 1.2

Denlinger, R. P. and Okubo, P. (1995). Structure of the mobile south flank of Kilauea Volcano, Hawaii. *Journal of Geophysical Research: Solid Earth*, **100**(B12), pp. 24499–24507. 1.2

Dick, H. J., Lin, J. and Schouten, H. (2003). An ultraslow-spreading class of ocean ridge. *Nature*, **426**(6965), pp. 405–412. doi:10.1038/nature02128. 1.2

Doubre, C., Déprez, A., Masson, F., Socquet, A., Lewi, E., Grandin, R., Nercessian, A., Ulrich, P., De Chabalier, J. B., Saad, I., Abayazid, A., Peltzer, G., Delorme, A., Calais, E. and Wright, T. (2017). Current deformation in Central Afar and triple junction kinematics deduced from GPS and InSAR measurements. *Geophysical Journal International*, **208**, pp. 936–953. doi:10.1093/gji/ggw434. 1.1

Drouin, V. (2016). *Constraints on deformation processes in Iceland from space geodesy: seasonal load variations, plate spreading, volcanoes, and geothermal fields*. Ph.D. thesis, University of Iceland. 1.3

Dugda, M. T., Nyblade, A. A., Julia, J., Langston, C. A., Ammon, C. J. and Simiyu, S. (2005). Crustal structure in Ethiopia and Kenya from receiver function analysis: Implications for rift development in eastern Africa. *Journal of Geophysical Research: Solid Earth*, **110**(B1). 1.2

Dunn, R. A., Lekić, V., Detrick, R. S. and Toomey, D. R. (2005). Three-dimensional seismic structure of the Mid-Atlantic Ridge (35°N): Evidence for focused melt supply and lower crustal dike injection. *Journal of Geophysical Research: Solid Earth*, **110**(B09101). doi:10.1029/2004JB003473. 1.2

Eagles, G., Gloaguen, R. and Ebinger, C. (2002). Kinematics of the Danakil microplate. *Earth and Planetary Science Letters*, **203**(2), pp. 607–620. doi:10.1016/S0012-821X(02)00916-0. 1.1

Ebinger, C. J. (2005). Continental break-up: the East African perspective. *Astronomy & Geophysics*, **46**(2), pp. 2–16. 1.3, 1.1, 1.4

Ebinger, C., Ayele, A., Keir, D., Rowland, J., Yirgu, G., Wright, T., Belachew, M. and Hamling, I. (2010). Length and Timescales of Rift Faulting and Magma Intrusion: The Afar Rifting Cycle from 2005 to Present. *Annual Review of Earth and Planetary Sciences*, **38**(1), pp. 439–466. doi:10.1146/annurev-earth-040809-152333. 1.2

Ebinger, C. J. and Casey, M. (2001). Continental breakup in magmatic provinces: An Ethiopian example. *Geology*, **29**(6), pp. 527–530. doi:10.1130/0091-7613(2001)029<0527:CBIMPA>2.0.CO;2. 1.1

Einarsson, P. and Sigmundsson, F. (2006). Geodynamic signals detected by geodetic methods in Iceland. *Geodäsie und Geoinformatik der Universität Hannover*, **258**, pp. 39–57. 1.3

Elliott, J. R., Biggs, J., Parsons, B. and Wright, T. J. (2008). InSAR slip rate determination on the Altyn Tagh Fault, northern Tibet, in the presence of topographically correlated atmospheric delays. *Geophysical Research Letters*, **35**(12), pp. 1–5. doi:10.1029/2008GL033659. 1.3

Ferguson, D. J., MacLennan, J., Bastow, I. D., Pyle, D. M., Jones, S. M., Keir, D., Blundy, J. D., Plank, T. and Yirgu, G. (2013). Melting during late-stage rifting in Afar is hot and deep. *Nature*, **499**(7456), pp. 70–73. doi:10.1038/nature12292. 1.1

Ferretti, A., Monti-Guarnieri, A. V., Prati, C., Rocca, F., Massonnet, D. et al. (2007). *InSAR Principles B*. ESA publications. 1.3, 1.3

Field, L., Barnie, T., Blundy, J., Brooker, R. A., Keir, D., Lewi, E. and Saunders, K. (2012a). Integrated field, satellite and petrological observations of the November 2010 eruption of Erta Ale. *Bulletin of Volcanology*, **74**, pp. 2251–2271. doi:10.1007/s00445-012-0660-7. 1.2

Field, L., Blundy, J., Brooker, R. A., Wright, T. and Yirgu, G. (2012b). Magma storage conditions beneath Dabbahu Volcano (Ethiopia) constrained by petrology, seismicity and satellite geodesy. *Bulletin of Volcanology*, **74**, pp. 981–1004. doi:10.1007/s00445-012-0580-6. 1.3

Fontijn, K., McNamara, K., Zafu Tadesse, A., Pyle, D. M., Dessalegn, F., Hutchison, W., Mather, T. A. and Yirgu, G. (2018). Contrasting styles of post-caldera volcanism along the Main Ethiopian Rift: Implications for contemporary volcanic hazards. *Journal of Volcanology and Geothermal Research*. doi:10.1016/j.jvolgeores.2018.02.001. 1.2

Froger, J.-L., Merle, O. and Briole, P. (2001). Active spreading and regional extension at Mount Etna imaged by SAR interferometry. *Earth and Planetary Science Letters*, **187**(3-4), pp. 245–258. 1.2

Furman, T., Bryce, J., Rooney, T., Hanan, B., Yirgu, G. and Ayalew, D. (2006). Heads and tails: 30 million years of the Afar plume. *Geological Society, London, Special Publications*, **259**, pp. 95–119. doi:10.1144/GSL.SP.2006.259.01.09. 1, 1.1

Gallacher, R. J., Keir, D., Harmon, N., Stuart, G., Leroy, S., Hammond, J. O., Kendall, J. M., Ayele, A., Goitom, B., Ogubazghi, G. and Ahmed, A. (2016). The initiation of segmented buoyancy-driven melting during continental breakup. *Nature Communications*, **7**(13110). doi:10.1038/ncomms13110. 1.1

González, P. J., Walters, R. J., Hatton, E. L., Spaans, K. and Hooper, A. (2016). LiCSAR: Tools for automated generation of Sentinel-1 frame interferograms. *AGU Fall Meeting*. 1.3

Gudmundsson, A. (2000). DYNAMICS OF VOLCANIC SYSTEMS IN ICELAND: Example of Tectonism and Volcanism at Juxtaposed Hot Spot and Mid-Ocean Ridge Systems. *Annual Review of Earth and Planetary Sciences*, **28**, pp. 107–40. doi:10.1146/annurev-earth-28-042010-200001. 1.2

Gudmundsson, M. T., Jónsdóttir, K., Hooper, A., Holohan, E. P., Halldórsson, S. A., Ófeigsson, B. G., Cesca, S., Vogfjörd, K. S., Sigmundsson, F., Högnadóttir, T., Einarsson, P., Sigmarsson, O., Jarosch, A. H., Jónasson, K., Magnússon, E., Hreinsdóttir, S., Bagnardi, M., Parks, M. M., Hjörleifsdóttir, V., Pálsson, F., Walter, T. R., Schöpfer, M. P., Heimann, S., Reynolds, H. I., Dumont, S., Bali, E., Gudfinnsson, G. H., Dahm, T., Roberts, M. J., Hensch, M., Belart, J. M., Spaans, K., Jakobsson, S., Gudmundsson, G. B., Fridriksdóttir, H. M., Drouin, V., Dürig, T., Adalgeirsdóttir, G., Riishuus, M. S., Pedersen, G. B., Van Boeckel, T., Oddsson, B., Pfeffer, M. A., Barsotti, S., Bergsson, B., Donovan, A., Burton, M. R. and Aiuppa, A. (2016). Gradual caldera collapse at Bárdarbunga volcano, Iceland, regulated by lateral magma outflow. *Science*, **353**(6296). doi:10.1126/science.aaf8988. 1.2

Hamling, I. J., Cevuard, S. and Garaebiti, E. (2019). Large-Scale Drainage of a Complex Magmatic System: Observations From the 2018 Eruption of Ambrym Volcano, Vanuatu. *Geophysical Research Letters*, **46**(9), pp. 4609–4617. 1.2

Hamling, I. J., Wright, T. J., Calais, E., Bennati, L. and Lewi, E. (2010). Stress transfer between thirteen successive dyke intrusions in Ethiopia. *Nature Geoscience*, **3**(10), pp. 713–717. doi:10.1038/ngeo967. 1.2

Hamling, I. J., Wright, T. J., Calais, E., Lewi, E. and Fukahata, Y. (2014). InSAR observations of post-rifting deformation around the Dabbahu rift segment, Afar, Ethiopia. *Geophysical Journal International*, **197**, pp. 33–49. doi:10.1093/gji/ggu003. 1.3

Hamlyn, J. E., Keir, D., Wright, T. J., Neuberg, J. W., Goitom, B., Hammond, J. O. S., Pagli, C., Oppenheimer, C., Kendall, J. M. and Grandin, R. (2014). Seismicity and subsidence following the 2011 Nabro eruption, Eritrea: Insights into the plumbing system of an off-rift volcano. *Journal of Geophysical Research: Solid Earth*, **119**, pp. 8267–8282. doi:10.1002/2014JB011395. 1.3

Hammond, J. O. S. (2014). Constraining melt geometries beneath the Afar Depression, Ethiopia from teleseismic receiver functions: The anisotropic H-κ stacking technique. *Geochemistry, Geophysics, Geosystems*, **15**(4), pp. 1316–1332. 1.1

Hammond, J. O. S. and Kendall, J. M. (2016). Constraints on melt distribution from seismology: a case study in Ethiopia. *Geological Society, London, Special Publications*, **420**, pp. 127–147. doi:10.1144/SP420.14. 1.1

Hammond, J. O. S., Kendall, J. M., Stuart, G. W., Keir, D., Ebinger, C., Ayele, A. and Belachew, M. (2011). The nature of the crust beneath the Afar triple junction: Evidence from receiver functions. *Geochemistry, Geophysics, Geosystems*, **12**(12). doi:10.1029/2011GC003738. 1.1, 1.2

Hanssen, R. (2001). *Radar Interferometry: Data Interpretation and Error Analysis*. Ph.D. thesis, Delft University of Technology, Netherlands. 1.3, 1.3

Harris, A., Murray, J., Aries, S., Davies, M., Flynn, L., Wooster, M., Wright, R. and Rothery, D. (2000). Effusion rate trends at Etna and Krafla and their implications for eruptive mechanisms. *Journal of Volcanology and Geothermal Research*, **102**(3-4), pp. 237–269. 1.2

Hayward, N. J. and Ebinger, C. J. (1996). Variations in the along-axis segmentation of the Afar Rift system. *Tectonics*, **15**(2), pp. 244–257. doi:10.1029/95TC02292. 1.1, 1.1, 1.2

Hefner, W. L., Nooner, S. L., Chadwick Jr, W. W. and Bohnenstiehl, D. R. (2020). Revised Magmatic Source Models for the 2015 Eruption at Axial Seamount Including Estimates of Fault-Induced Deformation. *Journal of Geophysical Research: Solid Earth*, **125**(4), p. e2020JB019356. 1.2

Hill, D. P. and Zucca, J. J. (1987). Geophysical constraints on the structure of Kilauea and Mauna Loa volcanoes and some implications for seismomagmatic processes. *US Geol. Surv. Prof. Pap*, **1350**(2), pp. 903–917. 1.2

Hooper, A., Bekaert, D., Spaans, K. and Arıkan, M. (2012). Recent advances in SAR interferometry time series analysis for measuring crustal deformation. *Tectonophysics*, **514**, pp. 1–13. 1.3, 1.3, 1.3, 1.9

Iddon, F., Jackson, C., Hutchison, W., Fontijn, K., Pyle, D. M., Mather, T. A., Yirgu, G. and Edmonds, M. (2019). Mixing and crystal scavenging in the Main Ethiopian Rift revealed by trace element systematics in feldspars and glasses. *Geochemistry, Geophysics, Geosystems*, **20**(1), pp. 230–259. 1.2

Illsley-Kemp, F., Bull, J., Keir, D., Gerya, T., Pagli, C., Gernon, T., Ayele, A., Goitom, B., Hammond, J. O. and Kendall, J. (2018a). Initiation of a proto-transform fault prior to seafloor spreading. *Geochemistry, Geophysics, Geosystems*, **19**(12), pp. 4744–4756. 1.1, 1.2

Illsley-Kemp, F., Keir, D., Bull, J. M., Gernon, T. M., Ebinger, C., Ayele, A., Hammond, J. O., Kendall, J. M., Goitom, B. and Belachew, M. (2018b). Seismicity during continental breakup in the Red Sea Rift of Northern Afar. *Journal of Geophysical Research: Solid Earth*, **123**, pp. 2345–2362. doi:10.1002/2017JB014902. 1.1, 1.3

Ito, G., Shen, Y., Hirth, G. and Wolfe, C. J. (1999). Mantle flow, melting, and dehydration of the Iceland mantle plume. *Earth and Planetary Science Letters*, **165**(1), pp. 81–96. 1.2

Jakobsson, S. P. (1972). Chemistry and distribution pattern of recent basaltic rocks in Iceland. *Lithos*, **5**(4), pp. 365–386. 1.2

Jenkins, J., Maclennan, J., Green, R. G., Cottaar, S., Deuss, A. and White, R. S. (2018). Crustal formation on a spreading ridge above a mantle plume: receiver function imaging of the Icelandic crust. *Journal of Geophysical Research: Solid Earth*, **123**(6), pp. 5190–5208. 1.2

Jerram, D. A. and Bryan, S. E. (2015). Plumbing systems of shallow level intrusive complexes. In Breitkreuz, C. and Rocchi, S. (eds.), *Physical Geology of Shallow Magmatic Systems. Advances in Volcanology (An Official Book Series of the International Association of Volcanology and Chemistry of the Earth's Interior)*. Springer, Cham, pp. 39–60. 1.2

Jones, J. P., Carniel, R. and Malone, S. D. (2012). Decomposition, location, and persistence of seismic signals recovered from continuous tremor at Erta 'Ale, Ethiopia. *Journal of Volcanology and Geothermal Research*, **213-214**, pp. 116–129. doi:10.1016/j.jvolgeores.2011.07.007. 1.3

Jung, J., Kim, D.-j. and Park, S.-E. (2013). Correction of atmospheric phase screen in time series InSAR using WRF model for monitoring volcanic activities. *IEEE Transactions on Geoscience and Remote Sensing*, **52**(5), pp. 2678–2689. 1.3

Karson, J. A. (2017). The Iceland Plate Boundary Zone: Propagating Rifts, Migrating Transforms, and Rift-Parallel Strike-Slip Faults. *Geochemistry, Geophysics, Geosystems*, **18**(11), pp. 4043–4054. doi:10.1002/2017GC007045. 1.2

Kay, R., Hubbard, N. and Gast, P. (1970). Chemical characteristics and origin of oceanic ridge volcanic rocks. *Journal of Geophysical Research*, **75**(8), pp. 1585–1613. 1.2

Keir, D., Bastow, I. D., Corti, G., Mazzarini, F. and Rooney, T. O. (2015). The origin of along-rift variations in faulting and magmatism in the Ethiopian Rift. *Tectonics*, **34**(3), pp. 464–477. doi:10.1002/2014TC003698. 1.1

Kidane, T. (2016). Strong clockwise block rotation of the Ali-Sabieh/Aïsha Block: evidence for opening of the Afar Depression by a 'saloon-door' mechanism. *Geological Society, London, Special Publications*, **420**, pp. 209–219. doi:10.1144/SP420.10. 1.1, 1.1

King, R., Floyd, M., Reilinger, R. and Bendick, R. (2019). GPS velocity field (MIT 2019.0) for the East African Rift System generated by King et al.. Interdisciplinary Earth Data Alliance (IEDA). *Accessed on 20 Sep 2019.* doi:10.1594/IEDA/324785. 1.7

Kumar, P., Kind, R., Priestley, K. and Dahl-Jensen, T. (2007). Crustal structure of Iceland and Greenland from receiver function studies. *Journal of Geophysical Research: Solid Earth*, **112**(B3). 1.2

Lanari, R., Casu, F., Manzo, M., Zeni, G., Berardino, P., Manunta, M. and Pepe, A. (2007). An overview of the Small BAseline Subset algorithm: A DInSAR technique for surface deformation analysis. *Pure and Applied Geophysics*, **164**(4), pp. 637–661. doi:10.1007/s00024-007-0192-9. 1.3

Lavayssière, A., Rychert, C., Harmon, N., Keir, D., Hammond, J. O., Kendall, J.-M., Doubre, C. and Leroy, S. (2018). Imaging lithospheric discontinuities beneath the Northern East African Rift Using S-to-P receiver functions. *Geochemistry, Geophysics, Geosystems*, **19**(10), pp. 4048–4062. 1.1

Lazeckỳ, M., Spaans, K., González, P. J., Maghsoudi, Y., Morishita, Y., Albino, F., Elliott, J., Greenall, N., Hatton, E., Hooper, A. et al. (2020). LiCSAR: An automatic InSAR tool for measuring and monitoring tectonic and volcanic activity. *Remote Sensing*, **12**(15), p. 2430. 1.3

Lewi, E., Keir, D., Birhanu, Y., Blundy, J., Stuart, G., Wright, T. and Calais, E. (2016). Use of a high-precision gravity survey to understand the formation of oceanic crust and the role of melt at the southern Red Sea rift in Afar, Ethiopia. *Geological Society, London, Special Publications*, **420**, pp. 165–180. doi:10.1144/SP420.13. 1.1

Liu, S., Hanssen, R., Samiei-Esfahany, S., Hooper, A. and Van Leijen, F. (2011). Separating non-linear deformation and atmospheric phase screen (APS) for InSAR time series analysis using least-squares collocation. In *Proceedings of the Advances in the Science and Applications of SAR Interferometry, ESA Fringe 2009, Workshop ESA*. 1.3

Liu, C., Lay, T. and Xiong, X. (2018). Rupture in the 4 May 2018 Mw 6.9 earthquake seaward of the Kilauea east rift zone fissure eruption in Hawaii. *Geophysical Research Letters*, **45**(18), pp. 9508–9515. 1.2

Macdonald, G. A. (1949). Hawaiian petrographic province. *Geological Society of America Bulletin*, **60**(10), pp. 1541–1596. 1.2

Maguire, P., Keller, G., Klemperer, S., Mackenzie, G., Keranen, K., Harder, S., O'Reilly, B., Thybo, H., Asfaw, L., Khan, M. and Amha, M. (2006). Crustal structure of the northern Main Ethiopian Rift from the EAGLE controlled-source survey; a snapshot of incipient lithospheric break-up. *Geological Society, London, Special Publications*, **259**, pp. 269–292. doi:10.1144/GSL.SP.2006.259.01.21. 1.1

Makris, J. and Ginzburg, A. (1987). The Afar Depression: transition between continental rifting and sea-floor spreading. *Tectonophysics*, **141**(1-3), pp. 199–214. doi:10.1016/0040-1951(87)90186-7. 1.1

Marjanović, M., Carbotte, S. M., Carton, H., Nedimović, M. R., Mutter, J. C. and Canales, J. P. (2014). A multi-sill magma plumbing system beneath the axis of the East Pacific Rise. *Nature Geoscience*, **7**(11), p. 825. 1.2

McClusky, S., Reilinger, R., Ogubazghi, G., Amleson, A., Healeb, B., Vernant, P., Sholan, J., Fisseha, S., Asfaw, L., Bendick, R. and Kogan, L. (2010). Kinematics of the southern Red Sea-Afar Triple Junction and implications for plate dynamics. *Geophysical Research Letters*, **37**(L05301). doi:10.1029/2009GL041127. 1.2, 1.1

McKenzie, D. (1978). Some remarks on the development of sedimentary basins. *Earth and Planetary science letters*, **40**(1), pp. 25–32. 1

Merryman Boncori, J. P. (2019). Measuring coseismic deformation with spaceborne Synthetic Aperture Radar: A review. *Frontiers in Earth Science*, **7**, pp. 1–16. 1.8

Michon, L., Ferrazzini, V., Di Muro, A., Villeneuve, N. and Famin, V. (2015). Rift zones and magma plumbing system of Piton de la Fournaise volcano: How do they differ from Hawaii and Etna? *Journal of Volcanology and Geothermal Research*, **303**, pp. 112–129. 1.2

Mogi, K. (1958). Relations between the Eruptions of Various Volcanoes and the Defomormations of the Ground Surfaces around them. *Bulletin of the Earthquake Research Institute*, **36**, pp. 99–134. 1.3

Moore, C., Wright, T. J. and Hooper, A. (in review). Rift Focussing and Magmatism During Late-Stage Rifting in Afar, Ethiopia. *Earth and Space Science Open Archive*, pp. 1–19. doi:10.1002/essoar.10503895.1. 1.7

Morishita, Y., Lazecky, M., Wright, T. J., Weiss, J. R., Elliott, J. R. and Hooper, A. (2020). LiCSBAS: An Open-Source InSAR Time Series Analysis Package Integrated with the LiCSAR Automated Sentinel-1 InSAR Processor. *Remote Sensing*, **12**(3), p. 424. 1.3, 1.3

Nobile, A., Pagli, C., Keir, D., Wright, T. J., Ayele, A., Ruch, J. and Acocella, V. (2012). Dike-fault interaction during the 2004 Dallol intrusion at the northern edge of the Erta Ale Ridge (Afar, Ethiopia). *Geophysical Research Letters*, **39**(L19305). doi:10.1029/2012GL053152. 1.2

Nooner, S. L. and Chadwick, W. W. (2009). Volcanic inflation measured in the caldera of axial seamount: Implications for magma supply and future eruptions. *Geochemistry, Geophysics, Geosystems*, **10**(2). doi:10.1029/2008GC002315. 1.2, 1.3

Okada, Y. (1985). Surface deformation due to shear and tensile faults in a half-space. *Bulletin of the seismological society of America*, **75**(4), pp. 1135–1154. 1.3

Pagli, C., Wang, H., Wright, T. J., Calais, E. and Lewi, E. (2014). Current plate boundary deformation of the Afar rift from a 3-D velocity field inversion of InSAR and GPS. *Journal of Geophysical Research: Solid Earth*, **119**, pp. 8562–8575. doi:10.1002/2014JB011391. 1.2, 1.3, 1.5

Pagli, C., Wright, T. J., Ebinger, C. J., Yun, S. H., Cann, J. R., Barnie, T. and Ayele, A. (2012). Shallow axial magma chamber at the slow-spreading Erta Ale Ridge. *Nature Geoscience*, **5**(4), pp. 284–288. doi:10.1038/ngeo1414. 1.1, 1.2, 1.3, 1.5

Patrick, M., Anderson, K., Poland, M., Orr, T. and Swanson, D. (2015). Lava lake level as a gauge of magma reservoir pressure and eruptive hazard. *Geology*, **43**(9), pp. 831–834. doi:10.1130/G36896.1. 1.2

Patrick, M., Johanson, I., Shea, T. and Waite, G. (2020). The historic events at Kīlauea Volcano in 2018: summit collapse, rift zone eruption, and Mw 6.9 earthquake: preface to the special issue. *Bulletin of Volcanology*, **82**, p. 46. 1.2

Patrick, M., Orr, T., Anderson, K. and Swanson, D. (2019). Eruptions in sync: Improved constraints on Kīlauea Volcano's hydraulic connection. *Earth and Planetary Science Letters*, **507**, pp. 50–61. 1.2

Peltier, A., Ferrazzini, V., Staudacher, T. and Bachèlery, P. (2005). Imaging the dynamics of dyke propagation prior to the 2000–2003 flank eruptions at Piton de La Fournaise, Reunion Island. *Geophysical Research Letters*, **32**(22). 1.2

Phipps Morgan, J. and Chen, Y. J. (1993). Dependence of ridge-axis morphology on magma supply and spreading rate. *Nature*, **364**(6439), pp. 706–708. doi:10.1038/364706a0. 1.2

Phipps Morgan, J., Parmentier, E. M. and Lin, J. (1987). Mechanisms for the origin of mid-ocean ridge axial topography: Implications for the thermal and mechanical structure of accreting plate boundaries. *Journal of Geophysical Research*, **92**(B12), pp. 12823–12836. doi:10.1029/JB092iB12p12823. 1.2, 1.2

Poland, M. P., Miklius, A. and Montgomery-Brown, E. K. (2014). Magma supply, storage, and transport at shield-stage Hawaiian Volcanoes. *Characteristics of Hawaiian Volcanoes*, **179**(1801), pp. 179–234. 1.2, 1.2

Refice, A., Belmonte, A., Bovenga, F. and Pasquariello, G. (2011). On the use of anisotropic covariance models in estimating atmospheric DInSAR contributions. *IEEE Geoscience and Remote Sensing Letters*, **8**(2), pp. 341–345. 1.3

Ritsema, J., Van Heijst, H. J. and Woodhouse, J. H. (1999). Complex shear wave velocity structure imaged beneath Africa and Iceland. *Science*, **286**(5446), pp. 1925–1931. doi:10.1126/science.286.5446.1925. 1.1

Rivalta, E. and Segall, P. (2008). Magma compressibility and the missing source for some dike intrusions. *Geophysical Research Letters*, **35**(L04306). doi:10.1029/2007GL032521. 1.3

Rooney, T. O., Furman, T., Yirgu, G. and Ayalew, D. (2005). Structure of the Ethiopian lithosphere: Xenolith evidence in the Main Ethiopian Rift. *Geochimica et Cosmochimica Acta*, **69**(15), pp. 3889–3910. doi:10.1016/j.gca.2005.03.043. 1.1

Rooney, T. O., Herzberg, C. and Bastow, I. D. (2012). Elevated mantle temperature beneath East Africa. *Geology*, **40**(1), pp. 27–30. doi:10.1130/G32382.1. 1.1

Ryall, A. and Bennett, D. L. (1968). Crustal structure of southern Hawaii related to volcanic processes in the upper mantle. *Journal of Geophysical Research*, **73**(14), pp. 4561–4582. 1.2

Saria, E., Calais, E., Stamps, D. S., Delvaux, D. and Hartnady, C. J. (2014). Present-day kinematics of the East African Rift. *Journal of Geophysical Research: Solid Earth*, **119**, pp. 3584–3600. doi:10.1002/2013JB010901. 1.1

Segall, P. (2010). *Earthquake and volcano deformation*. Princeton Univerity Press. 1.3, 1.3

Self, S. and Sparks, R. (1978). Characteristics of widespread pyroclastic deposits formed by the interaction of silicic magma and water. *Bulletin volcanologique*, **41**(3), p. 196. 1.2

Shen, L., Hooper, A. and Elliott, J. (2019). A Spatially Varying Scaling Method for InSAR Tropospheric Corrections Using a High-Resolution Weather Model. *Journal of Geophysical Research: Solid Earth*, **124**(4), pp. 4051–4068. 1.3

Shreve, T., Grandin, R., Boichu, M., Garaebiti, E., Moussallam, Y., Ballu, V., Delgado, F., Leclerc, F., Vallée, M., Henriot, N. et al. (2019). From prodigious volcanic degassing to caldera subsidence and quiescence at Ambrym (Vanuatu): the influence of regional tectonics. *Scientific reports*, **9**(1), pp. 1–13. 1.2

Sigmundsson, F. (2016). New insights into magma plumbing along rift systems from detailed observations of eruptive behavior at Axial volcano. *Geophysical Research Letters*, **43**(24), pp. 12–423. 1.2, 1.2

Sigmundsson, F., Hooper, A., Hreinsdóttir, S., Vogfjörd, K. S., Ófeigsson, B. G., Heimisson, E. R., Dumont, S., Parks, M., Spaans, K., Gudmundsson, G. B., Drouin, V., Árnadóttir, T., Jónsdóttir, K., Gudmundsson, M. T., Högnadóttir, T., Fridriksdóttir, H. M., Hensch, M., Einarsson, P., Magnússon, E., Samsonov, S., Brandsdóttir, B., White, R. S., Ágústsdóttir, T., Greenfield, T., Green, R. G., Hjartardóttir, Á. R., Pedersen, R., Bennett, R. A., Geirsson, H., la Femina, P. C., Björnsson, H., Pálsson, F., Sturkell, E., Bean, C. J., Möllhoff, M., Braiden, A. K. and Eibl, E. P. (2014). Segmented lateral dyke growth in a rifting event at Bárðarbunga volcanic system, Iceland. *Nature*, **517**(7533). doi:10.1038/nature14111. 1.2

Sigmundsson, F., Hreinsdóttir, S., Hooper, A., Arnadóttir, T., Pedersen, R., Roberts, M. J., Óskarsson, N., Auriac, A., Decriem, J., Einarsson, P. et al. (2010). Intrusion triggering of the 2010 Eyjafjallajökull explosive eruption. *Nature*, **468**(7322), pp. 426–430. 1.2

Sigurdsson, H. and Sparks, S. R. (1978a). Lateral magma flow within rifted Icelandic crust. *Nature*, **274**(5667), pp. 126–130. 1.2

Sigurdsson, H. and Sparks, R. S. (1978b). Rifting episode in north Iceland in 1874-1875 and the eruptions of Askja and Sveinagja. *Bulletin Volcanologique*, **41**(3), pp. 149–167. doi:10.1007/BF02597219. 1.2

Sinton, J. M. and Detrick, R. S. (1992). Mid-ocean ridge magma chambers. *Journal of Geophysical Research*, **97**(B1), p. 197. doi:10.1029/91JB02508. 1.2

Sousa, J. J., Hooper, A. J., Hanssen, R. F., Bastos, L. C. and Ruiz, A. M. (2011). Persistent Scatterer InSAR: A comparison of methodologies based on a model of temporal deformation vs. spatial correlation selection criteria. *Remote Sensing of Environment*, **115**(10), pp. 2652–2663. 1.3

Stork, A. L., Stuart, G. W., Henderson, C. M., Keir, D. and Hammond, J. O. (2013). Uppermost mantle (Pn) velocity model for the Afar region, Ethiopia: An insight into rifting processes. *Geophysical Journal International*, **193**, pp. 321–328. doi:10.1093/gji/ggs106. 1.1

Temtime, T., Biggs, J., Lewi, E., Hamling, I., Wright, T. and Ayele, A. (2018). Spatial and temporal patterns of deformation at the Tendaho geothermal prospect, Ethiopia. *Journal of Volcanology and Geothermal Research*, **357**, pp. 56–67. doi:10.1016/j.jvolgeores.2018.04.004. 1.3

Thordarson, T. and Self, S. (1993). The Laki (Skaftár Fires) and Grímsvötn eruptions in 1783–1785. *Bulletin of Volcanology*, **55**(4), pp. 233–263. 1.2

Tibaldi, A., Bonali, F. L. and Corazzato, C. (2014). The diverging volcanic rift system. *Tectonophysics*, **611**, pp. 94–113. doi:10.1016/j.tecto.2013.11.023. 1.2

Tiberi, C., Ebinger, C., Ballu, V., Stuart, G. and Oluma, B. (2005). Inverse models of gravity data from the Red Sea-Aden-East African rifts triple junction zone. *Geophysical Journal International*, **163**, pp. 775–787. doi:10.1111/j.1365-246X.2005.02736.x. 1.1, 1.2

Viltres, R., Jónsson, S., Ruch, J., Doubre, C., Reilinger, R., Floyd, M. and Ogubazghi, G. (2020). Kinematics and deformation of the southern Red Sea region from GPS observations. *Geophysical Journal International*, **221**(3), pp. 2143–2154. 1.1

Wang, H., Wright, T. J., Yu, Y., Lin, H., Jiang, L., Li, C. and Qiu, G. (2012). InSAR reveals coastal subsidence in the Pearl River Delta, China. *Geophysical Journal International*, **191**(3), pp. 1119–1128. 1.3

Wanless, V. D. and Behn, M. D. (2017). Spreading rate-dependent variations in crystallization along the global mid-ocean ridge system. *Geochemistry, Geophysics, Geosystems*, **18**(8), pp. 3016–3033. doi:10.1002/2017GC006924. 1.2, 1.5

Weiss, J. R., Walters, R. J., Morishita, Y., Wright, T. J., Lazecky, M., Wang, H., Hussain, E., Hooper, A. J., Elliott, J. R., Rollins, C. et al. (2020). High-resolution surface velocities and strain for Anatolia from Sentinel-1 InSAR and GNSS data. *Geophysical Research Letters*, **47**(17), p. e2020GL087376. 1.3

Werner, C., Wegmuller, U., Strozzi, T. and Wiesmann, A. (2000). GAMMA SAR and interferometric processing software. *European Space Agency, (Special Publication) ESA SP*, (461), pp. 211–219. 1.3

White, R. and McKenzie, D. (1989). Magmatism at rift zones: the generation of volcanic continental margins and flood basalts. *Journal of Geophysical Research: Solid Earth*, **94**(B6), pp. 7685–7729. 1

White, S. M., Meyer, J. D., Haymon, R. M., Macdonald, K. C., Baker, E. T. and Resing, J. A. (2008). High-resolution surveys along the hot spot-affected Galápagos spreading center: 2. Influence of magma supply on volcanic morphology. *Geochemistry, Geophysics, Geosystems*, **9**(9). doi:10.1029/2008GC002036. 1.2

Wolfe, C. J., Bjarnason, I. T., VanDecar, J. C. and Solomon, S. C. (1997). Seismic structure of the Iceland mantle plume. *Nature*, **385**(6613), pp. 245–247. 1.2

Wolfenden, E., Ebinger, C., Yirgu, G., Deino, A. and Ayalew, D. (2004). Evolution of the northern Main Ethiopian rift: Birth of a triple junction. *Earth and Planetary Science Letters*, **224**(1-2), pp. 213–228. doi:10.1016/j.epsl.2004.04.022. 1.1

Wright, T. J., Ebinger, C., Biggs, J., Ayele, A., Yirgu, G., Keir, D. and Stork, A. (2006). Magma-maintained rift segmentation at continental rupture in the 2005 Afar dyking episode. *Nature*, **442**(7100), pp. 291–294. doi:10.1038/nature04978. 1.2, 1.2

Wright, T. J., Sigmundsson, F., Pagli, C., Belachew, M., Hamling, I. J., Brandsdóttir, B., Keir, D., Pedersen, R., Ayele, A., Ebinger, C., Einarsson, P., Lewi, E. and Calais, E. (2012). Geophysical constraints on the dynamics of spreading centres from rifting episodes on land. doi:10.1038/ngeo1428. 1.2, 1.2

Xu, W., Rivalta, E. and Li, X. (2017). Magmatic architecture within a rift segment: Articulate axial magma storage at Erta Ale volcano, Ethiopia. *Earth and Planetary Science Letters*, **476**, pp. 79–86. doi:10.1016/j.epsl.2017.07.051. 1.1, 1.2

Yu, C., Li, Z. and Penna, N. T. (2018). Interferometric synthetic aperture radar atmospheric correction using a GPS-based iterative tropospheric decomposition model. *Remote Sensing of Environment*, **204**, pp. 109–121. doi:10.1016/j.rse.2017.10.038. 1.3

Yu, C., Penna, N. T. and Li, Z. (2017). Generation of real-time mode high-resolution water vapor fields from GPS observations. *Journal of Geophysical Research*, **122**(3), pp. 2008–2025. doi:10.1002/2016JD025753. 1.3

Chapter 2

The 2017 Eruption of Erta 'Ale Volcano, Ethiopia: Insights into the Shallow Axial Plumbing System of an Incipient Mid-Ocean Ridge

The work displayed in Chapter 2 (Sections 2.1-2.7) was published by AGU, Copyright (2019) American Geophysical Union:
Moore, C., Wright, T., Hooper, A. & Biggs, J. (2019). The 2017 eruption of Erta 'Ale volcano, Ethiopia: Insights into the shallow axial plumbing system of an incipient mid-ocean ridge. *Geochemistry, Geophysics, Geosystems*, **20**(12). https://doi.org/10.1029/2019GC008692
Supplementary Materials for Moore et al. (2019) are provided in Appendix A.

2.1 Abstract

The final stage of continental break-up is often accompanied by abundant magmatism. Erta 'Ale volcano lies on the Nubia-Arabia extensional boundary in Afar, Ethiopia, an incipient mid-ocean ridge. A fissure on the south flank of Erta 'Ale began erupting on 21 January 2017 and has remained active until at least July 2019. We use Sentinel-1 synthetic aperture radar (SAR) acquisitions to create a time series of ground displacement measurements at Erta 'Ale from October 2014 to June 2019, covering the eruption and its build-up. In the pre-eruption period we observe gradual extension centred on the lava lake, consistent with the opening of an axis-aligned dyke. Using SAR intensity shadows we show that the long-lived Erta 'Ale lava lake was stable in this

period, indicative of a steady pressure state in the shallow plumbing system. During the initial eruption, we observe surface displacements consistent with a shallow dyke intrusion below the eruption site and conduit contraction below the lava lake. The pressure change associated with the co-intrusive drop in the lava lake level is sufficient to reproduce the deformation pattern suggesting that the lava lake is well-connected to the shallow plumbing system. Subsidence and contraction during the long-lived eruption indicates the presence of an off-rift vertically extensive source. We suggest that this may represent a system of stacked sources throughout the upper crust, with melt being more distributed. We also propose that high magma flux on the slow-spreading Erta 'Ale segment may be facilitating the presence of shallow axial magma bodies.

2.2 Introduction

The geometry and dynamics of magma plumbing systems at sub-aerial volcanoes in extensional settings are still poorly understood (Wright et al., 2012, Pagli et al., 2012, Sigmundsson, 2016). Extensive studies on mid-ocean ridge (MOR) systems show that at fast-spreading ridges, a shallow sill structure is commonly found (Wanless and Behn, 2017, Marjanović et al., 2014, Carbotte et al., 2013). For example, at the East Pacific Rise (EPR) from 8°20'-10°10'N an axial magma lens is typically present at $\sim$ 1.6 km depth, with a deeper lens found between $\sim$ 1.7-2.4 km depth (Marjanović et al., 2018, Carbotte et al., 2013). Whilst fast-spreading MOR plumbing systems are well imaged, the movement of magma and dynamics within these plumbing systems are difficult to study (Sigmundsson, 2016). The slow-spreading Erta 'Ale volcanic segment (EAVS) in northern Afar, Ethiopia (Figure 2.1a), represents the southern end of the Red Sea Rift (RSR) and has been previously proposed as a sub-aerial analogue for a MOR (e.g. Ebinger, 2005). Although the spreading rate is low (5-15 mm/yr) (McClusky et al., 2010), the EAVS exhibits features typical of a fast-spreading MOR such as a broad axial ridge (Barberi and Varet, 1970), the presence of a shallow axial magma chambers below the EAVS (e.g. Pagli et al., 2012), and the formation of a proto-transform fault between the Erta 'Ale and Tat 'Ale segments (Illsley-Kemp et al., 2018a). Understanding the dynamics of magma movement at the EAVS can therefore give us insights into magma plumbing systems at fast-spreading MORs.

Erta 'Ale volcano lies at the southern end of the EAVS and is host to one of the few long-lived lava lakes in the world. The lava lake overflowed in January 2017, before a large fissure eruption $\sim$ 3 km to its SE (Global Volcanism Program, 2017). The eruption has remained active until at least June 2019. At Kilauea volcano, Hawaii, the interaction between the summit Halema'uma'u lava lake, and the established Pu'u'O'o vent in the East Rift Zone (ERZ) on the volcano flank has highlighted a strong interconnectivity in its shallow plumbing system (Patrick et al., 2019a,b, Neal et al., 2019,

Montagna and Gonnermann, 2013), with long-term fluctuations in the lava lake level giving an indication of the pressure state of the summit reservoir and the balance between magma in-flux and out-flux (Patrick et al., 2015, 2019b, Anderson et al., 2015). The 2017 Erta 'Ale flank eruption, and potential connectivity with the lava lake, provides a similar opportunity to understand the pressure state of the shallow plumbing system at Erta 'Ale.

2.2.1 Tectonic Setting

The ∼ 120 km long EAVS forms part of the RSR branch of the Afar triple junction, which initiated ∼ 30 Ma, and accommodates the separation of the Nubian, Somalian and Arabian plates (Wolfenden et al., 2005) (Figure 2.1a). Extension over the RSR of ∼ 18 mm/yr is gradually transferred into Afar between ∼ 13-16 °N which produces an extension of ∼ 12 mm/yr at Erta 'Ale volcano (Pagli et al., 2014, McClusky et al., 2010, ArRajehi et al., 2010). The EAVS lies within the Danakil Depression which has the most thinned crustal structure in Afar with a thickness of < 15 km, compared to

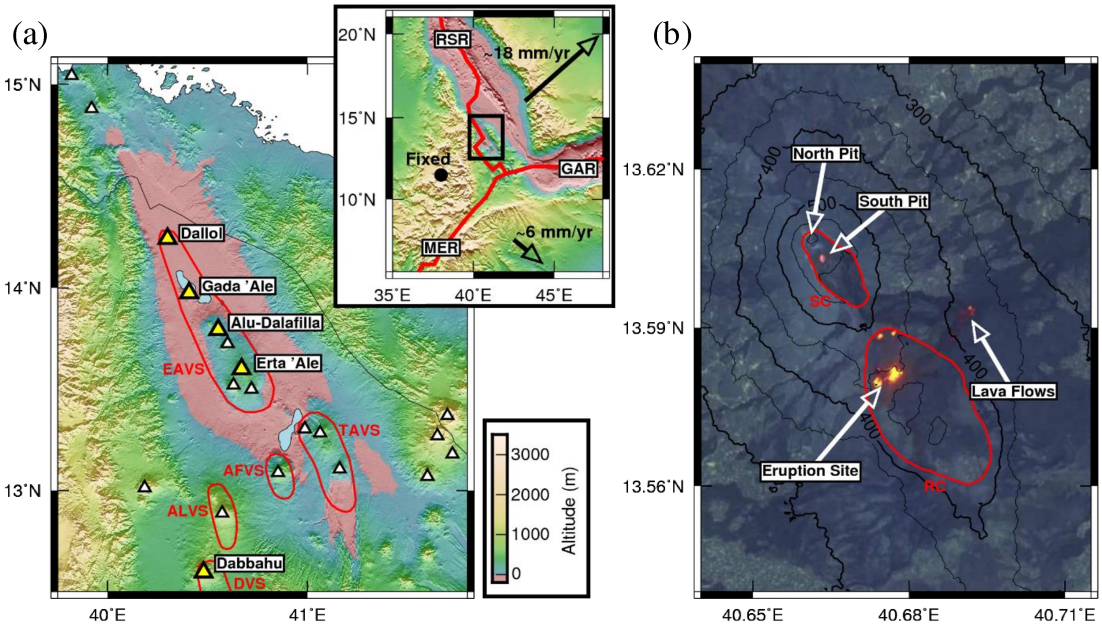

Figure 2.1: (a) The Danakil depression in northern Afar with Holocene volcano locations from the Smithsonian Institute Global Volcanism Program marked as white triangles and key volcanoes highlighted in yellow. Simplified volcanic segments (VS) (Wolfenden et al., 2005) are shown in red: EAVS - Erta 'Ale, TAVS - Tat 'Ale, AFVS - Afdera, ALVS - Alayta, DVS - Dabbahu. Inset map shows the relative movement of the Arabian and Somalian plates to the Nubian plate, with plate boundaries from Bird (2003). RSR - Red Sea Rift, GAR - Gulf of Aden Rift, MER - Main Ethiopian Rift. Region shown in (a) is outlined in black. (b) ESA Sentinel-2 false-colour optical image (bands 12, 11, 4) of Erta 'Ale volcano on 08 February 2017, with elevation contours, and the summit (SC) and relic (RC) calderas outlined in red. Areas of high thermal output from the eruption site, lava lake, and fresh lava flows, are shown as bright red/orange (from short-wave infrared bands).

20-26 km in central Afar, and 25-40 km on the rift margins (Hammond et al., 2011, Bastow and Keir, 2011, Tiberi et al., 2005). Seismicity at $\sim$ 12 km depth on the rift axis is indicative of melt storage near the base of the crust below the EAVS (Illsley-Kemp et al., 2018b), and supports the argument that that extensional strain is focussed on the rift axis and accommodated by magmatic intrusion (Ebinger et al., 2017, Ebinger and Casey, 2001, Hayward and Ebinger, 1996).

The EAVS is one of the most active magmatic segments in Afar. Amelung et al. (2000) identified subsidence at Gada 'Ale volcano between 1993 and 1996 attributed to magma withdrawal and normal faulting, and Nobile et al. (2012) observed a $\sim 60 \times 10^6$ m^3 dyke intrusion sourced from a reservoir at $\sim$ 2-3 km depth below Dallol in 2004 (Figure 2.1a). The 2008 eruption of Alu-Dalafilla produced $\sim 25 \times 10^6$ m^3 of erupted lava flows sourced from a shallow ($<$ 2 km) deep axial magma chamber (Pagli et al., 2012). Pagli et al. (2012) suggest that much of the erupted magma was present in the upper 4 km of the crust before the eruption, supporting the comparison between the EAVS and shallow sill complexes at fast-spreading MORs.

Erta 'Ale is the most persistently active volcano in the EAVS, hosting a long-lived active lava lake in the south pit of its summit caldera, with observations of lava lake activity extending for $>$ 90 years (Barnie et al., 2016, Varet, 1971) (Figure 2.1b). The north pit also hosted an active lava lake (Varet, 1971) which solidified between 1988 and 1992 (Field et al., 2012), but came close to reactivation in 2013 (Barnie et al., 2016). The south pit lava lake level has fluctuated through time (Barnie et al., 2016, Guern et al., 1979) with overflows being observed from 1967-1973 (Guern et al., 1979, Varet, 1971, Barberi and Varet, 1970), in 2010 (Field et al., 2012), and in January 2017 (Global Volcanism Program, 2017). The only previously observed ground deformation at Erta 'Ale volcano in 2004-2005 was not associated with an overflow (Barnie et al., 2016). Barnie et al. (2016) attribute the deformation to a shallow dyke intrusion aligned with the ridge axis in 2004-2005 producing 2.3×10^6 m^3 of volume change. Field et al. (2012) use melt inclusions in lavas erupted in 2010 to find that the magma crystallised over a period of $\sim$ 10-37 years at depths of $<$ 1.5 km, indicating the presence of a shallow reservoir below Erta 'Ale. This is in agreement with Gerlach (1980) who suggest that magma degassing originates in a large reservoir at $>$ 1 km depth.

2.2.2 2017 Erta 'Ale Eruption

Erta 'Ale lava lake overflows from 16-19 January 2017 produced $\sim$ 1 km long lava flows within the summit caldera (Global Volcanism Program, 2017). On 21 January 2017, a fissure eruption also opened $\sim$ 3 km SE of the lava lake within a relic caldera on the south flank of Erta 'Ale (Figure 2.1b), producing the highest level of SO_2 emissions ever observed at Erta 'Ale from space (Global Volcanism Program, 2017). The lava

lake level dropped at the time of the eruption by 80-100 m (Volcano Discovery, 2017). Following the initial eruption a new lava lake was formed at the eruption site, which remained active for $\sim$ 1 year (Global Volcanism Program, 2018). From January 2017 until at least June 2019, the south pit lava lake and extensive lava flows originating from the eruption site have remained active, producing persistent thermal anomalies (MIROVA, 2019), and weak SO_2 emissions (Carn, 2019) detected from satellite based sensors.

Xu et al. (2017) modelled the surface displacements from the eruption as a shallow dyke intrusion fed from a vertical conduit storage below the lava lake. Their model consisted of a 3 km long dyke with uniform opening below the eruption site and a volume increase of 1.9×10^6 m^3; this was combined with a 1 km long dyke below the lava lake with a contraction of -1.8×10^6 m^3. They suggest that the dyke-shaped conduit below the lava lake may be a long-lived feature of the shallow plumbing system at Erta 'Ale, with previous studies on Kilauea, Hawaii, also identifying a conduit contraction and a drop in lava lake levels during an eruption (Patrick et al., 2015, 2019a,b). Xu et al. (2017) also identify an area of post-intrusive uplift they model as an inflating sill below the eruption site at 1-2 km depth, indicating that the shallow axial melt observed at Alu-Dalafilla in 2008 (Pagli et al., 2012) may be representative of typical behaviour on the EAVS.

Here, we use dense time series of Sentinel-1 synthetic aperture radar (SAR) observations from October 2014 to June 2019 to study ground motions associated with the January 2017 fissure eruption, as well as long-term trends of deformation at Erta 'Ale in the period building-up to and following the initial eruption. We also assess how shallow magma storage is accommodated at Erta 'Ale using pressure change calculated from changes in the height of the Erta 'Ale lava lake, and the volume of material extruded from the eruption site. We propose a simple mechanical model to describe the behaviour of the shallow plumbing system at Erta 'Ale volcano, and discuss the implications for the dynamics of magmatic centres in rift zones.

2.3 InSAR Data

We use all the acquisitions of Sentinel-1A/B satellites from ascending track 14 (T14A) and descending track 79 (T79D) between October 2014 and June 2019 to measure surface deformation. We create a network of 204 ascending and 300 descending interferograms using GAMMA (Werner et al., 2000) and LiCSAR software (González et al., 2016) at 5:1 range to azimuth looks, equating to $\sim$ 20 $\times$ 20 m pixel size. We correct for topography using the 30 m Shuttle Radar Topography Mission (SRTM) elevation model (Farr and Kobrick, 2000). We perform post-processing on the network of in-

terferograms, to correct for a linear relationship between height and phase due to the atmosphere in each interferogram using a $\sim 14 \times 7$ km non-deforming region ~ 15 km to the south of Erta 'Ale volcano with similar topography (Elliott et al., 2008). We calculate the performance of this correction from the mean variance of the whole background non-deforming region by masking out a $\sim 15 \times 12$ km deforming area, centred on the eruption site, for all images. This results in a mean reduction in the phase root-mean-square-error (RMSE) in individual interferograms of ~ 9 % (~ 1 mm). We find that this linear height-phase atmospheric correction performs better on this small region around Erta 'Ale than a correction based on the GACOS atmospheric model (Yu et al., 2017, 2018), in which the mean RMSE is increased by ~ 90 %. We reference each interferogram to its background mean value.

To estimate the time varying atmospheric noise in the time-series, we estimate the contribution of the atmospheric phase screen (APS) to each epoch in the same background non-deforming region. To do this, we apply a least squares inversion to find the time-series of deformation in the non-deforming region using a small-baseline methodology (e.g. Berardino et al., 2002, Lanari et al., 2004, 2007). We include a minimum of three interferograms covering each deformation step. We then estimate the remaining atmospheric phase screen (APS) from the time series within the subset by firstly high-pass filtering in time by applying and then subtracting a low-pass weighted Laplacian filter from the time series. We then low-pass filter in space using a $\sim 100 \times 100$ m Gaussian kernel to give an estimate of the APS for each epoch. To estimate the level of noise for each epoch, we calculate the variance of phase by differencing the filtered (APS removed) and the un-filtered time series, assuming that within this subset region all phase variations in the filtered time-series are due to noise and not ground deformation. A small amount of residual noise remains associated with each epoch, resulting from small unwrapping and filtering errors, and random noise. We account for this by calculating the sum around a loop of interferograms associated with the epoch, and find that the mean residual phase is ~ 5 mm. We apply this noise value to each date in addition to the atmospheric noise calculated previously.

We perform a small-baseline style least-squares inversion for the line of sight (LOS) displacement time-series across the whole image for all time steps, incorporating the calculated variance on each epoch as weights using a variance-covariance matrix. This approach allows us to propagate the calculated data noise estimates into errors in displacement for each epoch, accounting for the variability in noise between epochs. We perform no further filtering on the whole image time-series. Further details are provided in Appendix A.

With ascending and descending data, we only have two components of a 3D displacement field (e.g. Wright et al., 2004). We use the ascending and descending data to invert for rift-perpendicular horizontal and vertical ground movement at Erta 'Ale, assuming all horizontal displacements are perpendicular to the ridge axis (e.g. Hamling et al., 2014). We solve for rift-perpendicular horizontal and vertical motions only where ascending and descending acquisition dates align to within $\lesssim$ 1 week in order to limit the amount of deformation that occurs between acquisitions.

2.4 Analysis

2.4.1 Ground Deformation

Figure 2.2 shows the full time series of surface displacements from October 2014 to June 2019 for ascending LOS, descending LOS, horizontal rift-perpendicular, and vertical motions. We divide the time series into four stages: the pre-eruption period from October 2014 to January 2017 (A), the initial intrusion in January 2017 (B), the early-stage eruption from January 2017 to April 2017 (C), and the late-stage eruption from April 2017 to June 2019 (D). Due to the lack of ascending acquisitions between February 2017 and September 2017, we combine periods C and D into a single late-stage eruption period from January 2017 to June 2019 (E) so that we can resolve horizontal rift-perpendicular and vertical motions. We extract the time series for 6 representative points around Erta 'Ale volcano (numbered 1-6 in the upper left panel of Figure 2.2) which are displayed in Figure 2.3. We selected the points in order to observe displacements as close as possible to the lava lake (1 and 2) and eruption site (4-6), whilst avoiding incoherence in the time series associated with lava flows and rapid co-intrusive surface displacements. Below we describe how Erta 'Ale deformed in each of the key time periods and discuss best-fit simple models that can explain the observations.

Pre-Eruption (A)

Time-period A in Figures 2.2-2.4 shows surface displacements in the build-up to the eruption between October 2014 and January 2017. This period is dominated by a gradual increase in rift-perpendicular extension focussed on the rift axis between the lava lake and eventual eruption site (Figure 2.2). The total extension over the rift axis is shown in Figure 2.4, and reaches a maximum of 140 $\pm$ 10 mm before the eruption date in January 2017 at an average rate of 60 $\pm$ 10 mm/yr, more than three times higher than the average plate spreading rate at Erta 'Ale. The extension rate also increases around April 2016 from a rate of 35 $\pm$ 7 mm/yr to 111 $\pm$ 30 mm/yr up to the eruption date. Vertical displacements during this period are small at $\pm$ 4-10 mm/yr, with slight uplift observed on the rift axis between the lava lake and eruption site.

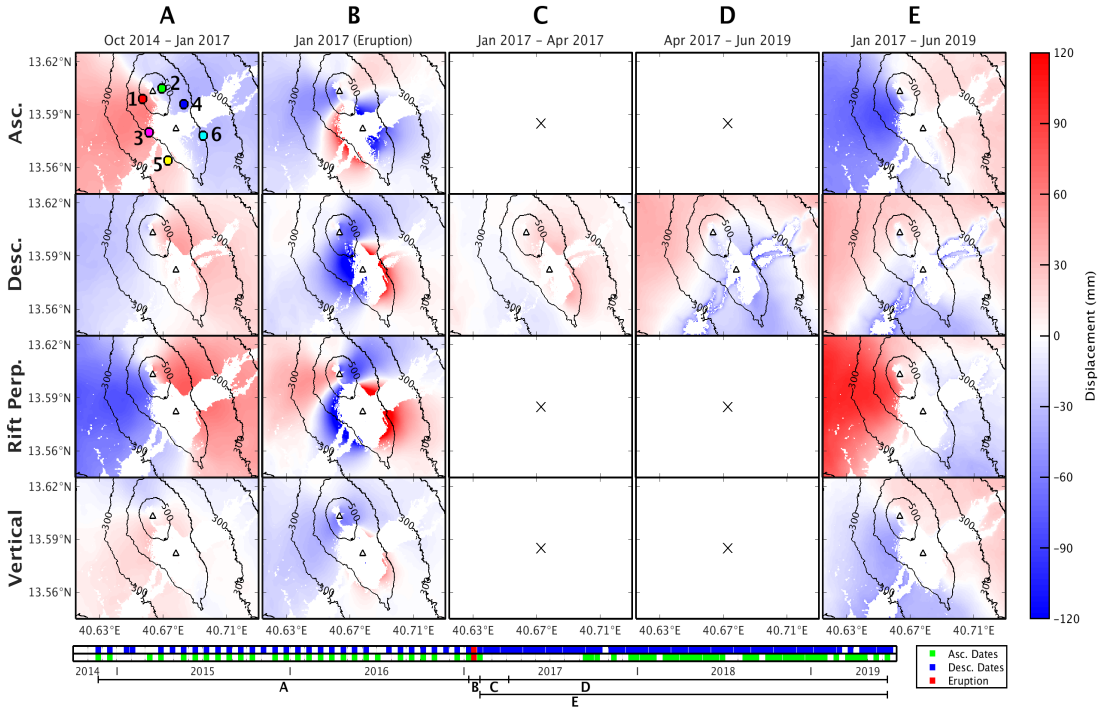

Figure 2.2: Displacement maps at Erta 'Ale volcano in the build-up to (A), during the initial stage (B), and during later stages (C, D, E) of the eruption, for ascending LOS, descending LOS, horizontal rift-perpendicular, and vertical motions (as in Figure 2.3). As ascending data is missing during periods C and D, we are unable to resolve rift-perpendicular and vertical motions for these periods. For the ascending and descending LOS maps, positive values show motion towards the satellite; for the rift-perpendicular maps, positive values show motion to to ∼NE; and for the vertical maps, positive values show uplift. Topographic contours are shown on every map for reference at 100 m spacing, along with the Erta 'Ale lava lake, and south flank eruption site (triangles). The six coloured points around Erta 'Ale are the points selected to show the time series of displacements in Figure 2.3. The points were selected in order to be as close to the lava lake and eruption site as possible, without losing coherence (white mask on maps). The pre- and co-intrusive phases (A-E) are shown on the time axis, with the acquisition dates for ascending and descending Sentinel-1A/B, and the eruption date.

We model the total observed extensional signal (October 2014 to January 2017) with the opening of a vertical dyke structure aligned with the rift axis and assuming deformation is caused by dislocations in an elastic homogeneous half-space (Okada, 1985). To find this solution, we sub-sampled the data using a quadtree approach (Jónsson et al., 2002), with a variance threshold of 9×10^{-4} m^2. We optimised the geometry and opening of the dislocation, and estimated uncertainties using the Geodetic Bayesian Inversion Software (GBIS) which implements the Markov Chain Monte Carlo method and Metropolis-Hastings algorithm to create probability density functions (PDFs) of model source parameters (Bagnardi and Hooper, 2018). From the pattern of surface deformation, we restrict the location of the source to the Erta 'Ale edifice and fix the dip of the dykes to 90° in order to reduce the number of free parameters. In order to explore a range of potential source geometries, we provide relaxed prior information on the source geometry and opening. Best-fit model parameters are selected from the

mode of the resulting PDFs, while the 2.5 and 97.5 percentiles are used to estimate the error in the optimal model or indicate a range of optimal fits.

The best-fit vertical dyke has dimensions $\sim 5 \times 5$ km with depth to the top of the dyke at ~ 500 m; it is aligned with the rift axis, and has a volume increase of $\sim 3 \times 10^6$ m^3 (a full list of model parameters and uncertainties is shown in Table 2.1). Ascending and descending data, model, and residual interferograms are shown in Figure A.2. This model has a similar geometry to both a pre-eruptive dyke between January 2016 and January 2017 modelled by Xu et al. (2017), and a dyke observed in 2004-2005 by Barnie et al. (2016) at Erta 'Ale which did not lead to an eruption. The similarity between the modelled dykes in 2004-05 and 2014-17, suggests that this style of intrusion may be typical at Erta 'Ale, and could be indicative of a long-lived region of accumulating shallow melt which is elongated along the ridge axis.

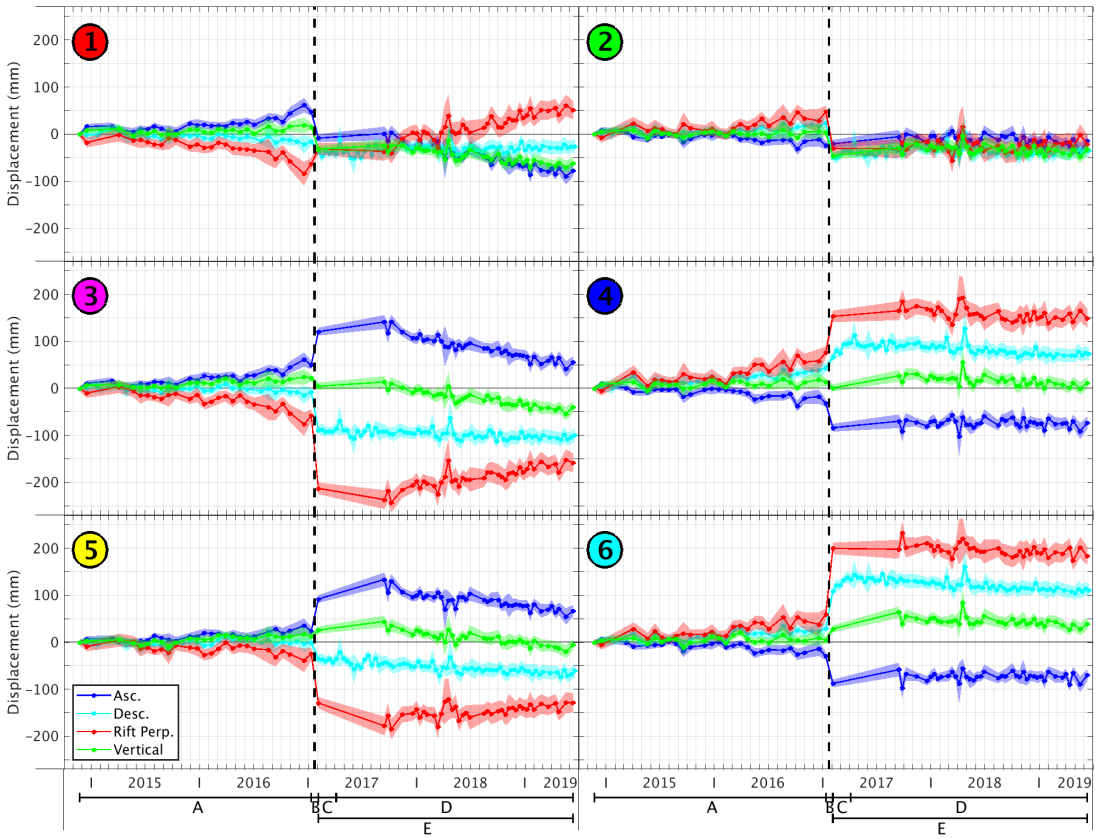

Figure 2.3: Time series of ascending LOS (dark blue), descending LOS (light blue), rift-perpendicular (red), and vertical (green) displacements at 6 points around Erta 'Ale volcano as shown in Figure 2.2. Points 1 and 2 are about the lava lake, points 3 and 4 are to the north of the eruption site, and points 5 and 6 are to the south of the eruption site. Points 1, 3, and 5 are on the SW side of the ridge, and points 2, 4, and 6 are on the NE side of the ridge. The points were selected in order to be as close to the lava lake and eruption site as possible, without losing coherence. Time periods shown in Figure 2.2 are shown below the time axis for pre-eruption (A), during the initial eruption (B), and during later stages of the eruption (C, D, and E).

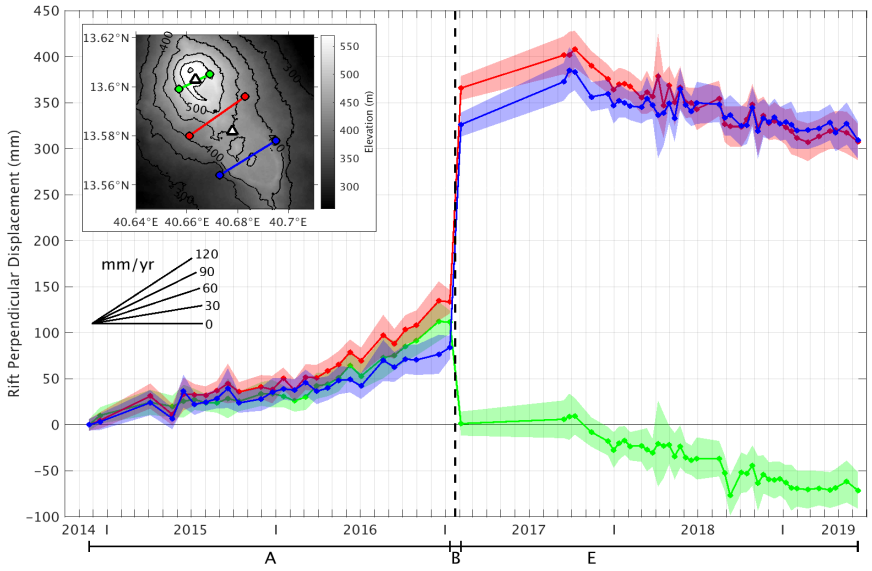

Figure 2.4: Time series of horizontal rift-perpendicular displacements between three pairs of points over the ridge axis at Erta 'Ale. Inset map shows the location of the pairs of points used. The points used are the same as shown in Figures 2.2 and 2.3, and are selected to be as close to the lava lake and eruption site as possible, without losing coherence. Green - points 1-2, red - points 3-4, blue - points 5-6. The eruption date in January 2017 is marked by a black dashed line. The pre- and co-intrusive phases shown in Figure 2.2 are indicated below the time axis.

Initial Eruption (B)

Ground observations show that the eruption began on 21 January 2017 (Global Volcanism Program, 2017) on the south flank of Erta 'Ale. The first post-eruption image was acquired on 28 January 2017. From 11-28 January 2017, we measure up to 400 ± 50 mm of extension over the ridge and 50 ± 10 mm of uplift at the eruption site (points 1-2 in Figures 2.2-2.4). At the same time, we measured up to 120 ± 20 mm of contraction and 60 ± 10 mm of subsidence near the lava lake (points 3-6 in Figures 2.2-2.4).

We can model this deformation well using two vertical dyke sources, one opening below the eruption site, and one closing below the summit caldera. We tried a variety of simple source mechanisms for the closing about the summit caldera signal including point and spherical sources, although a contracting planar dyke provided a significantly better fit than sources with radially symmetric deformation patterns. Below the summit caldera, we require a larger value of dyke closing at depths $\gtrsim$ 900 m than at depths $\lesssim$ 900 m (Figure 2.5), as a single value of closing is not able to fully reproduce the deformation pattern. For the portion of the data which shows contraction about the summit caldera, a single value of dyke closing is not able to match the magnitude of far-field displacements ($>$ 2 km from the summit caldera) without producing excessive near-field displacements ($<$ 1 km from the summit caldera). We preferred to keep the

model relatively simple, with two sources, rather than solving for a full distributed contraction model.

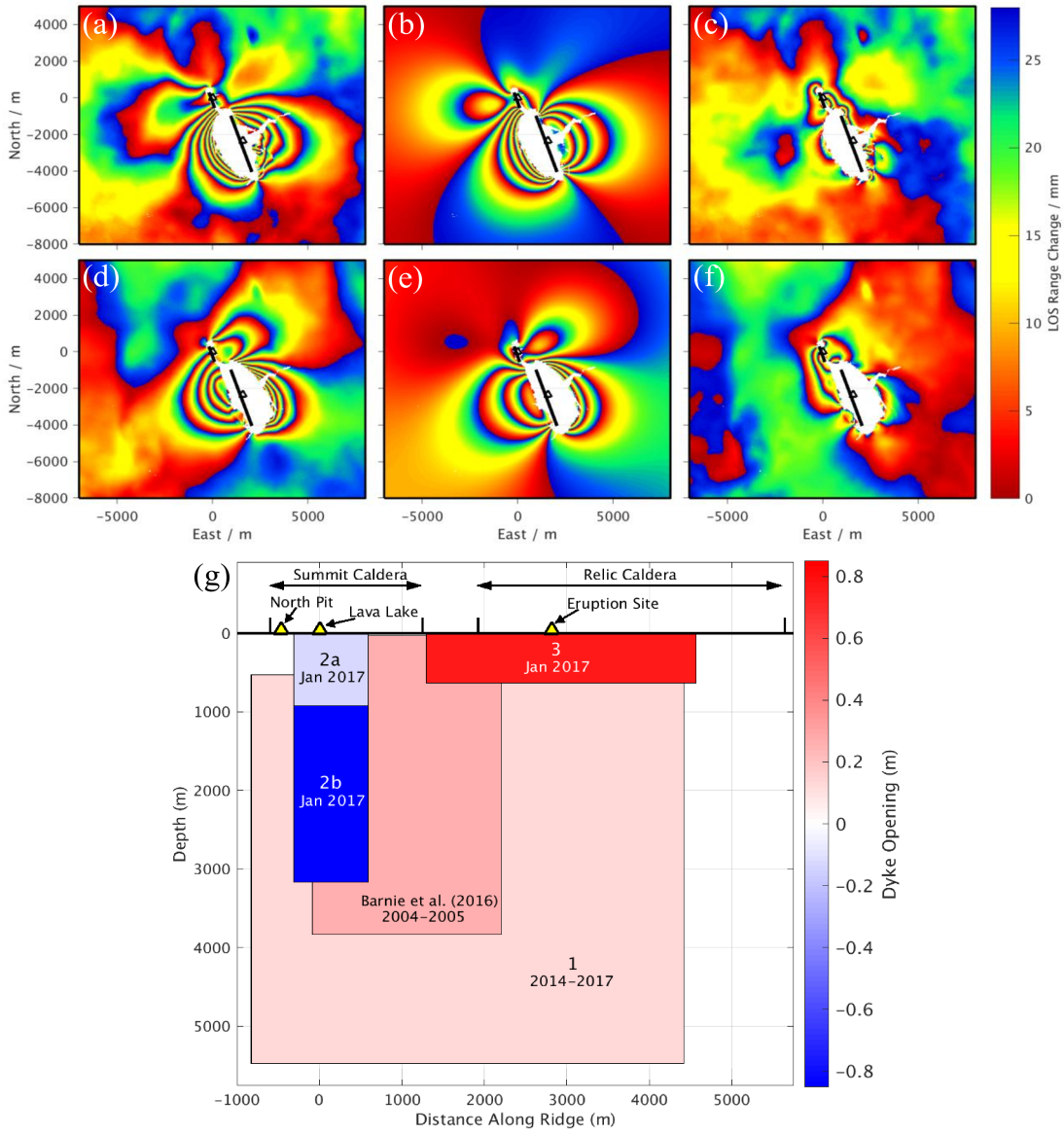

Figure 2.5: (a-c) Ascending and (d-f) descending Sentinel-1 data, model and residual for co-intrusive interferograms 11.01.2017-04.02.2017 and 04.01.2017-28.01.2017 respectively. One colour cycle (red-blue) represents 27 mm of line of sight (LOS) range change away from the satellite. Locations of dykes 2 and 3 are shown as black lines, with the lava lake and eruption site shown as triangles. (g) Rift-parallel cross-sectional view of the modelled dyke structure, where dyke 1 is pre-eruptive (October 2014 to January 2017), and dykes 2a, 2b, and 3, are co-intrusive. Dyke geometries were optimised using GBIS (Bagnardi and Hooper, 2018), with the parameters shown in Table 2.1. Also shown is the modelled dyke from Barnie et al. (2016) from January 2004 to May 2005. Locations of the lava lake, north pit, and the eruption site are shown as yellow triangles, with the locations of the summit and relic calderas also shown.

Parameters for the modelled dykes with error estimates are shown in Table 2.1 with volume changes for the dykes 2 (contraction under the lava lake) and 3 (extension SE of the lava lake) of -1.9±0.3 × 10^6 m^3 and 1.59±0.04 × 10^6 m^3 respectively. Predicted displacements from the model are represented in Figure 2.5b and 2.5e for ascending and descending LOS geometry, and shown in depth cross-section in Figure 2.5g. Areas of incoherence near the eruption site in Figure 2.5a-f are due to either fresh lava flows or the high deformation gradient associated with the intrusion.

Our findings for the geometry of the shallow dykes agree well with that found by Xu et al. (2017), who also suggest there were two sub-vertical dykes, opening below the eruption site and a contracting dyke below the Erta 'Ale lava lake. Our model reduces the RMSE of ascending and descending data by 45% in the area shown in Figure 2.5a-f, compared to a reduction of 32% for the model of Xu et al. (2017). Some residuals remain close to the eruption site, which are likely due to simplifications we have made in the model; such as the uniform opening of rectangular planar dykes, and the use of an elastic homogeneous half-space. Because of these simplifications, the model cannot fully reproduce the complex co-intrusive deformation pattern produced in the near-field. Additional residuals, particularly away from the eruption site, may be mostly due to uncorrected atmospheric errors.

We interpret the dyke below the lava lake as a contracting tabular conduit, reaching down to 900-950 m depth. Below this, there is an increase in dyke contraction below the lava lake, coincident with the depth of the bottom of the intruding dyke 3. Here, we cannot resolve in more detail the structure of this region of higher contraction, but considering the presence of melt storage at $\sim$ 1 km depth elsewhere on the EAVS (Pagli et al., 2012), and the inference of shallow melt storage below Erta 'Ale (Field et al., 2012), it may represent the top of a region of shallow storage at Erta 'Ale volcano at $\sim$ 1 km depth.

Late-Stage Eruption (C, D, E)

After the initial intrusion in January 2017, the eruption site on the south flank of Erta 'Ale remained active and produced extensive lava flows which are still active at the time of writing (August 2019), $\sim$ 2.5 years later. In the descending time series, regular 12-day acquisitions from February-September 2017 allow us to separately explore LOS motions between January and April 2017 (C) and April 2017 and June 2019 (D). During period C, a gradual range decrease (apparent uplift) signal of 45 ± 15 mm can be seen in the descending time series in Figures 2.2 and 2.3, at points 4 and 6 on the east side of the rift axis. Xu et al. (2017) model this apparent uplift signal as a shallow sill inflation at $\sim$ 1-2 km depth, similar to sills observed elsewhere on the EAVS during eruptions (e.g. Pagli et al., 2012). From April 2017, this gradual uplift is followed by a period of

		Depth (m)	Length (m)	Height (m)	Opening (m)	Volume ($\times 10^6$ m^3)
Dyke 1	2.5%	463	3420	3940	0.108	1.46
	Optimal	**528**	**5250**	**4940**	**0.130**	**3.37**
	97.5%	861	7400	4990	0.205	7.57
Dyke 2a	2.5%	-	898	891	-0.134	-0.104
	Optimal	**0.01***	**902**	**922**	**-0.133**	**-0.111**
	97.5%	-	915	955	-0.130	0.117
Dyke 2b	2.5%	891	898	2080	-0.931	-1.57
	Optimal	**922**	**902**	**2250**	**-0.886**	**-1.80**
	97.5%	955	915	2470	-0.841	-2.10
Dyke 3	2.5%	-	3270	626	0.759	1.55
	Optimal	**0.01***	**3280**	**635**	**0.763**	**1.59**
	97.5%	-	3280	640	0.771	1.62

Table 2.1: Table of dyke model parameters (all to 3 s.f.) for pre-eruptive (1) and co-intrusive dykes (2a, 2b, 3, see Figure 2.5). The 2.5 and 97.5 percentiles of the probability distribution functions for each parameter are shown alongside the optimal model. Parameters marked with * are fixed. We fix the dip of all dykes to 90°. Depth is to the top of the dykes.

slow range increase (gradual apparent subsidence) of roughly equal magnitude to the uplift between January and April 2017, resulting in small total displacements for time period E (C+D).

After the initial response to the eruption between January and April 2017 (C), the long-term response up to July 2019 (D) shows gradual rift-perpendicular contraction and subsidence at rates of 50 ± 20 mm/yr and 25 ± 15 mm/yr respectively (Figures 2.3 and 2.4). The horizontal contraction is focussed near the rift axis between the lava lake and eruption site, while the vertical subsidence is asymmetric over the rift axis, and focussed on the SE side of the edifice. We find that no simple source is able to fully reproduce the ascending and descending data from September 2017 to July 2019 (D). A vertically orientated prolate spheroidal source (Yang et al., 1988) produces the closest match, but the combination of a broad vertical signal and a sharp transition in the horizontal signal over the rift axis suggests there might be a vertically extended source. Using a Yang source, we find that it must be in an off-rift position, $\sim$ 3 km to the SW of the eruption site, with a depth extent of $\sim$ 1-14 km, and a volume change of $\sim$ 20-70 $\times$ 10^6 m^3 (Figure A.3).

2.4.2 Lava Lake Level & Pressure Changes

Lava Lake Depth from SAR

Changes in lava lake levels are potentially a direct measure of changes in pressure in a shallow magma chamber and have been used extensively to assist the understanding of shallow plumbing system dynamics at Kilauea (Patrick et al., 2015, Poland and

Carbone, 2018), Villarrica (Moussallam et al., 2016), Erebus (Jones et al., 2015, Oppenheimer et al., 2009), Nyiragongo (Burgi et al., 2014), and Erta 'Ale (Field et al., 2012, Barnie et al., 2016). Here, we use full resolution Sentinel-1 SAR intensity images ($\sim 5 \times 20$ m pixel spacing) to estimate the depth of both the south (active lava lake) and north pits at Erta 'Ale from the observed shadow lengths (see Figure 6). We define regions in shadow by a simple threshold in the reflection intensity, and count the length of shadows in range by the number of pixels that fall below the threshold. We show an example in Figure A.4. The method works well when the shadow is well defined, but for some acquisitions the shadow limits are more uncertain. For example, the north pit shadow in Figure A.4a is not well defined on the far range side. For this calculated shadow length of 7 pixels ($\sim$ 18 m pit depth), we give confidence bounds that the shadow is 6-14 pixels long ($\sim$ 15-42 m pit depth). In contrast, the south pit shadow in Figure A.4b has sharp edges, and we can give narrow confidence bounds in the shadow length of $\pm$ 1 pixel ($\pm$ 3 m pit depth). Pit depths of 0 m refer to when the pits are full (level with the pit rim) or overflowing.

Figures 2.7 and A.6 show the time series of pit depths for the south and north pits respectively at Erta 'Ale, from October 2014 to June 2019, from both ascending and descending Sentinel-1 intensity shadows. As shown in Figure A.5, we validate these measurements using field reports (Volcano Discovery, 2017), where the lava lake depth in the south pit is routinely reported, and lava lake depth estimates from tourist photos taken of the lava lake from the web (see Table A.1 for citations). We estimate uncertainties in field reports and tourist photos from either accompanying reports or, in the case of some tourist photos, estimations of depth using local features for scale. In general, these supplementary data agree well with depths calculated from Sentinel-1 intensity shadows for the south pit. We cannot apply the same check to the north pit (Figure A.6) as it is not routinely visited by tourists or field guides.

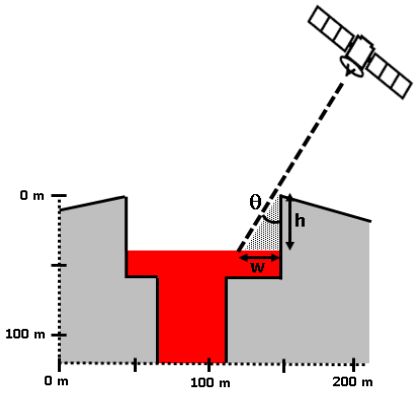

Figure 2.6: Sketch showing how we use SAR shadow lengths (w) and look angle (θ) to calculate pit depth (h). A lava lake depth of 0 m is when the lake level reaches the pit rim.

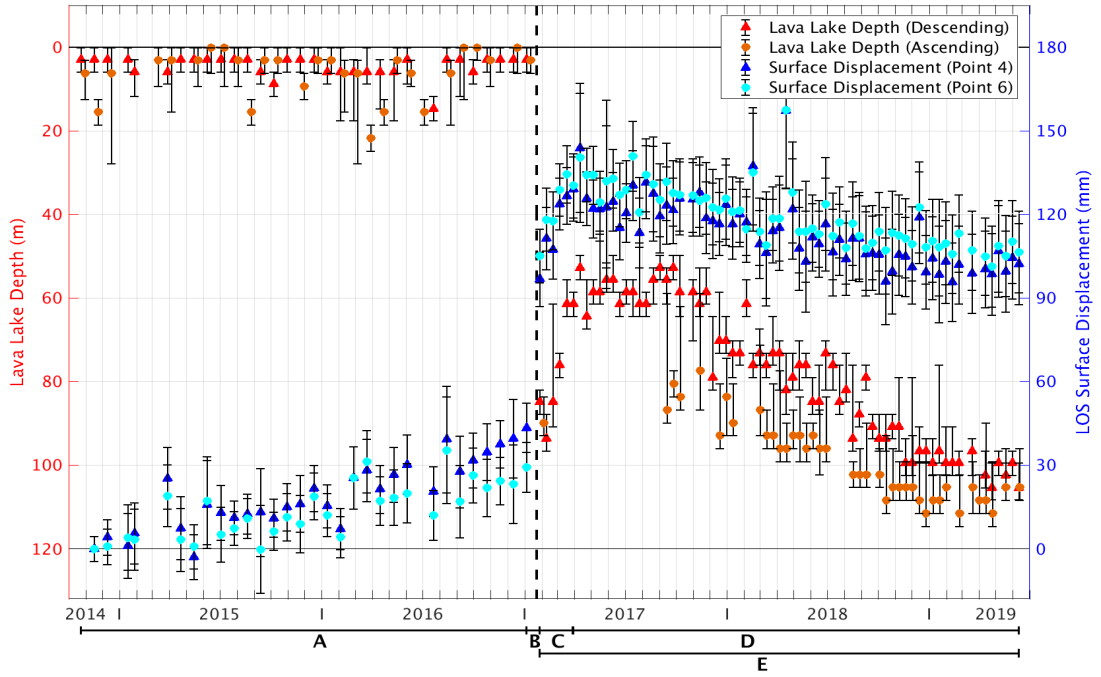

Figure 2.7: Left axis (red): Time series from October 2014 to June 2019 of Erta 'Ale lava lake depths calculated from Sentinel-1 ascending (orange circles) and descending (red triangles) SAR shadows. Right axis (blue): Descending Sentinel-1 line of sight (LOS) surface displacement time series at points 4 (dark blue triangles) and 6 (light blue circles), see Figures 2.2 and 2.3). Points 4 and 6 were selected as they lie closest to the maximum of the area of post-intrusion inflation in time period C (Figure 2.2). The eruption date in January 2017 is marked by the black dashed line. A lava lake depth of 0 m represents when the lake is level with the pit rim (Figure 2.6). Time periods A-E, as shown in Figure 2.2, are indicated below the time axis.

In the pre-eruption period (A), both the north and south pit levels were stable at shallow depths of < 20 m and $\lesssim 40$ m for the south and north pits respectively (Figures 2.7 and A.6), with lava lake overflows reported in January 2016, November 2016, and January 2017 (Volcano Discovery, 2017). As we only use Sentinel-1 for this study, we cannot measure surface displacements or lava lake levels earlier than October 2014. Barnie et al. (2016) monitor the Erta 'Ale lava lake levels from 2000-2015 using optical satellite imagery. From 2011-2015, following a period of lava lake overflows in 2010 (Field et al., 2012), the lava lake was at 20 ± 10 m depth (Barnie et al., 2016), suggesting that the high lava lake levels we observe in period A extend back to the last significant lava lake overflow in 2010. Over the eruption date (black dashed line), the lava lake level in both pits dropped rapidly to 80-100 m and 100-140 m in the south and north pits respectively. This is coincident with reports of a small plume arising from the south pit of Erta 'Ale at this time due to partial pit rim collapse (Global Volcanism Program, 2017), and the opening of the new eruption site and lava flow emplacement on the south flank of Erta 'Ale.

From January 2017 to June 2019, the north pit level has remained roughly stable at depths of 80-130 m. Between January and April 2017 (time period C), the south pit lava lake rose from 90 ± 10 m to 60 ± 10 m depth, at the same time as the sill inflation at 1-2 km depth, modelled from surface uplift in time period C by Xu et al. (2017). Between April 2017 and June 2019 (time period D), the lava lake level dropped gradually from 50-70 m back to the levels just after the eruption date of 80-100 m. As shown in Figure 2.7, this variation in lava lake level is temporally correlated with the descending LOS surface displacement time series with an apparent inflation and deflation of 45 ± 15 mm. This correlation supports the hypothesis that the south pit lava lake may be a good indicator of the pressure state in the shallow plumbing system at Erta 'Ale, similar to the Halema'uma'u lava lake at Kilauea, Hawaii (Patrick et al., 2015, 2019b). The north pit may not be as responsive to pressure changes due to the surface being solidified since ∼ 1990 (Field et al., 2012).

Lava Lake Pressure & Deformation

We use simple analysis of changes in pressure to investigate the state of the Erta 'Ale shallow plumbing system during the eruption period, following the approach previously used for the lava lake at Kilauea (e.g. Poland and Carbone, 2018). If the magma is homogeneous and incompressible, the change in pressure required to sustain pit levels in hydrostatic equilibrium (ΔP) from the observed changes in pit heights (Δh) is $\Delta P = \rho g \Delta h$, where g is the acceleration due to gravity (9.8 m/s^2). For magma density, ρ, we use a value of 2550-3100 kg/m^3 (Anderson and Poland, 2016), using Kilauea volcano, Hawaii, as a close analogue of the Erta 'Ale system. We use a large range in density as the gas content in the magma at Erta 'Ale is unknown. We find that for a co-intrusive drop in lava lake levels of 90 ± 10 m, the associated pressure loss is 2.5 ± 0.5 MPa, and for the post-intrusive rise and fall of the lava lake of 30 ± 20 m, the magnitude of pressure change is 0.8 ± 0.6 MPa.

Using the pressure changes calculated from lava lake level rise and fall, we use a boundary element model to establish whether the changes in pressure observed at the lava lake can reproduce the surface deformation observed at Erta 'Ale. We use the same co-intrusive dyke geometry modelled previously (Figure 2.5), divided into ∼ 150 × 150 m patches, within a homogeneous elastic half-space. Using the co-intrusive pressure change, we solve for the magnitude of patch opening, then convert into surface displacements using Okada's formulation (Okada, 1985). The magnitude of patch opening required to produce surface displacements is also dependant on the elastic shear modulus of the medium.

We find that for a pressure change of 2.5 ± 0.5 MPa, we can match the magnitude of the co-intrusive deformation signal shown in Figure 2.5, if the shear modulus is

6 ± 2 GPa. Within error, this value is consistent with the range of 7.5-13 GPa calculated by Hammond et al. (2011) for the upper 3 km of the Afar crust. It has also been previously established that the shear modulus close to the summit of basaltic shield volcanoes can be significantly lower than estimates from seismic studies (Hooper et al., 2002). At Kilauea, Hawaii, Hooper et al. (2002) estimated the shear modulus in the upper 2.7 km to be 4.5 GPa, whilst Montagna and Gonnermann (2013) use a shear modulus of 3 GPa, for modelling flow through a horizontal dyke between the Kilauea summit and Pu'u'O'o. As our model is consistent with these previous findings, we suggest that a shear modulus of 4-8 GPa is applicable to Erta 'Ale, and the lava lake level is sensitive to the pressure changes in the shallow plumbing system associated with the January 2017 intrusion.

2.4.3 Lava Flow Extent & Effusion Rate

We monitor the growth of extensive erupted lava flows by tracking changes in descending Sentinel-1 coherence. We use only the descending track due to the gap in ascending data between February and September 2017. The coherence of a pixel is an estimate from the similarity of phase scatterers from a group of neighbouring pixels in an interferogram (e.g. Massonnet and Feigl, 1998). Areas where the ground does not change between passes, such as the arid environment around Erta 'Ale, produce very high coherence; changing surfaces, such as vegetation, water, or active lava flows, result in low coherence (Massonnet and Feigl, 1998, Rosen et al., 1996). We use this contrast between the background level of high coherence and the low coherence of fresh lava flows to identify regions of active lava flow at Erta 'Ale, following the approached used to monitor lava flow growth in other location such as Hawaii (Dietterich et al., 2012). We identify pixels with low coherence using a threshold value of 0.35. We calculate the area covered by lava flows by summing the area extent of incoherent pixels identified for each post-intrusive interferogram. Areas of speckly noise in the NE and SW corners of Figure 2.8a, are likely due to small areas of vegetation. To account for this noise, we use all 29 pre-eruption 24 day interferograms (there are no 12 day pre-eruption interferograms available) of the same region shown in Figure 2.8a to establish a mean value for the amount of noise the small areas of vegetation produce. We then use this noise value to give error bounds on the lava flow area calculated in this region.

From January 2017 to June 2017, flows extended < 7 km to the NE of the eruption site, before developing new flows to the SW (< 6 km long). Between July and October 2017 a thin, rapidly extending flow occurred to the NE (< 14 km long). From October 2017 to at least June 2019, lava flows have remained active (MIROVA, 2019) and pooled in a basin region 14-16 km to the NE of the eruption site where the topographic gradient is shallow. Figure 2.8b shows a roughly linear flow area growth rate from the eruption up to November 2017, where the total flow area begins to level off at ~ 22 km^2. As

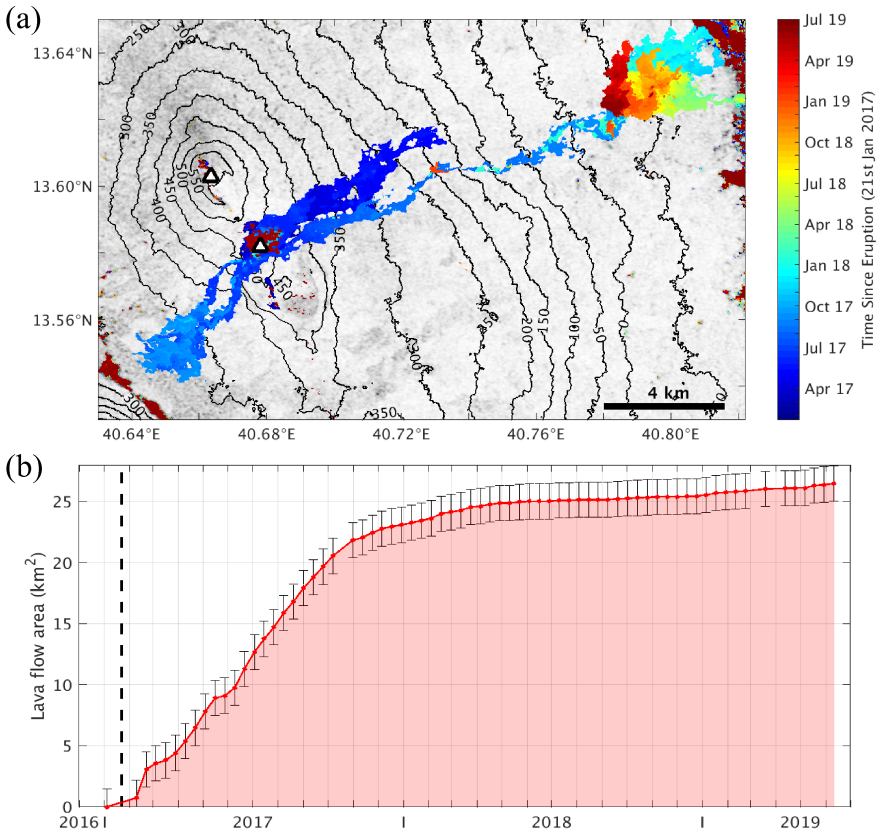

Figure 2.8: (a) Lava flow coverage from the eruption site and lava lakes (white triangles) at Erta 'Ale from the eruption date (21 January 2017) to June 2019. We define fresh lava flows as all incoherent pixels (coherence < 0.35) as typically the background coherence at Erta 'Ale is very good. Background image shows the coherence of a pre-eruption 24-day interferogram on a 0-1 grey-scale. Areas of additional incoherence in the NE and SW of the image are likely due to small patches of vegetation. 50 m contours show the topography around Erta 'Ale volcano. (b) Cumulative lava flow area from the eruption date (black dashed line) to March 2018. We calculate error bounds based on the mean pre-eruption incoherence of the area (incoherence not associated with lava flows).

there are no intensity shadows originating from the lava flows, the thickness of the flow is $\lesssim$ 15 m. Using the anecdotal evidence from a local field guide during a short field campaign in September 2017, we estimate the thickness of lava flows around this time to be in the range 0.5-2.5 m. This is in agreement with tourist photographs of the fresh lava flows which show thicknesses of 0.5-1 m at the SW extent of the flows (Global Volcanism Program, 2018). Applying this to a total area of lava flow coverage of 26 $\pm$ 1 km^2, we estimate the total volume of erupted material up to June 2019 is in the range 12.5-67.5 $\times$ 10^6 m^3. This is in agreement with our estimate of 20-70 $\times$ 10^6 m^3 from the deflation of an off-rift vertically extensive source during the long-lived eruption (September 2017 - July 2019).

We measure the effusion rate over the period of approximately linear growth in lava flow area shown in Figure 2.8b up to October 2017. Between November 2017

and October 2018, the flow area does not significantly increase. Persistent thermal anomalies from satellite-based MODIS data show that the NW extent of the flow has remained active up to at least June 2019 (MIROVA, 2019), indicating that the flow in this area may be thickening. Field reports are unable to validate this as the area is highly inaccessible. However, for the period of linear flow area growth, we can measure the effusion rate from the eruption date (21 January 2017) to 07 October 2017 (271 days). We find that for a total erupted area of 21 $\pm$ 2 km^2, the erupted volume is 10-58 $\times$ 10^6 m^3, with a mean effusion rate of 0.4-2.5 m^3/s. This rate is in agreement with the 2010 lava lake overflows where Field et al. (2012) estimate that the gas flux could be accounted for by a near-complete degassing of magma in the conduit, moving at rates of 1.1-2.6 m^3/s.

2.5 Discussion

Several key features of the Erta 'Ale shallow plumbing system show similarities to other volcanoes such as Kilauea and Mauna Loa, Hawaii, and Ambrym, Vanuatu, with the removal of melt from a summit caldera coincident with the horizontal propagation of a dyke into an established rift zone (e.g. Montagna and Gonnermann, 2013, Amelung et al., 2007, Poland et al., 2014, Shreve et al., 2019). At Kilauea, a synthesis of measurements, including InSAR, GNSS, tilt, and gravity, reveal a shallow magma reservoir at $\sim$ 1.5 km depth below the Halema'uma'u lava lake (Anderson et al., 2015, Poland et al., 2014, Bagnardi et al., 2014). At Erta 'Ale, pressure changes in the lava lake during the post-intrusion period are linked to the shallow sill inflation and subsequent deflation at 1-2 km depth (Xu et al., 2017). Our co-intrusive model also requires an increase in dyke contraction at $\sim$ 1 km depth, indicating a change in sub-surface conditions. The presence of a shallow sill overlying a dyke structure at Erta 'Ale is in agreement with analysis by Xu et al. (2017) of the stress state below Erta 'Ale from topographic loading. Axis-aligned dyke structures are preferred to sills within $\sim$ 5 km either side of the ridge axis and up to $\sim$ 10 km depth, except directly below the summit caldera where the relative topographic unloading allows the formation of sill structures within $\sim$ 0.5 km either side of the ridge axis and up to $\sim$ 1-1.5 km depth (Xu et al., 2017). Combined with petrological evidence of a potential reservoir at $<$ 1.5 km depth (Field et al., 2012), we propose that a shallow reservoir on the ridge axis is present at Erta 'Ale at $\sim$ 1 km depth, which likely sustains the long-lived lava lake.

A common feature of shallow plumbing systems in rift zones is the connectivity a shallow reservoir to a deeper magma chamber. At Kilauea, a reservoir at 3-5 km depth is connected to both the shallow reservoir at Halema'uma'u and the ERZ (Poland et al., 2014). On the EAVS, a magma reservoir at 4 km depth at Alu-Dalafilla was observed during the 2008 eruption and shallow sill inflation (Pagli et al., 2012). From subsidence

and contraction during the long-lived eruption (2017-2019), we infer a vertically extensive source from depths of $\sim$ 1-14 km, which is more likely representative of a system of smaller stacked sources, than a single body. The large pre-eruptive axial dyke inflation, which is similar to a previous intrusion at Erta 'Ale (Barnie et al., 2016), may also indicate that shallow melt at Erta 'Ale is not stored in a relatively contained magma reservoir, but is distributed through a zone of partial melt in the upper $\sim$ 5 km of the crust. A heavily intruded shallow crust may be typical on the EAVS, as most of the erupted material from the 2008 Alu-Dalafilla eruption was sourced from within the upper 4 km of the crust (Pagli et al., 2012). Illsley-Kemp et al. (2018b) also identify a lower crustal reservoir below Alu-Dalafilla from seismicity at $\sim$ 10-15 km depth, and suggest that a similar feature below Erta 'Ale may be present, but was not detected in their study due to a potentially high melt percentage in the crust. This is in agreement with the presence of a system of stacked mid-crustal sources from our analysis of surface deformation from 2017-2019, and with receiver function studies which identified a significant amount of magmatic intrusion in the Afar lower crust (e.g. Hammond et al., 2011).

During the pre-eruption period, gradual dyke opening along the rift axis corresponds to a total volume increase of 1.5-7.6 $\times$ 10^6 m^3, at a rate of 0.02-0.11 m^3/s. As the lava lake level does not significantly vary throughout this period, the pressure state in the shallow reservoir is stable. In order to maintain a steady pressure state at the top of the pre-eruptive dyke, magma flux from depth must be compensating for the extension on the rift axis at a rate at least equal to the opening of the dyke. We can therefore give a lower bound estimate on magma flux during this period of 0.02-0.11 m^3/s. The lack of any significant ground deformation across the total post-intrusive period indicates that the majority of erupted material is either being sourced from depth, or is highly compressible (Rivalta and Segall, 2008). The eruption rate of 0.4-2.5 m^3/s may therefore be a good indicator of magma flux through the shallow plumbing system during period E, up to two orders of magnitude larger than our estimate of magma flux during period A. The large volume of erupted material, in comparison to the volume of observed shallow intrusions at Erta 'Ale, is supported by Hutchison et al. (2018) who use petrology to establish that 2/3 of material at Erta 'Ale is erupted, and 1/3 intruded into the shallow crust. This in agreement with seismic evidence which suggests that during the final stage of break-up on the EAVS, there is a shift from intrusive to extrusive magmatism (Keir et al., 2013).

The presence of a potential shallow reservoir overlying a region of axial melt storage at Erta 'Ale and Alu-Dalafilla on the EAVS (Pagli et al., 2012), shows similarities to the stacked sill structure observed at spreading ridges with high melt flux, such as the fast spreading EPR (e.g. Wanless and Behn, 2017, Marjanović et al., 2014, Carbotte

et al., 2013). An important distinction at Erta 'Ale is the largely dyke-fed plumbing system, defined by the local topographic and regional tectonic stress fields (Xu et al., 2017, Wadge et al., 2016), rather than a system of stacked sills observed at MORs, although dykes at MORs may simply be difficult to image with reflection seismology (e.g. Marjanović et al., 2018). Yet the existence of a reservoir at $\sim$ 1 km depth at Erta 'Ale and Alu-Dalafilla indicates that shallow magma bodies may be supported on the EAVS. High melt flux on the EAVS may be contributing to this, given the heavily intruded crust beneath the Danakil Depression (Hammond et al., 2011, Bastow and Keir, 2011, Tiberi et al., 2005). At the Galapagos spreading centre, high melt flux produces a stacked sill structure similar to the EPR, whilst spreading at intermediate rates of 53-58 mm/yr (Boddupalli and Canales, 2019). We suggest that despite the slow-spreading rates on the EAVS, high melt flux is allowing the presence of shallow axial magma bodies typical of fast-spreading ridges.

2.6 Conclusions

Erta 'Ale volcano and the EAVS represent the final stage of continental break-up and the development of systems analogous to MORs. We use a time series of Sentinel-1 InSAR observations at Erta 'Ale from October 2014 to June 2019 to study the behaviour of the shallow plumbing system in the build-up to, and during the long-lived January 2017 eruption. The eruption on the south flank of Erta 'Ale, $\sim$ 3 km to the SE of the long-lived lava lake, began on 21 January 2017, and produced lava flows that were still active at time of writing (August 2019) (MIROVA, 2019).

In the build-up to the eruption, from October 2014 - January 2017, we observe gradual extension across the ridge axis at a rate of 60 $\pm$ 10 mm/yr, over three times higher than the long-term plate spreading rate at Erta 'Ale. This is consistent with the opening of a $\sim$ 5 $\times$ 5 km dyke at $\sim$ 500 m depth below the Erta 'Ale summit caldera and eruption site. The lava lake level remains steady at $<$ 20 m below the pit rim during the pre-eruption period. In order to sustain both the lava lake level, and continuous extension, we propose that the magma flux during this time period was at least equal to the rate of dyke opening of 0.02-0.11 m^3/s.

The co-intrusive deformation pattern is consistent with a shallow dyke intrusion extending from the summit caldera to the eruption site on the south flank of Erta 'Ale, and conduit contraction below the summit caldera. Coincident with the initial eruption, we observe a 90 $\pm$ 10 m drop in lava lake level, which was overflowing immediately before the eruption. We find that the pressure loss of 2.5 $\pm$ 0.5 MPa associated with the drop in lava lake level is able to reproduce the observed deformation pattern, indicating that the lava lake is well connected to the shallow plumbing system at Erta 'Ale. The

lava lake level is also sensitive to the post-intrusion inflation and gradual deflation of a shallow sill at $\sim$ 1.3 km depth (Xu et al., 2017). From petrological evidence by Field et al. (2012), we suggest that the Erta 'Ale lava lake may be sustained by a shallow reservoir at $\sim$ 1 km depth.

We do not detect a deeper concentrated magma body below the shallow plumbing system, as is observed elsewhere on the EAVS (Pagli et al., 2012), on Hawaii (e.g. Poland et al., 2014), and at fast-spreading MORs (e.g. Marjanović et al., 2018). Instead, we detect an off-rift deflating vertically extensive source from $\sim$ 1-14 km depth, which likely represents a more complex system of smaller stacked sources. We suggest that melt storage at Erta 'Ale may also be distributed throughout the upper crust, with episodes of melt in-flux forming axial dyke structures as observed between 2014-2017, and 2004-2005 (Barnie et al., 2016).

We monitor the area of extruded lava flows using InSAR coherence measurements, and establish an eruption rate of 0.4-2.5 m^3/s from a period of linear flow area growth between January and November 2017. Over the total post-eruption period, we observe no significant ground deformation, indicating that the rate of eruption is roughly equal to rate of magma flux through the shallow plumbing system at Erta 'Ale. Our estimate of erupted volume up to June 2019 of 12.5-67.5 $\times 10^6$ m^3 is consistent with our modelled co-eruptive sources of deformation, in agreement with a relative increase in extruded material as the EAVS develops through continental breakup (Keir et al., 2013).

Magma plumbing systems at Erta 'Ale and Alu-Dalafilla on the slow-spreading EAVS show features typical of those found at fast-spreading MORs, such as shallow axial magma bodies overlying a system of deeper stacked sills, distributed melt, or a dyke-fed structure (Pagli et al., 2012, Wanless and Behn, 2017). We propose that high magma flux on the EAVS may facilitate the development of these shallow bodies on a slow-spreading ridge.

2.7 Acknowledgements

All Sentinel-1 data is sourced from the European Union Copernicus Programme. We perform data processing on the JASMIN facility, operated by the Centre for Environmental Data Analysis (CEDA), and post-processing and figure generation using MATLAB and GMT. This work was funded by the National Environment Research Council (NERC) RiftVolc project (NE/L013649/1), and supported by the Centre for Observation and Modelling of Earthquakes, Volcanoes, and Tectonics (COMET). Data were archived with NERC's National Geoscience Data Centre (NGDC) and can be

found via the following link: `https://www.bgs.ac.uk/services/ngdc/accessions/index.html?simpleText=ethiopia`

References

Amelung, F., Oppenheimer, C., Segall, P. and Zebker, H. (2000). Ground deformation near Gada 'Ale volcano, Afar, observed by radar interferometry. *Geophysical Research Letters*, **27**(19), pp. 3093–3096. doi:10.1029/2000GL008497. 2.2.1

Amelung, F., Yun, S.-H., Walter, T. R., Segall, P. and Kim, S.-W. (2007). Stress control of deep rift intrusion at Mauna Loa Volcano, Hawaii. *Science*, **316**(5827), pp. 1026–1030. 2.5

Anderson, K. R. and Poland, M. P. (2016). Bayesian estimation of magma supply, storage, and eruption rates using a multiphysical volcano model: Kīlauea Volcano, 2000-2012. *Earth and Planetary Science Letters*, **447**, pp. 161–171. doi:10.1016/j.epsl.2016.04.029. 2.4.2

Anderson, K. R., Poland, M. P., Johnson, J. H. and Miklius, A. (2015). Episodic deflation-inflation events at Kīlauea Volcano and implications for the shallow magma system. *Hawaiian Volcanoes: From Source to Surface*, **208**, p. 229. 2.2, 2.5

ArRajehi, A., McClusky, S., Reilinger, R., Daoud, M., Alchalbi, A., Ergintav, S., Gomez, F., Sholan, J., Bou-Rabee, F., Ogubazghi, G., Haileab, B., Fisseha, S., Asfaw, L., Mahmoud, S., Rayan, A., Bendik, R. and Kogan, L. (2010). Geodetic constraints on present-day motion of the Arabian Plate: Implications for Red Sea and Gulf of Aden rifting. *Tectonics*, **29**(TC3011). doi:10.1029/2009TC002482. 2.2.1

Bagnardi, M. and Hooper, A. (2018). Inversion of Surface Deformation Data for Rapid Estimates of Source Parameters and Uncertainties: A Bayesian Approach. *Geochemistry, Geophysics, Geosystems*, **19**. doi:10.1029/2018GC007585. 2.4.1, 2.5

Bagnardi, M., Poland, M. P., Carbone, D., Baker, S., Battaglia, M. and Amelung, F. (2014). Gravity changes and deformation at Kilauea Volcano, Hawaii, associated with summit eruptive activity, 2009-2012. *Journal of Geophysical Research: Solid Earth*, **119**, pp. 7288–7305. doi:10.1002/2014JB011506. 2.5

Barberi, F. and Varet, J. (1970). The Erta Ale volcanic range (Danakil depression, northern afar, ethiopia). *Bulletin Volcanologique*, **34**(4), pp. 848–917. doi:10.1007/BF02596805. 2.2, 2.2.1

Barnie, T. D., Oppenheimer, C. and Pagli, C. (2016). Does the lava lake of Erta 'Ale volcano respond to regional magmatic and tectonic events? An investigation using Earth Observation data. *Geological Society, London, Special Publications*, **420**, pp. 181–208. doi:10.1144/SP420.15. 2.2.1, 2.4.1, 2.5, 2.4.2, 2.4.2, 2.5, 2.6

Bastow, I. D. and Keir, D. (2011). The protracted development of the continent-ocean transition in Afar. *Nature Geoscience*, **4**(4), pp. 248–250. doi:10.1038/ngeo1095. 2.2.1, 2.5

Berardino, P., Fornaro, G., Lanari, R. and Sansosti, E. (2002). A new algorithm for surface deformation monitoring based on small baseline differential SAR interferograms. *IEEE Transactions on Geoscience and Remote Sensing*, **40**(11), pp. 2375–2383. doi:10.1109/TGRS.2002.803792. 2.3

Bird, P. (2003). An updated digital model of plate boundaries. *Geochemistry, Geophysics, Geosystems*, **4**(3). doi:10.1029/2001GC000252. 2.1

Boddupalli, B. and Canales, J. P. (2019). Distribution of crustal melt bodies at the hotspot-influenced section of the Galápagos Spreading Centre from seismic reflection images. *Geophysical Research Letters*, **46**(9), pp. 4664–4673. doi:10.1029/2019GL082201. 2.5

Burgi, P.-Y., Darrah, T. H., Tedesco, D. and Eymold, W. K. (2014). Dynamics of the Mount Nyiragongo lava lake. *Journal of Geophysical Research: Solid Earth*, **119**(5), pp. 4106–4122. 2.4.2

Carbotte, S. M., Marjanović, M., Carton, H., Mutter, J. C., Canales, J. P., Nedimović, M. R., Han, S. and Perfit, M. R. (2013). Fine-scale segmentation of the crustal magma reservoir beneath the East Pacific Rise. *Nature Geoscience*, **6**(10), pp. 866–870. doi:10.1038/ngeo1933. 2.2, 2.5

Carn, S. (2019). 12 March. *[Online]. [Accessed 15 March 2019]. Available from: https://twitter.com/simoncarn.* 2.2.2

Dietterich, H. R., Poland, M. P., Schmidt, D. A., Cashman, K. V., Sherrod, D. R. and Espinosa, A. T. (2012). Tracking lava flow emplacement on the east rift zone of Klauea, Hawaii, with synthetic aperture radar coherence. *Geochemistry, Geophysics, Geosystems*, **13**(5). doi:10.1029/2011GC004016. 2.4.3

Ebinger, C. J. (2005). Continental break-up: the East African perspective. *Astronomy & Geophysics*, **46**(2), pp. 2–16. 2.2

Ebinger, C. J. and Casey, M. (2001). Continental breakup in magmatic provinces: An Ethiopian example. *Geology*, **29**(6), pp. 527–530. doi:10.1130/0091-7613(2001)029<0527:CBIMPA>2.0.CO;2. 2.2.1

Ebinger, C. J., Keir, D., Bastow, I. D., Whaler, K., Hammond, J. O., Ayele, A., Miller, M. S., Tiberi, C. and Hautot, S. (2017). Crustal Structure of Active Deformation Zones in Africa: Implications for Global Crustal Processes. *Tectonics*, **36**(12), pp. 3298–3332. doi:10.1002/2017TC004526. 2.2.1

Elliott, J. R., Biggs, J., Parsons, B. and Wright, T. J. (2008). InSAR slip rate determination on the Altyn Tagh Fault, northern Tibet, in the presence of topographically correlated atmospheric delays. *Geophysical Research Letters*, **35**(12), pp. 1–5. doi:10.1029/2008GL033659. 2.3

Farr, T. G. and Kobrick, M. (2000). Shuttle Radar Topography Mission produces a wealth of data, Eos Trans. *Eos, Transactions American Geophysical Union*, **81**(48), pp. 583–585. doi:10.1029/EO081i048p00583. 2.3

Field, L., Barnie, T., Blundy, J., Brooker, R. A., Keir, D., Lewi, E. and Saunders, K. (2012). Integrated field, satellite and petrological observations of the November 2010 eruption of Erta Ale. *Bulletin of Volcanology*, **74**, pp. 2251–2271. doi:10.1007/s00445-012-0660-7. 2.2.1, 2.4.1, 2.4.2, 2.4.2, 2.4.2, 2.4.3, 2.5, 2.6

Gerlach, T. M. (1980). Investigation of volcanic gas analyses and magma outgassing from Erta'Ale lava lake, Afar, Ethiopia. *Journal of Volcanology and Geothermal Research*, **7**(3-4), pp. 415–441. 2.2.1

Global Volcanism Program (2017). Report on Erta Ale (Ethiopia). *In: Sennert, S K (ed.), Weekly Volcanic Activity Report, 25 January-31 January 2017. Smithsonian Institution and US Geological Survey.* 2.2, 2.2.1, 2.2.2, 2.4.1, 2.4.2

Global Volcanism Program (2018). Report on Erta Ale (Ethiopia). *In: Venzke, E (ed.), Bulletin of the Global Volcanism Network, 43:4. Smithsonian Institution.* 2.2.2, 2.4.3

González, P. J., Walters, R. J., Hatton, E. L., Spaans, K. and Hooper, A. (2016). LiCSAR: Tools for automated generation of Sentinel-1 frame interferograms. *AGU Fall Meeting.* 2.3

Guern, F. L., Carbonnelle, J. and Tazieff, H. (1979). Erta'Ale lava lake: heat and gas transfer to the atmosphere. *Journal of Volcanology and Geothermal Research*, **6**, pp. 27–48. 2.2.1

Hamling, I. J., Wright, T. J., Calais, E., Lewi, E. and Fukahata, Y. (2014). InSAR observations of post-rifting deformation around the Dabbahu rift segment, Afar, Ethiopia. *Geophysical Journal International*, **197**, pp. 33–49. doi:10.1093/gji/ggu003. 2.3

Hammond, J. O. S., Kendall, J. M., Stuart, G. W., Keir, D., Ebinger, C., Ayele, A. and Belachew, M. (2011). The nature of the crust beneath the Afar triple junction: Evidence from receiver functions. *Geochemistry, Geophysics, Geosystems*, **12**(12). doi:10.1029/2011GC003738. 2.2.1, 2.4.2, 2.5, 2.5

Hayward, N. J. and Ebinger, C. J. (1996). Variations in the along-axis segmentation of the Afar Rift system. *Tectonics*, **15**(2), pp. 244–257. doi:10.1029/95TC02292. 2.2.1

Hooper, A., Segall, P., Johnson, K. and Rubinstein, J. (2002). Reconciling seismic and geodetic models of the 1989 Kilauea south flank earthquake. *Geophysical Research Letters*, **29**(22). 2.4.2

Hutchison, W., Mather, T. A., Pyle, D. M., Boyce, A. J., Gleeson, M. L., Yirgu, G., Blundy, J. D., Ferguson, D. J., Vye-Brown, C., Millar, I. L., Sims, K. W. and Finch, A. A. (2018). The evolution of magma during continental rifting: New constraints from the isotopic and trace element signatures of silicic magmas from Ethiopian volcanoes. *Earth and Planetary Science Letters*, **489**, pp. 203–218. doi:10.1016/j.epsl.2018.02.027. 2.5

Illsley-Kemp, F., Bull, J., Keir, D., Gerya, T., Pagli, C., Gernon, T., Ayele, A., Goitom, B., Hammond, J. O. and Kendall, J. (2018a). Initiation of a proto-transform fault prior to seafloor spreading. *Geochemistry, Geophysics, Geosystems*, **19**(12), pp. 4744–4756. 2.2

Illsley-Kemp, F., Keir, D., Bull, J. M., Gernon, T. M., Ebinger, C., Ayele, A., Hammond, J. O., Kendall, J. M., Goitom, B. and Belachew, M. (2018b). Seismicity during continental breakup in the Red Sea Rift of Northern Afar. *Journal of Geophysical Research: Solid Earth*, **123**, pp. 2345–2362. doi:10.1002/2017JB014902. 2.2.1, 2.5

Jones, L. K., Kyle, P. R., Oppenheimer, C., Frechette, J. D. and Okal, M. H. (2015). Terrestrial laser scanning observations of geomorphic changes and varying lava lake levels at Erebus volcano, Antarctica. *Journal of Volcanology and Geothermal Research*, **295**, pp. 43–54. 2.4.2

Jónsson, S., Zebker, H., Segall, P. and Amelung, F. (2002). Fault slip distribution of the 1999 Mw 7.1 Hector Mine, California, earthquake, estimates from satellite radar and GPS measurements. *Bulletin of the Seismological Society of America*, **92**(4), pp. 1377–1389. 2.4.1

Keir, D., Bastow, I. D., Pagli, C. and Chambers, E. L. (2013). The development of extension and magmatism in the Red Sea rift of Afar. *Tectonophysics*, **607**, pp. 98–114. doi:10.1016/j.tecto.2012.10.015. 2.5, 2.6

Lanari, R., Casu, F., Manzo, M., Zeni, G., Berardino, P., Manunta, M. and Pepe, A. (2007). An overview of the Small BAseline Subset algorithm: A DInSAR technique for surface deformation analysis. *Pure and Applied Geophysics*, **164**(4), pp. 637–661. doi:10.1007/s00024-007-0192-9. 2.3

Lanari, R., Mora, O., Manunta, M., Mallorqui, J., Berardino, P. and Sansosti, E. (2004). A Small Baseline Approach for Investigating Deformations on Full Resolution Differential SAR Interferograms. *IEEE Trans. Geosci. Remote Sensing*, **42**(7), pp. 1377–1386. 2.3

Marjanović, M., Carbotte, S. M., Carton, H. D., Nedimović, M. R., Canales, J. P. and Mutter, J. C. (2018). Crustal Magmatic System Beneath the East Pacific Rise (8° 20' to 10° 10' N): Implications for Tectonomagmatic Segmentation and Crustal Melt Transport at Fast-Spreading Ridges. *Geochemistry, Geophysics, Geosystems*, **19**(11), pp. 4584–4611. 2.2, 2.5, 2.6

Marjanović, M., Carbotte, S. M., Carton, H., Nedimović, M. R., Mutter, J. C. and Canales, J. P. (2014). A multi-sill magma plumbing system beneath the axis of the East Pacific Rise. *Nature Geoscience*, **7**(11), p. 825. 2.2, 2.5

Massonnet, D. and Feigl, K. L. (1998). Radar interferometry and its application to changes in the Earth's surface. *Reviews of Geophysics*, **36**(4), pp. 441–500. doi:10.1029/97RG03139. 2.4.3

McClusky, S., Reilinger, R., Ogubazghi, G., Amleson, A., Healeb, B., Vernant, P., Sholan, J., Fisseha, S., Asfaw, L., Bendick, R. and Kogan, L. (2010). Kinematics of the southern Red Sea-Afar Triple Junction and implications for plate dynamics. *Geophysical Research Letters*, **37**(L05301). doi:10.1029/2009GL041127. 2.2, 2.2.1

MIROVA (2019). Middle InfraRed Observation of Volcanic Activity (MIROVA): Erta Ale. *[Online]. [Accessed 03 July 2019]. Available from: www.mirovaweb.it.* 2.2.2, 2.4.3, 2.4.3, 2.6

Montagna, C. P. and Gonnermann, H. M. (2013). Magma flow between summit and Pu‘u‘ō‘ō at Kilauea Volcano, Hawaii. *Geochemistry, Geophysics, Geosystems*, **14**(7), pp. 2232–2246. 2.2, 2.4.2, 2.5

Moore, C., Wright, T., Hooper, A. and Biggs, J. (2019). The 2017 eruption of Erta 'Ale volcano, Ethiopia: Insights in the shallow axial plumbing system of an incipient mid-ocean ridge. *Geochemistry, Geophysics, Geosystems*, **20**(12). 2

Moussallam, Y., Bani, P., Curtis, A., Barnie, T., Moussallam, M., Peters, N., Schipper, C. I., Aiuppa, A., Giudice, G., Amigo, Á., Velasquez, G. and Cardona, C. (2016). Sustaining persistent lava lakes: Observations from high-resolution gas measurements at Villarrica volcano, Chile. *Earth and Planetary Science Letters*, **454**, pp. 237–247. doi:10.1016/j.epsl.2016.09.012. 2.4.2

Neal, C., Brantley, S., Antolik, L., Babb, J., Burgess, M., Calles, K., Cappos, M., Chang, J., Conway, S., Desmither, L., Dotray, P., Elias, T., Fukumaga, P., Fuke, S., IA, J., Kamibayashi, K., Kauahikaua, J., Lee, R., Pekalib, S., Miklius, A., Million, W., Moniz, C. et al. (2019). The 2018 rift eruption and summit collapse of Kīlauea Volcano. *Science*, **363**(6425), pp. 367–374. 2.2

Nobile, A., Pagli, C., Keir, D., Wright, T. J., Ayele, A., Ruch, J. and Acocella, V. (2012). Dike-fault interaction during the 2004 Dallol intrusion at the northern edge of the Erta Ale Ridge (Afar, Ethiopia). *Geophysical Research Letters*, **39**(L19305). doi:10.1029/2012GL053152. 2.2.1

Okada, Y. (1985). Surface deformation due to shear and tensile faults in a half-space. *Bulletin of the seismological society of America*, **75**(4), pp. 1135–1154. 2.4.1, 2.4.2

Oppenheimer, C., Lomakina, A. S., Kyle, P. R., Kingsbury, N. G. and Boichu, M. (2009). Pulsatory magma supply to a phonolite lava lake. *Earth and Planetary Science Letters*, **284**(3), pp. 392–398. 2.4.2

Pagli, C., Wang, H., Wright, T. J., Calais, E. and Lewi, E. (2014). Current plate boundary deformation of the Afar rift from a 3-D velocity field inversion of InSAR and GPS. *Journal of Geophysical Research: Solid Earth*, **119**, pp. 8562–8575. doi:10.1002/2014JB011391. 2.2.1

Pagli, C., Wright, T. J., Ebinger, C. J., Yun, S. H., Cann, J. R., Barnie, T. and Ayele, A. (2012). Shallow axial magma chamber at the slow-spreading Erta Ale Ridge. *Nature Geoscience*, **5**(4), pp. 284–288. doi:10.1038/ngeo1414. 2.2, 2.2.1, 2.2.2, 2.4.1, 2.4.1, 2.5, 2.5, 2.6, 2.6

Patrick, M., Anderson, K., Poland, M., Orr, T. and Swanson, D. (2015). Lava lake level as a gauge of magma reservoir pressure and eruptive hazard. *Geology*, **43**(9), pp. 831–834. doi:10.1130/G36896.1. 2.2, 2.2.2, 2.4.2, 2.4.2

Patrick, M., Orr, T., Anderson, K. and Swanson, D. (2019a). Eruptions in sync: Improved constraints on Kīlauea Volcano's hydraulic connection. *Earth and Planetary Science Letters*, **507**, pp. 50–61. 2.2, 2.2.2

Patrick, M., Swanson, D. and Orr, T. (2019b). A review of controls on lava lake level: insights from Halema'uma'u Crater, Kīlauea Volcano. *Bulletin of Volcanology*, **81**(3), p. 13. 2.2, 2.2.2, 2.4.2

Poland, M. P. and Carbone, D. (2018). Continuous Gravity and Tilt Reveal Anomalous Pressure and Density Changes Associated With Gas Pistoning Within the Summit Lava Lake of Kīlauea Volcano, Hawai'i. *Geophysical Research Letters*, **45**, pp. 2319–2327. doi:10.1002/2017GL076936. 2.4.2, 2.4.2

Poland, M. P., Miklius, A. and Montgomery-Brown, E. K. (2014). Magma supply, storage, and transport at shield-stage Hawaiian Volcanoes. *Characteristics of Hawaiian Volcanoes*, **179**(1801), pp. 179–234. 2.5, 2.5, 2.6

Rivalta, E. and Segall, P. (2008). Magma compressibility and the missing source for some dike intrusions. *Geophysical Research Letters*, **35**(L04306). doi:10.1029/2007GL032521. 2.5

Rosen, P. A., Hensley, S., Zebker, H. A., Webb, F. H. and J, F. E. (1996). Surface deformation and coherence measurements of Kilauea Volcano, Hawaii, from SIR-C radar interferometry. *Journal of Geophysical Research*, **101**(E10), pp. 23109–23125. 2.4.3

Shreve, T., Grandin, R., Boichu, M., Garaebiti, E., Moussallam, Y., Ballu, V., Delgado, F., Leclerc, F., Vallée, M., Henriot, N. et al. (2019). From prodigious volcanic degassing to caldera subsidence and quiescence at Ambrym (Vanuatu): the influence of regional tectonics. *Scientific reports*, **9**(1), pp. 1–13. 2.5

Sigmundsson, F. (2016). New insights into magma plumbing along rift systems from detailed observations of eruptive behavior at Axial volcano. *Geophysical Research Letters*, **43**(24), pp. 12–423. 2.2

Tiberi, C., Ebinger, C., Ballu, V., Stuart, G. and Oluma, B. (2005). Inverse models of gravity data from the Red Sea-Aden-East African rifts triple junction zone. *Geophysical Journal International*, **163**, pp. 775–787. doi:10.1111/j.1365-246X.2005.02736.x. 2.2.1, 2.5

Varet, J. (1971). Erta'Ale activity (Afar, Ethiopia). *Bulletin of the Geophysical Observatory, Addis Ababa*, **13**, pp. 115–119. 2.2.1

Volcano Discovery (2017). Erta Ale (Ethiopia) volcano news. *[Online]. [Accessed 15 March 2019]. Available from: www.volcanodiscovery.com/erta_ale/news.html.* 2.2.2, 2.4.2, 2.4.2

Wadge, G., Biggs, J., Lloyd, R. and Kendall, J.-M. (2016). Historical Volcanism and the State of Stress in the East African Rift System. *Frontiers in Earth Science*, **4**(86). doi:10.3389/feart.2016.00086. 2.5

Wanless, V. D. and Behn, M. D. (2017). Spreading rate-dependent variations in crystallization along the global mid-ocean ridge system. *Geochemistry, Geophysics, Geosystems*, **18**(8), pp. 3016–3033. doi:10.1002/2017GC006924. 2.2, 2.5, 2.6

Werner, C., Wegmuller, U., Strozzi, T. and Wiesmann, A. (2000). GAMMA SAR and interferometric processing software. *European Space Agency, (Special Publication) ESA SP*, (461), pp. 211–219. 2.3

Wolfenden, E., Ebinger, C., Yirgu, G., Renne, P. R. and Kelley, S. P. (2005). Evolution of a volcanic rifted margin: Southern Red Sea, Ethiopia. *Bulletin of the Geological Society of America*, **117**(7/8), pp. 846–864. doi:10.1130/B25516.1. 2.2.1, 2.1

Wright, T. J., Parsons, B. E. and Zhong, L. (2004). Toward mapping surface deformation in three dimensions using InSAR. *Geophysical Research Letters*, **31**(L01607). doi:10.1029/2003GL018827. 2.3

Wright, T. J., Sigmundsson, F., Pagli, C., Belachew, M., Hamling, I. J., Brandsdóttir, B., Keir, D., Pedersen, R., Ayele, A., Ebinger, C., Einarsson, P., Lewi, E. and Calais, E. (2012). Geophysical constraints on the dynamics of spreading centres from rifting episodes on land. doi:10.1038/ngeo1428. 2.2

Xu, W., Rivalta, E. and Li, X. (2017). Magmatic architecture within a rift segment: Articulate axial magma storage at Erta Ale volcano, Ethiopia. *Earth and Planetary Science Letters*, **476**, pp. 79–86. doi:10.1016/j.epsl.2017.07.051. 2.2.2, 2.4.1, 2.4.1, 2.4.1, 2.4.2, 2.5, 2.5, 2.6

Yang, X.-M., Davis, P. M. and Dieterich, J. H. (1988). Deformation from inflation of a dipping finite prolate spheroid in an elastic half-space as a model for volcanic stressing. *Journal of Geophysical Research: Solid Earth*, **93**(B5), pp. 4249–4257. 2.4.1

Yu, C., Li, Z. and Penna, N. T. (2018). Interferometric synthetic aperture radar atmospheric correction using a GPS-based iterative tropospheric decomposition model. *Remote Sensing of Environment*, **204**, pp. 109–121. doi:10.1016/j.rse.2017.10.038. 2.3

Yu, C., Penna, N. T. and Li, Z. (2017). Generation of real-time mode high-resolution water vapor fields from GPS observations. *Journal of Geophysical Research*, **122**(3), pp. 2008–2025. doi:10.1002/2016JD025753. 2.3

Chapter 3

Rift Focussing and Magmatism During Late-Stage Rifting in Afar, Ethiopia

The work displayed in Chapter 3 (Sections 3.1-3.6) is in peer-review with the Journal of Geophysical Research, AGU, Copyright (2020) American Geophysical Union, following an invitation to resubmit:
Moore, C., Wright, T. & Hooper, A. (2020). Rift Focussing and Magmatism During Late-Stage Rifting in Afar, Ethiopia. *Journal of Geophysical Research: Solid Earth.* `https://doi.org/10.1002/essoar.10503895.1`
Supplementary Materials for Moore et al. (2020) are provided in Appendix B.

3.1 Abstract

Processes that facilitate the transition between continental rifting and sea-floor spreading remain unclear. Variations in the spatial distribution of extension through Afar and into the Red Sea are indicative of temporal evolution of the rift. We develop a time series of Sentinel-1 interferometric synthetic aperture radar (InSAR) observations of ground deformation covering the whole Afar Rift from 2014-2019, to study the distribution of extension across all magmatic segments. By incorporating GNSS observations, we resolve 3D average velocities in the vertical, rift-perpendicular, and rift-parallel directions. Results show the spatial distribution of long-term plate motions over the rift, as well as deformation at individual volcanic centres, including Dallol, Nabro, and Erta 'Ale. We find that in northern and central Afar, the majority of extension is accommodated within ± 15-30 km of magmatic spreading centres. In southern Afar, near the Nubia-Arabia-Somalia triple-junction, amagmatic extension is distributed over 80-160 km, which may indicate an increase in rift focussing with rift maturity. We also observe rapid surface uplift and rift-perpendicular extension at the Dabbahu-Manda-

Hararo segment with velocities of 33 ± 4 mm/yr and 37 ± 4 mm/yr respectively. These are higher than the background extension rate of 18-20 mm/yr, but have decreased by 55-70 % since 2006-10. The data suggests that this is due to an on-going long-lived response to the 2005-10 rifting episode, with potential continued processes below the segment including a lower-crustal viscous response and magma movement. Continued long-term observations of surface deformation provide key constraints on tectono-magmatic processes in Afar.

3.2 Introduction

Magma plays a significant role in accommodating the final stages of continental breakup and the transition into early sea-floor spreading, and the Afar region of Ethiopia is uniquely placed to allow the observation of these processes sub-aerially (e.g. Ebinger, 2005, Kendall et al., 2005, Wright et al., 2012). Extensional strain in Afar is accommodated by elongate rifting segments (Ebinger and Casey, 2001), maintained by rifting episodes that include effusive eruptions and dyking, and amagmatic tectonic extension, where strain may be broadly distributed (Wright et al., 2006, Doubre and Peltzer, 2007, Ebinger et al., 2010). Magmatic intrusions at these spreading segments produce time-dependent surface deformation, observable using time series of interferometric synthetic aperture radar (InSAR). These long time series can help separate surface deformation related to magma movement and viscoelastic relaxation, and have been used to constrain, and highlight the importance of viscous rheology in late-stage rifting (Nooner and Chadwick, 2009, Pagli et al., 2014, Hamlyn et al., 2018).

3.2.1 Regional Setting

Upwelling of a mantle plume initiated rifting in Afar around 30 Ma with abundant flood-basalt volcanism, which has evolved into the ridge-ridge-ridge triple junction observed in Afar today (Wolfenden et al., 2004, Furman et al., 2006, Hammond et al., 2013). Relative to the Nubian Plate, the Arabian Plate is moving at a rate of 18-20 mm/yr to the NE (McClusky et al., 2010, ArRajehi et al., 2010, Doubre et al., 2017, Viltres et al., 2020), accommodated by the opening of the Red Sea Rift (RSR); while the Somalian Plate is moving to the SE at $\sim$ 6 mm/yr (Saria et al., 2014, Birhanu et al., 2016), accommodated by the Main Ethiopian Rift (MER) which is the northern-most segment of the larger East African Rift.

The crust beneath Afar is significantly thinned in comparison to the surrounding Ethiopian highlands and MER. Crustal thicknesses range from 20-45 km in the Ethiopian plateau, 18-30 km in central Afar, and 15-20 km in northern Afar (Tiberi et al., 2005, Bastow and Keir, 2011, Hammond et al., 2011, Lavayssière et al., 2018). Low seismic velocities indicate partial melt within the crust (Gallacher et al., 2016),

particularly below volcanic segments in Afar (Stork et al., 2013, Hammond, 2014, Hammond and Kendall, 2016). Seismicity in the upper and lower crust along the Erta 'Ale volcanic segment (EAVS) also indicates the presence of melt below the Erta 'Ale and Alu-Dalafilla volcanic centres (Illsley-Kemp et al., 2018).

Active volcansim in Afar is largely concentrated within discrete rifting segments. The EAVS is the immediate on-land expression of the RSR. Erta 'Ale volcano on the EAVS is host to a lava lake with recent overflows in 2010 (Field et al., 2012, Barnie et al., 2016b) and 2017, where a flank eruption indicated the presence of a shallow magma body at $\sim$ 1 km depth (Moore et al., 2019, Xu et al., 2017). At Gada 'Ale, magma withdrawal and normal faulting caused subsidence from 1993-1996 (Amelung et al., 2000), and a dyke intrusion fed from a magma chamber 2-3 km below Dallol was

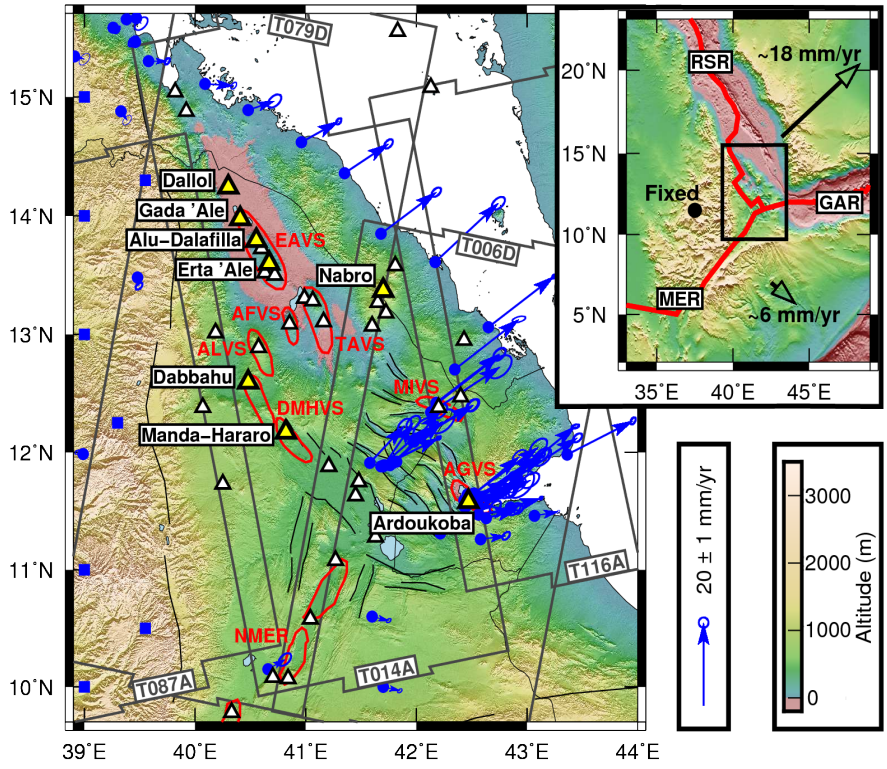

Figure 3.1: The Afar Rift with white triangles indicating Holocene volcanoes and key volcanoes highlighted in yellow. Simplified volcanic segments (VS) are shown in red: AFVS - Afdera, ALVS - Alayta, AGVS - Asal-Ghoubbet, DMHVS - Dabbahu-Manda-Hararo, EAVS - Erta 'Ale, MI - Manda-Inakir, NMER - Northern Main Ethiopian Rift, TAVS - Tat 'Ale. Faults in central Afar and simplified rift margin faults are displayed as black lines. A subset of GNSS velocity vectors with 95% confidence error ellipses (blue arrows) from King et al. (2019) show the long-term plate motions. GNSS sites from King et al. (2019) (blue circles) are supplemented by additional fabricated GNSS sites with zero velocity on the stable Nubian plate (blue squares). Grey box outlines show the Sentinel-1 coverage from three ascending (T014A, T087A, T116A) and two descending (T006D, T079D) tracks. Inset map shows the relative movement of the Arabian and Somalian plates to the Nubian plate, with plate boundaries from Bird (2003). RSR - Red Sea Rift, GAR - Gulf of Aden Rift, MER - Main Ethiopian Rift.

detected in 2004 (Nobile et al., 2012). The 2008 eruption at Alu-Dalafilla was sourced from a $\sim$ 1 km deep axis-aligned reservoir and a magma chamber at $\sim$ 4 km depth (Pagli et al., 2012).

The largest recent volcano-tectonic rifting episode in Afar occurred from 2005-10 on the Dabbahu-Manda-Hararo volcanic segment (DMHVS) (Barnie et al., 2016a). The initial dyke in September 2005 ruptured the whole 60 km long segment, and intruded 2.4-2.6 km^3 of magma over $\sim$ 2 weeks (Wright et al., 2006). Seismicity indicates that this dyke initiated beneath the Dabbahu and Gabho volcanoes at the northern end of the DMHVS, before focussing on the segment centre (Ayele et al., 2009). 13 subsequent dykes were emplaced between 2006-2010, drawing comparisons to the 1975-1984 Krafla rifting episode where extension in both settings is accommodated by magmatic intrusions (Hamling et al., 2010, Ferguson et al., 2010, Wright et al., 2012, Barnie et al., 2016a). Throughout the rifting episode there was an ongoing post-rifting response to the initial 2005 intrusion, which was modelled using magmatic sources in the upper crust, and the inflation of a deeper source at the segment centre, as viscoelastic relaxation alone was insufficient to reproduce geodetic observations (Grandin et al., 2010, Hamling et al., 2014).

The Manda-Inakir (MIVS) and Asal-Ghoubbet (AGVS) volcanic segments in southern Afar have also shown recent activity with the 1928-1929 eruption of Kammourta volcano in the MIVS (Audin et al., 1990), and the 1978 eruption at Ardoukoba volcano in the AGVS (Allard et al., 1979, Tarantola et al., 1979). Cattin et al. (2005) identified a post-rifting response in the AGVS to the 1978 eruption, with rift-perpendicular velocities decaying back to the long-term spreading rate 6-8 years after the eruption.

The Nabro Volcanic Range (NVR) is an off-axis volcanic-centre that sits within the Danakil Block, a rigid micro-plate which is moving away from Nubia with extension in Afar (Eagles et al., 2002). The NVR has hosted explosive eruptions at Dubbi volcano in 1861 (Wiart and Oppenheimer, 2000), and Nabro volcano in 2011 (Hamlyn et al., 2014, Goitom et al., 2015). Persistent subsidence was detected at Nabro for $>$ 1 year following the 2011 eruption which was attributed to viscoelastic relaxation around a magma chamber at 6.4 $\pm$ 0.3 km depth (Hamlyn et al., 2018).

3.2.2 InSAR Velocity Methods & Applications in Afar

Methods for extracting a one-dimensional line-of-sight (LOS) displacement time series from a sequence or network of interferograms are well established. These small-baseline algorithms utilise multiple interferogram connections between acquisition dates to produce a more robust estimate of the incremental LOS ground displacement than a simple stacking of interferograms (Berardino et al., 2002, Lanari et al., 2007, Biggs et al.,

2007). This methodology may be automated by software packages such as Π-RATE (Wang et al., 2012; and references therein), StaMPS (Hooper et al., 2012), GIAnT (Agram et al., 2013), and LiCSBAS (Morishita et al., 2020) in order to obtain linear displacement rates and uncertainties at each pixel, while reducing the effect of common sources of error such as atmospheric and orbital delays. These methods may be supplemented by additional filtering to remove the atmospheric phase screen (APS) from the time series, by firstly high-pass filtering in time, then low-pass filtering in space to calculate the APS, which is then removed from the time series (e.g. Sousa et al., 2011). The conventional method for APS calculation relies on the assumption that the atmospheric delay is not temporally correlated. With recent SAR missions providing shorter satellite re-visit times, this assumption may no longer be appropriate. Previous studies have proposed improvements to the APS correction, including applying a global weather model (e.g. Jung et al., 2013), and accounting for the temporal variance of a pixel (e.g. Liu et al., 2011, Refice et al., 2011).

The only previous InSAR derived velocity map covering the whole Afar region was developed by Pagli et al. (2014), who used Π-RATE to produce a displacement time series between 2005-10. After removing large deformation steps associated with the DMH dyke intrusion events, Pagli et al. (2014) smoothed the time series by removing the APS, employing consistent Gaussian temporal and Butterworth spatial filters. Pagli et al. (2014) extracted 3D (east, north, vertical) velocities from ascending and descending LOS and Global Navigation Satellite Systems (GNSS) observations on a 10-20 km resolution mesh following the method of Wang and Wright (2012). Surface velocities between 2005-10 from Pagli et al. (2014) showed a long-term plate spreading rate of 15-20 mm/yr in Eastern Afar (relative to a stable Nubian plate), and large extension rates of $\sim$ 100 mm/yr at Dabbahu associated with the background response during the 2005-10 DMH rifting episode. Other InSAR velocity maps within Afar have focussed on individual rift segments, such as the DMHVS (Hamling et al., 2014) from 2006-10, the AGVS from 1997-2005 (Doubre and Peltzer, 2007) and 2003-10 (Doubre et al., 2017), and around the Tendaho Graben from 2004-10 (Temtime et al., 2018).

In this study, we make use of the high temporal and spatial resolution data from the Sentinel-1 satellite to extract surface velocities from 2014-19 across the whole of the Afar region. We develop and apply a small-baseline methodology with spatial and temporal variance weighted filtering to improve the removal of the APS, reference the data to a stable Nubia GNSS reference frame, and calculate 3D (vertical, rift-perpendicular horizontal, and rift-parallel horizontal) velocities.

3.3 Data Processing and Time Series Methods

3.3.1 Sentinel-1 Data

We use Sentinel-1A/B acquisitions from ascending tracks 14 (014A), 87 (087A), and 116 (116A), and descending tracks 6 (006D) and 79 (079D) between October 2014 and August 2019. For processing efficiency, we divide each track into 12 ($\sim$ 250×250 km) frames (Table S1). We produce a network of geocoded unwrapped interferograms for each frame from single-look complex (SLC) images of each date using the LiCSAR software (González et al., 2016, Lazeckỳ et al., 2020), which automates the mass production of interferograms using GAMMA (Werner et al., 2000). To reduce noise and data size, we multi-look the SLCs at 20:4 range to azimuth looks, equating to $\sim$ 100×100 m pixel size. We apply a topographic correction using an SRTM (Shuttle Radar Topography Mission) 3-arc-second ($\sim$ 90 m resolution) DEM (Digital Elevation Model) (Farr and Kobrick, 2000), filter the interferograms using using a power spectrum filter (Goldstein et al., 1998), and unwrap using SNAPHU (Chen and Zebker, 2002). We manually quality check the interferogram network for each frame to remove interferograms with decorrelation, co-registration, or obvious unwrapping errors. We ensure that each epoch is connected to the network by a minimum of three interferograms by creating new interferograms as needed. Each interferogram is referenced to the mean value, excluding areas of deformation around volcanic centres.

To mitigate for atmospheric phase delay for each interferogram we compare the effectiveness of corrections from a linear trend of phase with elevation over the whole frame (e.g. Elliott et al., 2008), and the GACOS atmospheric model (e.g. Yu et al., 2017, 2018). For a linear phase-elevation trend correction, the mean root-mean-square (RMS) misfit for all 12 frames is reduced by 2.9 mm in comparison to the mean RMS misfit for all frames with no atmospheric correction. The GACOS correction gives a reduction in mean RMS misfit of 4.2 mm, but increases the RMS misfit in 29 % of interferograms. To reduce this we follow an approach similar to Shen et al. (2019), scaling the GACOS correction for each interferogram in order to minimise the resulting RMS misfit. This improves the atmospheric correction further, producing a reduction in mean RMS misfit of 5.7 mm (see Figure B.1). In order to account for any residual topographic atmospheric signal in each frame, we remove a linear trend of phase with elevation from each epoch, after time series filtering.

3.3.2 Time Series

We apply an SBAS style methodology to invert for the displacement time series at each pixel in the frame, using all interferograms where the pixel is coherent. We assess the spatial and temporal variance of the time series by firstly, filtering using a Laplacian

filter with a temporal width of three epochs and scale factor of 3, then calculating the RMS misfit from this trend at each pixel for every epoch. We calculate the spatial distribution of RMS misfit from the time series misfits at each point, and the temporal distribution of RMS misfit from the misfits of all pixels at each epoch (see Figure B.2). To resolve the RMS misfit value of each pixel at every epoch, we scale the spatial RMS misfit map to the temporal RMS misfit value at each epoch (see Appendix B). We use these error estimates to provide weights during time series filtering, and in the inversion of filtered displacement time series for average velocities.

In order to reduce the remaining APS in the displacement time series, we filter the time series using a high-pass temporal and a low-pass spatial filter to produce the APS, which we then remove from the time series. To calculate a low-pass temporal filter, we apply a weighted linear trend with a fixed temporal width of 1 year centred on each point. To calculate the weighting for the local trend, we use the RMS misfit as a proxy for standard error, and convert the RMS misfit values into weights using the Bi-Square function where no weight is given to RMS values that exceed 6 standard deviations of the local misfits (e.g. Cleveland and Devlin, 1988). We also scale these weights by their temporal distance from the target epoch of the local time series (see Appendix B). Having calculated the low-pass temporal filter, we remove it from the time series to create a high-pass temporal filter. We then apply a Gaussian spatial filter with a half-width of $\sim$ 2 km in order to resolve the APS for each epoch.

After we remove the APS, we remove a planar ramp in space and a linear trend with height to correct for any remnant long-wavelength and elevation-correlated atmospheric delay. We later restore any long-wavelength deformation removed here, using GNSS observations, which we assume correctly capture deformation on length scales of the $\sim$ 250×250 km Sentinel-1 frames. For each frame, we compute the average velocity at each pixel by inverting for a single linear trend through time, allowing for a constant offset. We produce a variance-covariance matrix (VCM) for each pixel, treating the temporal variation of the scaled RMS misfit as independent errors. By including a VCM in the inversion, we can quantify the uncertainty of the resulting velocities.

De Zan et al. (2015) demonstrate how a potential systematic phase-bias in interferograms with decreasing temporal baseline can influence the resulting time series. We test the magnitude of this bias by selecting consecutive 12, 24, and 36-day interferograms from frame 079D_07694_131313 covering $\sim$ 1 year (see Figure B.3). We use a 'daisy-chain' stack approach to resolve the cumulative displacements from the 12, 24, and 36 day unwrapped interferograms between December 2017 and February 2019. Any differences between these stacks indicates the presence of phase-bias and/or unwrapping errors. We find residual differences between the 12 and 24-day, and 12 and 36-day

stacks of up to 50 mm, and residuals of up to 10 mm between the 24 and 36-day stacks. While this indicates that the 12-day interferograms are susceptible to a phase-bias, we find that removing the 12-day interferograms from the network effects our displacement time series by < 5 mm per epoch, and our average velocities by < 1 mm/yr. While we are not able to account for any bias in the 36-day interferograms, Ansari et al. (2020) indicate that the velocity bias is small in comparison to 12-day interferograms.

3.3.3 3D Velocities

We tie frames together within their respective tracks by sub-sampling the InSAR data points to a 5×5 km spacing in the overlap between frames, and 10×10 km spacing elsewhere, then solving for and removing a planar ramp for each frame that minimises residuals in the along-track frame overlap regions. Removing these ramps does not bias the results as long-wavelength signals are later corrected using GNSS data. In the frame overlap region, we use the mean value of LOS velocity for each point. We find that using linear ramps to combine frames within tracks produces the fewest boundary artefacts when compared to using a single offset value calculated from the median value in the frame overlap region, or solving for a 2D quadratic function for each frame. Boundary artefacts within tracks can occur due to differences between frames in time series length, the variation in acquisition dates used, relative weighting during time-series filtering, and orbital ramp removal. Although in principle it would be possible to only process and use interferograms that cover the whole along-track extent of the study region, this would require excluding several epochs where data were not acquired over the whole area, resulting in truncated time series.

To reference the LOS velocity in each track to a stable Nubian plate, we use a network of 105 GNSS stations in the Afar region to characterise long-wavelength plate motions. These data are a subset of the GeoPRISMS community velocity field for East Africa in a Nubia-fixed International Terrestrial Reference Frame (ITRF2014), and include continuous and campaign observations acquired between 1994 and 2018 with time spans of $\gtrsim 2.4$ years (King et al., 2019). For details of the data sources included, see King et al. (2019). We assume that these velocities are steady-state and do not vary significantly through time. We remove 32 stations in central Afar where the velocities are not steady-state, but are dominated by the ground motions associated with the 2005-10 DMH rifting episode. As the resulting network is sparse (Figure B.4), with the majority of stations concentrated in Eastern Afar and few points on the Nubian and Somalian plates; we add 17 additional fabricated GNSS stations on the stable Nubian plate, with an assumed zero velocity (with uncertainties of ± 1 mm/yr and ± 2 mm/yr in the horizontal and vertical components), to help constrain the velocity field where data are sparse. We project East and North GNSS horizontal velocities into the rift-perpendicular (e.g. Hamling et al., 2014), and rift-parallel directions, oriented at 61°N

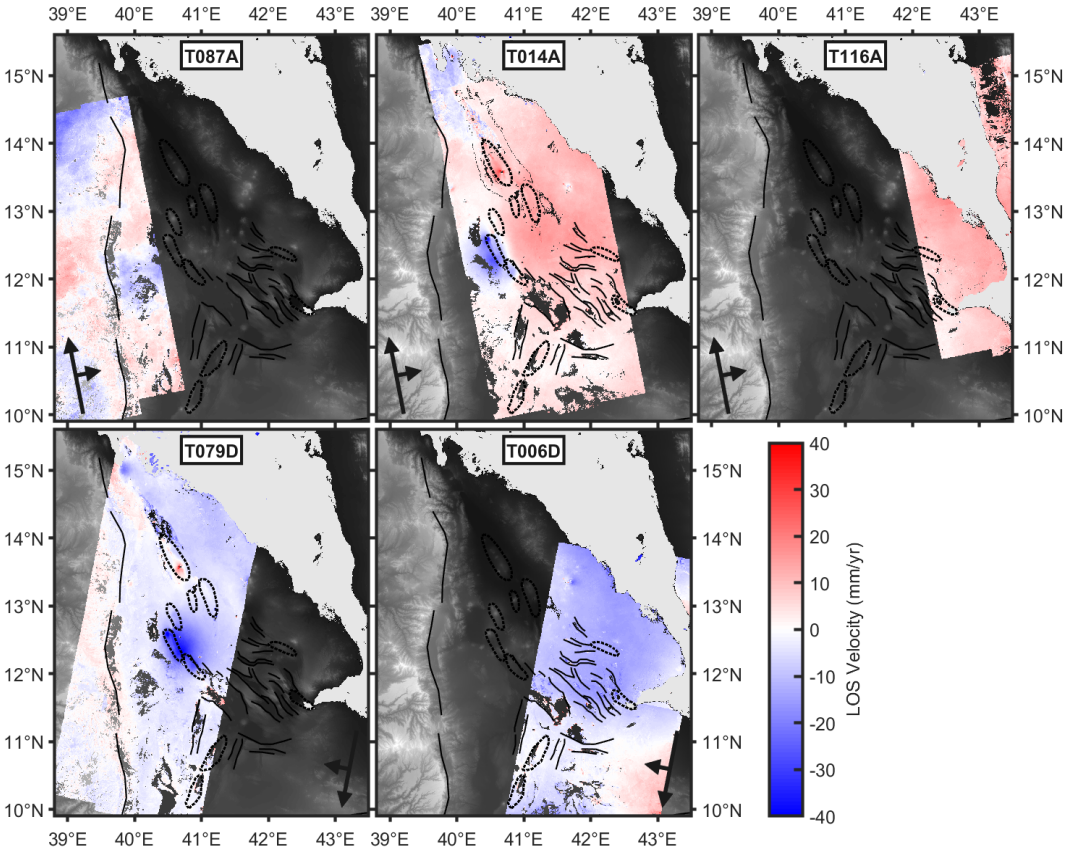

Figure 3.2: LOS average velocities over the Afar region between November 2014 and August 2019 from Sentinel-1 tracks T087A, T014A, T116A, T079D, and T006D. LOS velocities are referenced to a stable Nubia reference frame using long-term plate motions from the regional GNSS network (King et al., 2019). Arrows indicate the track look directions. Volcanic segments and key faults are shown as black dashed outlines and black solid lines respectively.

and -29°N respectively.

From this network, we interpolate a smooth GNSS velocity field in the rift-perpendicular and rift-parallel directions over the whole Afar region at 100×100 m grid spacing (Figure B.4) using the natural neighbour algorithm (e.g. Boissonnat and Cazals, 2002). As the additional pseudo-observations define where this interpolated field reaches zero velocity, we selected these points such that they are on the Nubian plate, away from the rift border faults. We are not concerned with the precise locations, as where the interpolated velocity field reaches zero does not significantly influence the data within the Afar Rift. We estimate the error in the interpolated velocities by systematically removing each GNSS station from the network, interpolating new velocity fields in the rift-perpendicular and rift-parallel directions from the reduced network, then calculating the residual between the interpolated fields and the GNSS observation. We take the standard deviation of these residuals as the error in the rift-perpendicular and rift-parallel GNSS velocity field.

We sub-sample the InSAR LOS track velocities as previously, then extract points where there are ascending, descending, and interpolated GNSS data. We also mask points around the active rift segments so that volcanic ground deformation does not interfere with the referencing to the long-term plate motions. Using these points, we solve for the 3D velocity (rift-perpendicular, rift-parallel, vertical) at each point and a residual 2D (East, North) quadratic function for each track. We remove the respective quadratic from each InSAR track to resolve LOS velocity in a stable Nubia reference frame. The resulting LOS velocities and standard deviations are shown in Figures 3.2 and B.5 respectively.

In order to resolve a full 3D velocity field (vertical, rift-perpendicular horizontal, rift-parallel horizontal) at 100×100 m resolution, we use the smooth rift-parallel GNSS field to provide a constraint on the rift-parallel velocity at each point, as the rift-parallel velocities are small in comparison to the rift-perpendicular and vertical velocities. We include this constraint with the ascending and descending LOS InSAR observations to calculate 3D velocities at each point using a least-squares inversion (Wright et al., 2004, Hussain et al., 2016, Weiss et al., 2020). The decomposition of InSAR LOS velocities (L) into rift-perpendicular ($H1$), rift-parallel ($H2$), and vertical (Z) velocities is shown in Equation 3.1 for the incidence angle (θ), satellite heading (α), rift angle from North (ϕ). We weight the inversion and resolve uncertainties by including a diagonal VCM using the previously calculated variance at each point.

Results (Figure 3.3), discussed in Section 3.3, show both the long-term plate motion and surface deformation associated with magmatism. As we use the interpolated GNSS velocity field as an additional constraint in the rift-parallel direction, the resulting rift-parallel error estimates are lower than the rift-perpendicular errors, which we calculate using only the InSAR observations to retain high spatial resolution (see Figure 3.3).

$$L = \Big[-\sin(\theta)\cos(\alpha+\phi) + \sin(\theta)\sin(\alpha+\phi) - \cos(\theta) \Big] \begin{bmatrix} H1 \\ H2 \\ Z \end{bmatrix} \tag{3.1}$$

3.4 Key Findings & Discussion

3.4.1 Plate Motions & Uncertainties

Our 2014-2019 horizontal velocity maps (Figure 3.3) show the rift-perpendicular extension over the Afar rift at rates of up to 25 ± 5 mm/yr, with negligible motions in the rift-parallel direction. We also observe the rotation of the Danakil micro-plate

relative to the stable Nubian plate (Kidane, 2016, Viltres et al., 2020), where rift-perpendicular extension in the RSR is gradually transferred into Afar between 13-16°N.

Areas of noise up to ± 10 mm/yr over the Ethiopian highlands region on the Nubain plate, are highlighted in the standard deviation maps shown in Figure 3.3. The regions of high error in T087A, and the northern-most portion of T014A (see Figure B.5), are a result of the shorter time series length in these regions producing more uncertainty in the long-term velocity estimates. Elsewhere, errors of up to ± 5 mm/yr are likely due to uncorrected atmospheric delays, and artefacts over track boundaries, where we are unable to account for small LOS velocity variations between overlapping tracks. These discontinuities may arise from variations in atmospheric filtering between overlapping

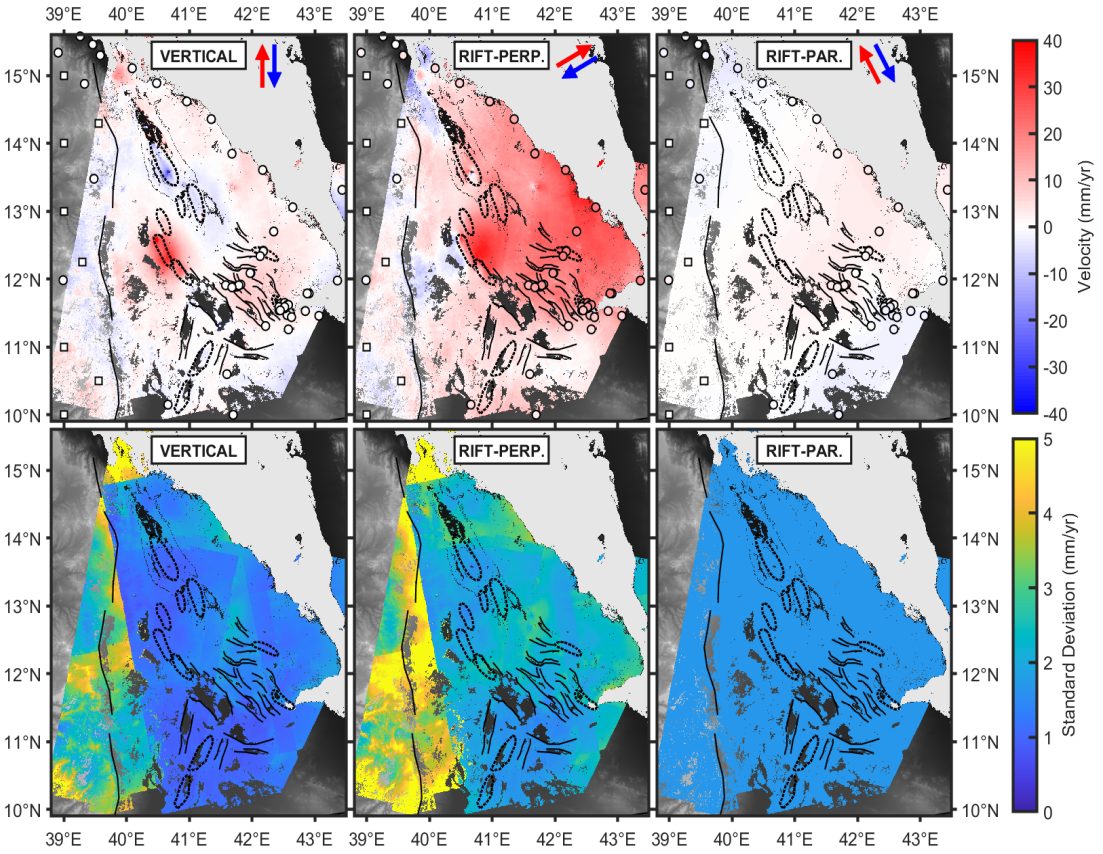

Figure 3.3: Vertical, rift-perpendicular, and rift-parallel average velocities and standard deviation over the Afar region between November 2014 and August 2019. All velocities are referenced to a stable Nubian plate. Vertical velocities are positive upwards, rift-perpendicular velocities are positive to the NE (61°N), and rift-parallel velocities are positive to the NW (-29°N). Standard deviation colour-scale is limited to 5 mm/yr to highlight variation in regions of low variance. Maximum standard deviations are (2 s.f.): 7.2 mm/yr (vertical), 9.5 mm/yr (rift-perpendicular), and 1.7 mm/yr (rift-parallel). Real (circles) and fabricated (squares) GNSS stations used in the inversion are shown with GNSS velocities on the same colour-scale as the InSAR velocities. Volcanic segments and key faults are shown as black dashed outlines and black solid lines respectively.

frames, and in GNSS referencing between overlapping tracks. The relatively uniform errors in the rift-parallel direction are due to the GNSS velocity field being used to constrain the velocities in this component, where the velocities are small in comparison to the vertical and rift-perpendicular components.

Using the overlap region between each of the tracks, we test the internal consistency of our LOS InSAR data using cross-validation by excluding each track in turn from the 3D inversion, projecting the resulting velocity field into the LOS of the excluded track, and calculating the residuals. The RMSE of the residuals in each track overlap region (Figure B.6) range from 2.7-4.2 mm/yr. These are consistent with the combination of the uncertainties in our LOS velocities (1.5-6.6 mm/yr) and the propagated uncertainties of the predicted LOS velocities from our 3D velocity field with one track excluded (2.8-2.9 mm/yr), and support our estimate of uncertainties shown in Figure 3.3.

We also test the isolated contribution of the LOS InSAR velocities to the rift-perpendicular and rift-parallel horizontal velocity maps by subtracting the interpolated GNSS velocities from the final 3D velocity map. We only test the horizontal directions of the velocity field here as we do not use GNSS data to constrain the vertical direction. As shown in Figure B.7, velocities in the rift-perpendicular direction use contributions from both InSAR and GNSS, while the rift-parallel velocities are constrained only by the GNSS component as described previously. In the rift-perpendicular direction, the InSAR component is dominated by local tectono-magmatic signals and residual atmospheric and processing artefact signals, indicating that our referencing of LOS InSAR velocities to far-field plate motions is consistent.

3.4.2 Rift Extension & Focussing

Profiles taken across the rift highlight the focussing of extension in Afar. Profiles covering the Alid graben, at northern-most tip of the Afar rift (Figures 3.4B and 3.5B), show that a broad uplift and extensional signal of up to $\sim$ 20 mm/yr is centred within $\pm$ 10-15 km of the rift axis. This may be indicative of deep magmatic intrusion in an area with the smallest background extension rates throughout Afar, but it is comparable to extension rates at the active volcanic islands at the southern end of the oceanic RSR (Eyles et al., 2018). Uncertainty estimates in this region are also significantly higher than elsewhere in Afar and as such we do not investigate this signal any further. Profiles traversing the EAVS in the Danakil Depression (Figures 3.4C and 3.5C) highlight that the majority of extension here is focussed into a region within $\pm$ 15-20 km of the rift axis. Outside of this region, the rate of extension does not significantly vary, with velocities in agreement with long-term GNSS observations (Figure 3.4C). We also observe subsidence on the EAVS between the Erta 'Ale and Alu Dalafilla volcanoes

(Figure 3.4C), which could be linked to magma withdrawal associated with the 2017-19 eruption at Erta 'Ale (Moore et al., 2019, Xu et al., 2017, 2020).

Profiles between the EAVS and the DMHVS (Figure 3.5C) show that extension in this region is shared between the ALVS and the TAVS, and focussed to within ± 10-

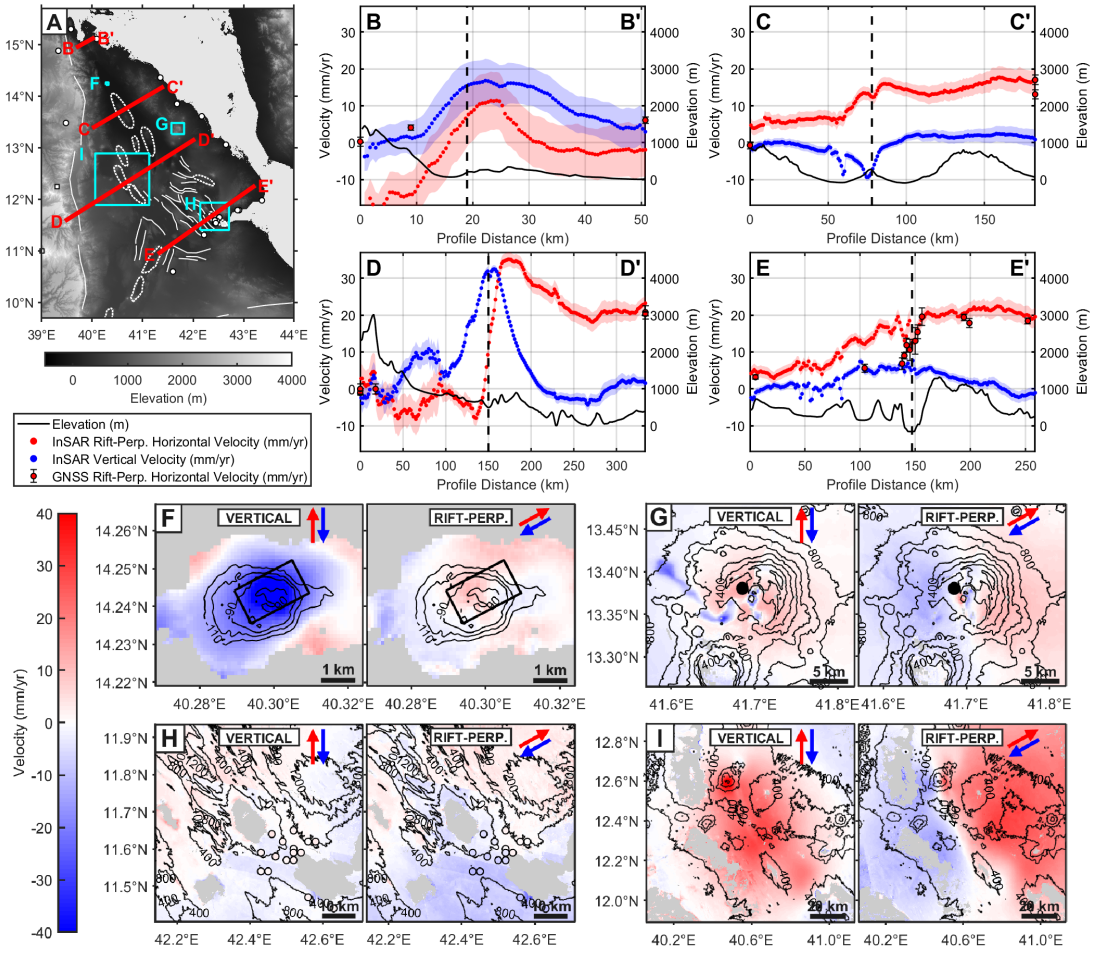

Figure 3.4: (A) The location of profiles (B-E) and subsets (F-I), with rift segments shown by white dashed outlines, and faults by solid white lines. The location of real (white circles) and fabricated (white squares) GNSS sites used in (B-E) are shown in (A). Where GNSS sites are beyond the extents of the profiles, they are displayed at the profile limits on (B-E). (B-E) Vertical (blue, positive up) and rift-perpendicular (red, positive towards 61°N) velocities over four 10 km wide cross-rift profiles marked on insert map, covering (B) the northern tip of the Afar triangle, (C) the Erta 'Ale volcanic segment, (D) the Dabbahu-Manda-Hararo volcanic segment (DMHVS), and (E) the Asal-Ghoubbet volcanic segment (AGVS). Black lines show surface elevation along the profiles, with vertical dashed lines indicating the location of the major rift axis on the profile. (F-I) Vertical and rift-perpendicular velocity maps at (F) Dallol volcano, (G) Nabro volcano, (H) the AGVS, and (I) the DMHVS. Velocities in each subset are referenced to the local background mean value, with contours indicating elevation, and circles indicating GNSS velocities. The location of modelled deformation sources for a 0.9-1.3 km deep sill (Okada, 1985) at Dallol (F, Figure B.8) and a 5.5-6.8 km deep point source (Mogi, 1958) at Nabro (G, Figure B.9) are shown as black outlines.

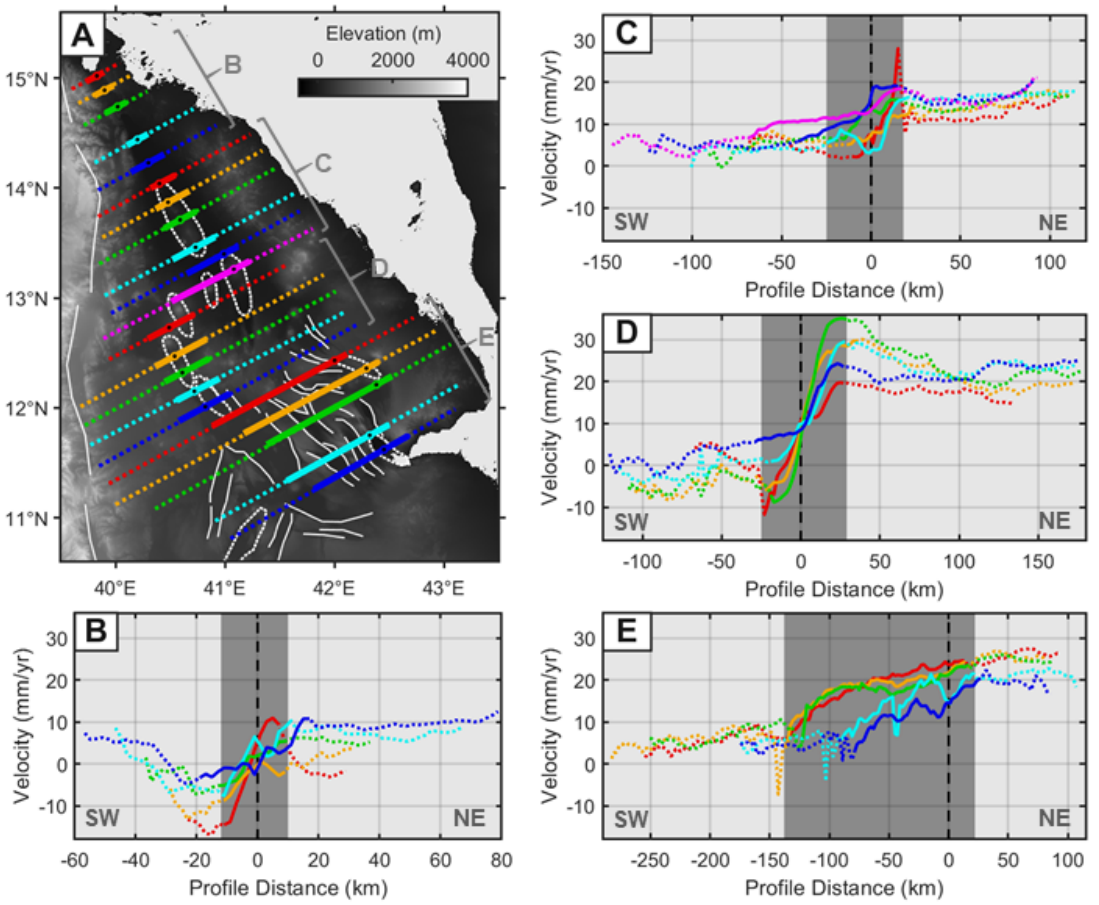

Figure 3.5: Map of 21 10 km wide rift-perpendicular velocity (relative to stable Nubia, positive towards 61°N) profiles over the Afar rift (A), with rift segments shown by white dashed outlines, and faults by solid white lines. The velocity profiles cover northern Afar (B), the Erta 'Ale and Tat 'Ale segments (C), the Dabbahu-Manda-Hararo segment (D), and southern Afar (E). The region on each profile where the majority of extension is accommodated, is indicated by the solid portion of the profile lines in (A) and (B-E), with the rest of the profile marked as dotted lines. This region of extension is approximated for each subset by the dark grey shaded portions of (B-E). The standard deviation of rift-perpendicular velocities varies from ± 2-7 mm/yr (see Figure 3.3). Profile distances are measured arbitrarily, relative to where the profile coincides with a magmatic segment, with positive towards the NE. Zero profile distance is marked by black circles on (A), and dashed black lines on (B-E).

20 km of the rift segments. Profiles covering the DMHVS (Figures 3.4D and 3.5D) also show that the long-term extension is concentrated near the rift-axis, with only small variations in rift-perpendicular velocity away from ± 20-30 km of the segment centre. The spatial distribution of rift-perpendicular extension at the DMHVS is in agreement with the 2006-10 InSAR dervied velocities from Pagli et al. (2014), although the magnitude of extension close to the segment is reduced by 55-70 % between 2006-10 and 2014-19. Elevated velocities close to the segment centre are associated with the 2005-10 DMHVS rifting episode, and are discussed in Section 3.3.

Profiles over southern central Afar and the AGVS (Figures 3.4E and 3.5E) show a more distributed pattern of extension with an initial increase in rift-perpendicular velocities 70-140 km to the SW of the rift axis near the Tendaho Graben, before velocities stabilise at $\sim$ 20 mm/yr on the Danakil micro-plate within 10-20 km to the NE of the rift axis. The distribution of strain shows good agreement with GNSS observations in Figure 3.4E, with the differences likely occurring due to the distances between the profiles and GNSS sites (see Figure 3.4A), particularly for the AGVS, where our rift-perpendicular velocities vary strongly along the rift. In southern Afar, extension between 2014-19 may be largely accommodated by tectonic rather than magmatic mechanisms, with strain being distributed across a sequence of horst and graben structures (e.g. Tapponnier et al., 1990, Manighetti et al., 2001). Previous studies have also shown that strain in southern central Afar is distributed across a broad region of the rift, with InSAR derived velocities from 2003-10 (Doubre et al., 2017) and 2006-10 (Pagli et al., 2014) indicating that along-profile extension is distributed over $\sim$ 50-100 km and $\sim$ 70-120 km respectively. The detailed GNSS observations of Doubre et al. (2017) demonstrate how this extension is accommodated within the central Afar fault structures, where extension is accommodated by tectonic processes (Manighetti et al., 1998, 2001). Pagli et al. (2019) suggest that the elevated strain and seismicity in this region demonstrates linkage between the DMHVS and AGVS. Doubre and Peltzer (2007) and Doubre et al. (2017) also show small steps in extension close to the AGVS with an increase of $\sim$ 2-6 mm/yr over the rift segment, in agreement to the step shown in Figure 3.4E of $\sim$ 1-7 mm/yr.

Our results indicate that at the more mature segments with active magmatism in central and northern Afar, extension is largely focussed to within $\pm$ 15-30 km of the rift axis; while at less mature segments without active magmatism in southern Afar, extension may be distributed of a over 80-160 km. The broad distribution of strain in southern Afar is comparable with previous GNSS and InSAR based studies including Kogan et al. (2012), Pagli et al. (2014), Doubre et al. (2017). Kogan et al. (2012) show that extension along a profile in southern Afar occurs over $\sim$ 175 km, but also suggest that extension becomes more distributed with rift development. In contrast, our results suggest an increase in focussing with rift maturity during late-stage continental break-up, in keeping with strain localisation assisting the transition into oceanic spreading centres (e.g. Manighetti et al., 1998). Our findings are also in keeping with other studies of rift development in Afar (e.g. Bastow et al., 2018, Keir et al., 2013), who also suggest an increase in localisation in northern Afar, with significant plate thinning and extrusive magmatism.

3.4.3 Magmatic Deformation

Figure 3.4 highlights the surface deformation at Dallol (3.4F) and Nabro (3.4G) volcanoes, and at the DMHVS (3.4I), where localised deformation, likely associated with magma migration, is visible. As magmatic deformation may not be steady in time, we look at time series for points located in the middle of these centres. Time series of vertical displacements at the Dallol, Nabro, Dabbahu, and Manda-Hararo volcanic centres show that the deformation is linear through time, indicating that the velocities displayed in Figure 3.4F-I are approximately representative of long-term ground motions. For Erta 'Ale volcano, we select a point $\sim$ 2 km to the north of the summit caldera in order to avoid the step surface deformation associated with a dyke intrusion in January 2017 (Moore et al., 2019, Xu et al., 2017, 2020). Following this intrusion the Erta 'Ale edifice shows linear subsidence at a rate of 15 $\pm$ 4 mm/yr (Figure 3.6).

Figure 3.4H over the AGVS indicates the lack of significant magma related deformation at this segment from 2014-19, with the change in rift-perpendicular extension over the segment being discussed in Section 3.4.2. Smittarello et al. (2016) observe vertical deformation associated with post-rifting relaxation from the 1978 rifting event on the AGVS up to 1999-2003, with a return to long-term spreading rates up to 2014 supported by Doubre et al. (2017). Our results suggest a continuation of the inter-dyking

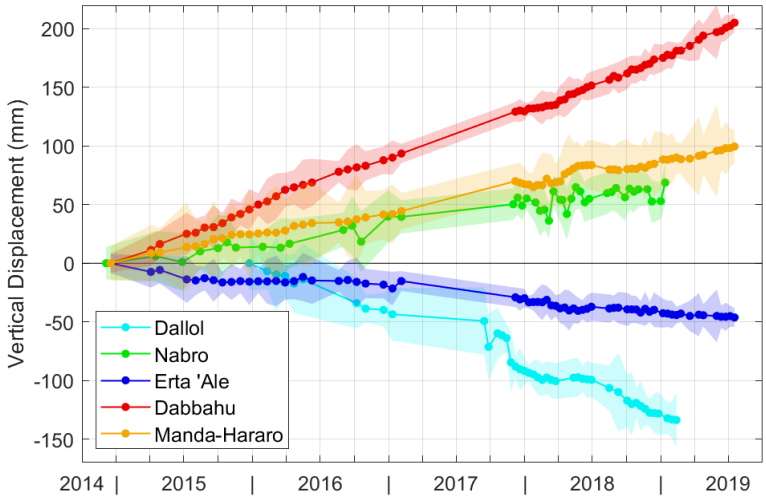

Figure 3.6: 2014-19 time series of vertical displacements (uplift positive) with 1 standard deviation estimates, at five deforming volcanic centres in Afar. The points used for the time series are representative of the whole edifice deformation and are positioned at the centre of the volcanic edifice; with the exception of Erta 'Ale where the point selected is $\sim$ 2 km North of the summit lava lake in order to avoid surface deformation associated with the Jan 2017 dyke intrusion event (Moore et al., 2019, Xu et al., 2017, 2020). Coordinates of points used for each volcanic centre: Dallol - 40.3°E/14.243°N, Nabro - 41.685°E/13.38°N, Erta 'Ale - 40.65°E/13.62°N, Dabbahu - 40.48°E/12.58°N, Manda-Hararo - 40.88°E/12.13°N.

period at the AGVS, with negligible vertical deformation.

At Dallol volcano, at the northern end on the EAVS, we observe a high rate of subsidence of up to 45 ± 4 mm/yr, with negligible horizontal movement. The subsidence signal is focussed on the central cone at Dallol. We model this signal using the Markov-Chain Monte-Carlo Geodetic Bayesian Inversion Software (GBIS) (Bagnardi and Hooper, 2018). For the T014A and T079D LOS deformation between 2014-19, we test source geometries including a point pressure source (Mogi, 1958), a planar dislocation (Okada, 1985), and a penny-shaped crack (Fialko et al., 2001). We find that a $\sim 1\times2$ km horizontal sill at 0.9-1.3 km depth with $\sim$ 0.27 m of contraction gives the lowest residual RMS misfit (Figure B.8). This is in agreement with Nobile et al. (2012) who inferred the presence of a deflating magma body at 1.5-3.3 km depth beneath Dallol between 2004-06, and (López-García et al., 2020) who attribute the presence of the shallow magma body to the abundant hydrothermal activity at Dallol.

At Nabro volcano, we observe edifice uplift and extension at rates of up to 12 ± 3 mm/yr, combined with the subsidence of lava flows from the 2011 eruption (Hamlyn et al., 2014), and a highly localised subsidence and contraction signal of up to 14 ± 3 mm/yr at the centre of the Nabro caldera. This uplift of the Nabro edifice shows a change from InSAR observed subsidence of 150-200 mm/yr from 2011-12, after the 2011 eruption (Hamlyn et al., 2018). As our vertical displacement time series (Figure 3.6) indicates that the uplift at Nabro is linear between 2014-19, we suggest that this post-eruption edifice subsidence must have stopped between 2012-14. We model T006D, T014A, and T079D LOS observations at Nabro volcano between 2014-19 using a point pressure source (Mogi, 1958), and penny-shaped crack (Fialko et al., 2001) using GBIS (Bagnardi and Hooper, 2018). Figure B.9 shows the optimal Mogi source at 5.5-6.8 km depth with a volume increase of 7-11$\times10^6$ m^3. The location of this source is in agreement with the magma chamber at 6.4 ± 0.3 km depth inferred by (Hamlyn et al., 2018) between 2011-12, indicating re-charge of the melt storage below Nabro volcano.

After the initial 2005 intrusion at the DMHVS, background uplift and rift-perpendicular extension continued throughout the 2005-10 rifting episode at rates of up to 80-240 mm/yr and 110-180 mm/yr respectively, from 2006-10 at the segment centre (Pagli et al., 2014, Hamling et al., 2014). We show that this uplift and extension is ongoing between 2014-19 at average rates of 33 ± 4 mm/yr and 37 ± 4 mm/yr respectively (Figure 3.4c,h). Our vertical velocities also show that an area of $\sim$ 20 mm/yr subsidence from 2006-10 at the southern end of the DMHVS (40.9°E/12.1°N) uplifts at an average rate of 18 ± 4 mm/yr from 2014-19. This decaying post-rifting response to the initial 2005 intrusion may be indicative of continued magma movement beneath the DMHVS and/or a time-dependant viscous response due to a more ductile rheology generated from re-

peated intrusions at the rift segment. Expanding on the study of Hamling et al. (2014), further work is required to model the long-term response to the 2005-10 rifting episode at the DMHVS, incorporating a viscous response and continued magma movement by combining the InSAR time series of Pagli et al. (2014), with the data presented here.

3.5 Conclusions

We develop Sentinel-1 displacement time series at 100×100 m resolution between 2014-19 over three ascending and two descending tracks, covering the whole Afar rift. We implement a RMS misfit weighted APS correction to clean the time series, and produce average velocity maps for each frame. Using GNSS observations of long-term plate motions (King et al., 2019), we reference the InSAR velocities to the stable Nubian plate, and convert LOS into 3D velocities (vertical, rift-perpendicular, rift-parallel).

We are able to resolve deformation at individual volcanic centres, with subsidence of 45 ± 4 mm/yr at Dallol volcano, consistent with the deflation of a shallow sill at 0.9-1.3 km depth. We also show that edifice uplift at Nabro volcano of 12 ± 3 mm/yr is sourced from a magma chamber at 5.5-6.8 km depth, consistent with the source of post-eruption subsidence observed between 2011-12 (Hamlyn et al., 2018).

Pagli et al. (2014) and Hamling et al. (2014) identify vertical and rift-perpendicular horizontal surface velocities between 2006-10 of 80-240 mm/yr and 110-180 mm/yr, respectively associated with a background post-rift response to the initial 2005 dyking episode at the DMHVS. We show that this response is ongoing between 2014-19, but at lower rates of 33 ± 4 mm/yr and 37 ± 4 mm/yr respectively. We suggest that this ∼ 15 year response to the 2005 dyke intrusion is indicative of continued magma movement and/or time-dependant viscous processes within the crust below the rift segment.

We resolve the long-term motion of the Danakil micro-plate with rift-perpendicular velocities of up to 25 ± 5 mm/yr, with negligible motions in the rift-parallel direction. From cross-rift profiles, we find that extension is largely focussed to within ± 15-30 km of the rift-axis on the active magmatic segments in northern Afar, while strain in central and southern Afar is distributed across 80-160 km of the rift. This trend of increased focussing of extension with magmatic rift maturity is consistent with strain localisation assisting the transition into oceanic spreading centres.

3.6 Acknowledgements

All Sentinel-1 data is sourced from the European Union Copernicus Programme. We perform data processing on the JASMIN facility, operated by the Centre for Environmental Data Analysis (CEDA), and post-processing and figure generation using MATLAB and GMT. Processed LiCSAR interferograms are available in the Centre for Environmental Data Analysis (CEDA) archive (`http://archive.ceda.ac.uk`) here: `http://data.ceda.ac.uk/neodc/comet/data/licsar_products`. This work was funded by the NERC RiftVolc project (NE/L013649/1), and supported by the Centre for Observation and Modelling of Earthquakes, Volcanoes, and Tectonics (COMET).

References

Agram, P., Jolivet, R., Riel, B., Lin, Y., Simons, M., Hetland, E., Doin, M.-P. and Lasserre, C. (2013). New radar interferometric time series analysis toolbox released. *Eos, Transactions American Geophysical Union*, **94**(7), pp. 69–70. 3.2.2

Allard, P., Tazieff, H. and Dajlevic, D. (1979). Observations of seafloor spreading in Afar during the November 1978 fissure eruption. *Nature*, **279**(5708), pp. 30–33. doi:10.1038/279030a0. 3.2.1

Amelung, F., Oppenheimer, C., Segall, P. and Zebker, H. (2000). Ground deformation near Gada 'Ale volcano, Afar, observed by radar interferometry. *Geophysical Research Letters*, **27**(19), pp. 3093–3096. doi:10.1029/2000GL008497. 3.2.1

Ansari, H., De Zan, F. and Parizzi, A. (2020). Study of Systematic Bias in Measuring Surface Deformation with SAR Interferometry. *IEEE Transactions on Geoscience and Remote Sensing*, pp. 1–1. 3.3.2

ArRajehi, A., McClusky, S., Reilinger, R., Daoud, M., Alchalbi, A., Ergintav, S., Gomez, F., Sholan, J., Bou-Rabee, F., Ogubazghi, G., Haileab, B., Fisseha, S., Asfaw, L., Mahmoud, S., Rayan, A., Bendik, R. and Kogan, L. (2010). Geodetic constraints on present-day motion of the Arabian Plate: Implications for Red Sea and Gulf of Aden rifting. *Tectonics*, **29**(TC3011). doi:10.1029/2009TC002482. 3.2.1

Audin, J., Vellutini, P. J., Coulon, C., Piguet, P. and Vincent, J. (1990). The 1928-1929 eruption of Kammourta volcano - Evidence of tectono-magmatic activity in the Manda-Inakir rift and comparison with the Asal Rift, Afar depression, Republic of Djibuti. *Bulletin of Volcanology*, **52**, pp. 551–561. 3.2.1

Ayele, A., Keir, D., Ebinger, C., Wright, T. J., Stuart, G. W., Buck, W. R., Jacques, E., Ogubazghi, G. and Sholan, J. (2009). September 2005 mega-dike emplacement in the Manda-Harraro nascent oceanic rift (Afar depression). *Geophysical Research Letters*, **36**(L20306). doi:10.1029/2009GL039605. 3.2.1

Bagnardi, M. and Hooper, A. (2018). Inversion of Surface Deformation Data for Rapid Estimates of Source Parameters and Uncertainties: A Bayesian Approach. *Geochemistry, Geophysics, Geosystems*, **19**. doi:10.1029/2018GC007585. 3.4.3, 3.4.3

Barnie, T. D., Keir, D., Hamling, I., Hofmann, B., Belachew, M., Carn, S., Eastwell, D., Hammond, J. O. S., Ayele, A., Oppenheimer, C. and Wright, T. (2016a). A multidisciplinary study of the final episode of the Manda Hararo dyke sequence, Ethiopia, and implications for trends in volcanism during the rifting cycle. *Geological Society, London, Special Publications*, **420**, pp. 149–163. doi:10.1144/SP420.6. 3.2.1

Barnie, T. D., Oppenheimer, C. and Pagli, C. (2016b). Does the lava lake of Erta 'Ale volcano respond to regional magmatic and tectonic events? An investigation using Earth Observation data. *Geological Society, London, Special Publications*, **420**, pp. 181–208. doi:10.1144/SP420.15. 3.2.1

Bastow, I. D., Booth, A. D., Corti, G., Keir, D., Magee, C., Jackson, C. A.-L., Warren, J., Wilkinson, J. and Lascialfari, M. (2018). The development of late-stage continental breakup: Seismic reflection and borehole evidence from the Danakil Depression, Ethiopia. *Tectonics*, **37**(9), pp. 2848–2862. 3.4.2

Bastow, I. D. and Keir, D. (2011). The protracted development of the continent-ocean transition in Afar. *Nature Geoscience*, **4**(4), pp. 248–250. doi:10.1038/ngeo1095. 3.2.1

Berardino, P., Fornaro, G., Lanari, R. and Sansosti, E. (2002). A new algorithm for surface deformation monitoring based on small baseline differential SAR interferograms. *IEEE Transactions on Geoscience and Remote Sensing*, **40**(11), pp. 2375–2383. doi:10.1109/TGRS.2002.803792. 3.2.2

Biggs, J., Wright, T., Lu, Z. and Parsons, B. (2007). Multi-interferogram method for measuring interseismic deformation: Denali Fault, Alaska. *Geophysical Journal International*, **170**(3), pp. 1165–1179. doi:10.1111/j.1365-246X.2007.03415.x. 3.2.2

Bird, P. (2003). An updated digital model of plate boundaries. *Geochemistry, Geophysics, Geosystems*, **4**(3). doi:10.1029/2001GC000252. 3.1

Birhanu, Y., Bendick, R., Fisseha, S., Lewi, E., Floyd, M., King, R. and Reilinger, R. (2016). GPS constraints on broad scale extension in the Ethiopian Highlands and Main Ethiopian Rift. *Geophysical Research Letters*, **43**(13), pp. 6844–6851. 3.2.1

Boissonnat, J.-D. and Cazals, F. (2002). Smooth surface reconstruction via natural neighbour interpolation of distance functions. *Computational Geometry*, **22**(1-3), pp. 185–203. 3.3.3

Cattin, R., Doubre, C., de Chabalier, J. B., King, G., Vigny, C., Avouac, J. P. and Ruegg, J. C. (2005). Numerical modelling of quaternary deformation and post-rifting displacement in the Asal-Ghoubbet rift (Djibouti, Africa). *Earth and Planetary Science Letters*, **239**(3-4), pp. 352–367. doi:10.1016/j.epsl.2005.07.028. 3.2.1

Chen, C. W. and Zebker, H. A. (2002). Phase unwrapping for large SAR interferograms: Statistical segmentation and generalized network models. *IEEE Transactions on Geoscience and Remote Sensing*, **40**(8), pp. 1709–1719. 3.3.1

Cleveland, W. S. and Devlin, S. J. (1988). Locally weighted regression: An approach to regression analysis by local fitting. *Journal of the American statistical association*, **83**(403), pp. 596–610. 3.3.2

De Zan, F., Zonno, M. and Lopez-Dekker, P. (2015). Phase inconsistencies and multiple scattering in SAR interferometry. *IEEE Transactions on Geoscience and Remote Sensing*, **53**(12), pp. 6608–6616. 3.3.2

Doubre, C., Déprez, A., Masson, F., Socquet, A., Lewi, E., Grandin, R., Nercessian, A., Ulrich, P., De Chabalier, J. B., Saad, I., Abayazid, A., Peltzer, G., Delorme, A., Calais, E. and Wright, T. (2017). Current deformation in Central Afar and triple junction kinematics deduced from GPS and InSAR measurements. *Geophysical Journal International*, **208**, pp. 936–953. doi:10.1093/gji/ggw434. 3.2.1, 3.2.2, 3.4.2, 3.4.2, 3.4.3

Doubre, C. and Peltzer, G. (2007). Fluid-controlled faulting process in the Asal Rift, Djibouti, from 8 yr of radar interferometry observations. *Geology*, **35**(1), pp. 69–72. doi:10.1130/G23022A.1. 3.2, 3.2.2, 3.4.2

Eagles, G., Gloaguen, R. and Ebinger, C. (2002). Kinematics of the Danakil microplate. *Earth and Planetary Science Letters*, **203**(2), pp. 607–620. doi:10.1016/S0012-821X(02)00916-0. 3.2.1

Ebinger, C. J. (2005). Continental break-up: the East African perspective. *Astronomy & Geophysics*, **46**(2), pp. 2–16. 3.2

Ebinger, C., Ayele, A., Keir, D., Rowland, J., Yirgu, G., Wright, T., Belachew, M. and Hamling, I. (2010). Length and Timescales of Rift Faulting and Magma Intrusion: The Afar Rifting Cycle from 2005 to Present. *Annual Review of Earth and Planetary Sciences*, **38**(1), pp. 439–466. doi:10.1146/annurev-earth-040809-152333. 3.2

Ebinger, C. J. and Casey, M. (2001). Continental breakup in magmatic provinces: An Ethiopian example. *Geology*, **29**(6), pp. 527–530. doi:10.1130/0091-7613(2001)029<0527:CBIMPA>2.0.CO;2. 3.2

Elliott, J. R., Biggs, J., Parsons, B. and Wright, T. J. (2008). InSAR slip rate determination on the Altyn Tagh Fault, northern Tibet, in the presence of topographically correlated atmospheric delays. *Geophysical Research Letters*, **35**(12), pp. 1–5. doi:10.1029/2008GL033659. 3.3.1

Eyles, J. H., Illsley-Kemp, F., Keir, D., Ruch, J. and Jónsson, S. (2018). Seismicity associated with the formation of a new island in the Southern Red Sea. *Frontiers in Earth Science*, **6**, p. 141. 3.4.2

Farr, T. G. and Kobrick, M. (2000). Shuttle Radar Topography Mission produces a wealth of data, Eos Trans. *Eos, Transactions American Geophysical Union*, **81**(48), pp. 583–585. doi:10.1029/EO081i048p00583. 3.3.1

Ferguson, D. J., Barnie, T. D., Pyle, D. M., Oppenheimer, C., Yirgu, G., Lewi, E., Kidane, T., Carn, S. and Hamling, I. (2010). Recent rift-related volcanism in Afar, Ethiopia. *Earth and Planetary Science Letters*, **292**(3-4), pp. 409–418. doi:10.1016/j.epsl.2010.02.010. 3.2.1

Fialko, Y., Khazan, Y. and Simons, M. (2001). Deformation due to a pressurized horizontal circular crack in an elastic half-space, with applications to volcano geodesy. *Geophysical Journal International*, **146**(1), pp. 181–190. 3.4.3, 3.4.3

Field, L., Barnie, T., Blundy, J., Brooker, R. A., Keir, D., Lewi, E. and Saunders, K. (2012). Integrated field, satellite and petrological observations of the November 2010 eruption of Erta Ale. *Bulletin of Volcanology*, **74**, pp. 2251–2271. doi:10.1007/s00445-012-0660-7. 3.2.1

Furman, T., Bryce, J., Rooney, T., Hanan, B., Yirgu, G. and Ayalew, D. (2006). Heads and tails: 30 million years of the Afar plume. *Geological Society, London, Special Publications*, **259**, pp. 95–119. doi:10.1144/GSL.SP.2006.259.01.09. 3.2.1

Gallacher, R. J., Keir, D., Harmon, N., Stuart, G., Leroy, S., Hammond, J. O., Kendall, J. M., Ayele, A., Goitom, B., Ogubazghi, G. and Ahmed, A. (2016). The initiation of segmented buoyancy-driven melting during continental breakup. *Nature Communications*, **7**(13110). doi:10.1038/ncomms13110. 3.2.1

Goitom, B., Oppenheimer, C., Hammond, J. O., Grandin, R., Barnie, T., Donovan, A., Ogubazghi, G., Yohannes, E., Kibrom, G., Kendall, J. M., Carn, S. A., Fee, D., Sealing, C., Keir, D., Ayele, A., Blundy, J., Hamlyn, J., Wright, T. and Berhe, S. (2015). First recorded eruption of Nabro volcano, Eritrea, 2011. *Bulletin of Volcanology*, **77**(85), pp. 1–21. doi:10.1007/s00445-015-0966-3. 3.2.1

Goldstein, J., Reed, I. and Scharf, L. (1998). A multistage representation of the Wiener filter based on orthogonal projections. *IEEE Transactions on Information Theory*, **44**(7), pp. 2943–2959. doi:10.1109/18.737524. 3.3.1

González, P. J., Walters, R. J., Hatton, E. L., Spaans, K. and Hooper, A. (2016). LiCSAR: Tools for automated generation of Sentinel-1 frame interferograms. *AGU Fall Meeting*. 3.3.1

Grandin, R., Socquet, A., Doin, M. P., Jacques, E., De Chabalier, J. B. and King, G. C. (2010). Transient rift opening in response to multiple dike injections in the Manda Hararo rift (Afar, Ethiopia) imaged by time-dependent elastic inversion of interferometric synthetic aperture radar data. *Journal of Geophysical Research: Solid Earth*, **115**(B09403). doi:10.1029/2009JB006883. 3.2.1

Hamling, I. J., Wright, T. J., Calais, E., Bennati, L. and Lewi, E. (2010). Stress transfer between thirteen successive dyke intrusions in Ethiopia. *Nature Geoscience*, **3**(10), pp. 713–717. doi:10.1038/ngeo967. 3.2.1

Hamling, I. J., Wright, T. J., Calais, E., Lewi, E. and Fukahata, Y. (2014). InSAR observations of post-rifting deformation around the Dabbahu rift segment, Afar, Ethiopia. *Geophysical Journal International*, **197**, pp. 33–49. doi:10.1093/gji/ggu003. 3.2.1, 3.2.2, 3.3.3, 3.4.3, 3.5

Hamlyn, J. E., Keir, D., Wright, T. J., Neuberg, J. W., Goitom, B., Hammond, J. O. S., Pagli, C., Oppenheimer, C., Kendall, J. M. and Grandin, R. (2014). Seismicity and subsidence following the 2011 Nabro eruption, Eritrea: Insights into the plumbing system of an off-rift volcano. *Journal of Geophysical Research: Solid Earth*, **119**, pp. 8267–8282. doi:10.1002/2014JB011395. 3.2.1, 3.4.3

Hamlyn, J., Wright, T., Walters, R., Pagli, C., Sansosti, E., Casu, F., Pepe, S., Edmonds, M., Kilbride, B. M., Keir, D. et al. (2018). What causes subsidence following the 2011 eruption at Nabro (Eritrea)? *Progress in Earth and Planetary Science*, **5**(1), p. 31. 3.2, 3.2.1, 3.4.3, 3.5

Hammond, J. O. S. (2014). Constraining melt geometries beneath the Afar Depression, Ethiopia from teleseismic receiver functions: The anisotropic H-κ stacking technique. *Geochemistry, Geophysics, Geosystems*, **15**(4), pp. 1316–1332. 3.2.1

Hammond, J. O. S. and Kendall, J. M. (2016). Constraints on melt distribution from seismology: a case study in Ethiopia. *Geological Society, London, Special Publications*, **420**, pp. 127–147. doi:10.1144/SP420.14. 3.2.1

Hammond, J. O. S., Kendall, J. M., Stuart, G. W., Ebinger, C. J., Bastow, I. D., Keir, D., Ayele, A., Belachew, M., Goitom, B., Ogubazghi, G. and Wright, T. J. (2013). Mantle upwelling and initiation of rift segmentation beneath the Afar Depression. *Geology*, **41**(6), pp. 635–638. doi:10.1130/G33925.1. 3.2.1

Hammond, J. O. S., Kendall, J. M., Stuart, G. W., Keir, D., Ebinger, C., Ayele, A. and Belachew, M. (2011). The nature of the crust beneath the Afar triple junction: Evidence from receiver functions. *Geochemistry, Geophysics, Geosystems*, **12**(12). doi:10.1029/2011GC003738. 3.2.1

Hooper, A., Bekaert, D., Spaans, K. and Arıkan, M. (2012). Recent advances in SAR interferometry time series analysis for measuring crustal deformation. *Tectonophysics*, **514**, pp. 1–13. 3.2.2

Hussain, E., Hooper, A., Wright, T. J., Walters, R. J. and Bekaert, D. P. (2016). Interseismic strain accumulation across the central North Anatolian Fault from iteratively unwrapped InSAR measurements. *Journal of Geophysical Research: Solid Earth*, **121**, pp. 9000–9019. doi:10.1002/2016JB013108. 3.3.3

Illsley-Kemp, F., Keir, D., Bull, J. M., Gernon, T. M., Ebinger, C., Ayele, A., Hammond, J. O., Kendall, J. M., Goitom, B. and Belachew, M. (2018). Seismicity during continental breakup in the Red Sea Rift of Northern Afar. *Journal of Geophysical Research: Solid Earth*, **123**, pp. 2345–2362. doi:10.1002/2017JB014902. 3.2.1

Jung, J., Kim, D.-j. and Park, S.-E. (2013). Correction of atmospheric phase screen in time series InSAR using WRF model for monitoring volcanic activities. *IEEE Transactions on Geoscience and Remote Sensing*, **52**(5), pp. 2678–2689. 3.2.2

Keir, D., Bastow, I. D., Pagli, C. and Chambers, E. L. (2013). The development of extension and magmatism in the Red Sea rift of Afar. *Tectonophysics*, **607**, pp. 98–114. doi:10.1016/j.tecto.2012.10.015. 3.4.2

Kendall, J. M., Stuart, G. W., Ebinger, C. J., Bastow, I. D. and Keir, D. (2005). Magma-assisted rifting in Ethiopia. *Nature*, **433**(7022), pp. 146–148. doi:10.1038/nature03161. 3.2

Kidane, T. (2016). Strong clockwise block rotation of the Ali-Sabieh/Aïsha Block: evidence for opening of the Afar Depression by a 'saloon-door' mechanism. *Geological Society, London, Special Publications*, **420**, pp. 209–219. doi:10.1144/SP420.10. 3.4.1

King, R., Floyd, M., Reilinger, R. and Bendick, R. (2019). GPS velocity field (MIT 2019.0) for the East African Rift System generated by King et al.. Interdisciplinary Earth Data Alliance (IEDA). *Accessed on 20 Sep 2019.* doi:10.1594/IEDA/324785. 3.1, 3.3.3, 3.2, 3.5

Kogan, L., Fisseha, S., Bendick, R., Reilinger, R., McClusky, S., King, R. and Solomon, T. (2012). Lithospheric strength and strain localization in continental extension from observations of the East African Rift. *Journal of Geophysical Research: Solid Earth*, **117**(B03402). doi:10.1029/2011JB008516. 3.4.2

Lanari, R., Casu, F., Manzo, M., Zeni, G., Berardino, P., Manunta, M. and Pepe, A. (2007). An overview of the Small BAseline Subset algorithm: A DInSAR technique for surface deformation analysis. *Pure and Applied Geophysics*, **164**(4), pp. 637–661. doi:10.1007/s00024-007-0192-9. 3.2.2

Lavayssière, A., Rychert, C., Harmon, N., Keir, D., Hammond, J. O., Kendall, J.-M., Doubre, C. and Leroy, S. (2018). Imaging lithospheric discontinuities beneath the Northern East African Rift Using S-to-P receiver functions. *Geochemistry, Geophysics, Geosystems*, **19**(10), pp. 4048–4062. 3.2.1

Lazeckỳ, M., Spaans, K., González, P. J., Maghsoudi, Y., Morishita, Y., Albino, F., Elliott, J., Greenall, N., Hatton, E., Hooper, A. et al. (2020). LiCSAR: An automatic InSAR tool for measuring and monitoring tectonic and volcanic activity. *Remote Sensing*, **12**(15), p. 2430. 3.3.1

Liu, S., Hanssen, R., Samiei-Esfahany, S., Hooper, A. and Van Leijen, F. (2011). Separating non-linear deformation and atmospheric phase screen (APS) for InSAR time series analysis using least-squares collocation. In *Proceedings of the Advances in the Science and Applications of SAR Interferometry, ESA Fringe 2009, Workshop ESA*. 3.2.2

López-García, J. M., Moreira, D., Benzerara, K., Grunewald, O. and López-García, P. (2020). Origin and evolution of the halo-volcanic complex of Dallol: proto-volcanism in Northern Afar (Ethiopia). *Frontiers in Earth Science*, **7**, p. 351. 3.4.3

Manighetti, I., Tapponnier, P., Courtillot, V., Gallet, Y., Jacques, E. and Gillot, P.-Y. (2001). Strain transfer between disconnected, propagating rifts in Afar. *Journal of Geophysical Research: Solid Earth*, **106**(B7), pp. 13613–13665. 3.4.2

Manighetti, I., Tapponnier, P., Gillot, P., Jacques, E., Courtillot, V., Armijo, R., Ruegg, J. and King, G. (1998). Propagation of rifting along the Arabia-Somalia plate boundary: Into Afar. *Journal of Geophysical Research: Solid Earth*, **103**(B3), pp. 4947–4974. 3.4.2, 3.4.2

McClusky, S., Reilinger, R., Ogubazghi, G., Amleson, A., Healeb, B., Vernant, P., Sholan, J., Fisseha, S., Asfaw, L., Bendick, R. and Kogan, L. (2010). Kinematics of the southern Red Sea-Afar Triple Junction and implications for plate dynamics. *Geophysical Research Letters*, **37**(L05301). doi:10.1029/2009GL041127. 3.2.1

Mogi, K. (1958). Relations between the Eruptions of Various Volcanoes and the Defomormations of the Ground Surfaces around them. *Bulletin of the Earthquake Research Institute*, **36**, pp. 99–134. 3.4, 3.4.3, 3.4.3

Moore, C., Wright, T., Hooper, A. and Biggs, J. (2019). The 2017 eruption of Erta 'Ale volcano, Ethiopia: Insights in the shallow axial plumbing system of an incipient mid-ocean ridge. *Geochemistry, Geophysics, Geosystems*, **20**(12). 3.2.1, 3.4.2, 3.4.3, 3.6

Morishita, Y., Lazecky, M., Wright, T. J., Weiss, J. R., Elliott, J. R. and Hooper, A. (2020). LiCSBAS: An Open-Source InSAR Time Series Analysis Package Integrated with the LiCSAR Automated Sentinel-1 InSAR Processor. *Remote Sensing*, **12**(3), p. 424. 3.2.2

Nobile, A., Pagli, C., Keir, D., Wright, T. J., Ayele, A., Ruch, J. and Acocella, V. (2012). Dike-fault interaction during the 2004 Dallol intrusion at the northern edge of the Erta Ale Ridge (Afar, Ethiopia). *Geophysical Research Letters*, **39**(L19305). doi:10.1029/2012GL053152. 3.2.1, 3.4.3

Nooner, S. L. and Chadwick, W. W. (2009). Volcanic inflation measured in the caldera of axial seamount: Implications for magma supply and future eruptions. *Geochemistry, Geophysics, Geosystems*, **10**(2). doi:10.1029/2008GC002315. 3.2

Okada, Y. (1985). Surface deformation due to shear and tensile faults in a half-space. *Bulletin of the seismological society of America*, **75**(4), pp. 1135–1154. 3.4, 3.4.3

Pagli, C., Wang, H., Wright, T. J., Calais, E. and Lewi, E. (2014). Current plate boundary deformation of the Afar rift from a 3-D velocity field inversion of InSAR and GPS. *Journal of Geophysical Research: Solid Earth*, **119**, pp. 8562–8575. doi:10.1002/2014JB011391. 3.2, 3.2.2, 3.4.2, 3.4.2, 3.4.2, 3.4.3, 3.5

Pagli, C., Wright, T. J., Ebinger, C. J., Yun, S. H., Cann, J. R., Barnie, T. and Ayele, A. (2012). Shallow axial magma chamber at the slow-spreading Erta Ale Ridge. *Nature Geoscience*, **5**(4), pp. 284–288. doi:10.1038/ngeo1414. 3.2.1

Pagli, C., Yun, S.-H., Ebinger, C., Keir, D. and Wang, H. (2019). Strike-slip tectonics during rift linkage. *Geology*, **47**(1), pp. 31–34. 3.4.2

Refice, A., Belmonte, A., Bovenga, F. and Pasquariello, G. (2011). On the use of anisotropic covariance models in estimating atmospheric DInSAR contributions. *IEEE Geoscience and Remote Sensing Letters*, **8**(2), pp. 341–345. 3.2.2

Saria, E., Calais, E., Stamps, D. S., Delvaux, D. and Hartnady, C. J. (2014). Present-day kinematics of the East African Rift. *Journal of Geophysical Research: Solid Earth*, **119**, pp. 3584–3600. doi:10.1002/2013JB010901. 3.2.1

Shen, L., Hooper, A. and Elliott, J. (2019). A Spatially Varying Scaling Method for InSAR Tropospheric Corrections Using a High-Resolution Weather Model. *Journal of Geophysical Research: Solid Earth*, **124**(4), pp. 4051–4068. 3.3.1

Smittarello, D., Grandin, R., De Chabalier, J.-B., Doubre, C., Deprez, A., Masson, F., Socquet, A. and Saad, I. (2016). Transient deformation in the Asal-Ghoubbet Rift (Djibouti) since the 1978 diking event: Is deformation controlled by magma supply rates? *Journal of Geophysical Research: Solid Earth*, **121**(8), pp. 6030–6052. 3.4.3

Sousa, J. J., Hooper, A. J., Hanssen, R. F., Bastos, L. C. and Ruiz, A. M. (2011). Persistent Scatterer InSAR: A comparison of methodologies based on a model of temporal deformation vs. spatial correlation selection criteria. *Remote Sensing of Environment*, **115**(10), pp. 2652–2663. 3.2.2

Stork, A. L., Stuart, G. W., Henderson, C. M., Keir, D. and Hammond, J. O. (2013). Uppermost mantle (Pn) velocity model for the Afar region, Ethiopia: An insight into rifting processes. *Geophysical Journal International*, **193**, pp. 321–328. doi:10.1093/gji/ggs106. 3.2.1

Tapponnier, P., Armijo, R., Manighetti, I. and Courtillot, V. (1990). Bookshelf faulting and horizontal block rotations between overlapping rifts in southern Afar. *Geophysical Research Letters*, **17**(1), pp. 1–4. 3.4.2

Tarantola, A., Ruegg, J. C. and Lepine, J. C. (1979). Geodetic evidence for rifting in Afar a brittle-elastic model of the behaviour of the lithosphere. *Earth and Planetary Science Letters*, **45**, pp. 435–444. doi:10.1016/0012-821X(79)90142-0. 3.2.1

Temtime, T., Biggs, J., Lewi, E., Hamling, I., Wright, T. and Ayele, A. (2018). Spatial and temporal patterns of deformation at the Tendaho geothermal prospect, Ethiopia. *Journal of Volcanology and Geothermal Research*, **357**, pp. 56–67. doi:10.1016/j.jvolgeores.2018.04.004. 3.2.2

Tiberi, C., Ebinger, C., Ballu, V., Stuart, G. and Oluma, B. (2005). Inverse models of gravity data from the Red Sea-Aden-East African rifts triple junction zone. *Geophysical Journal International*, **163**, pp. 775–787. doi:10.1111/j.1365-246X.2005.02736.x. 3.2.1

Viltres, R., Jónsson, S., Ruch, J., Doubre, C., Reilinger, R., Floyd, M. and Ogubazghi, G. (2020). Kinematics and deformation of the southern Red Sea region from GPS observations. *Geophysical Journal International*, **221**(3), pp. 2143–2154. 3.2.1, 3.4.1

Wang, H. and Wright, T. (2012). Satellite geodetic imaging reveals internal deformation of western Tibet. *Geophysical Research Letters*, **39**(7). 3.2.2

Wang, H., Wright, T. J., Yu, Y., Lin, H., Jiang, L., Li, C. and Qiu, G. (2012). InSAR reveals coastal subsidence in the Pearl River Delta, China. *Geophysical Journal International*, **191**(3), pp. 1119–1128. 3.2.2

Weiss, J. R., Walters, R. J., Morishita, Y., Wright, T. J., Lazecky, M., Wang, H., Hussain, E., Hooper, A. J., Elliott, J. R., Rollins, C. et al. (2020). High-resolution surface velocities and strain for Anatolia from Sentinel-1 InSAR and GNSS data. *Geophysical Research Letters*, **47**(17), p. e2020GL087376. 3.3.3

Werner, C., Wegmuller, U., Strozzi, T. and Wiesmann, A. (2000). GAMMA SAR and interferometric processing software. *European Space Agency, (Special Publication) ESA SP*, (461), pp. 211–219. 3.3.1

Wiart, P. and Oppenheimer, C. (2000). Largest known historical eruption in Africa: Dubbi volcano, Eritrea, 1861. *Geology*, **28**(4), pp. 291–294. doi:10.1130/0091-7613(2000)28<291:LKHEIA>2.0.CO;2. 3.2.1

Wolfenden, E., Ebinger, C., Yirgu, G., Deino, A. and Ayalew, D. (2004). Evolution of the northern Main Ethiopian rift: Birth of a triple junction. *Earth and Planetary Science Letters*, **224**(1-2), pp. 213–228. doi:10.1016/j.epsl.2004.04.022. 3.2.1

Wright, T. J., Ebinger, C., Biggs, J., Ayele, A., Yirgu, G., Keir, D. and Stork, A. (2006). Magma-maintained rift segmentation at continental rupture in the 2005 Afar dyking episode. *Nature*, **442**(7100), pp. 291–294. doi:10.1038/nature04978. 3.2, 3.2.1

Wright, T. J., Parsons, B. E. and Zhong, L. (2004). Toward mapping surface deformation in three dimensions using InSAR. *Geophysical Research Letters*, **31**(L01607). doi:10.1029/2003GL018827. 3.3.3

Wright, T. J., Sigmundsson, F., Pagli, C., Belachew, M., Hamling, I. J., Brandsdóttir, B., Keir, D., Pedersen, R., Ayele, A., Ebinger, C., Einarsson, P., Lewi, E. and Calais, E. (2012). Geophysical constraints on the dynamics of spreading centres from rifting episodes on land. doi:10.1038/ngeo1428. 3.2, 3.2.1

Xu, W., Rivalta, E. and Li, X. (2017). Magmatic architecture within a rift segment: Articulate axial magma storage at Erta Ale volcano, Ethiopia. *Earth and Planetary Science Letters*, **476**, pp. 79–86. doi:10.1016/j.epsl.2017.07.051. 3.2.1, 3.4.2, 3.4.3, 3.6

Xu, W., Xie, L., Aoki, Y., Rivalta, E. and Jónsson, S. (2020). Volcano-wide deformation after the 2017 Erta Ale dike intrusion, Ethiopia, observed with radar interferometry. *Journal of Geophysical Research: Solid Earth*, **125**(8), p. e2020JB019562. 3.4.2, 3.4.3, 3.6

Yu, C., Li, Z. and Penna, N. T. (2018). Interferometric synthetic aperture radar atmospheric correction using a GPS-based iterative tropospheric decomposition model. *Remote Sensing of Environment*, **204**, pp. 109–121. doi:10.1016/j.rse.2017.10.038. 3.3.1

Yu, C., Penna, N. T. and Li, Z. (2017). Generation of real-time mode high-resolution water vapor fields from GPS observations. *Journal of Geophysical Research*, **122**(3), pp. 2008–2025. doi:10.1002/2016JD025753. 3.3.1

Chapter 4

Post-Rift Relaxation at the Dabbahu-Manda-Hararo Segment in Afar, Ethiopia

The work displayed in Chapter 4 (Sections 4.1-4.6) is a manuscript to be submitted to the journal Geophysical Research Letters:
Moore, C., Wright, T. & Hooper, A. (in prep.). Post-Rift Relaxation at the Dabbahu-Manda-Hararo Segment in Afar, Ethiopia.
Supplementary Materials for this manuscript are provided in Appendix C.

4.1 Abstract

Major magmatic rifting events such as at the Dabbahu-Manda-Hararo segment in Afar from 2005-10, and at Krafla from 1975-84, provide crucial insights into the subsurface processes at subaerial spreading segments. These events are characterised by a post-rifting period with elevated surface deformation in the decades following the rifting episode, where the processes involved include viscous relaxation in the lower crust and continued magma movement within the segment. As these events are rare, previous models have not been able to observe the full spatial distribution of deformation over the long-time scales at which these processes likely operate. By combining Envisat and Sentinel-1 InSAR time series of surface displacements at the Dabbahu-Manda-Hararo segment over a period of $\sim$ 14 years, we find that average inflation at the segment centre has decayed from 80-240 mm/yr in 2006-10 to 29-37 mm/yr in 2014-19, while at the southern end of the segment, surface deflation of 45-65 mm/yr in 2006-10 switches to an inflation of 17-25 mm/yr in 2014-19. Using a two-layer homogeneous elastic-viscoelastic model, we develop a joint inversion for the viscous relaxation following 14 successive dyke intrusions from 2005-10, and the viscoelastic response from continued magma movement below four volcanic centres along the segment. We find the opti-

mal models for the period 2006-19 consist of an elastic lid thickness of 17-22 km, and a viscosity of 0.6-1.8 $\times$ 10^{18} Pa s within the viscoelastic half-space. The preferred model viscosity may also decrease from 10^{18}-10^{19} Pa s from 2006-10 to $\sim$ 10^{18} Pa s from 2014-19, indicating that time-dependant processes act throughout the post-rifting period. Our best-fit models require a magmatic inflation source below the segment centre of 0.5 $\pm$ 0.1$\times10^8$ m^3 from 2006-19, and a source below the southern end of the segment with a cumulative volume change of -2.8 $\pm$ 0.8$\times10^8$ m^3 from 2006-10 and 0.0 $\pm$ 0.4$\times10^8$ m^3 from 2014-19. We find that both viscous relaxation and continued magma movement contribute significantly to transient deformation observed following rifting episodes.

4.2 Introduction

Magmatic intrusions play a significant role in accommodating extension during late stage rifting (Ebinger, 2005, Kendall et al., 2005, Wright et al., 2012). Far-field plate motions generate the accumulation of extensional deviatoric stresses at spreading segments in an inter-rifting period, which may be released in major dyke intrusions during a co-rifting period. Following a rifting event, a post-rift relaxation signal has been observed to dominate surface deformation in Afar, Ethiopia, at Asal-Ghobbet (1978) (Cattin et al., 2005, Doubre and Peltzer, 2007, Vigny et al., 2007, Smittarello et al., 2016) and Dabbahu-Manda-Hararo (2005-10) (Nooner et al., 2009, Grandin et al., 2010a, Hamling et al., 2014), and in Iceland at Krafla (1975-84) (Foulger et al., 1992, Sigmundsson et al., 1997, Sturkell et al., 2008), over periods of up to $\sim$ 30 years until ground motions return to long-term plate spreading rates (Pedersen et al., 2009, Doubre et al., 2017, Moore et al., in review). These deformation signals are detectable using time series of observations from interferometric synthetic aperture radar (InSAR) and Global Navigation Satellite Systems (GNSS). As these major rifting events are rare and the processes involved are slow, the contributions of viscoelastic relaxation and continued magma movement to surface deformation in the post-rifting period are not fully understood (Grandin et al., 2010a, Wright et al., 2012, Hamling et al., 2014). The 2005-2019 Dabbahu-Manda-Hararo episode in Afar is the first such event with a long time series of spatially dense observations.

4.2.1 Afar Tectonic Setting

The Afar region of Ethiopia is situated at the divergent triple junction of the Red Sea Rift (RSR), the Gulf of Aden Rift (GAR), and the Main Ethiopian Rift (MER). Long-term extensional strain within the Afar rift is driven by the movement of the Arabian plate away from the Nubian plate at rates of up to 18-20 mm/yr (McClusky et al., 2010, ArRajehi et al., 2010, Viltres et al., 2020), with a gradual transfer of extension between $\sim$ 13-16°N from the southern RSR onto spreading segments in northern Afar (Figure

4.1a). The onset of rifting in Afar is marked by voluminous flood basalts at $\sim$ 30 Ma, initiated by a mantle plume situated beneath the region (Wolfenden et al., 2005, Furman et al., 2006, Rooney et al., 2012). Present day extension is largely accommodated within discrete magmatic spreading segments in northern and central Afar, linked by amagmatic shear zones (La Rosa et al., 2019, Illsley-Kemp et al., 2018a), and across a broad sequence of amagmatic faults in southern Afar (Moore et al., in review, Doubre et al., 2017, Pagli et al., 2014), with a general increase in strain localisation with rift development (Hayward and Ebinger, 1996, Wolfenden et al., 2005, Moore et al., in review).

The crust beneath the Afar rift is in a transitional state between continental and oceanic crust. Extensive thinning has resulted in a crustal thickness of 15-30 km in central Afar, compared to 20-45 km beneath the Ethiopian plateau (Tiberi et al., 2005, Hammond et al., 2011, Bastow and Keir, 2011), with significant alteration from magmatic intrusions beneath spreading segments (Stork et al., 2013, Hammond, 2014, Hammond and Kendall, 2016). Elevated mantle temperatures allow partial melting below a 60-80 km thick lithospheric lid (Ferguson et al., 2013). Seismicity and magnetotelluric surveys suggest that beneath the Dabbahu-Manda-Hararo (DMHVS) and Erta 'Ale (EAVS) spreading segments, this melt may be stored in large reservoirs at the base of the crust (Stork et al., 2013, Desissa et al., 2013, Illsley-Kemp et al., 2018b). Sequences of stacked sills may then provide the plumbing system to sustain long-lived volcanism below volcanic centres such as Dabbahu (Field et al., 2013) and Erta 'Ale (Moore et al., 2019, Xu et al., 2020). Several volcanic centres may also interact during large rifting events in Afar, such as during the 2005-10 DMHVS rifting episode where melt was sourced from reservoirs at Gabho, Dabbahu, and Ado 'Ale (Ayele et al., 2009, Grandin et al., 2009, Hamling et al., 2010).

4.2.2 Major Rifting Events

Several small basaltic eruptions and intrusions at volcanic centres have been recently observed in Afar using satellite geodesy (e.g. Amelung et al., 2000, Nobile et al., 2012, Field et al., 2012, Pagli et al., 2012, Xu et al., 2017). In Afar, and in other rift zones, larger rifting events are less frequent, and typically involve repeated intrusions over the course of several years. The recent examples of such events include the 1975-84 Krafla rifting episode in the northern volcanic zone (NVZ) of Iceland, and the 2005-10 DMHVS rifting episode in Afar, with the 2005-10 DMHVS event being the first to be fully observed using InSAR (Wright et al., 2012). Other notable rifting events include the 1978 Asal-Ghoubbet eruption in Afar (Allard et al., 1979, Cattin et al., 2005), and the 2014-15 Bardarbunga-Holuhraun eruption in Iceland (Sigmundsson et al., 2014, Gudmundsson et al., 2016).

The 1975-84 rifting episode at Krafla consisted of ∼ 20 dyke intrusions, the largest of which was the initial ∼ 60 km long intrusion in December 1975 (Björnsson et al., 1977). Co-dyking subsidence at the Krafla caldera indicated that the intrusions were linked to the magma reservoir at 3-5 km depth beneath the caldera (Einarsson, 1978, Brandsdóttir et al., 1997). The composition of the erupted lavas away from the caldera indicated that melt sourced from the base of the crust replenished shallow reservoirs during the rifting episode (Tryggvason, 1986, Árnadóttir et al., 1998), in agreement with a deep source of inflation following the event (de Zeeuw-van Dalfsen et al., 2004).

The 2005-10 rifting episode at the DMHVS was also initiated in September 2005 by a ∼ 60 km long, 2.4-2.6 km^3 dyke intrusion (Wright et al., 2006, Ayele et al., 2007). 13

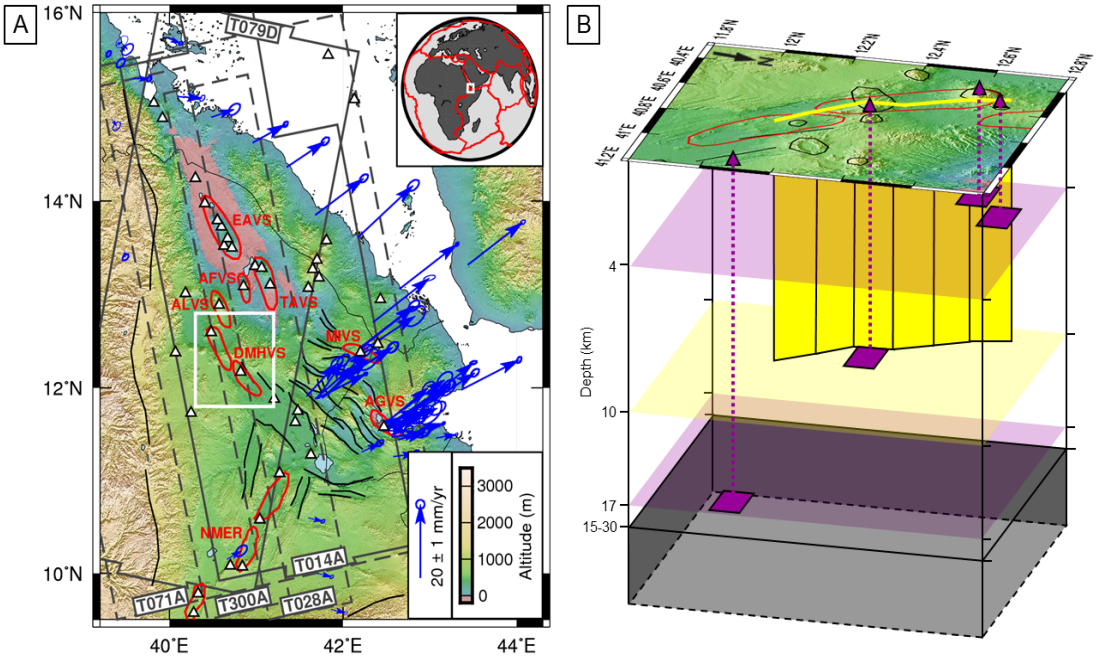

Figure 4.1: (A) Tectonic map of the Afar region with simplified rifting segments (red) and faults (black), volcanoes (white triangles), and long term GNSS velocities with error ellipses from King et al. (2019) (blue arrows) showing plate motions relative to the Nubian plate. Labelled volcanic segments: Erta 'Ale (EAVS), Tat 'Ale (TAVS), Afdera (AFVS), Alayta (ALVS), Dabbahu-Manda-Hararo (DMHVS), Manda-Inakir (MIVS), Asal-Ghoubbet (AGVS), Northern Main Ethiopian Rift (NMER). Solid grey outlines show the Sentinel-1 tracks (T014A, T079D) used while dashed grey outlines show the Envisat tracks (T071A, T300A, T028A) used. White outline indicates the region shown in (B). Inset map shows tectonic plate boundaries from Bird (2003) with the region in (A) in white. (B) 3D sketch (not to scale) of the subsurface structure below the Dabbahu-Manda-Hararo volcanic segment. Surface map view shows topography with volcanic centres indicated in black, the rift segment outlined in red, the location of active volcanic centres shown by purple triangles, and the surface expression of the initial 2005 dyke intrusion shown in yellow. The subsurface is split into regions elastic and viscoelastic (grey shading) rheology, with the boundary at 15-30 km depth (Hamling et al., 2014). The location and depth extent of planar dyke (yellow) and sill (purple) sources (Okada, 1985) in the subsurface are shown for the initial 2005 intrusion and active volcanic centres respectively, with depths from Hamling et al. (2014).

subsequent intrusions were focussed around the Ado 'Ale complex at the segment centre, with an initial deflation at the Dabbahu and Gabho volcanic centres at the northern end of the segment attributed to the contribution of melt from magma reservoirs at $\sim$ 4 km depth (Ayele et al., 2009, Grandin et al., 2010b, Hamling et al., 2010). A further source of deflation at $\sim$ 17 km depth at the southern end of the segment indicated that magma movement during the rifting episode occurred at depth throughout the crust (Grandin et al., 2010a, Hamling et al., 2014). Recent seismic (Stork et al., 2013, Hammond, 2014), magnetotelluric (Desissa et al., 2013), and gravity (Lewi et al., 2016) surveys also indicate the presence of significant partial melt at the base of the crust beneath the DMHVS.

4.2.3 Post-Intrusion Deformation Modelling

At volcanic centres and rift zones, the viscoelasticity of the crust and mantle can significantly influence the magnitude of surface deformation resulting from pressure sources at depth (Bürgmann and Dresen, 2008, Segall, 2019). Reduced crustal viscosities may be caused by elevated temperatures and the presence of partial melt within the crust. Various models of crustal structure and rheology have been applied to address this both at individual volcanic centres (e.g. Hamlyn et al., 2018, Yamasaki et al., 2018, Sigmundsson et al., 2020), and rift zones (e.g. Foulger et al., 1992, Pollitz and Sacks, 1996, Pedersen et al., 2009, Nooner et al., 2009, Hamling et al., 2014). Models of post-rift relaxation have typically made use of homogeneous elastic and viscoelastic regions, with a linear rheology (e.g. Nooner et al., 2009, Hamling et al., 2014), while in rift zones viscous regions may be both spatially and temporally variable (e.g. Pedersen et al., 2009), and non-linear stress dependant rheologies may also be applicable.

During the 2005-10 DMHVS episode, background uplift and extension rates of 80-240 mm/yr and 110-180 mm/yr respectively (Hamling et al., 2014, Pagli et al., 2014) were attributed to the post-rifting response from the initial 2005 intrusion. This signal has been modelled using a viscoelastic response (Nooner et al., 2009), magmatic sources (Grandin et al., 2010a), and the combination of viscoelastic and magmatic sources (Hamling et al., 2014). While InSAR observations accurately capture the spatial distribution of deformation, data has not previously been available to observe long-term post-rifting relaxation. Here, we combine the 2006-10 Envisat derived displacements from Pagli et al. (2014), with the 2014-19 Sentinel-1 derived displacements from Moore et al. (in review), to model viscoelastic relaxation and continued magma movement at the DMHVS over a period of $\sim$ 14 years.

4.3 Time Series & Modelling Methodology

4.3.1 InSAR Time Series

For our analysis, we use the InSAR line-of-sight (LOS) displacement time series for 2006-2010 processed by Pagli et al. (2014) for ascending Envisat tracks T028A, T071A, and T300A, and the LOS displacement time series for 2014-19 processed by Moore et al. (in review) for ascending Sentinel-1 track T014A and descending track T079D. Any significant atmospheric and noise signals have previously been removed from these datasets (Pagli et al., 2014, Moore et al., in review), with co-intrusive deformation associated with dyking during the 2005-10 rifting episode being removed from the Envisat time series using a cross-correlation technique (Pagli et al., 2014). As both of these datasets formed part of regional velocity maps, we subset the data to a $\sim 160\times160$ km area covering the DMHVS. We reference the displacement maps at each epoch to a single point, $\sim$ 50 km North of Dabbahu, which we assume is sufficient distance from the segment to be unaffected by the deformation. We then remove a planar ramp from each displacement map, to correct for any linear long-wavelength ground motions associated with the regional deformation field. We also reference displacements for each track to the first epoch of its time series. In order to reduce the computational load during modelling, we subsample the data to an even grid spacing of 10×10 km with a finer grid spacing of 5×5 km for points within 15 km of a deformation source.

4.3.2 Viscoelastic Model

The semi-analytic Fourier-domain solver Relax (Barbot and Fialko, 2010a,b) employs Green's functions to solve for displacements and stress in a half-space from various sources, and the time dependant deformation that follows due to the defined model rheology. Within Relax, we use a two-layer homogeneous elastic-viscoelastic model, with Maxwell rheology, to calculate deformation resulting from the elastic and viscous responses to the initial perturbation at each point on a $512\times512\times256$ km grid, with 1 km grid spacing in the East, North, and Vertical directions respectively. We calculate the displacement time series for a period of 15 years from September 2005, with time increments of 0.1 years, for the 14 successive dyke intrusions associated with the 2005-10 DMHVS rifting episode, and for four magmatic sources along the segment. As the co-intrusive displacements associated with dyking have been removed from the Envisat time series (Pagli et al., 2014), we use only the viscous relaxation deformation resulting from each of the 14 dyke intrusions between 2005 and 2010.

We assume the dyke sources are vertical planar dislocations with uniform opening (Okada, 1985), with the exception of the initial September 2005 intrusion, which we divide into six 10 km long segments extending from 1-10 km depth, following the

source used by Hamling et al. (2014). We take the approximate length, depth extent, and opening of 13 subsequent dykes from Grandin et al. (2010b) and Barnie et al. (2016). We use the magmatic source locations established by Grandin et al. (2010a) and Hamling et al. (2014), with magma reservoirs at 4 km depth beneath Gabho and Dabbahu, 10 km depth beneath Ado 'Ale, and 17 km depth below a Southern source of deformation at $\sim$ 40.85°E/12.1°N. We apply these as 5×5 km sill dislocations (Okada, 1985) with unit opening, in keeping with the Relax stability requirements of 5 grid nodes for each source edge. We do not use point sources (Mogi, 1958) as they can cause instability when the source is close to the elastic-viscoelastic boundary (S. Barbot, personal communication). Figure 4.1b shows a 3D visualisation of the model beneath the DMHVS, with the location of the dislocation sources, and an elastic lid overlaying a viscoelastic half-space. For the sill sources, we calculate displacement histories from 1 m of opening for each model setup, which we later use as Green's functions. The surface viscoelastic and viscous vertical displacement time series for unit opening of each of the sill sources are shown in Figure C.1 for an elastic lid thickness of 18 km and a viscosity of 10^{18} Pa s beneath the lid. To establish an optimum model of the subsurface structure, we vary the thickness of the elastic lid and the viscosity of the viscoelastic half-space between 14-30 km and $1\times10^{17-19}$ Pa s respectively, based around the values estimated by Hamling et al. (2014), using the depth averaged estimates of elastic parameters from Makris and Ginzburg (1987) and Tiberi et al. (2005).

In order to account for continued magma movement at the volcanic centres throughout post-rift relaxation, we develop an inverse model to solve for the opening of each sill at every epoch, using the Green's function responses for each of the sill sources. Setting out the problem as a linear least squares formulation, we convert the Relax model displacement maps for each source into the LOS for each InSAR track at each subsampled point in space, and interpolate the Relax model time series to correlate with the track acquisition dates. We include a constant dyke strength scaling factor, and also solve for constant displacement offset at each spatial point to account for residual noise in the first epoch of the InSAR time series. We find that evaluating the sill sources only at epochs where we have data coverage is sufficient as the viscous relaxation component of deformation from the sill sources is small in comparison to the initial elastic component, and the influence of these "missing" sources is small on the remainder of the displacement time series. We also include a Laplacian smoothing factor on the source time series ensure that the resulting model represents the long-term movement of magma within the DMHVS. This joint inversion of both the viscous response to dyking and viscoelastic response to magma movement represents a more robust approach to modelling deformation during post-rifting than previous models including Hamling et al. (2014), Grandin et al. (2010a), and Nooner et al. (2009), as it rigorously accounts for the relaxation of the magmatic sources in a self-consistent manner.

We apply this inversion to each of the model setups and calculate LOS residual misfits between the resulting displacement time series and the InSAR displacement time series for each track. Using these misfits, we calculate the spatial and temporal distribution of the root-mean-square-error (RMSE) of the misfits, by evaluating the spatial distribution of misfits at each epoch and the time series of misfits at each spatial point respectively (see Figure C.2). For each model setup, we then take the RMSE of these residual misfit distributions to produce a single LOS RMS misfit value for every track. The total RMS misfit value for each track is shown in Figure 4.2 for all the evaluated model setups, where we have refined distribution of models to explore the parameter space close to the minimum RMS misfit value.

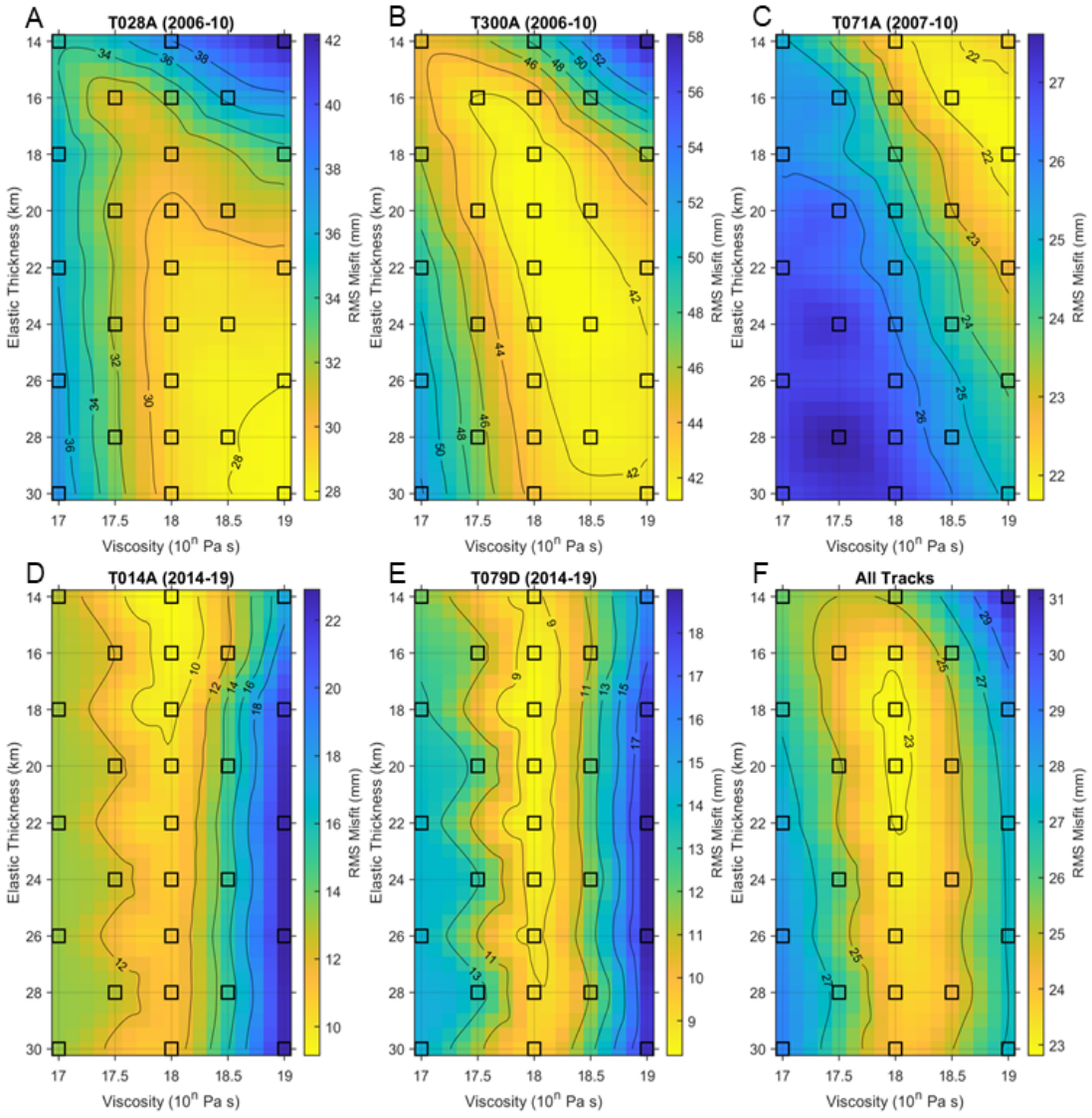

Figure 4.2: The distribution of model RMSE with model rheology for the time period of LOS observations covered by each track. RMSE values for each model setup (black squares) are linearly interpolated to produce the smooth background field, and contoured to aid interpretation. RMSE values in (F) for all tracks show the mean values from (A-E).

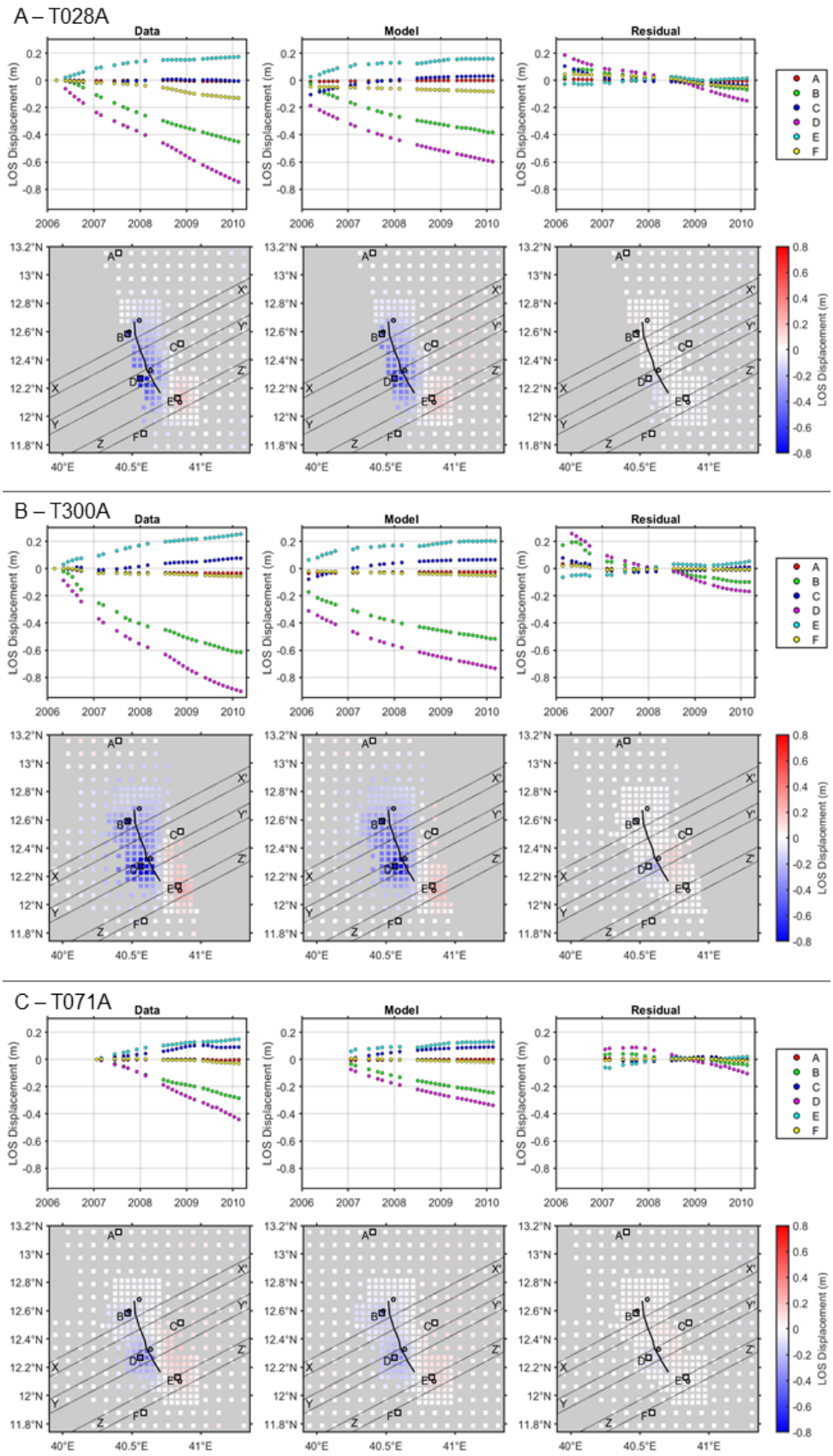
A – T028A
B – T300A
C – T071A
Data
Model
Residual
LOS Displacement (m)
2006
2007
2008
2009
2010
13.2°N
13°N
12.8°N
12.6°N
12.4°N
12.2°N
12°N
11.8°N
40°E
40.5°E
41°E
A
B
C
D
E
F
X
X'
Y
Y'
Z
Z'
0.8
0.6
0.4
0.2
0
-0.2
-0.4
-0.6
-0.8

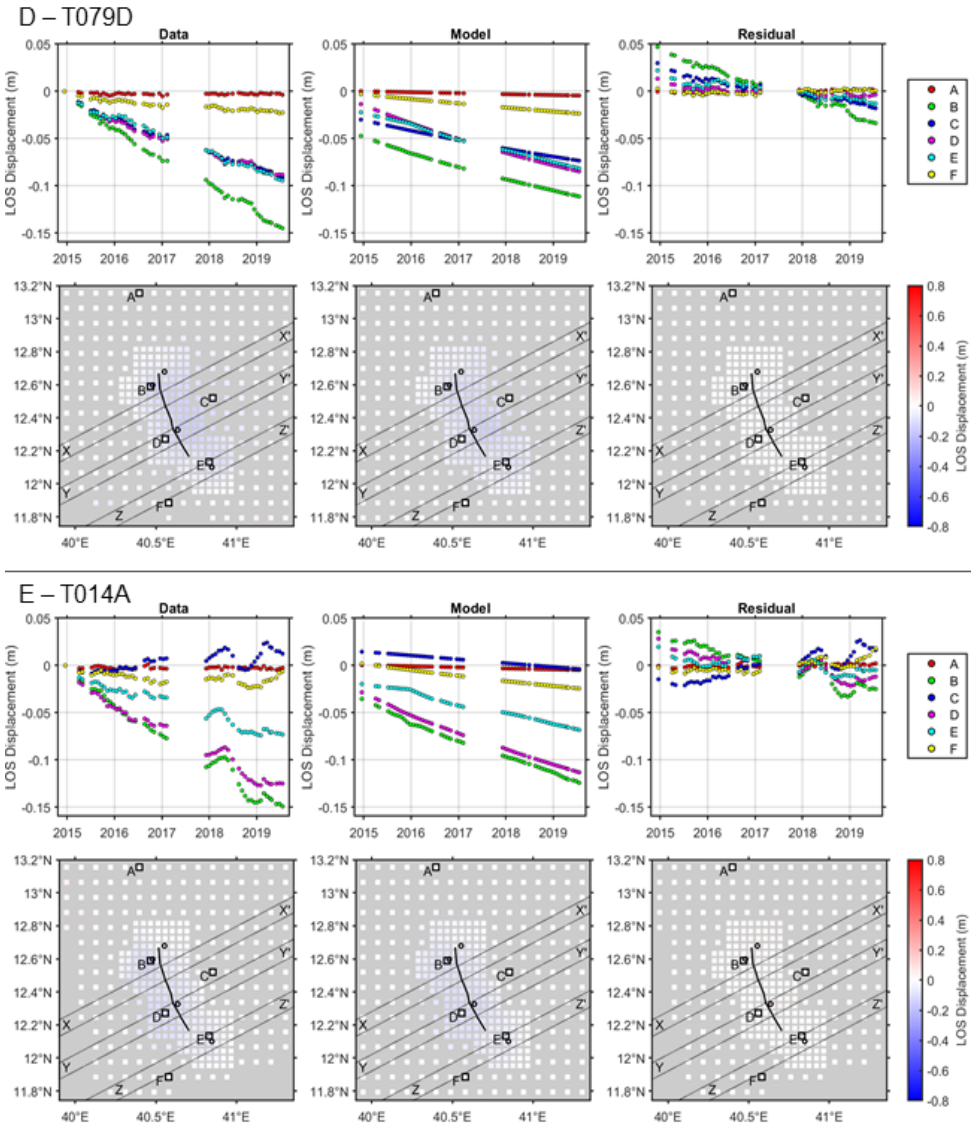

Figure 4.3: The data, model, and residual of LOS displacements for each track. Model displacements are taken from the optimal model of an 18 km elastic lid thickness above a layer with a viscosity of 10^{18} Pa s. Map views show the cumulative deformation at the end of each track's time period. Surface trace of the September 2005 dyke is shown as a black solid line, with sill sources below Dabbahu, Gabho, Ado 'Ale, and the Southern sources are marked as black circles. Time series points A-F are marked in map view as black squares, with black dotted lines indicating the location of profiles shown in Figure 4.4.

4.4 Analysis & Discussion

For the entire period 2006-2019, we find that the best fit model of the subsurface structure below the DMHVS consists of an elastic lid thickness of 17-22 km and a viscosity of $10^{17.75}$-$10^{18.25}$ Pa s (0.6-1.8 $\times 10^{18}$ Pa s) in the viscoelastic half-space, as shown in Figure 4.2f as the region with an RMS misfit of $\lesssim$ 23 mm. This is in strong agreement with the model of Hamling et al. (2014), and models from other subaerial

rift zones (Foulger et al., 1992, Pollitz and Sacks, 1996, Pedersen et al., 2009, Nooner et al., 2009). Figure 4.2 also shows how the best-fit solutions vary with the time window of observations. T028A and T300A give broadly similar optimum parameters with an elastic thickness of ∼ 20-30 km and a viscosity of 10^{18}-10^{19} Pa s for the period 2006-10, rejecting models with stiffer rheologies and thin elastic lids. T071A shows a different distribution of optimum models for the period 2007-10 to those for 2006-10 (T028A, T300A). This change is likely due to the significant amount of deformation recorded in 2006 as a result of the initial 2005 intrusion, which is not included in the time series for T071A (see Figure 4.3c). The more linear displacement rates for 2007-10 produce the preferred models of a ∼ 14-18 km elastic lid thickness and a viscosity of $10^{18.5}$-10^{19} Pa s. This preference shifts for the period 2014-19 (T014A, T070D) to allow a thinner elastic lid with thickness of ∼ 14-26 km, but with a much tighter constraint on viscosity around 10^{18} Pa s. This decrease in the preferred viscosity through time is the opposite of the trend following earthquakes, where viscosity is typically inferred to increase during the post-seismic period (e.g. Ryder et al., 2007, Weiss et al., 2019), although the apparent decrease here is within error bounds. A decrease in the viscosity of the sub-surface could be caused by the presence of melt bodies in the lower crust and upper mantle intruded following the DMHVZ rifting episode, while during the rifting episode melt sourced from depth was erupted rather than intruded.

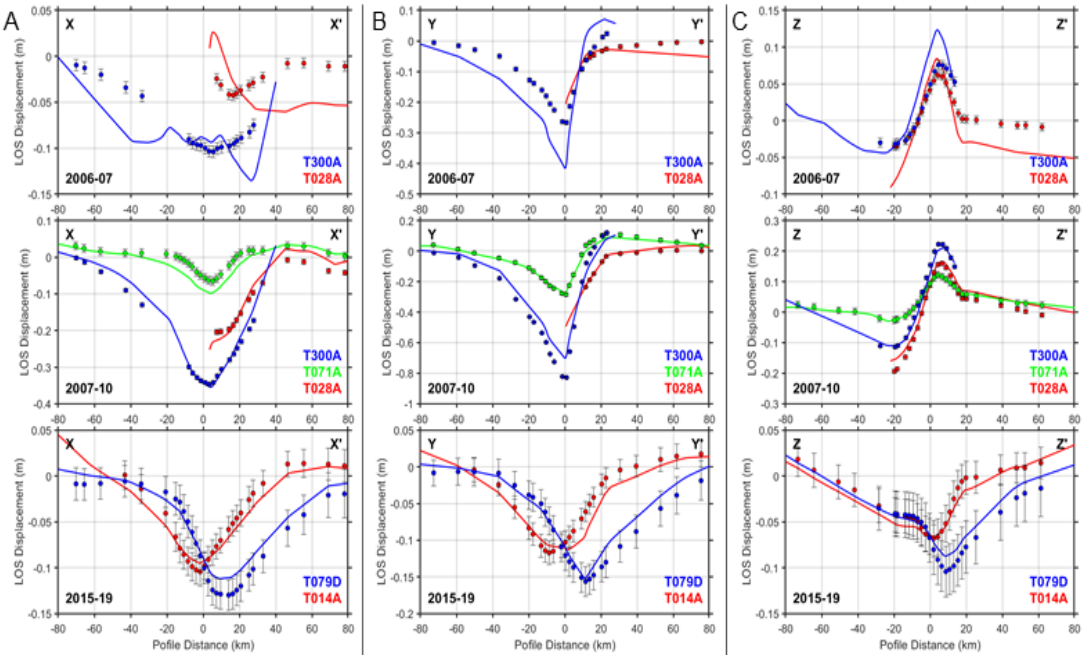

Figure 4.4: Cross-rift profiles showing LOS data (circles with error bars) and model (solid lines) displacements from the optimal model of an 18 km elastic lid thickness above a layer with a viscosity of 10^{18} Pa s. Profiles show the cumulative displacement from the time periods indicated, and include the tracks with data coverage in these periods (colours indicated on each). The location of the profiles X-Z are shown in Figure 4.3. Zero distance indicates where the profile intersects the DMHVS, with positive profile distance towards the NE.

Figure 4.3 shows the cumulative LOS displacement maps and time series for the optimal model of an 18 km thick elastic lid and a viscosity of 10^{18} Pa s, in the LOS of each track. The model residual misfits are also shown in Figure 4.3, with RMS misfit values at each point in space and at every epoch shown in Figure C.2. The displacement maps show that the model has a good spatial fit to the data, with small residuals focussed around the region of peak deformation (point D). All models underestimate the magnitude of the post-rift deformation during 2006, giving rise to the offsets in the time series shown in Figure 4.3. While lower viscosities may be able to replicate these high strain rates, in order to fit the whole deformation time series from 2006-10, our models require higher values of $\sim 10^{18}$ Pa s. This may be indicative that a non-linear rheology may be able to better represent the full deformation time series during the DMHVS rifting episode.

The range of model fits for all time series points (A-F) in Figure 4.3 are shown in Figure C.4. Points away from the majority of deformation (A, C, F) indicate good agreement in the far-field, away from the segment. The time series misfits at points over the Gabho and Southern volcanic sources (B, E) are also generally small as the deformation here is dominated by the time variable opening of the sill sources. Cross-rift profiles X-Z (Figure 4.4) show the spatial fit to data within the 2006-07, 2007-10, and 2014-19 time windows, where we selected time steps based on track data coverage. Profiles X and Y traverse the main LOS range-shortening signal, with Profile Y covering the peak of deformation and the Ado 'Ale magmatic source. Our overall best-fit model gives a good fit to data in the later post-rifting periods of 2007-10 and 2014-19, with a weaker fit in the earlier 2006-07 period, which may be a result of simplifications in the model setup. As we model each track displacement time series as a whole, the viscosity of the viscoelastic layer remains constant for each track time period, while a variation of viscosity through time, or a non-linear rheology may improve the fit to the deformation time series. As rift segments also likely consist of intrusions and partial melt reservoirs, spatial variations in viscosity, with lower values close to the segment, may also improve the model performance.

Profile Z (Figure 4.4c) and time series point E (Figure 4.3) describe the surface displacements from the Southern source which changes from LOS range-lengthening (apparent subsidence) from 2006-10, to LOS range-shortening (apparent uplift) from 2014-19. Deformation here is controlled by magma movement beneath the DMHVS which we resolve as the volume change of each sill source at every epoch (see Figure C.3). Table C.1 shows the cumulative sill volume changes for each source and every model setup for the time periods 2006-10 and 2014-19. Using the models with low RMS misfit values (see Figure 4.2), we identify that the Southern source requires a deflation of -2.8 $\pm$ 0.8$\times 10^8$ m^3 for the period 2006-10 and a volume change of 0.0 $\pm$ 0.4$\times 10^8$ m^3

from 2014-19, indicating that apparent surface uplift between 2014-19 may be a result of either sill inflation, or the long-term viscous response to previous sill deflation from 2006-10. This agrees well with Hamling et al. (2014), who estimate a volume change of -2.8 ± 2.0×10^8 m^3 for 2006-10. We also find that the Ado 'Ale source requires a persistent inflation of 0.5 ± 0.1×10^8 m^3 from 2006-19, while cumulative volume changes at the Dabbahu and Gabho volcanic centres are small with magnitudes of up to ± 0.2×10^8 m^3 from 2006-19. Hamling et al. (2014) estimate a significantly larger volume change for 2006-10 at the 10 km deep Ado 'Ale source of 4.70 ± 0.08×10^8 m^3, which may be a result of the differing inversion methodologies, or our inclusion of 13 additional dyke intrusions between 2006-10 while Hamling et al. (2014) use only the initial 2005 intrusion. We find that magmatic activity at the shallow Dabbahu and Gabho volcanic centres is generally limited to the early portion of the time series (2006-07), consistent with their contribution to the initial magmatic intrusion in 2005 (Wright et al., 2006, Ayele et al., 2009). The Ado 'Ale and Southern sources show continued activity throughout the post-rifting period, suggesting that magmatic sources at the base of the crust on the DMHVS may remain connected by a larger body of partial melt. Seismic (Stork et al., 2013, Hammond, 2014), magnetotelluric (Desissa et al., 2013), and gravity studies (Lewi et al., 2016) on the DMHVS have also previously predicted the presence of a large body of partial melt beneath whole segment, with the centre located ∼ 10-30 km off axis to the SW of the segment centre and at a depth of ∼ 20 km.

4.5 Conclusions

We combine the 2006-10 (Pagli et al., 2014) and 2014-19 (Moore et al., in review) InSAR time series of ground motions to model the long-term post-rifting deformation at the DMHVS in central Afar, accounting for viscous relaxation and continued magma movement. We calculate responses from the 2005-10 dyke intrusions and four magmatic sources using a two-layer elastic-viscoelastic model, varying the elastic lid thickness and the viscosity of the viscoelastic half-space. Using sill sources as Green's functions we jointly invert for the time variable volume change at each sill source and the magnitude of the viscous response.

For the period 2006-19, we find that the best-fit models have elastic thicknesses of 17-22 km, and viscosities of 0.6-1.8 ×10^{18} Pa s. The preferred model viscosities suggest a slight decrease during the post-rifting period from 10^{18}-10^{19} Pa s from 2006-10 to ∼ 10^{18} Pa s from 2014-19, which may indicate a change from extrusive magmatism during the 2005-10 DMHVS rifting episode, to intrusive magmatism in the lower crust and upper mantle during the post-rift period. We also find that the best-fit models require a continued inflation at 10 km depth below the segment centre of 0.5 ± 0.1×10^8 m^3

from 2006-19, and a deflation of -2.8 ± 0.8×10^8 m^3 at 17 km depth below the Southern end of the segment for the period 2006-10 with a volume change of 0.0 ± 0.4×10^8 m^3 from 2014-19. Long-term activity at these deeper sources emphasises the roles of both viscous relaxation and continued magma movement during post-rifting at spreading segments.

4.6 Acknowledgements

We would like to thank Carolina Pagli for the use of the 2006-10 Envisat derived InSAR time series in this study. The Envisat SAR data used are copyright to the European Space Agency from CAT 1 3435. All Envisat interferograms are archived at the University of Leeds (contact T.J.Wright@leeds.ac.uk). All Sentinel-1 data is sourced from the European Union Copernicus Programme, and was processed on the JASMIN facility, operated by the Centre for Environmental Data Analysis (CEDA). Sentinel-1 interferograms used here are available in the CEDA archive (`http://archive.ceda.ac.uk`) here: `http://data.ceda.ac.uk/neodc/comet/data/licsarproducts`. Forward models were run using the open-source code Relax, with inverse modelling and figure generation in Matlab and GMT. This work was funded by the NERC RiftVolc project (NE/L013649/1), and supported by the Centre for Observation and Modelling of Earthquakes, Volcanoes, and Tectonics (COMET).

References

Allard, P., Tazieff, H. and Dajlevic, D. (1979). Observations of seafloor spreading in Afar during the November 1978 fissure eruption. *Nature*, **279**(5708), pp. 30–33. doi:10.1038/279030a0. 4.2.2

Amelung, F., Oppenheimer, C., Segall, P. and Zebker, H. (2000). Ground deformation near Gada 'Ale volcano, Afar, observed by radar interferometry. *Geophysical Research Letters*, **27**(19), pp. 3093–3096. doi:10.1029/2000GL008497. 4.2.2

Árnadóttir, T., Sigmundsson, F. and Delaney, P. T. (1998). Sources of crustal deformation associated with the Krafla, Iceland, eruption of September 1984. *Geophysical research letters*, **25**(7), pp. 1043–1046. 4.2.2

ArRajehi, A., McClusky, S., Reilinger, R., Daoud, M., Alchalbi, A., Ergintav, S., Gomez, F., Sholan, J., Bou-Rabee, F., Ogubazghi, G., Haileab, B., Fisseha, S., Asfaw, L., Mahmoud, S., Rayan, A., Bendik, R. and Kogan, L. (2010). Geodetic constraints on present-day motion of the Arabian Plate: Implications for Red Sea and Gulf of Aden rifting. *Tectonics*, **29**(TC3011). doi:10.1029/2009TC002482. 4.2.1

Ayele, A., Jacques, E., Kassim, M., Kidane, T., Omar, A., Tait, S., Nercessian, A., de Chabalier, J. B. and King, G. (2007). The volcano-seismic crisis in Afar, Ethiopia, starting September 2005. *Earth and Planetary Science Letters*, **255**, pp. 177–187. doi:10.1016/j.epsl.2006.12.014. 4.2.2

Ayele, A., Keir, D., Ebinger, C., Wright, T. J., Stuart, G. W., Buck, W. R., Jacques, E., Ogubazghi, G. and Sholan, J. (2009). September 2005 mega-dike emplacement in the Manda-Harraro nascent oceanic rift (Afar depression). *Geophysical Research Letters*, **36**(L20306). doi:10.1029/2009GL039605. 4.2.1, 4.2.2, 4.4

Barbot, S. and Fialko, Y. (2010a). Fourier-domain Green's function for an elastic semi-infinite solid under gravity, with applications to earthquake and volcano deformation. *Geophysical Journal International*, **182**(2), pp. 568–582. 4.3.2

Barbot, S. and Fialko, Y. (2010b). A unified continuum representation of post-seismic relaxation mechanisms: semi-analytic models of afterslip, poroelastic rebound and viscoelastic flow. *Geophysical Journal International*, **182**(3), pp. 1124–1140. 4.3.2

Barnie, T. D., Keir, D., Hamling, I., Hofmann, B., Belachew, M., Carn, S., Eastwell, D., Hammond, J. O. S., Ayele, A., Oppenheimer, C. and Wright, T. (2016). A multidisciplinary study of the final episode of the Manda Hararo dyke sequence, Ethiopia, and implications for trends in volcanism during the rifting cycle. *Geological Society, London, Special Publications*, **420**, pp. 149–163. doi:10.1144/SP420.6. 4.3.2

Bastow, I. D. and Keir, D. (2011). The protracted development of the continent-ocean transition in Afar. *Nature Geoscience*, **4**(4), pp. 248–250. doi:10.1038/ngeo1095. 4.2.1

Bird, P. (2003). An updated digital model of plate boundaries. *Geochemistry, Geophysics, Geosystems*, **4**(3). doi:10.1029/2001GC000252. 4.1

Björnsson, A., Saemundsson, K., Einarsson, P., Tryggvason, E. and Grönvold, K. (1977). Current rifting episode in north Iceland. *Nature*, **266**(5600), pp. 318–323. 4.2.2

Brandsdóttir, B., Menke, W., Einarsson, P., White, R. S. and Staples, R. K. (1997). Færoe-Iceland ridge experiment 2. Crustal structure of the Krafla central volcano. *Journal of Geophysical Research: Solid Earth*, **102**(B4), pp. 7867–7886. 4.2.2

Bürgmann, R. and Dresen, G. (2008). Rheology of the Lower Crust and Upper Mantle: Evidence from Rock Mechanics, Geodesy, and Field Observations. *Annual Review of Earth and Planetary Sciences*, **36**(1), pp. 531–567. doi:10.1146/annurev.earth.36.031207.124326. 4.2.3

Cattin, R., Doubre, C., de Chabalier, J. B., King, G., Vigny, C., Avouac, J. P. and Ruegg, J. C. (2005). Numerical modelling of quaternary deformation and post-rifting displacement in the Asal-Ghoubbet rift (Djibouti, Africa). *Earth and Planetary Science Letters*, **239**(3-4), pp. 352–367. doi:10.1016/j.epsl.2005.07.028. 4.2, 4.2.2

de Zeeuw-van Dalfsen, E., Pedersen, R., Sigmundsson, F. and Pagli, C. (2004). Satellite radar interferometry 1993–1999 suggests deep accumulation of magma near the crust-mantle boundary at the Krafla volcanic system, Iceland. *Geophysical Research Letters*, **31**(13). 4.2.2

Desissa, M., Johnson, N. E., Whaler, K. A., Hautot, S., Fisseha, S. and Dawes, G. J. (2013). A mantle magma reservoir beneath an incipient mid-ocean ridge in Afar, Ethiopia. *Nature Geoscience*, **6**(10), pp. 861–865. doi:10.1038/ngeo1925. 4.2.1, 4.2.2, 4.4

Doubre, C., Déprez, A., Masson, F., Socquet, A., Lewi, E., Grandin, R., Nercessian, A., Ulrich, P., De Chabalier, J. B., Saad, I., Abayazid, A., Peltzer, G., Delorme, A., Calais, E. and Wright, T. (2017). Current deformation in Central Afar and triple junction kinematics deduced from GPS and InSAR measurements. *Geophysical Journal International*, **208**, pp. 936–953. doi:10.1093/gji/ggw434. 4.2, 4.2.1

Doubre, C. and Peltzer, G. (2007). Fluid-controlled faulting process in the Asal Rift, Djibouti, from 8 yr of radar interferometry observations. *Geology*, **35**(1), pp. 69–72. doi:10.1130/G23022A.1. 4.2

Ebinger, C. J. (2005). Continental break-up: the East African perspective. *Astronomy & Geophysics*, **46**(2), pp. 2–16. 4.2

Einarsson, P. (1978). S-wave shadows in the Krafla caldera in NE-Iceland, evidence for a magma chamber in the crust. *Bulletin Volcanologique*, **41**(3), pp. 187–195. 4.2.2

Ferguson, D. J., MacLennan, J., Bastow, I. D., Pyle, D. M., Jones, S. M., Keir, D., Blundy, J. D., Plank, T. and Yirgu, G. (2013). Melting during late-stage rifting in Afar is hot and deep. *Nature*, **499**(7456), pp. 70–73. doi:10.1038/nature12292. 4.2.1

Field, L., Blundy, J., Brooker, R. A., Wright, T. and Yirgu, G. (2012). Magma storage conditions beneath Dabbahu Volcano (Ethiopia) constrained by petrology, seismicity and satellite geodesy. *Bulletin of Volcanology*, **74**, pp. 981–1004. doi:10.1007/s00445-012-0580-6. 4.2.2

Field, L., Blundy, J., Calvert, A. and Yirgu, G. (2013). Magmatic history of Dabbahu, a composite volcano in the Afar Rift, Ethiopia. *Bulletin of the Geological Society of America*, **125**(1/2), pp. 128–147. doi:10.1130/B30560.1. 4.2.1

Foulger, G. R., Jahn, C.-H., Seeber, G., Einarsson, P., Julian, B. R. and Heki, K. (1992). Post-rifting stress relaxation at the divergent plate boundary in Northeast Iceland. *Nature*, **358**(6386), pp. 488–490. doi:10.1038/358488a0. 4.2, 4.2.3, 4.4

Furman, T., Bryce, J., Rooney, T., Hanan, B., Yirgu, G. and Ayalew, D. (2006). Heads and tails: 30 million years of the Afar plume. *Geological Society, London, Special Publications*, **259**, pp. 95–119. doi:10.1144/GSL.SP.2006.259.01.09. 4.2.1

Grandin, R., Socquet, A., Binet, R., Klinger, Y., Jacques, E., De Chabalier, J. B., King, G. C., Lasserre, C., Tait, S., Tapponnier, P., Delorme, A. and Pinzuti, P. (2009). September 2005 Manda hararo-dabbahu rifting event, Afar (Ethiopia): Constraints provided by geodetic data. *Journal of Geophysical Research: Solid Earth*, **114**(B08404). doi:10.1029/2008JB005843. 4.2.1

Grandin, R., Socquet, A., Doin, M. P., Jacques, E., De Chabalier, J. B. and King, G. C. (2010a). Transient rift opening in response to multiple dike injections in the Manda Hararo rift (Afar, Ethiopia) imaged by time-dependent elastic inversion of interferometric synthetic aperture radar data. *Journal of Geophysical Research: Solid Earth*, **115**(B09403). doi:10.1029/2009JB006883. 4.2, 4.2.2, 4.2.3, 4.3.2, 4.3.2

Grandin, R., Socquet, A., Jacques, E., Mazzoni, N., de Chabalier, J.-B. and King, G. (2010b). Sequence of rifting in Afar, Manda-Hararo rift, Ethiopia, 2005–2009: Time-space evolution and interactions between dikes from interferometric synthetic aperture radar and static stress change modeling. *Journal of Geophysical Research: Solid Earth*, **115**(B10). 4.2.2, 4.3.2

Gudmundsson, M. T., Jónsdóttir, K., Hooper, A., Holohan, E. P., Halldórsson, S. A., Ófeigsson, B. G., Cesca, S., Vogfjörd, K. S., Sigmundsson, F., Högnadóttir, T., Einarsson, P., Sigmarsson, O., Jarosch, A. H., Jónasson, K., Magnússon, E., Hreinsdóttir, S., Bagnardi, M., Parks, M. M., Hjörleifsdóttir, V., Pálsson, F., Walter, T. R., Schöpfer, M. P., Heimann, S., Reynolds, H. I., Dumont, S., Bali, E., Gudfinnsson, G. H., Dahm, T., Roberts, M. J., Hensch, M., Belart, J. M., Spaans, K., Jakobsson, S., Gudmundsson, G. B., Fridriksdóttir, H. M., Drouin, V., Dürig, T., Adalgeirsdóttir, G., Riishuus, M. S., Pedersen, G. B., Van Boeckel, T., Oddsson, B., Pfeffer, M. A., Barsotti, S., Bergsson, B., Donovan, A., Burton, M. R. and Aiuppa, A. (2016). Gradual caldera collapse at Bárdarbunga volcano, Iceland, regulated by lateral magma outflow. *Science*, **353**(6296). doi:10.1126/science.aaf8988. 4.2.2

Hamling, I. J., Wright, T. J., Calais, E., Bennati, L. and Lewi, E. (2010). Stress transfer between thirteen successive dyke intrusions in Ethiopia. *Nature Geoscience*, **3**(10), pp. 713–717. doi:10.1038/ngeo967. 4.2.1, 4.2.2

Hamling, I. J., Wright, T. J., Calais, E., Lewi, E. and Fukahata, Y. (2014). InSAR observations of post-rifting deformation around the Dabbahu rift segment, Afar, Ethiopia. *Geophysical Journal International*, **197**, pp. 33–49. doi:10.1093/gji/ggu003. 4.2, 4.1, 4.2.2, 4.2.3, 4.2.3, 4.3.2, 4.3.2, 4.4, 4.4

Hamlyn, J., Wright, T., Walters, R., Pagli, C., Sansosti, E., Casu, F., Pepe, S., Edmonds, M., Kilbride, B. M., Keir, D. et al. (2018). What causes subsidence following the 2011 eruption at Nabro (Eritrea)? *Progress in Earth and Planetary Science*, **5**(1), p. 31. 4.2.3

Hammond, J. O. S. (2014). Constraining melt geometries beneath the Afar Depression, Ethiopia from teleseismic receiver functions: The anisotropic H-κ stacking technique. *Geochemistry, Geophysics, Geosystems*, **15**(4), pp. 1316–1332. 4.2.1, 4.2.2, 4.4

Hammond, J. O. S. and Kendall, J. M. (2016). Constraints on melt distribution from seismology: a case study in Ethiopia. *Geological Society, London, Special Publications*, **420**, pp. 127–147. doi:10.1144/SP420.14. 4.2.1

Hammond, J. O. S., Kendall, J. M., Stuart, G. W., Keir, D., Ebinger, C., Ayele, A. and Belachew, M. (2011). The nature of the crust beneath the Afar triple junction: Evidence from receiver functions. *Geochemistry, Geophysics, Geosystems*, **12**(12). doi:10.1029/2011GC003738. 4.2.1

Hayward, N. J. and Ebinger, C. J. (1996). Variations in the along-axis segmentation of the Afar Rift system. *Tectonics*, **15**(2), pp. 244–257. doi:10.1029/95TC02292. 4.2.1

Illsley-Kemp, F., Bull, J., Keir, D., Gerya, T., Pagli, C., Gernon, T., Ayele, A., Goitom, B., Hammond, J. O. and Kendall, J. (2018a). Initiation of a proto-transform fault prior to seafloor spreading. *Geochemistry, Geophysics, Geosystems*, **19**(12), pp. 4744–4756. 4.2.1

Illsley-Kemp, F., Keir, D., Bull, J. M., Gernon, T. M., Ebinger, C., Ayele, A., Hammond, J. O., Kendall, J. M., Goitom, B. and Belachew, M. (2018b). Seismicity during continental breakup in the Red Sea Rift of Northern Afar. *Journal of Geophysical Research: Solid Earth*, **123**, pp. 2345–2362. doi:10.1002/2017JB014902. 4.2.1

Kendall, J. M., Stuart, G. W., Ebinger, C. J., Bastow, I. D. and Keir, D. (2005). Magma-assisted rifting in Ethiopia. *Nature*, **433**(7022), pp. 146–148. doi:10.1038/nature03161. 4.2

King, R., Floyd, M., Reilinger, R. and Bendick, R. (2019). GPS velocity field (MIT 2019.0) for the East African Rift System generated by King et al.. Interdisciplinary Earth Data Alliance (IEDA). *Accessed on 20 Sep 2019*. doi:10.1594/IEDA/324785. 4.1

La Rosa, A., Pagli, C., Keir, D., Sani, F., Corti, G., Wang, H. and Possee, D. (2019). Observing oblique slip during rift linkage in northern Afar. *Geophysical Research Letters*, **46**(19), pp. 10782–10790. 4.2.1

Lewi, E., Keir, D., Birhanu, Y., Blundy, J., Stuart, G., Wright, T. and Calais, E. (2016). Use of a high-precision gravity survey to understand the formation of oceanic crust and the role of melt at the southern Red Sea rift in Afar, Ethiopia. *Geological Society, London, Special Publications*, **420**, pp. 165–180. doi:10.1144/SP420.13. 4.2.2, 4.4

Makris, J. and Ginzburg, A. (1987). The Afar Depression: transition between continental rifting and sea-floor spreading. *Tectonophysics*, **141**(1-3), pp. 199–214. doi:10.1016/0040-1951(87)90186-7. 4.3.2

McClusky, S., Reilinger, R., Ogubazghi, G., Amleson, A., Healeb, B., Vernant, P., Sholan, J., Fisseha, S., Asfaw, L., Bendick, R. and Kogan, L. (2010). Kinematics of the southern Red Sea-Afar Triple Junction and implications for plate dynamics. *Geophysical Research Letters*, **37**(L05301). doi:10.1029/2009GL041127. 4.2.1

Mogi, K. (1958). Relations between the Eruptions of Various Volcanoes and the Defomormations of the Ground Surfaces around them. *Bulletin of the Earthquake Research Institute*, **36**, pp. 99–134. 4.3.2

Moore, C., Wright, T. J. and Hooper, A. (in review). Rift Focussing and Magmatism During Late-Stage Rifting in Afar, Ethiopia. *Earth and Space Science Open Archive*, pp. 1–19. doi:10.1002/essoar.10503895.1. 4.2, 4.2.1, 4.2.3, 4.3.1, 4.5

Moore, C., Wright, T., Hooper, A. and Biggs, J. (2019). The 2017 eruption of Erta 'Ale volcano, Ethiopia: Insights in the shallow axial plumbing system of an incipient mid-ocean ridge. *Geochemistry, Geophysics, Geosystems*, **20**(12). 4.2.1

Nobile, A., Pagli, C., Keir, D., Wright, T. J., Ayele, A., Ruch, J. and Acocella, V. (2012). Dike-fault interaction during the 2004 Dallol intrusion at the northern edge of the Erta Ale Ridge (Afar, Ethiopia). *Geophysical Research Letters*, **39**(L19305). doi:10.1029/2012GL053152. 4.2.2

Nooner, S. L., Bennati, L., Calais, E., Buck, W. R., Hamling, I. J., Wright, T. J. and Lewi, E. (2009). Post-rifting relaxation in the Afar region, Ethiopia. *Geophysical Research Letters*, **36**(21). 4.2, 4.2.3, 4.2.3, 4.3.2, 4.4

Okada, Y. (1985). Surface deformation due to shear and tensile faults in a half-space. *Bulletin of the seismological society of America*, **75**(4), pp. 1135–1154. 4.1, 4.3.2

Pagli, C., Wang, H., Wright, T. J., Calais, E. and Lewi, E. (2014). Current plate boundary deformation of the Afar rift from a 3-D velocity field inversion of InSAR and GPS. *Journal of Geophysical Research: Solid Earth*, **119**, pp. 8562–8575. doi:10.1002/2014JB011391. 4.2.1, 4.2.3, 4.3.1, 4.3.2, 4.5

Pagli, C., Wright, T. J., Ebinger, C. J., Yun, S. H., Cann, J. R., Barnie, T. and Ayele, A. (2012). Shallow axial magma chamber at the slow-spreading Erta Ale Ridge. *Nature Geoscience*, **5**(4), pp. 284–288. doi:10.1038/ngeo1414. 4.2.2

Pedersen, R., Sigmundsson, F. and Masterlark, T. (2009). Rheologic controls on inter-rifting deformation of the Northern Volcanic Zone, Iceland. *Earth and Planetary Science Letters*, **281**(1-2), pp. 14–26. doi:10.1016/j.epsl.2009.02.003. 4.2, 4.2.3, 4.4

Pollitz, F. F. and Sacks, I. S. (1996). Viscosity structure beneath northeast Iceland. *Journal of Geophysical Research: Solid Earth*, **101**(B8), pp. 17771–17793. 4.2.3, 4.4

Rooney, T. O., Herzberg, C. and Bastow, I. D. (2012). Elevated mantle temperature beneath East Africa. *Geology*, **40**(1), pp. 27–30. doi:10.1130/G32382.1. 4.2.1

Ryder, I., Parsons, B., Wright, T. J. and Funning, G. J. (2007). Post-seismic motion following the 1997 Manyi (Tibet) earthquake: InSAR observations and modelling. *Geophysical Journal International*, **169**(3), pp. 1009–1027. 4.4

Segall, P. (2019). Magma chambers: what we can, and cannot, learn from volcano geodesy. *Philosophical Transactions of the Royal Society A*, **377**(2139), p. 20180158. 4.2.3

Sigmundsson, F., Hooper, A., Hreinsdóttir, S., Vogfjörd, K. S., Ófeigsson, B. G., Heimisson, E. R., Dumont, S., Parks, M., Spaans, K., Gudmundsson, G. B., Drouin, V., Árnadóttir, T., Jónsdóttir, K., Gudmundsson, M. T., Högnadóttir, T., Fridriksdóttir, H. M., Hensch, M., Einarsson, P., Magnússon, E., Samsonov, S., Brandsdóttir, B., White, R. S., Ágústsdóttir, T., Greenfield, T., Green, R. G., Hjartardóttir, Á. R., Pedersen, R., Bennett, R. A., Geirsson, H., la Femina, P. C., Björnsson, H., Pálsson, F., Sturkell, E., Bean, C. J., Möllhoff, M., Braiden, A. K. and Eibl, E. P. (2014). Segmented lateral dyke growth in a rifting event at Bárðarbunga volcanic system, Iceland. *Nature*, **517**(7533). doi:10.1038/nature14111. 4.2.2

Sigmundsson, F., Pinel, V., Grapenthin, R., Hooper, A., Halldórsson, S. A., Einarsson, P., Ófeigsson, B. G., Heimisson, E. R., Jónsdóttir, K., Gudmundsson, M. T. et al. (2020). Unexpected large eruptions from buoyant magma bodies within viscoelastic crust. *Nature communications*, **11**(1), pp. 1–11. 4.2.3

Sigmundsson, F., Vadon, H. and Massonnet, D. (1997). Readjustment of the Krafla spreading segment to crustal rifting measured by satellite radar interferometry. *Geophysical Research Letters*, **24**(15), pp. 1843–1846. doi:10.1029/97GL01934. 4.2

Smittarello, D., Grandin, R., De Chabalier, J.-B., Doubre, C., Deprez, A., Masson, F., Socquet, A. and Saad, I. (2016). Transient deformation in the Asal-Ghoubbet Rift (Djibouti) since the 1978 diking event: Is deformation controlled by magma supply rates? *Journal of Geophysical Research: Solid Earth*, **121**(8), pp. 6030–6052. 4.2

Stork, A. L., Stuart, G. W., Henderson, C. M., Keir, D. and Hammond, J. O. (2013). Uppermost mantle (Pn) velocity model for the Afar region, Ethiopia: An insight into rifting processes. *Geophysical Journal International*, **193**, pp. 321–328. doi:10.1093/gji/ggs106. 4.2.1, 4.2.2, 4.4

Sturkell, E., Sigmundsson, F., Geirsson, H., Ólafsson, H. and Theodórsson, T. (2008). Multiple volcano deformation sources in a post-rifting period: 1989–2005 behaviour of Krafla, Iceland constrained by levelling, tilt and GPS observations. *Journal of Volcanology and Geothermal Research*, **177**(2), pp. 405–417. 4.2

Tiberi, C., Ebinger, C., Ballu, V., Stuart, G. and Oluma, B. (2005). Inverse models of gravity data from the Red Sea-Aden-East African rifts triple junction zone. *Geophysical Journal International*, **163**, pp. 775–787. doi:10.1111/j.1365-246X.2005.02736.x. 4.2.1, 4.3.2

Tryggvason, E. (1986). Multiple magma reservoirs in a rift zone volcano: Ground deformation and magma transport during the September 1984 eruption of Krafla, Iceland. *Journal of volcanology and geothermal research*, **28**(1-2), pp. 1–44. 4.2.2

Vigny, C., de Chabalier, J. B., Ruegg, J. C., Huchon, P., Feigl, K. L., Cattin, R., Asfaw, L. and Kanbari, K. (2007). Twenty-five years of geodetic measurements along the Tadjoura-Asal rift system, Djibouti, East Africa. *Journal of Geophysical Research: Solid Earth*, **112**(B06410). doi:10.1029/2004JB003230. 4.2

Viltres, R., Jónsson, S., Ruch, J., Doubre, C., Reilinger, R., Floyd, M. and Ogubazghi, G. (2020). Kinematics and deformation of the southern Red Sea region from GPS observations. *Geophysical Journal International*, **221**(3), pp. 2143–2154. 4.2.1

Weiss, J. R., Qiu, Q., Barbot, S., Wright, T. J., Foster, J. H., Saunders, A., Brooks, B. A., Bevis, M., Kendrick, E., Ericksen, T. L. et al. (2019). Illuminating subduction zone rheological properties in the wake of a giant earthquake. *Science advances*, **5**(12), p. eaax6720. doi:10.1126/sciadv.aax6720. 4.4

Wolfenden, E., Ebinger, C., Yirgu, G., Renne, P. R. and Kelley, S. P. (2005). Evolution of a volcanic rifted margin: Southern Red Sea, Ethiopia. *Bulletin of the Geological Society of America*, **117**(7/8), pp. 846–864. doi:10.1130/B25516.1. 4.2.1

Wright, T. J., Ebinger, C., Biggs, J., Ayele, A., Yirgu, G., Keir, D. and Stork, A. (2006). Magma-maintained rift segmentation at continental rupture in the 2005 Afar dyking episode. *Nature*, **442**(7100), pp. 291–294. doi:10.1038/nature04978. 4.2.2, 4.4

Wright, T. J., Sigmundsson, F., Pagli, C., Belachew, M., Hamling, I. J., Brandsdóttir, B., Keir, D., Pedersen, R., Ayele, A., Ebinger, C., Einarsson, P., Lewi, E. and Calais, E. (2012). Geophysical constraints on the dynamics of spreading centres from rifting episodes on land. doi:10.1038/ngeo1428. 4.2, 4.2.2

Xu, W., Rivalta, E. and Li, X. (2017). Magmatic architecture within a rift segment: Articulate axial magma storage at Erta Ale volcano, Ethiopia. *Earth and Planetary Science Letters*, **476**, pp. 79–86. doi:10.1016/j.epsl.2017.07.051. 4.2.2

Xu, W., Xie, L., Aoki, Y., Rivalta, E. and Jónsson, S. (2020). Volcano-wide deformation after the 2017 Erta Ale dike intrusion, Ethiopia, observed with radar interferometry. *Journal of Geophysical Research: Solid Earth*, **125**(8), p. e2020JB019562. 4.2.1

Yamasaki, T., Kobayashi, T., Wright, T. J. and Fukahata, Y. (2018). Viscoelastic crustal deformation by magmatic intrusion: A case study in the Kutcharo caldera, eastern Hokkaido, Japan. *Journal of Volcanology and Geothermal Research*, **349**, pp. 128–145. doi:10.1016/j.jvolgeores.2017.10.011. 4.2.3

Chapter 5

Discussion & Conclusions

In this thesis I have presented works using satellite-borne InSAR observations to investigate the present state of magmatic rifting in Afar during the transition from continental to oceanic rifting in the region. In order to achieve this, the works presented in Chapters 2-4 target the simple questions of "Where is the magma?", "Where is the strain?", and "What is the rheological structure of the crust?", as shown in Section 1.4. In this chapter, I will summarise my key findings and discuss their importance to the wider scientific community.

5.1 Magma Plumbing Systems at Rift Volcanoes

Within Chapters 2-4, I observe and model surface deformation at several volcanic centres in Afar including Dallol and Erta 'Ale on the EAVS, Dabbahu, Gabho, and Ado 'Ale on the DMHVS, and Nabro. I also show how certain volcanic centres which were previously deforming, such as on the AGVS, have no recent magmatic activity. Monitoring both the presence and absence of surface deformation during the pre-, co-, and post-eruptive periods is crucial to furthering the understanding of the magma storage and dynamics beneath these volcanic centres. By employing simple models, surface deformation at volcanic centres is generally interpreted as being caused by a change in volume of a magmatic source at depth. Biggs et al. (2014) show that volcanic eruptions rarely occur with no recorded surface deformation, while the presence of deformation, particularly in rift settings, does not guarantee an eruption. The deformation recorded at the surface is also controlled by factors such as the compressibility of the magma, the gas content and de-gassing of the magma, the viscosity of the crust surrounding the magma body, and the likely complex geometry of a magma mush zone involving connected pockets of melt and significant thermal alteration of the crust. While difficult to include in models of geodetic observations, due to their variability and the lack constraints on the geochemistry and rheology of sub-surface magmas, these factors should always be considered when interpreting geodetic models of magma plumbing systems.

As shown in Chapter 2, the surface deformation at the Erta 'Ale volcano in the build-up to the 2017-19 flank eruption, and during the initial and late stages of the eruption, emphasises how the pre- and co-eruptive stages of an eruption can provide different insights into the shallow magmatic plumbing system beneath volcanoes. Between 2014-17, in the build-up to the eruption, in general agreement with Xu et al. (2017), I modelled gradual surface extension by the continuous inflation of a dyke-like structure aligned with the rift axis, which extended from $\sim$ 0.5-5.5 km depth. This appears to be a consistent style of melt accumulation at Erta 'Ale, with an axial dyke also attributed to local extension in 2004-05 (Barnie et al., 2016). As magma tends to reside in horizontal rather then vertical structures, these sources likely represent the movement of melt from depth in order to sustain a shallow reservoir at $\sim$ 1 km depth below the summit caldera, as suggested in Chapter 2. As this shallow body supports the active long-lived lava lake at the Erta 'Ale summit caldera, any increase in pressure associated with magma re-charge may not have resulted in any detectable surface deformation. Persistently high levels in the summit lava lake (see Figure A.5), indicative of a high pressure state within the shallow reservoir, are consistent with magma recharge during the pre-eruptive period.

In January 2017, additional pressure in the summit magma reservoir caused the lava lake to overflow, before a shallow dyke was intruded down-rift from the summit caldera to an eruption site on the flank of Erta 'Ale (Global Volcanism Program, 2017). This was coincident with a rapid draining of the lava lake (see Figure A.5), consistent with observations of surface contraction around the summit caldera (Xu et al., 2017), while the volume reduction of the lava lake conduit feature was roughly equal to the volume of the intruded dyke. As shown in Chapter 2, the pressure loss calculated from the drop in the lava lake level was also sufficient to replicate the co-intrusive ground deformation, indicating that shallow sources ($\lesssim$ 3 km depth) at Erta 'Ale drove the initial intrusion. In the following few months, from January to April 2017, a rise in the level of the lava lake (see Figure 2.7) coincided with the inflation of a shallow sill at $\sim$ 1 km depth between the summit caldera and the eruption site (Xu et al., 2017), and the formation of a sustained lava lake at the eruption site (Global Volcanism Program, 2018). Following this period of higher pressure in the early stage of the eruption, the remainder of the erupted material (from April 2017 to June 2019) was sourced from a deeper, more complex body, situated $\sim$ 3 km off-axis between Erta 'Ale and the nearby Ale Bagu volcanic centre. This body, first identified in Chapter 2 and modelled in further detail by Xu et al. (2020), may be modelled by either a vertically extensive ellipsoidal source, representative of a series of stacked sills from shallow depths to the base of the crust (1-14 km), or as shallow dyke contraction below the summit caldera combined with the deflation of a deep sill at a depth of $\sim$ 11 km (Xu et al., 2020). Both sources represent systems of magma transport from the base of the crust to shallow

levels below Erta 'Ale, in agreement with observations of deep seismicity on the EAVS, interpreted as the presence of magma reservoirs at the base of the crust beneath volcanic centres at $\sim$ 12 km depth (Illsley-Kemp et al., 2018b). Further detail in these models of lower and mid-crustal magma plumbing systems at Erta 'Ale are limited by the ability of InSAR observations to resolve these sources at depth. Ideally, models based on geodesy would be constrained by other geophysical observations from magnetotelluric, gravity, or seismic surveys, such as on the DMHVS (e.g. Stork et al., 2013, Hammond, 2014, Desissa et al., 2013, Lewi et al., 2016), the AGVS (e.g. Van et al., 1981), and in the MER (e.g. Lloyd et al., 2018, Hübert et al., 2018, Nowacki et al., 2018); but the extreme remote environment of the EAVS, even in comparison to other rift segments in Afar, limits the diversity of data available.

The linkage between shallow axial magma chambers and deeper magma reservoirs at the base of the crust is present elsewhere on the EAVS at Alu-Dalafilla (Pagli et al., 2012), as well as at other volcanoes with established rift zones. At Kilauea, Hawaii, the extensive monitoring systems both around the summit caldera and along the East Rift Zone (ERZ), have enabled a perhaps unparalleled understanding of a single magmatic plumbing system where a deeper central reservoir feeds both the summit reservoir and Halema'uma'u lava lake, as well as long-lived vents in the ERZ such as Pu'u'O'o. Similar to at Erta 'Ale, the Halema'uma'u lava lake has been frequently observed to react to magma movement elsewhere in the system, indicating that plumbing systems that support long-lived lava lakes may consist of well developed, hydraulically connected magma pathways. Shallow axial magma chambers have also been observed at MORs with fast-spreading rates such as on the East Pacific Rise (EPR) at 1-3 km depth (Carbotte et al., 2013, Marjanović et al., 2014, Wanless and Behn, 2017). Where MORs with slow/intermediate spreading rates coincide with hot-spot activity, such as at the Galapagos spreading centre (GSC) (White et al., 2008, Boddupalli and Canales, 2019) and Axial Seamount (Nooner and Chadwick, 2009, Sigmundsson, 2016), the additional magma flux may also sustain shallow magma lenses as well as other features of fast-spreading ridges such as an axial rise (Chen and Morgan, 1996, Chen and Lin, 2004). The additional supply of magma from the Afar plume may then explain similar features on the slow-spreading EAVS, which exhibits both shallow axial magma bodies and an axial rise along the segment, in comparison to the DMHVS which exhibits an axial graben. The lack of hydro-thermal cooling in Afar, which plays a significant role in counteracting the formation of shallow magma lenses at MORs (Phipps Morgan and Chen, 1993a,b), may also contribute to sustaining axial magma bodies on the slow-spreading EAVS.

The interaction of several magma bodies within a rift segment during a single event is also indicative of a link to a larger common body at depth. During the 2005-10 rift-

ing event at the DMHVS, shallow magma bodies at $\sim$ 4 km depth beneath Dabbahu and Gabho at the northern end of the segment initially deflated with the initial intrusion, but then indicated sustained inflation during the subsequent 12 dyke intrusions. Inflation from a source at $\sim$ 10 km depth (Hamling et al., 2014), or from multiple sources at 4-25 km depth (Grandin et al., 2010), was also observed below Ado 'Ale at the segment centre during the rifting episode, combined with the deflation of a source at the southern end of the DMHVS at $\sim$ 17 km depth (Hamling et al., 2014, Grandin et al., 2010). The results shown in Chapter 4 (see Figure C.3 and Table C.1) agree with these observations, and show that the Ado 'Ale source has sustained its inflation up to 2019, while the Southern source now likely requires an inflation to produce the uplift signal observed from 2014-19. The continued activity at sources throughout the DMHVS both during and following the 2005-10 rifting episode shows similarities to the interaction of magma reservoirs during the 1975-84 Krafla rifting episode in Iceland where melt was sourced from a shallow chamber beneath the central caldera (Einarsson, 1978, Brandsdóttir et al., 1997, Sigmundsson et al., 1997), as well as from magma bodies within and at the base of the crust (Tryggvason, 1986, Árnadóttir et al., 1998) which exhibited inflation during the post-rifting period (de Zeeuw-van Dalfsen et al., 2004).

5.2 Sub-Surface Structure below Volcanic Rift Segments

Deformation signals in the years to decades following large rifting events provide rare insights into the sub-surface rheological structure beneath volcanic rift segments. The long-term viscoelastic relaxation of the upper mantle has been observed following several rifting events such as the 2005-10 DMHVS (Hamling et al., 2014, Nooner et al., 2009) and the 1978 AGVS (Cattin et al., 2005, Smittarello et al., 2016) episodes in Afar, and the 1975-84 Krafla episode in Iceland (Pedersen et al., 2009, Sigmundsson et al., 1997). Continued magma movement within volcanic segments throughout the rift cycle also contributes significantly to the observable surface deformation as shown in Chapter 4 and by Hamling et al. (2014) for the 2005-10 DMHVS episode, and for the 1975-84 Krafla episode (e.g. Sigmundsson et al., 1997, Árnadóttir et al., 1998, de Zeeuw-van Dalfsen et al., 2004). The rheological structure of the subsurface which controls the magnitude and longevity of the viscoelastic response is then partially dependent on the segment magma plumbing system from deeper bodies of melt at the base of the crust to shallow reservoirs beneath volcanic centres. Regions of partial melt are less viscous than surrounding host rock, although this is likely to increase as melt cools and crystallises. A large mush zone of partial melt is also likely to have a significant influence on the surrounding crust through thermal alteration, distorting how the region responds to deformation. As melt bodies and plumbing systems are spatially limited, their effect on the nearby rheology of the crust may also then be spatially limited, producing a ductile

zone close to the rift axis. Pedersen et al. (2009) incorporate this spatial variation to model the surface deformation over the Krafla and Askja rift segments in Iceland, and find that a best fit model includes both a shallowed viscoelastic region and a weakened elastic lid beneath the segments. As shown in Chapter 4, the subsurface rheology also controls the amount of magmatic activity that is required in a model as each magmatic source induces a time dependent viscoelastic response which may then counteract or amplify the initial inflation/deflation depending on the depth of the source relative to the base of the elastic crust (see Figure C.1 and Table C.1).

A further source of complication comes from whether the viscoelastic subsurface deforms linearly with time, such as with a Maxwell rheology, or non-linearly, such as with a Kelvin-Voigt, Burgers', or Power-Law creep rheology. Previous models of post-rift deformation (e.g. Nooner et al., 2009, Pedersen et al., 2009, Hamling et al., 2014), as well as the model described in Chapter 4, make use of the simplest Maxwell rheology, but when considering the time series of surface deformation over the whole post-rifting period, such as for the DMHVS (Chapter 4) and the AGVS (Cattin et al., 2005), a non-linear viscoelastic rheology may be required to fit both the initial high rate and the later low rates of surface deformation. The biggest limitation of the model described in Chapter 4 is the fit to the earliest part of the time series ($\sim$ 2006-07) where the highest rates of deformation are observed. It is also in this part of the time series where a non-linear rheology may provide the biggest difference to a linear Maxwell response to the initial September 2005 dyke intrusion at the DMHVS. The inclusion of a weak zone within the elastic lid and/or a shallower viscoelastic region (Pedersen et al., 2009) may also act to improve the fit in this time period. As well as any spatial variations, temporal changes in viscosity may also be a contributing factor to how deformation is expressed at the surface during post-rift relaxation. In a rift zone, a change in viscosity through time may arise due to mechanisms such as the intrusion or replenishment of a melt body, which would reduce the average viscosity, or the cooling and crystallisation of partial melt, which would act to increase the local viscosity. Following earthquakes, the viscosity of the upper mantle has been modelled as increasing through the post-seismic period (Ryder et al., 2007), while the results of Chapter 4 suggest that the viscosity of the upper mantle at the DMHVS may have decreased through the post-rift period from 10^{18}-10^{19} Pa s from 2006-10 to $\sim 10^{18}$ Pa s from 2014-19. I speculate that this is perhaps due to a shift from extrusive magmatism during the 2005-10 rifting event to intrusive magmatism from 2014-19, although the change in viscosity is within error estimates.

The sub-surface rheology beneath rift segments not only influences the post-rift relaxation signal, but also how magma movement in the segment is expressed at the surface. Previous studies have incorporated viscoelasticity into models of magma reservoirs in

order to better represent the rheology of a mush zone with pockets of melt, or a body of melt surrounded by a thermally altered region (e.g. Dragoni and Magnanensi, 1989, Segall, 2016). When accounting for viscoelasticity, smaller volume changes are typically required as shown by subsidence at the Nabro volcano in Afar following the 2011 eruption, where magma degassing and compressibility are also thought to have important contributions to the observed surface deformation (Hamlyn et al., 2018). Inelasticity in the subsurface may also facilitate larger eruptions than anticipated by sustaining magma pathways from reservoirs at depth, as shown during the 2014-15 Bardarbunga-Holuhraun rifting event (Sigmundsson et al., 2020). A similar mechanism may also apply to both the 2005-10 DMHVS rifting episode and the long-lived 2017-19 Erta 'Ale eruption where both segments are predicted to be connected to magma reservoirs at the base of the crust (Stork et al., 2013, Desissa et al., 2013, Illsley-Kemp et al., 2018b, Xu et al., 2020).

5.3 Strain Localisation & Rift Development

The transition of continental to oceanic style rifting is shown in Afar by a number of factors including the thinning and stretching of the crust (e.g. Hammond et al., 2011, Bastow et al., 2018), high density crust being created at spreading segments (Lewi et al., 2016), the formation of early-stage transform faults between segments (Illsley-Kemp et al., 2018a, La Rosa et al., 2019), the presence of shallow axial magma lenses beneath spreading centres (see Chapter 2; Pagli et al., 2012, Xu et al., 2020), and the localisation of extensional strain as shown in Chapter 3. Within Afar there are also key differences between the DMHVS in central Afar and the EAVS in the Danakil Depression in northern Afar, with a distinct axial graben and axial rise respectively, indicating a change in rifting style between the segments (Wright et al., 2012, Pagli et al., 2015). At MORs, whether a ridge forms a rise or a graben is dependent on the spreading rate and crustal thickness, while a higher magma flux may also produce an axial rise with shallow axial magma lenses (Chen and Morgan, 1996, Dick et al., 2003, Chen and Lin, 2004) as discussed previously for the EAVS. Chapter 3 highlighted an increase in the localisation of plate extension from within ± 20-30 km of the DMHVS rift axis to within ± 15-20 km of the EAVS rift axis. This rift focussing continues towards the oceanic RSR into northern Afar to ± 10-15 km, while closer to the NMER in south central and southern Afar extension is significantly more distributed across 80-160 km of the rift with amagmatic faulting accommodating much of the strain (see Figure 3.5). The rotation of the Danakil microplate with plate extension may also play a role in determining the width of the Afar rift. The gradual transition of extension from the RSR to the EAVS from ∼ 13-16 °N (e.g. Kidane, 2016, Viltres et al., 2020) produces the anti-clockwise motion of the Danakil block, and a significantly narrower rift zone in northern Afar, than in central and southern Afar.

The EAVS also exhibits a higher recent rate of magmatism in comparison to other segments in Afar with active deformation at Dallol and Erta 'Ale (see Chapters 2-3; Nobile et al., 2012, Xu et al., 2020), as well as recent activity at Alu-Dalafilla and Gada 'Ale (Pagli et al., 2012, Amelung et al., 2000). This is in accordance with the expected shift from intrusive to extrusive magmatism during the transition into oceanic style rifting (Keir et al., 2013), and findings from petrology which estimate that 2/3 of material on the EAVS is extruded rather than intruded into the crust (Hutchison et al., 2018). The additional load from this erupted material, combined with the smallest crustal thickness in Afar of 15-20 km (e.g. Hammond et al., 2011, Bastow and Keir, 2011), may contribute to the plate stretching and basin formation observed near Dallol in the Danakil Depression (Bastow et al., 2018), and the formation of seaward dipping reflectors which are frequently observed at volcanic continental margins (Corti et al., 2015, Buck, 2017).

5.4 Limitations & Future Work

5.4.1 Afar Surface Velocity Map

In Chapter 3, I developed a weighted filtering methodology to remove the APS from the displacement time series for each Sentinel-1 frame. This method was able to effectively identify particularly noisy pixels and epochs, and significantly reduce their influence on the resulting filtered time series. The point weighting was calculated using the misfits to a Laplacian smoothed time series at each pixel, assuming that the surface deformation is gradual through time. The resulting velocity maps shown in Chapter 3 are then an average rate of the displacements from the time series at each pixel. Close to volcanic centres this assumption does not hold if there has been a step in surface deformation due to an intrusion or rapid inflation/deflation of a magma reservoir, such as can be seen at Erta 'Ale due to the deformation associated with the complex interplay of magmatic sources during the 2017-19 eruption, as shown in Chapter 2. Minor signal artefacts can also be identified in the 3D surface velocity maps shown in Figure 3.3, with steps between frames resulting from differences in the APS filtering in the individual frames, and steps between tracks resulting from differences in the referencing to the GNSS regional velocity field.

The GNSS referencing method in Chapter 3 was developed to account for the very sparse network of GNSS observations of long-term plate motions. Previous studies that have similarly referenced Sentinel-1 InSAR derived velocity maps to a regional GNSS network have done so in regions where the GNSS network provides a relatively even regional coverage (e.g. Weiss et al., 2020). As the GNSS observations in central Afar are dominated by deformation associated with the 2005-10 DMHVS rifting episode and

post-rifting response, the resulting network is generally limited to points around the edge of the Afar rift. In order to solve for the quadratic functions which are then removed from the InSAR data to reference the velocity field, I interpolated a smooth GNSS velocity field across the Afar rift (see Figure B.4). While this smooth field is representative of the far-field plate motions, it assumes wide distribution of extension, while the InSAR data shows the localisation of strain on volcanic segments in central and northern Afar. This novel method provides a viable solution to referencing InSAR velocity maps using sparse GNSS networks, but an improvement may be to iterate the referencing methodology such that the velocity field used to reference the InSAR data is more representative of the distribution of extension within the rift.

5.4.2 Post-Rift Relaxation Model

The model of surface deformation at the DMHVS during post-rift relaxation I developed in Chapter 4 highlights the importance of accounting for both the viscoelastic relaxation of the upper mantle and the continued activity at volcanic centres within the segment. As discussed previously in Section 5.2, there are several factors that could be added to this model to improve the fit to the high rates of deformation during early portion of the time series, as well as making the model more representative of the subsurface structure. The addition of a weakened zone beneath the rift segment, as demonstrated by Pedersen et al. (2009) for the Krafla and Askja rift segments in Iceland, may provide a significant improvement to the model whilst also being relatively straightforward to implement within Relax. The difficulty in implementing this lies in constraining the size and geometry of the weak zone, and the degree of weakening required. Other geophysical observations, such as from magnetotelluric (Desissa et al., 2013) or gravity (Lewi et al., 2016) studies, could be used to constrain the location of melt and the localised thinning of the elastic crust, such as was done for post-rift relaxation on the AGVS where the location of a magma reservoir was fixed by magnetotelluric observations (Cattin et al., 2005, Van et al., 1981). 3D models of heterogeneous subsurface viscosity have been established using geodetic data following large subduction zone earthquakes (Moore et al., 2017, Qiu et al., 2018, Weiss et al., 2019). If the model of Barbot et al. (2017) and Barbot (2018) could be adapted to rift zones, it could provide further insights into the spatial and temporal distribution of viscosity following rifting episodes. Other potential improvements such as the use of non-linear rheological models, would require a more in-depth analysis to determine the optimal style of non-linear deformation for the DMHVS.

The magmatic sources I use in the model developed in Chapter 4 may also be much more complex than simple sill sources. For simplicity, I used the depths for these sources estimated by Hamling et al. (2014), but Grandin et al. (2010) suggest that there may be three different sources below Ado 'Ale at the segment centre, while Field

et al. (2012) find that the magma plumbing system below Dabbahu at the northern end of the segment likely consists of a sequence of stacked sills. While the addition of more magmatic sources may improve the fit of the model, they should only be included in future models if there is sufficient justification and constraints for additional sources.

A valuable source of constraints for both constraining magmatic sources and the subsurface rheology would be an extension to the InSAR time series shown here as Sentinel-1 data continues to be acquired. The addition of even 1-2 years to the dataset may show further decay of the viscous response with time, or identify whether the magmatic sources at the centre and southern end of the segment continue to contribute to the deformation signal. A crucial supplement to the InSAR time series data would be the addition of GNSS observations during the Sentinel-1 time period, which would provide points with high temporal sampling rate, upon which the spatial coverage of InSAR data could be pinned, improving the confidence in the dataset as a whole.

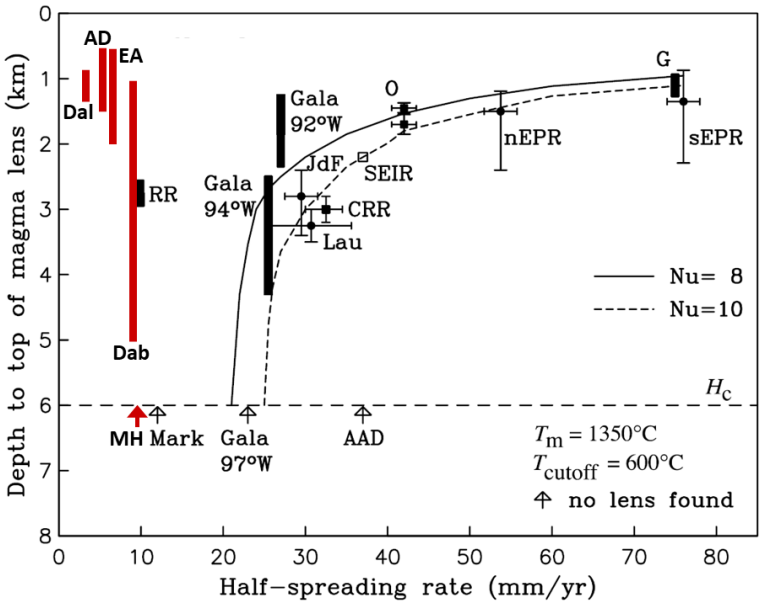

Figure 5.1: Distribution of magma lens depth at MORs (black) and in Afar (red) with rift spreading-rate and crustal thickness. Solid and dashed lines indicate numerical models from Chen and Lin (2004). Model parameters: H_c - crustal thickness, T_m - mantle temperature, T_{cutoff} - temperature below which hydrothermal circulation has an effect, Nu - Nusselt number (ratio of convective to conductive heat transfer). Afar spreading centres: Dal - Dallol (Chapter 3), AD - Alu-Dalafilla (Pagli et al., 2012), EA - Erta 'Ale (Chapter 2, Xu et al., 2017), Dab - Dabbahu (Field et al., 2012), MH - Manda Hararo. MOR spreading centres: RR - Reykjanes Ridge, Mark - Mid-Atlantic Ridge at Kane fracture zone, Gala - Galapagos Spreading Centre, JdF - Juan de Fuca Ridge, Lau - Lau Basin, CRR - Costa Rica Ridge, SEIR - South East Indian Ridge, AAD - Australia-Antarctica Discordance. East Pacific Rise spreading centres: nEPR - northern, sEPR - southern, O - north of Orozco transform, G - south of Garret transform. *Figure modified from Chen and Lin (2004).*

5.4.3 Shallow Axial Magma Bodies

A final area of further study may be focussed around whether the same factors that control the structure of MORs may be applied to spreading segments in Afar. To the first order, spreading rate and crustal thickness define the bathymetry (axial rise or graben) of the ridge and whether the ridge may sustain a shallow axial magma lens (e.g. Dick et al., 2003, Wanless and Behn, 2017), while the rate of melt supply also has an effect (Chen and Lin, 2004). The thermal model of Phipps Morgan and Chen (1993a,b) and Chen and Lin (2004), as shown in Figure 5.1, fits the distribution of axial magma lens depths at several intermediate and fast-spreading MORs. In Figure 5.1, I have included the depths of axial magma bodies at spreading centres in Afar to demonstrate how the spreading-rate does not account for ridges with elevated melt flux. As previously suggested by Pagli et al. (2012, 2015), developments could be made to this numerical model to test whether additional melt flux and a lack of hydrothermal cooling on sub-aerial ridges would be sufficient to predict an axial high and the presence of shallow axial magma bodies as observed on the EAVS. This may also work to identify whether the increase in crustal thickness between the EAVS and the DMHVS is sufficient to change the segment topography from an axial high to an axial graben, or whether a difference in melt flux is also required between the segments. Any change in the controlling parameters between segments would provide further crucial insights into the development of rift segments within Afar and their similarities to MORs. Alternatively, if thermal models of MORs cannot be adapted to sub-aerial spreading segments, it would indicate that spreading segments in Afar may not be classed as incipient MORs and that this stage of rifting is yet to take place in Afar.

5.5 Concluding Remarks

In this thesis I have used InSAR observations of ground motions in the Afar rift to map and model the localisation of extensional strain, the role of magmatic intrusions in accommodating this strain, and the structure of shallow magmatic plumbing systems at spreading centres, to provide an insight into the state of the Afar rift during a transition from continental to oceanic rifting. I present a new map of surface velocities across Afar, developing novel APS filtering and GNSS referencing techniques to produce 3D average velocities at a high spatial resolution. I also present models of surface deformation at several volcanic centres in Afar, including the complex interaction of sources in the build-up to and during the 2017-19 Erta 'Ale eruption, and the $\sim$ 14 year post-rifting response to the 2005-10 DMHVS rifting episode. Here, I develop a new robust technique to consider both the viscoelastic relaxation of the upper mantle, and the contribution of continued magmatic activity in the segment which I show to be crucial in order to reproduce the spatial distribution of deformation on the rift segment.

The Afar rift is a complex system which has been and will continue to be the focus of many studies and theses. I believe that I have advanced the understanding of magmatic plumbing systems within the rift by establishing that the maturity of the rift, and the degree of strain localisation, increases into northern Afar where the presence of a shallow magma reservoirs, that are connected to melt at depth by means of vertically extensive pathways, further indicates that the EAVS is representative of an incipient MOR. I also demonstrate how magmatic centres interact within segments both during and following large rifting events, of which modern observations are rare. I hope that my findings inspire further study into the behaviour of magmatic rifts in Afar, Iceland, and other volcanic centres in extensional settings.

References

Amelung, F., Oppenheimer, C., Segall, P. and Zebker, H. (2000). Ground deformation near Gada 'Ale volcano, Afar, observed by radar interferometry. *Geophysical Research Letters*, **27**(19), pp. 3093–3096. doi:10.1029/2000GL008497. 5.3

Árnadóttir, T., Sigmundsson, F. and Delaney, P. T. (1998). Sources of crustal deformation associated with the Krafla, Iceland, eruption of September 1984. *Geophysical research letters*, **25**(7), pp. 1043–1046. 5.1, 5.2

Barbot, S. (2018). Deformation of a Half-Space from Anelastic Strain Confined in a Tetrahedral VolumeDeformation of a Half-Space from Anelastic Strain Confined in a Tetrahedral Volume. *Bulletin of the Seismological Society of America*, **108**(5A), pp. 2687–2712. doi:10.1785/0120180058. 5.4.2

Barbot, S., Moore, J. D. and Lambert, V. (2017). Displacement and stress associated with distributed anelastic deformation in a half-space. *Bulletin of the Seismological Society of America*, **107**(2), pp. 821–855. doi:10.1785/0120160237. 5.4.2

Barnie, T. D., Oppenheimer, C. and Pagli, C. (2016). Does the lava lake of Erta 'Ale volcano respond to regional magmatic and tectonic events? An investigation using Earth Observation data. *Geological Society, London, Special Publications*, **420**, pp. 181–208. doi:10.1144/SP420.15. 5.1

Bastow, I. D., Booth, A. D., Corti, G., Keir, D., Magee, C., Jackson, C. A.-L., Warren, J., Wilkinson, J. and Lascialfari, M. (2018). The development of late-stage continental breakup: Seismic reflection and borehole evidence from the Danakil Depression, Ethiopia. *Tectonics*, **37**(9), pp. 2848–2862. 5.3, 5.3

Bastow, I. D. and Keir, D. (2011). The protracted development of the continent-ocean transition in Afar. *Nature Geoscience*, **4**(4), pp. 248–250. doi:10.1038/ngeo1095. 5.3

Biggs, J., Ebmeier, S., Aspinall, W., Lu, Z., Pritchard, M., Sparks, R. and Mather, T. (2014). Global link between deformation and volcanic eruption quantified by satellite imagery. *Nature communications*, **5**(1), pp. 1–7. 5.1

Boddupalli, B. and Canales, J. P. (2019). Distribution of crustal melt bodies at the hotspot-influenced section of the Galápagos Spreading Centre from seismic reflection images. *Geophysical Research Letters*, **46**(9), pp. 4664–4673. doi:10.1029/2019GL082201. 5.1

Brandsdóttir, B., Menke, W., Einarsson, P., White, R. S. and Staples, R. K. (1997). Færoe-Iceland ridge experiment 2. Crustal structure of the Krafla central volcano. *Journal of Geophysical Research: Solid Earth*, **102**(B4), pp. 7867–7886. 5.1

Buck, W. R. (2017). The role of magmatic loads and rift jumps in generating seaward dipping reflectors on volcanic rifted margins. *Earth and Planetary Science Letters*, **466**, pp. 62–69. doi:10.1016/j.epsl.2017.02.041. 5.3

Carbotte, S. M., Marjanović, M., Carton, H., Mutter, J. C., Canales, J. P., Nedimović, M. R., Han, S. and Perfit, M. R. (2013). Fine-scale segmentation of the crustal magma reservoir beneath the East Pacific Rise. *Nature Geoscience*, **6**(10), pp. 866–870. doi:10.1038/ngeo1933. 5.1

Cattin, R., Doubre, C., de Chabalier, J. B., King, G., Vigny, C., Avouac, J. P. and Ruegg, J. C. (2005). Numerical modelling of quaternary deformation and post-rifting displacement in the Asal-Ghoubbet rift (Djibouti, Africa). *Earth and Planetary Science Letters*, **239**(3-4), pp. 352–367. doi:10.1016/j.epsl.2005.07.028. 5.2, 5.2, 5.4.2

Chen, Y. J. and Lin, J. (2004). High sensitivity of ocean ridge thermal structure to changes in magma supply: The Galápagos Spreading Center. *Earth and Planetary Science Letters*, **221**(1-4), pp. 263–273. doi:10.1016/S0012-821X(04)00099-8. 5.1, 5.3, 5.1, 5.4.3

Chen, Y. J. and Morgan, J. P. (1996). The effects of spreading rate, the magma budget, and the geometry of magma emplacement on the axial heat flux at mid-ocean ridges. *Journal of Geophysical Research-Solid Earth*, **101**(B5), pp. 11475–11482. doi:10.1029/96JB00330. 5.1, 5.3

Corti, G., Agostini, A., Keir, D., Van Wijk, J., Bastow, I. D. and Ranalli, G. (2015). Magma-induced axial subsidence during final-stage rifting: Implications for the development of seaward-dipping reflectors. *Geosphere*, **11**(3), pp. 563–571. doi:10.1130/GES01076.1. 5.3

de Zeeuw-van Dalfsen, E., Pedersen, R., Sigmundsson, F. and Pagli, C. (2004). Satellite radar interferometry 1993–1999 suggests deep accumulation of magma near the crust-mantle boundary at the Krafla volcanic system, Iceland. *Geophysical Research Letters*, **31**(13). 5.1, 5.2

Desissa, M., Johnson, N. E., Whaler, K. A., Hautot, S., Fisseha, S. and Dawes, G. J. (2013). A mantle magma reservoir beneath an incipient mid-ocean ridge in Afar, Ethiopia. *Nature Geoscience*, **6**(10), pp. 861–865. doi:10.1038/ngeo1925. 5.1, 5.2, 5.4.2

Dick, H. J., Lin, J. and Schouten, H. (2003). An ultraslow-spreading class of ocean ridge. *Nature*, **426**(6965), pp. 405–412. doi:10.1038/nature02128. 5.3, 5.4.3

Dragoni, M. and Magnanensi, C. (1989). Displacement and stress produced by a pressurized, spherical magma chamber, surrounded by a viscoelastic shell. *Physics of the Earth and Planetary Interiors*, **56**(3-4), pp. 316–328. doi:10.1016/0031-9201(89)90166-0. 5.2

Einarsson, P. (1978). S-wave shadows in the Krafla caldera in NE-Iceland, evidence for a magma chamber in the crust. *Bulletin Volcanologique*, **41**(3), pp. 187–195. 5.1

Field, L., Blundy, J., Brooker, R. A., Wright, T. and Yirgu, G. (2012). Magma storage conditions beneath Dabbahu Volcano (Ethiopia) constrained by petrology, seismicity and satellite geodesy. *Bulletin of Volcanology*, **74**, pp. 981–1004. doi:10.1007/s00445-012-0580-6. 5.4.2, 5.1

Global Volcanism Program (2017). Report on Erta Ale (Ethiopia). *In: Venzke, E (ed.), Bulletin of the Global Volcanism Network, 42:7. Smithsonian Institution.* 5.1

Global Volcanism Program (2018). Report on Erta Ale (Ethiopia). *In: Venzke, E (ed.), Bulletin of the Global Volcanism Network, 43:4. Smithsonian Institution.* 5.1

Grandin, R., Socquet, A., Doin, M. P., Jacques, E., De Chabalier, J. B. and King, G. C. (2010). Transient rift opening in response to multiple dike injections in the Manda Hararo rift (Afar, Ethiopia) imaged by time-dependent elastic inversion of interferometric synthetic aperture radar data. *Journal of Geophysical Research: Solid Earth*, **115**(B09403). doi:10.1029/2009JB006883. 5.1, 5.4.2

Hamling, I. J., Wright, T. J., Calais, E., Lewi, E. and Fukahata, Y. (2014). InSAR observations of post-rifting deformation around the Dabbahu rift segment, Afar, Ethiopia. *Geophysical Journal International*, **197**, pp. 33–49. doi:10.1093/gji/ggu003. 5.1, 5.2, 5.2, 5.4.2

Hamlyn, J., Wright, T., Walters, R., Pagli, C., Sansosti, E., Casu, F., Pepe, S., Edmonds, M., Kilbride, B. M., Keir, D. et al. (2018). What causes subsidence following the 2011 eruption at Nabro (Eritrea)? *Progress in Earth and Planetary Science*, **5**(1), p. 31. 5.2

Hammond, J. O. S. (2014). Constraining melt geometries beneath the Afar Depression, Ethiopia from teleseismic receiver functions: The anisotropic H-κ stacking technique. *Geochemistry, Geophysics, Geosystems*, **15**(4), pp. 1316–1332. 5.1

Hammond, J. O. S., Kendall, J. M., Stuart, G. W., Keir, D., Ebinger, C., Ayele, A. and Belachew, M. (2011). The nature of the crust beneath the Afar triple junction: Evidence from receiver functions. *Geochemistry, Geophysics, Geosystems*, **12**(12). doi:10.1029/2011GC003738. 5.3, 5.3

Hübert, J., Whaler, K. and Fisseha, S. (2018). The electrical structure of the central main Ethiopian Rift as imaged by magnetotellurics: implications for magma storage and pathways. *Journal of Geophysical Research: Solid Earth*, **123**(7), pp. 6019–6032. doi:10.1029/2017JB015160. 5.1

Hutchison, W., Mather, T. A., Pyle, D. M., Boyce, A. J., Gleeson, M. L., Yirgu, G., Blundy, J. D., Ferguson, D. J., Vye-Brown, C., Millar, I. L., Sims, K. W. and Finch, A. A. (2018). The evolution of magma during continental rifting: New constraints from the isotopic and trace element signatures of silicic magmas from Ethiopian volcanoes. *Earth and Planetary Science Letters*, **489**, pp. 203–218. doi:10.1016/j.epsl.2018.02.027. 5.3

Illsley-Kemp, F., Bull, J., Keir, D., Gerya, T., Pagli, C., Gernon, T., Ayele, A., Goitom, B., Hammond, J. O. and Kendall, J. (2018a). Initiation of a proto-transform fault prior to seafloor spreading. *Geochemistry, Geophysics, Geosystems*, **19**(12), pp. 4744–4756. 5.3

Illsley-Kemp, F., Keir, D., Bull, J. M., Gernon, T. M., Ebinger, C., Ayele, A., Hammond, J. O., Kendall, J. M., Goitom, B. and Belachew, M. (2018b). Seismicity during continental breakup in the Red Sea Rift of Northern Afar. *Journal of Geophysical Research: Solid Earth*, **123**, pp. 2345–2362. doi:10.1002/2017JB014902. 5.1, 5.2

Keir, D., Bastow, I. D., Pagli, C. and Chambers, E. L. (2013). The development of extension and magmatism in the Red Sea rift of Afar. *Tectonophysics*, **607**, pp. 98–114. doi:10.1016/j.tecto.2012.10.015. 5.3

Kidane, T. (2016). Strong clockwise block rotation of the Ali-Sabieh/Aïsha Block: evidence for opening of the Afar Depression by a 'saloon-door' mechanism. *Geological Society, London, Special Publications*, **420**, pp. 209–219. doi:10.1144/SP420.10. 5.3

La Rosa, A., Pagli, C., Keir, D., Sani, F., Corti, G., Wang, H. and Possee, D. (2019). Observing oblique slip during rift linkage in northern Afar. *Geophysical Research Letters*, **46**(19), pp. 10782–10790. 5.3

Lewi, E., Keir, D., Birhanu, Y., Blundy, J., Stuart, G., Wright, T. and Calais, E. (2016). Use of a high-precision gravity survey to understand the formation of oceanic crust and the role of melt at the southern Red Sea rift in Afar, Ethiopia. *Geological Society, London, Special Publications*, **420**, pp. 165–180. doi:10.1144/SP420.13. 5.1, 5.3, 5.4.2

Lloyd, R., Biggs, J., Wilks, M., Nowacki, A., Kendall, J. M., Ayele, A., Lewi, E. and Eysteinsson, H. (2018). Evidence for cross rift structural controls on deformation and seismicity at a continental rift caldera. *Earth and Planetary Science Letters*, **487**, pp. 190–200. doi:10.1016/j.epsl.2018.01.037. 5.1

Marjanović, M., Carbotte, S. M., Carton, H., Nedimović, M. R., Mutter, J. C. and Canales, J. P. (2014). A multi-sill magma plumbing system beneath the axis of the East Pacific Rise. *Nature Geoscience*, **7**(11), p. 825. 5.1

Moore, J. D., Yu, H., Tang, C.-H., Wang, T., Barbot, S., Peng, D., Masuti, S., Dauwels, J., Hsu, Y.-J., Lambert, V. et al. (2017). Imaging the distribution of transient viscosity after the 2016 Mw 7.1 Kumamoto earthquake. *Science*, **356**(6334), pp. 163–167. doi:10.1126/science.aal3422. 5.4.2

Nobile, A., Pagli, C., Keir, D., Wright, T. J., Ayele, A., Ruch, J. and Acocella, V. (2012). Dike-fault interaction during the 2004 Dallol intrusion at the northern edge of the Erta Ale Ridge (Afar, Ethiopia). *Geophysical Research Letters*, **39**(L19305). doi:10.1029/2012GL053152. 5.3

Nooner, S. L., Bennati, L., Calais, E., Buck, W. R., Hamling, I. J., Wright, T. J. and Lewi, E. (2009). Post-rifting relaxation in the Afar region, Ethiopia. *Geophysical Research Letters*, **36**(21). 5.2, 5.2

Nooner, S. L. and Chadwick, W. W. (2009). Volcanic inflation measured in the caldera of axial seamount: Implications for magma supply and future eruptions. *Geochemistry, Geophysics, Geosystems*, **10**(2). doi:10.1029/2008GC002315. 5.1

Nowacki, A., Wilks, M., Kendall, J.-M., Biggs, J. and Ayele, A. (2018). Characterising hydrothermal fluid pathways beneath Aluto volcano, Main Ethiopian Rift, using shear wave splitting. *Journal of Volcanology and Geothermal Research*, **356**, pp. 331–341. doi:10.1016/j.jvolgeores.2018.03.023. 5.1

Pagli, C., Mazzarini, F., Keir, D., Rivalta, E. and Rooney, T. O. (2015). Introduction: Anatomy of rifting: Tectonics and magmatism in continental rifts, oceanic spreading centers, and transforms. *Geosphere*, **11**(5), pp. 1256–1261. doi:10.1130/GES01082.1. 5.3, 5.4.3

Pagli, C., Wright, T. J., Ebinger, C. J., Yun, S. H., Cann, J. R., Barnie, T. and Ayele, A. (2012). Shallow axial magma chamber at the slow-spreading Erta Ale Ridge. *Nature Geoscience*, **5**(4), pp. 284–288. doi:10.1038/ngeo1414. 5.1, 5.3, 5.3, 5.1, 5.4.3

Pedersen, R., Sigmundsson, F. and Masterlark, T. (2009). Rheologic controls on inter-rifting deformation of the Northern Volcanic Zone, Iceland. *Earth and Planetary Science Letters*, **281**(1-2), pp. 14–26. doi:10.1016/j.epsl.2009.02.003. 5.2, 5.2, 5.4.2

Phipps Morgan, J. and Chen, Y. J. (1993a). Dependence of ridge-axis morphology on magma supply and spreading rate. *Nature*, **364**(6439), pp. 706–708. doi:10.1038/364706a0. 5.1, 5.4.3

Phipps Morgan, J. and Chen, Y. J. (1993b). The genesis of oceanic crust: Magma injection, hydrothermal circulation, and crustal flow. *Journal of Geophysical Research: Solid Earth*, **98**(B4), pp. 6283–6297. doi:10.1029/92JB02650. 5.1, 5.4.3

Qiu, Q., Moore, J. D., Barbot, S., Feng, L. and Hill, E. M. (2018). Transient rheology of the sumatran mantle wedge revealed by a decade of great earthquakes. *Nature communications*, **9**(1), pp. 1–13. doi:10.1038/s41467-018-03298-6. 5.4.2

Ryder, I., Parsons, B., Wright, T. J. and Funning, G. J. (2007). Post-seismic motion following the 1997 Manyi (Tibet) earthquake: InSAR observations and modelling. *Geophysical Journal International*, **169**(3), pp. 1009–1027. 5.2

Segall, P. (2016). Repressurization following eruption from a magma chamber with a viscoelastic aureole. *Journal of Geophysical Research: Solid Earth*, **121**(12), pp. 8501–8522. doi:10.1002/2016JB013597. 5.2

Sigmundsson, F. (2016). New insights into magma plumbing along rift systems from detailed observations of eruptive behavior at Axial volcano. *Geophysical Research Letters*, **43**(24), pp. 12–423. 5.1

Sigmundsson, F., Pinel, V., Grapenthin, R., Hooper, A., Halldórsson, S. A., Einarsson, P., Ófeigsson, B. G., Heimisson, E. R., Jónsdóttir, K., Gudmundsson, M. T. et al. (2020). Unexpected large eruptions from buoyant magma bodies within viscoelastic crust. *Nature communications*, **11**(1), pp. 1–11. 5.2

Sigmundsson, F., Vadon, H. and Massonnet, D. (1997). Readjustment of the Krafla spreading segment to crustal rifting measured by satellite radar interferometry. *Geophysical Research Letters*, **24**(15), pp. 1843–1846. doi:10.1029/97GL01934. 5.1, 5.2

Smittarello, D., Grandin, R., De Chabalier, J.-B., Doubre, C., Deprez, A., Masson, F., Socquet, A. and Saad, I. (2016). Transient deformation in the Asal-Ghoubbet Rift (Djibouti) since the 1978 diking event: Is deformation controlled by magma supply rates? *Journal of Geophysical Research: Solid Earth*, **121**(8), pp. 6030–6052. 5.2

Stork, A. L., Stuart, G. W., Henderson, C. M., Keir, D. and Hammond, J. O. (2013). Uppermost mantle (Pn) velocity model for the Afar region, Ethiopia: An insight into rifting processes. *Geophysical Journal International*, **193**, pp. 321–328. doi:10.1093/gji/ggs106. 5.1, 5.2

Tryggvason, E. (1986). Multiple magma reservoirs in a rift zone volcano: Ground deformation and magma transport during the September 1984 eruption of Krafla, Iceland. *Journal of volcanology and geothermal research*, **28**(1-2), pp. 1–44. 5.1

Van, N. P., Boyer, D., Le Mouël, J.-L. and Courtillot, V. (1981). Identification of a magma chamber in the Ghoubbet-Asal Rift (Djibouti) from a magnetotelluric experiment. *Earth and Planetary Science Letters*, **52**(2), pp. 372–380. doi:10.1016/0012-821X(81)90190-4. 5.1, 5.4.2

Viltres, R., Jónsson, S., Ruch, J., Doubre, C., Reilinger, R., Floyd, M. and Ogubazghi, G. (2020). Kinematics and deformation of the southern Red Sea region from GPS observations. *Geophysical Journal International*, **221**(3), pp. 2143–2154. 5.3

Wanless, V. D. and Behn, M. D. (2017). Spreading rate-dependent variations in crystallization along the global mid-ocean ridge system. *Geochemistry, Geophysics, Geosystems*, **18**(8), pp. 3016–3033. doi:10.1002/2017GC006924. 5.1, 5.4.3

Weiss, J. R., Qiu, Q., Barbot, S., Wright, T. J., Foster, J. H., Saunders, A., Brooks, B. A., Bevis, M., Kendrick, E., Ericksen, T. L. et al. (2019). Illuminating subduction zone rheological properties in the wake of a giant earthquake. *Science advances*, **5**(12), p. eaax6720. doi:10.1126/sciadv.aax6720. 5.4.2

Weiss, J. R., Walters, R. J., Morishita, Y., Wright, T. J., Lazecky, M., Wang, H., Hussain, E., Hooper, A. J., Elliott, J. R., Rollins, C. et al. (2020). High-resolution surface velocities and strain for Anatolia from Sentinel-1 InSAR and GNSS data. *Geophysical Research Letters*, **47**(17), p. e2020GL087376. 5.4.1

White, S. M., Meyer, J. D., Haymon, R. M., Macdonald, K. C., Baker, E. T. and Resing, J. A. (2008). High-resolution surveys along the hot spot-affected Galápagos spreading center: 2. Influence of magma supply on volcanic morphology. *Geochemistry, Geophysics, Geosystems*, **9**(9). doi:10.1029/2008GC002036. 5.1

Wright, T. J., Sigmundsson, F., Pagli, C., Belachew, M., Hamling, I. J., Brandsdóttir, B., Keir, D., Pedersen, R., Ayele, A., Ebinger, C., Einarsson, P., Lewi, E. and Calais, E. (2012). Geophysical constraints on the dynamics of spreading centres from rifting episodes on land. doi:10.1038/ngeo1428. 5.3

Xu, W., Rivalta, E. and Li, X. (2017). Magmatic architecture within a rift segment: Articulate axial magma storage at Erta Ale volcano, Ethiopia. *Earth and Planetary Science Letters*, **476**, pp. 79–86. doi:10.1016/j.epsl.2017.07.051. 5.1, 5.1, 5.1

Xu, W., Xie, L., Aoki, Y., Rivalta, E. and Jónsson, S. (2020). Volcano-wide deformation after the 2017 Erta Ale dike intrusion, Ethiopia, observed with radar interferometry. *Journal of Geophysical Research: Solid Earth*, **125**(8), p. e2020JB019562. 5.1, 5.2, 5.3, 5.3

Appendix A

Supplementary Materials for Chapter 2

A.1 Time Series Methods

We implement a small-baseline style least-squares inversion for the line of sight (LOS) displacement time-series. We incorporate the calculated variance at each epoch into a variance-covariance matrix, $\mathbf{Q_{dd}}$ (Equation A.4), as shown below for a system of 3 interferograms i_{12}, i_{13}, and i_{23}, with variance σ_{12}^2, σ_{13}^2, and σ_{23}^2, associated with the variance of each epoch σ_1^2, σ_2^2, and σ_3^2 (Equations A.1-A.3).

$$\sigma_{12}^2 = \sigma_1^2 + \sigma_2^2 \tag{A.1}$$

$$\sigma_{13}^2 = \sigma_1^2 + \sigma_3^2 \tag{A.2}$$

$$\sigma_{23}^2 = \sigma_2^2 + \sigma_3^2 \tag{A.3}$$

$$\mathbf{Q_{dd}} = \begin{bmatrix} \sigma_1^2 + \sigma_2^2 & \sigma_1^2 & -\sigma_2^2 \\ \sigma_1^2 & \sigma_1^2 + \sigma_3^2 & \sigma_3^2 \\ -\sigma_2^2 & \sigma_3^2 & \sigma_2^2 + \sigma_3^2 \end{bmatrix} \tag{A.4}$$

We introduce an additional variance of 5 mm to each interferogram (on the diagonal of the variance-covariance matrix) to account for random noise introduced during interferogram creation (such as residual unwrapping and filtering errors). Introducing this additional noise estimate also means that the variance-covariance matrix is well-conditioned and invertible.

Equations A.6-A.7 show the solution for the best linear unbiased estimator (BLUE) of a linear least squares problem in the format of Equation A.5, with the data vector, $\mathbf{d}$, the vector of model parameters, $\mathbf{m}$, and the design matrix, $\mathbf{G}$. The BLUE approach allows us to include the data variance ($\mathbf{Q_{dd}}$) into a least-squares inversion for the minimum-norm of the model parameters ($\hat{\mathbf{m}}$), and extract model variances from the model variance-covariance matrix ($\mathbf{Q_{mm}}$) (Henderson, 1975). We perform no further filtering on the whole image time-series.

$$\mathbf{d} = \mathbf{Gm} \tag{A.5}$$

$$\hat{\mathbf{m}} = \mathbf{Q_{mm}G^T Q_{dd}^{-1} d} \tag{A.6}$$

$$\mathbf{Q_{mm}} = (\mathbf{G^T Q_{dd}^{-1} G})^{-1} \tag{A.7}$$

In order to resolve horizontal rift-perpendicular and vertical motions from the ascending and descending LOS time series, we implement a least-squares inversion after Wright et al. (2004), utilising the look vectors for each pixel which point from the ground to the satellite. As we only have 2 observations for each point (ascending and descending) we cannot resolve true 3D ground motions (East, North, Vertical). To resolve this we assume all horizontal motion is perpendicular to the rift (extension/contraction), which allows us to only solve for ground motion in the vertical and horizontal rift-perpendicular directions (2D). Due to the variation in acquisitions in the ascending and descending time series, we cannot solve for 2D motions at every epoch (note the gap in the 2D time series between Feb-Sep 2017 due to missing ascending acquisitions). We set a maximum time difference of 1 week between the ascending and descending acquisitions used to resolve 2D ground motions at an epoch, in order to maintain that the ground does not significantly change between the acquisitions. The date used for the 2D epoch is set to the later of the 2 acquisition dates.

A.2 Supplementary Figures & Tables

Date	Depth (m)	Type	Credit	Source
20.10.2014	10-20	TP	Wolfgang Piecha	mountain-forecast.com
01-31.12.2014	5-10	TP	Joshua Paul Shefman	shefman.com
10.01.2015	5-10	TP	Joel Santos	gettyimages.ca
01-28.02.2015	5-20	TP	Martin Hertel	volcanodiscovery.com
01-28.02.2015	1-10	FR	Volcano Discovery	volcanodiscovery.com
12.02.2015	10-20	TP	Martin Hertel	gettyimages.ca
24.02.2015	5-20	TP	Manfred Thuerig	dreamstime.com
25.02.2015	10-20	TP	Manfred Thuerig	dreamstime.com
19-21.11.2015	1-5	FR	Volcano Discovery	volcanodiscovery.com
21.11.2015	5-10	TP	Volcano Discovery	volcanodiscovery.com
03.01.2016	5-10	TP	Yi Sun	nationalgeographic.com
15-16.01.2016	0	FR	Volcano Discovery	volcanodiscovery.com
12-15.02.2016	5-7	FR	Volcano Discovery	volcanodiscovery.com
01-30.11.2016	0	FR	Volcano Discovery	volcanodiscovery.com
29.12.2016	5-15	TP	Volcano Discovery	volcanodiscovery.com
29-31.12.2016	0.5-1	FR	Volcano Discovery	volcanodiscovery.com
16-19.01.2017	0	FR	Volcano Discovery	volcanodiscovery.com
17.01.2017	0	TP	Volcano Discovery	volcanodiscovery.com
01-14.02.2017	80-100	FR	Volcano Discovery	volcanodiscovery.com
20.03.2017	30-60	TP	Jean-Michel Escarpit	volcano.si.edu
01-30.04.2017	30-60	TP	toucan.photo	volcano.si.edu
11-15.04.2017	40-50	FR	Volcano Discovery	volcanodiscovery.com
01-15.06.2017	35-45	FR	Volcano Discovery	volcanodiscovery.com
16.09.2017	50-80	TP	Chris Moore	Author's photo
16.12.2017	30-40	FR	Volcano Discovery	volcanodiscovery.com
31.12.2017	30-60	TP	Culture Volcan	volcano.si.edu
13-26.01.2018	80-130	TP	Stephan Tommasini	volcanodiscovery.com
26.06.2018	50-80	TP	Simeon Brown	volcanodiscovery.com
01-31.09.2018	65-85	FR	Volcano Discovery	volcanodiscovery.com

Table A.1: Table of all tourist photos (TP) and field reports (FR) describing the Erta 'Ale lava lake depth. Depths of 0 m indicate observations of lava lake overflows.

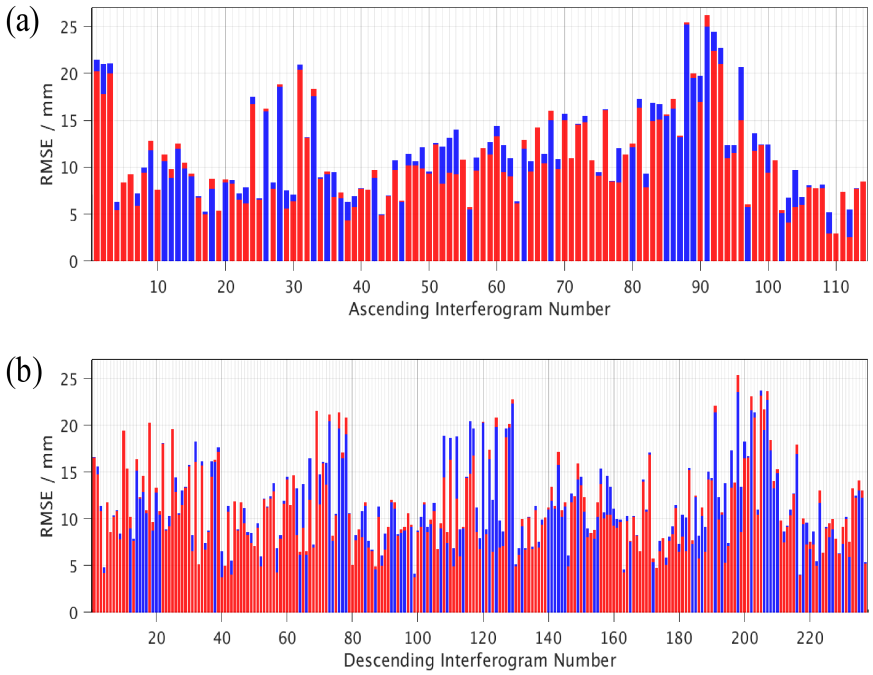

Figure A.1: Performance of removing a linear atmospheric trend (red) against uncorrected phase (blue) in the non-deforming background region around Erta Ale (masking a $\sim 10 \times 10$ km region, centred on the eruption site), for each ascending (a) and descending (b) Sentinel-1 interferogram. The lower value of RMSE (from either the linear atmosphere corrected or uncorrected phase) is plotted on-top of the higher value for each interferogram. The linear atmospheric trend is calculated from a $\sim 12 \times 5$ km subset of this region, to the south of Erta Ale. The linear atmospheric correction provides a mean improvement of ~ 9 % (1 mm) in mean root-mean-square error (RMSE) of the residual phase, relative to the mean value, over the whole background region.

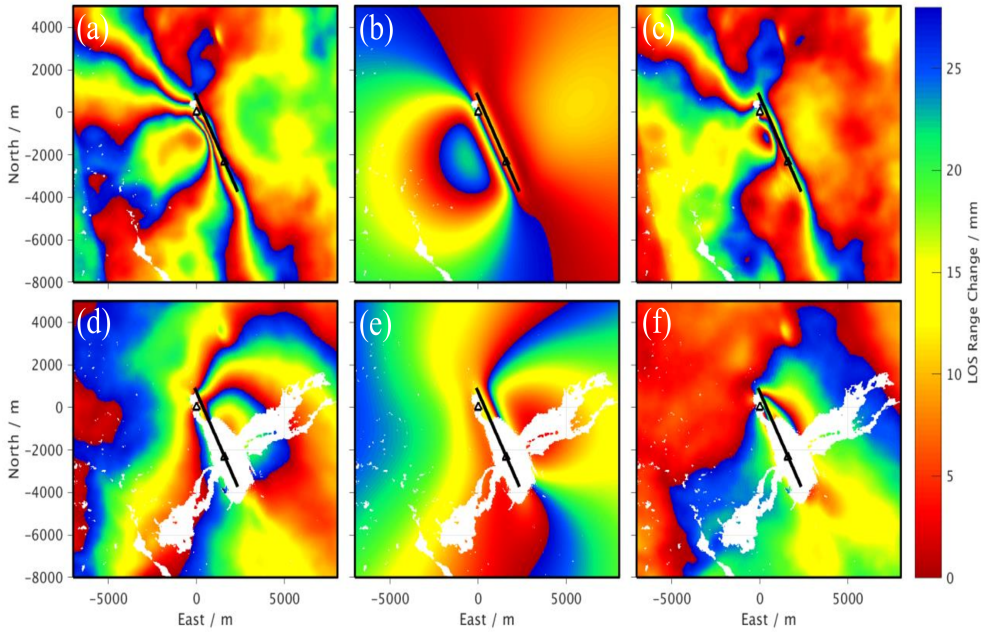

Figure A.2: Ascending (a-c) Sentinel-1 data, model and residual for pre-eruptive interferogram 23.11.2014-11.01.2017. Descending (d-f) Sentinel-1 data, model and residual for pre-eruptive interferogram 16.11.2014-04.01.2017. One colour cycle (red-blue) represents 27 mm of line of sight (LOS) range change away from the satellite. Location of dyke 1 is shown as a black line, with the lava lake and eruption site shown as triangles.

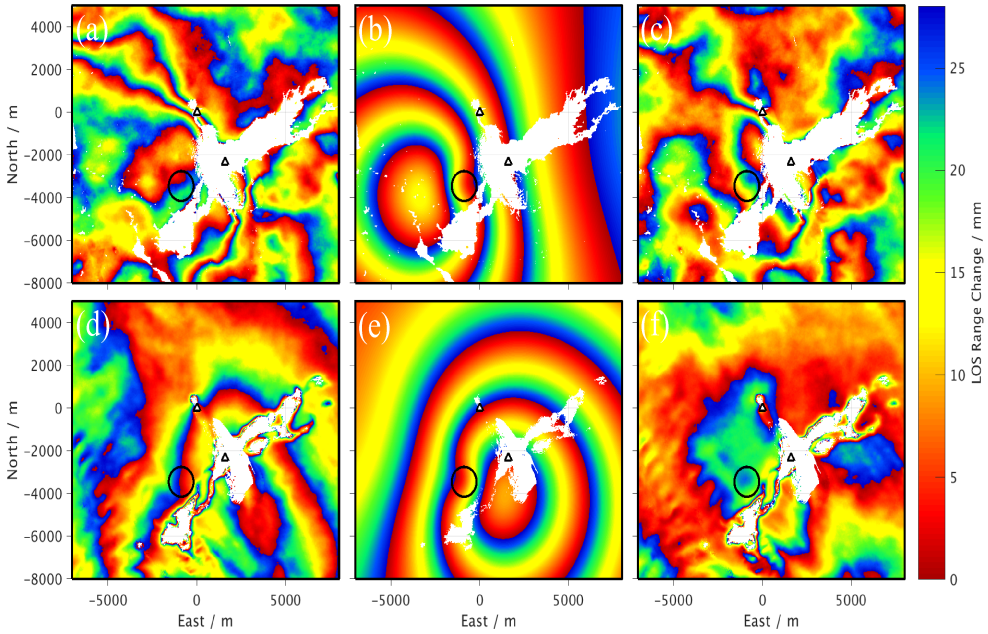

Figure A.3: Ascending (a-c) Sentinel-1 data, model and residual for late-stage eruption interferogram 14.09.2017-12.06.2019. Descending (d-f) Sentinel-1 data, model and residual for late-stage eruption interferogram 13.09.2017-11.06.2019. One colour cycle (red-blue) represents 27 mm of line of sight (LOS) range change away from the satellite. Location of vertical prolate spheroidal source is shown as a black circle (top down view), with the lava lake and eruption site shown as triangles.

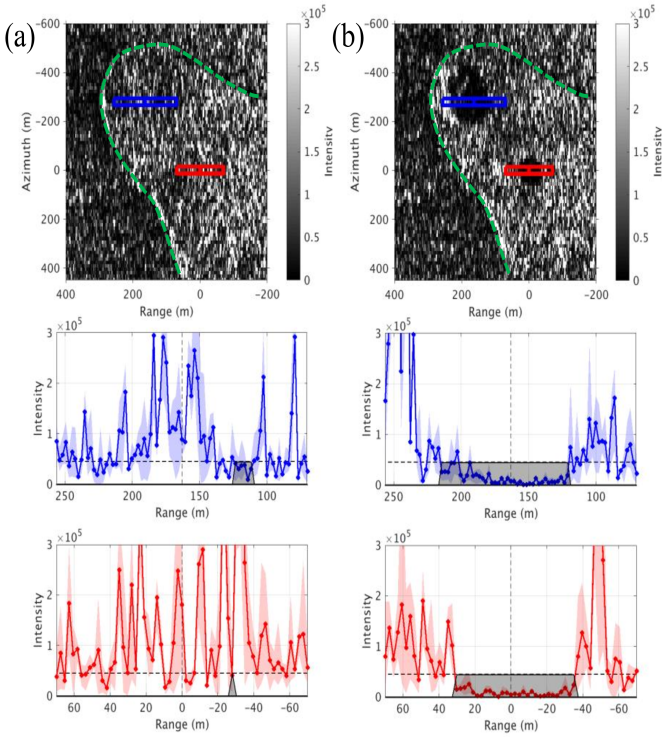

Figure A.4: Descending Sentinel-1 re-sampled single look complex images of the north and south pits at Erta 'Ale before the eruption on 04 January 2017 (a), and after the initial intrusion on 28 January 2017 (b). Images are in radar coordinates, relative to the Erta 'Ale lava lake. Profiles through the north (blue) and south (red) pits show the lengths of shadows created by the depth of the pits (grey shading on profiles). Profiles show the mean, and the maximum and minimum values of reflection intensity at each increment along the profile. The green dashed line shows the outline of the Erta 'Ale summit caldera.

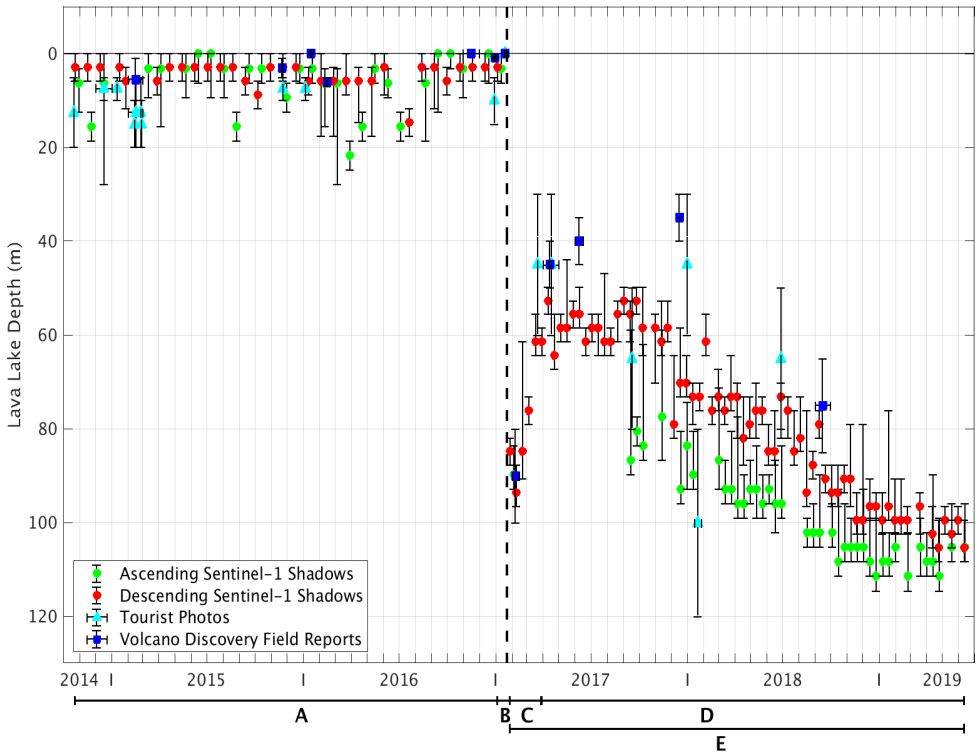

Figure A.5: Time series from October 2014 to April 2018 of Erta 'Ale lava lake depths calculated from Sentinel-1 ascending (green circles) and descending (red circles) SAR shadows. Tourist photos (light blue triangles) taken from the internet (see Table A.1 for citations), and Volcano Discovery field reports (dark blue squares) Volcano Discovery (2017) are included to help validate the SAR shadow depths. The eruption date in Jan 2017 is marked by the black dashed line. A lava lake depth of 0 m represents when the lake is level with the pit rim (Figure 2.6). Time periods A-E, as shown in Figure 2.2, are indicated below the time axis.

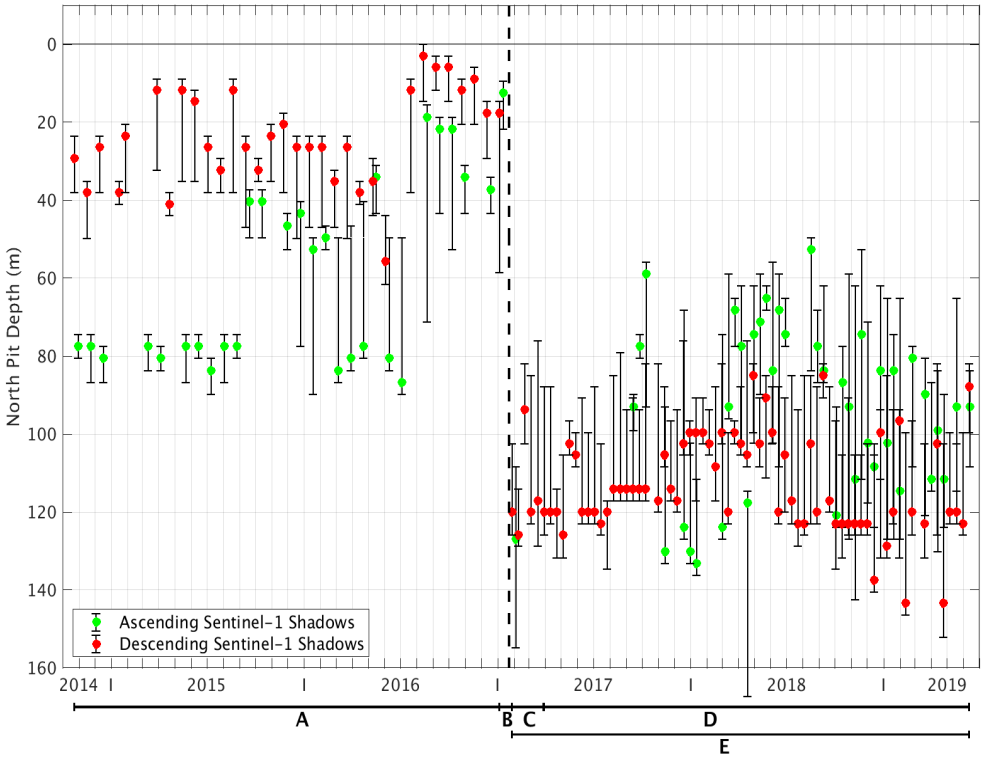

Figure A.6: Time series of Erta 'Ale north pit depths calculated from ascending (green) and descending (red) Sentinel-1 SAR shadow lengths. The eruption date is marked by the black dashed line. A pit depth of 0 m represents when the pit level with the pit rim (Figure 2.6). Time periods A-E, as shown in Figure 2.2, are indicated below the time axis.

References

Henderson, C. R. (1975). Best Linear Unbiased Estimation and Prediction under a Selection Model. *Biometrics*, **31**(2). doi:10.2307/2529430. A.1

Volcano Discovery (2017). Erta Ale (Ethiopia) volcano news. *[Online]. [Accessed 15 March 2019]. Available from: www.volcanodiscovery.com/erta_ale/news.html.* A.5

Wright, T. J., Parsons, B. E. and Zhong, L. (2004). Toward mapping surface deformation in three dimensions using InSAR. *Geophysical Research Letters*, **31**(L01607). doi:10.1029/2003GL018827. A.1

Appendix B

Supplementary Materials for Chapter 3

B.1 Time Series Methodology

Our SBAS style and time series methodology from unwrapped interferograms to 3D (rift-perpendicular, rift-parallel, vertical) average velocities consists of the following steps:

1. Invert each pixel for a LOS displacement time series using an SBAS style least-squares inversion as shown in Equation B.1 for a network of 5 interferograms (i_{01}, i_{02}, i_{12}, i_{13}, i_{23}) covering 4 epochs (d_0, d_1, d_2, d_3) with zero displacement at the first epoch ($d_0 = 0$). We perform this inversion at each pixel in the frame using all available coherent interferograms, rejecting pixels where the interferogram network at any epoch is disconnected.

$$\begin{bmatrix} i_{01} \\ i_{02} \\ i_{12} \\ i_{13} \\ i_{23} \end{bmatrix} = \begin{bmatrix} 1 & 0 & 0 \\ 0 & 1 & 0 \\ -1 & 1 & 0 \\ -1 & 0 & 1 \\ 0 & -1 & 1 \end{bmatrix} \begin{bmatrix} d_1 & d_2 & d_3 \end{bmatrix} \tag{B.1}$$

2. Estimate the error in the time series using the RMS misfit.

   (a) Filter the displacement time series at each pixel using a Laplacian filter with a temporal width of 3 epochs with a scaling factor (K) of 3 (see Equation B.2 for a time series of unfiltered displacements (d_0, d_1, d_2, d_3), filtered displacements (f_0, f_1, f_2, f_3) and the time gaps between epochs (t_{01}, t_{12},

t_{23}).

$$\begin{bmatrix} d_0 \\ d_1 \\ d_2 \\ d_3 \end{bmatrix} = K \begin{bmatrix} 1/K & 0 & 0 & 0 \\ -t_{01} & t_{01}+t_{12} & -t_{12} & 0 \\ 0 & -t_{12} & t_{12}+t_{23} & -t_{23} \\ 0 & 0 & 0 & 1/K \end{bmatrix} \begin{bmatrix} f_0 & f_1 & f_2 & f_3 \end{bmatrix} \tag{B.2}$$

(b) For each pixel, we calculate the misfit of the unfiltered time series against the Laplacian filtered time series at every epoch ($m_{xyt} = d_{xyt} - f_{xyt}$).

(c) Using Equation B.3, we calculate the RMS misfit of each pixel (r_{xy}) using the time series of misfits (m_t), and the RMS misfit of each epoch (r_t) using the misfit of every pixel (m_{xy}), where N is the total number of points in time or space.

$$r = \sqrt{\frac{m_1^2 + m_2^2 + ...m_N^2}{N}} \tag{B.3}$$

(d) To resolve an RMS misfit value for each pixel at every epoch (r_{xyt}), we scale the spatial RMS misfit map (r_{xy}) to the value of temporal RMS misfit at each epoch (r_t) using the RMS misfit of r_{xy}, where N and M are the total number of points space in the East and North directions respectively.

$$r_{xyt} = r_{xy} \frac{r_t}{\sqrt{\frac{r_{11}^2 + r_{12}^2 + r_{21}^2 + ...r_{NM}^2}{NM}}} \tag{B.4}$$

3. Calculate the APS and remove from the LOS displacement time series.

(a) Low-pass filter the time series of each pixel using a local linear trend with a fixed filter width of ± 0.5 years from the target epoch. The weighting of the epoch displacements is dependant on the temporal distance from the target epoch, the RMS misfit value, and outlier rejection. By editing the "smooth" function in Matlab, we convert the RMS misfit values into weights using the Bi-Square function (Cleveland and Devlin, 1988), where zero weight is given to RMS values that are > 6 standard deviations of the local misfits.

(b) Remove the low-pass filtered time series from the unfiltered data to create a high-pass filtered time series.

(c) On the high-pass temporal filtered data, apply a low-pass spatial filter for each epoch using a Gaussian kernel with a half-width of $\sim$ 2 km to resolve the APS.

(d) Remove the calculated APS from the displacement time series, and correct for any residual orbital or atmospheric errors by inverting for and removing planar ramps in space, and a linear trend of phase with elevation.

4. Calculate the average LOS velocity for each pixel from the time series of displacements (d_1, d_2, ... d_N, with time steps t_1, t_2, ... t_N) by inverting for the average displacement rate (v) and a constant offset (c, to allow the displacement at $t = 0$ to be non-zero). To resolve uncertainties in the average velocity estimates (Q_{mm}), we include a data VCM (Q_{dd}) by using the time series of RMS misfit values at each pixel (r_1, r_2, ... r_N) as independent error sources (see Equations B.5-B.8).

$$Q_{dd} = \begin{bmatrix} r_1^2 & 0 & ... & 0 \\ 0 & r_2^2 & ... & 0 \\ ... & ... & ... & ... \\ 0 & 0 & ... & r_N^2 \end{bmatrix} \tag{B.5}$$

$$G = \begin{bmatrix} t_1 & 1 \\ t_2 & 1 \\ ... & ... \\ t_N & 1 \end{bmatrix} \tag{B.6}$$

$$Q_{mm} = (G^T Q_{dd}^{-1} G)^{-1} \tag{B.7}$$

$$\begin{bmatrix} v & c \end{bmatrix} = Q_{mm} G^T Q_{dd}^{-1} \begin{bmatrix} d_1 \\ d_2 \\ ... \\ d_N \end{bmatrix} \tag{B.8}$$

5. Connect the frame LOS velocity maps within their respective tracks.

   (a) For each track, we sub-sample the frame velocity maps to 5×5 km in frame overlap regions, and 10×10 km elsewhere.

   (b) Keeping one frame in the track uncorrected, we reference the other frames to it by inverting for planar ramps in space for each frame such that the values in the frame overlap regions are equal. We then remove the ramps from the respective frames, and use the mean value in the frame overlap regions when combining the frames into a single track.

6. Reference the track LOS velocities to a stable Nubia GNSS reference frame.

   (a) Convert the GNSS velocities in the east (E) and north (N) directions to rift-perpendicular ($H1$) and rift-parallel ($H2$) directions using Equation B.9, using the orientation of the rift axis (α) of 151°N. Then interpolate smooth GNSS velocity fields in the rift-perpendicular and rift-parallel directions using the natural neighbour algorithm and the "griddata" function in Matlab.

$$\begin{bmatrix} E \\ N \end{bmatrix} = \begin{bmatrix} \cos(\alpha) & -\sin(\alpha) \\ \sin(\alpha) & -\cos(\alpha) \end{bmatrix} \begin{bmatrix} H1 & H2 \end{bmatrix} \tag{B.9}$$

(b) After masking areas with surface deformation that is not related to the long-wavelength plate spreading (i.e. related to volcanic or anthropogenic activity), we sub-sample the track velocities to 5×5 km in track overlap regions, and 10×10 km elsewhere.

(c) Using the points where there are ascending, descending, and interpolated GNSS data, we invert for 3D velocities (rift-perpendicular, rift-parallel, vertical, see Equation 3.1) and a quadratic function for each track. We then remove the quadratic function from each track to resolve LOS velocities referenced to stable Nubia.

7. Resolve 3D velocities (rift-perpendicular, rift-parallel, vertical) at each pixel (see Equation 3.1), using the smooth GNSS rift-parallel velocity field to help constrain the inversion (e.g. Weiss et al., 2020), and uncertainties in LOS velocity as independent errors in a VCM (as shown in Equation B.5).

B.2 Supplementary Tables & Figures

Supplementary Table B.1 and Supplementary Figures B.1-B.9.

Frame	Start Date	End Date	No. of IFGs
006D_07728_131313	11.11.2014	30.06.2019	198
006D_07929_131313	18.10.2014	17.08.2019	334
014A_07524_101303	23.11.2014	24.02.2019	85
014A_07688_131313	23.11.2014	18.07.2019	223
014A_07885_131313	30.10.2014	18.07.2019	187
079D_07503_061113	23.11.2015	10.08.2019	178
079D_07694_131313	23.10.2014	17.07.2019	337
079D_07894_131313	23.10.2014	17.07.2019	277
087A_07674_131313	11.10.2014	11.03.2017	92
087A_07889_131313	11.10.2014	11.03.2017	82
116A_07590_071313	13.10.2014	13.07.2019	316
116A_07768_131305	12.12.2014	13.07.2019	193

Table B.1: Start date, end date (DD.MM.YYYY), and the number of interferograms (IFGs) used to build the displacement time series for each frame. Frame names are defined by the track (e.g. 006D for descending track 6), the frame ID (e.g. 07728), and the number of bursts in each of the 3 sub-swaths within the frame (e.g. 131313 for a maximum of 13 bursts in each sub-swath).

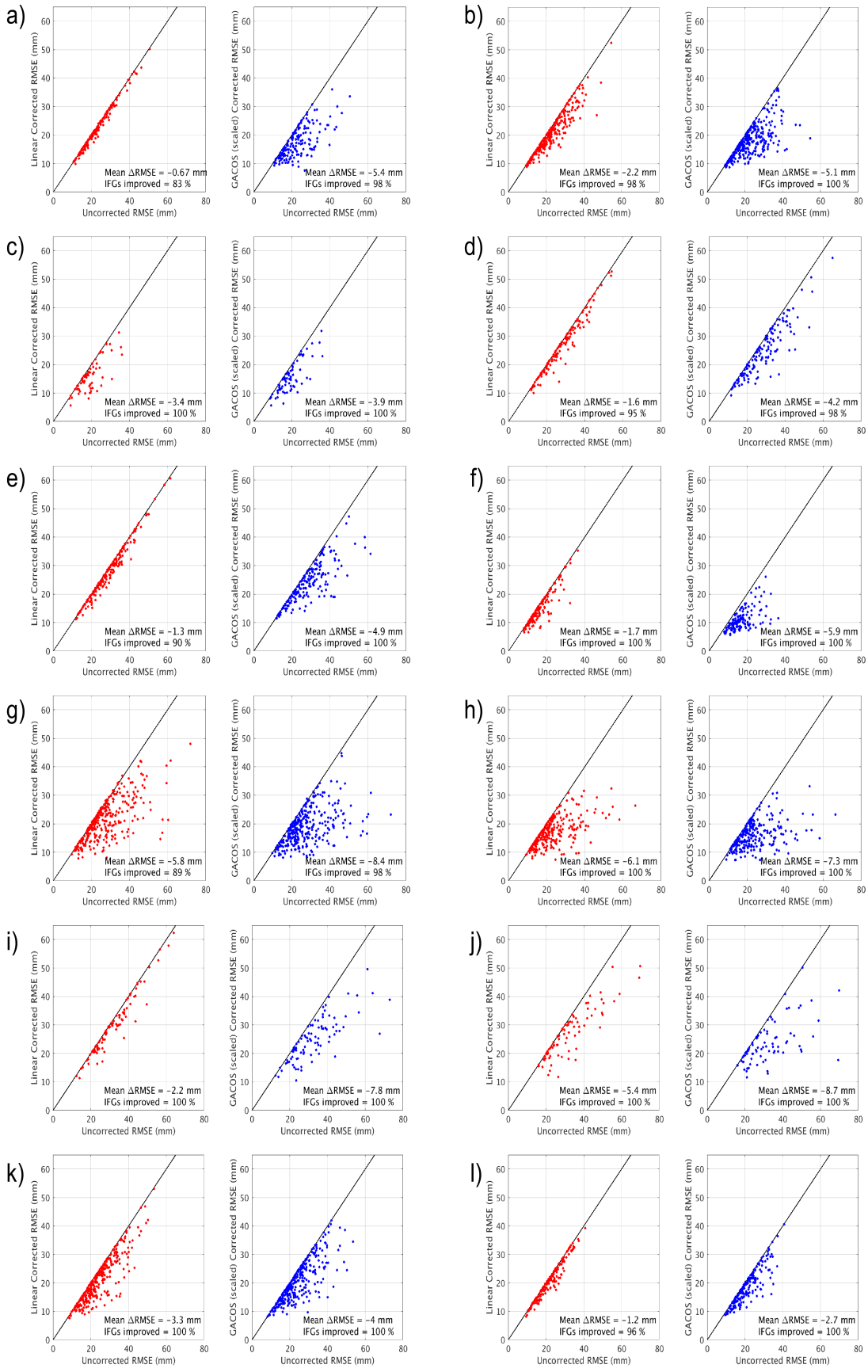
a)
Linear Corrected RMSE (mm)
Mean ΔRMSE = -0.67 mm
IFGs improved = 83 %
GACOS (scaled) Corrected RMSE (mm)
Mean ΔRMSE = -5.4 mm
IFGs improved = 98 %
Uncorrected RMSE (mm)
b)
Mean ΔRMSE = -2.2 mm
IFGs improved = 98 %
Mean ΔRMSE = -5.1 mm
IFGs improved = 100 %
c)
Mean ΔRMSE = -3.4 mm
IFGs improved = 100 %
Mean ΔRMSE = -3.9 mm
IFGs improved = 100 %
d)
Mean ΔRMSE = -1.6 mm
IFGs improved = 95 %
Mean ΔRMSE = -4.2 mm
IFGs improved = 98 %
e)
Mean ΔRMSE = -1.3 mm
IFGs improved = 90 %
Mean ΔRMSE = -4.9 mm
IFGs improved = 100 %
f)
Mean ΔRMSE = -1.7 mm
IFGs improved = 100 %
Mean ΔRMSE = -5.9 mm
IFGs improved = 100 %
g)
Mean ΔRMSE = -5.8 mm
IFGs improved = 89 %
Mean ΔRMSE = -8.4 mm
IFGs improved = 98 %
h)
Mean ΔRMSE = -6.1 mm
IFGs improved = 100 %
Mean ΔRMSE = -7.3 mm
IFGs improved = 100 %
i)
Mean ΔRMSE = -2.2 mm
IFGs improved = 100 %
Mean ΔRMSE = -7.8 mm
IFGs improved = 100 %
j)
Mean ΔRMSE = -5.4 mm
IFGs improved = 100 %
Mean ΔRMSE = -8.7 mm
IFGs improved = 100 %
k)
Mean ΔRMSE = -3.3 mm
IFGs improved = 100 %
Mean ΔRMSE = -4 mm
IFGs improved = 100 %
l)
Mean ΔRMSE = -1.2 mm
IFGs improved = 96 %
Mean ΔRMSE = -2.7 mm
IFGs improved = 100 %

Figure B.1: Residual root-mean-square error (RMSE) for all interferograms in each frame after applying atmospheric phase delay corrections using a linear correlation of phase with elevation (red), and a scaled GACOS atmospheric model (blue) (Yu et al., 2017, 2018). Also shown is the mean change in RMSE, and the percentage of interferograms where the RMSE was improved following the correction. Frames: (a) 006D-07728-131313, (b) 006D-07929-131313, (c) 014A-07524-101303, (d) 014A-07688-131313, (e) 014A-07885-131313, (f) 079D-07503-061113, (g) 079D-07694-131313, (h) 079D-07894-131313, (i) 087A-07674-131313, (j) 087A-07889-131313, (k) 116A-07590-071313, (l) 116A-07768-131305.

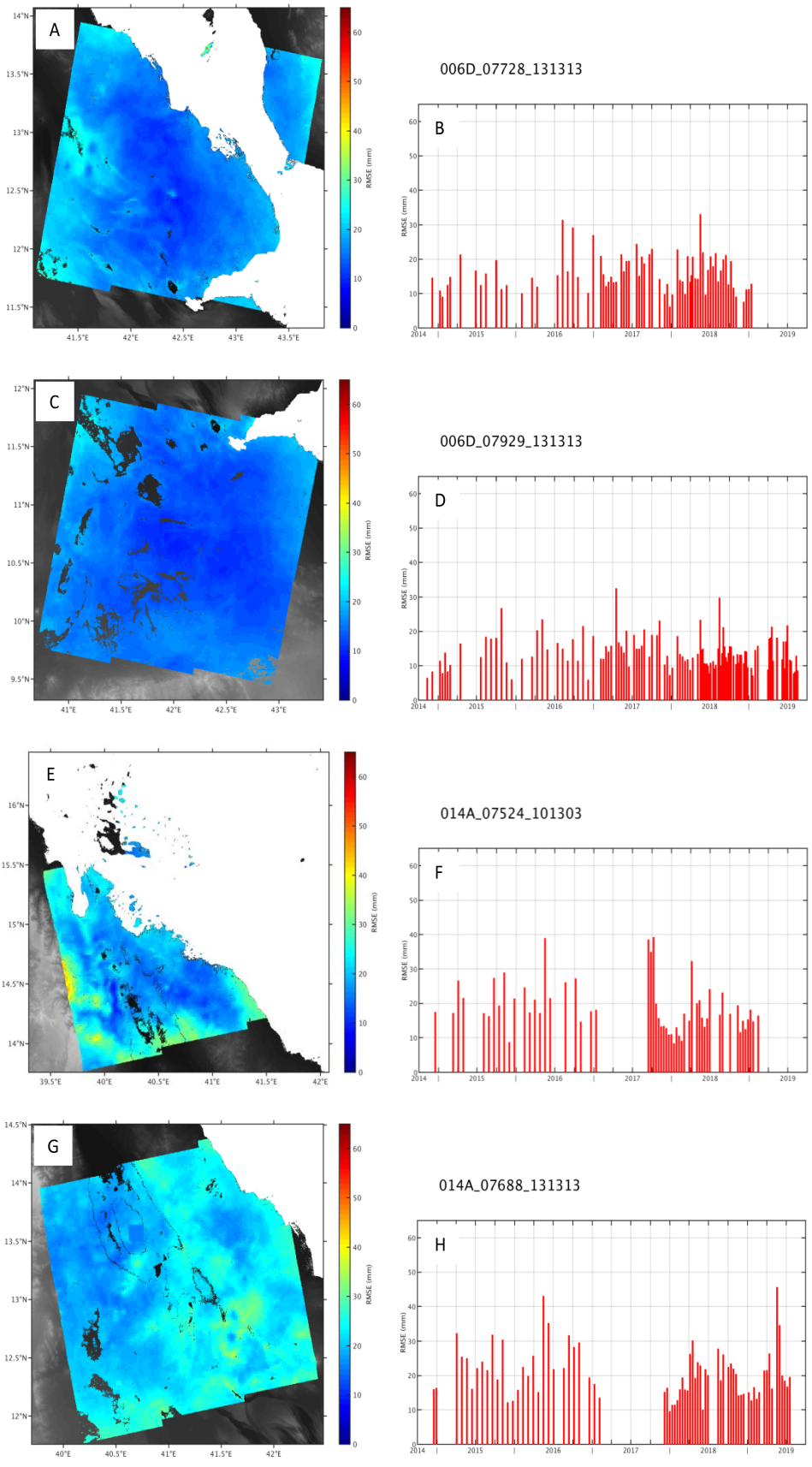
A
006D_07728_131313
B
C
006D_07929_131313
D
E
014A_07524_101303
F
G
014A_07688_131313
H
RMSE (mm)

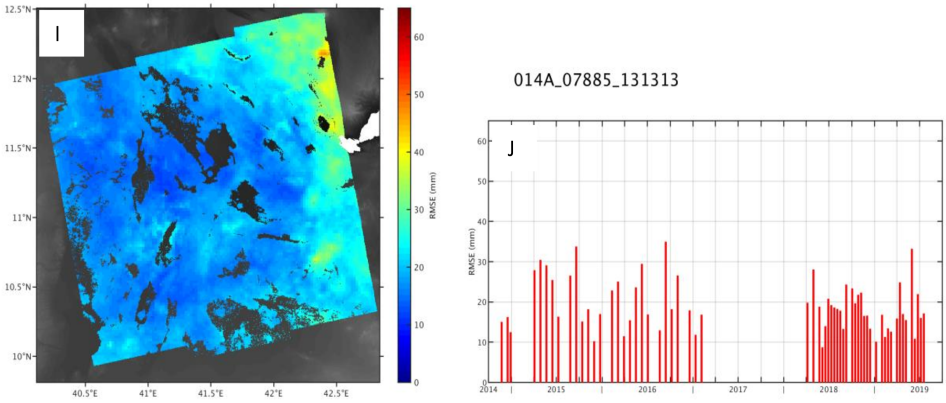
I
014A_07885_131313
J
RMSE (mm)

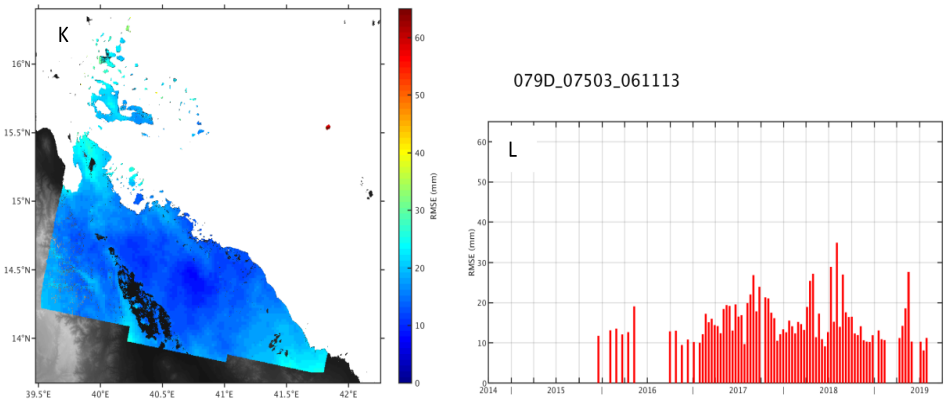
K
079D_07503_061113
L
RMSE (mm)

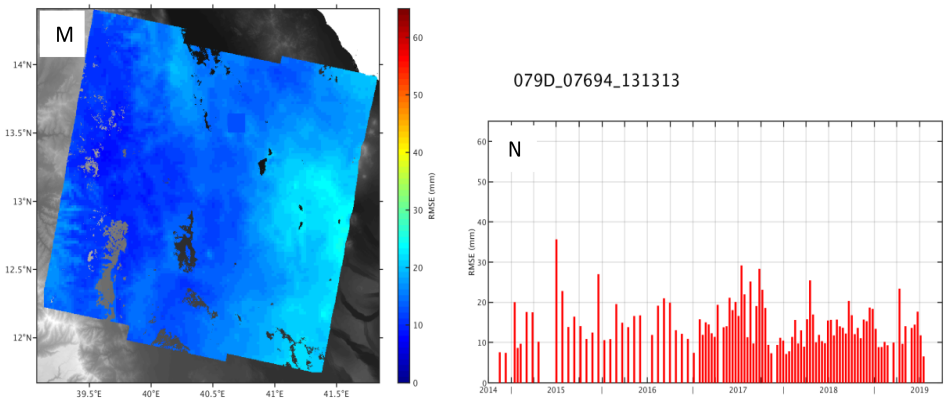
M
079D_07694_131313
N
RMSE (mm)

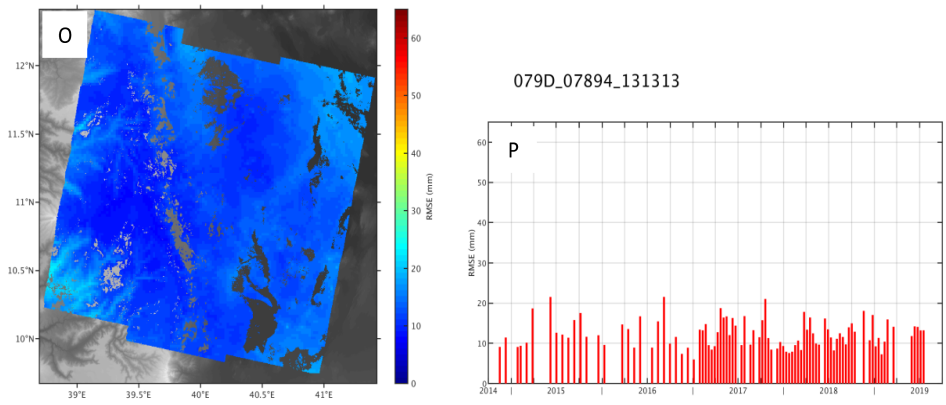
O
079D_07894_131313
P
RMSE (mm)

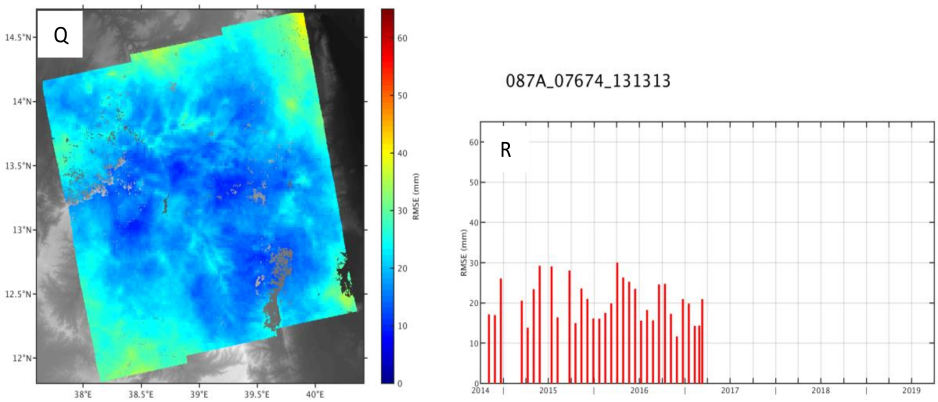
Q
087A_07674_131313
R
RMSE (mm)

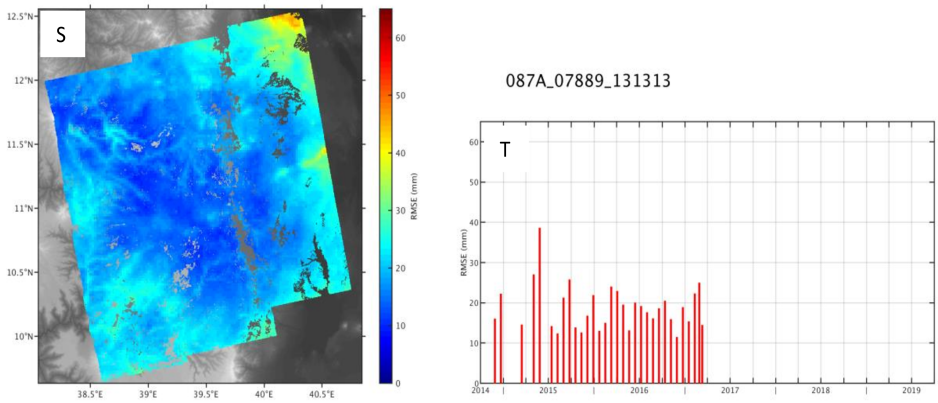
S
087A_07889_131313
T
RMSE (mm)

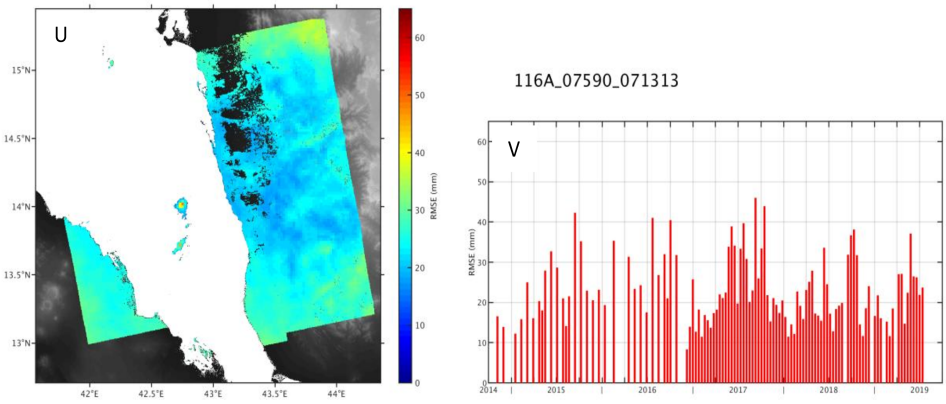
U
116A_07590_071313
V
RMSE (mm)

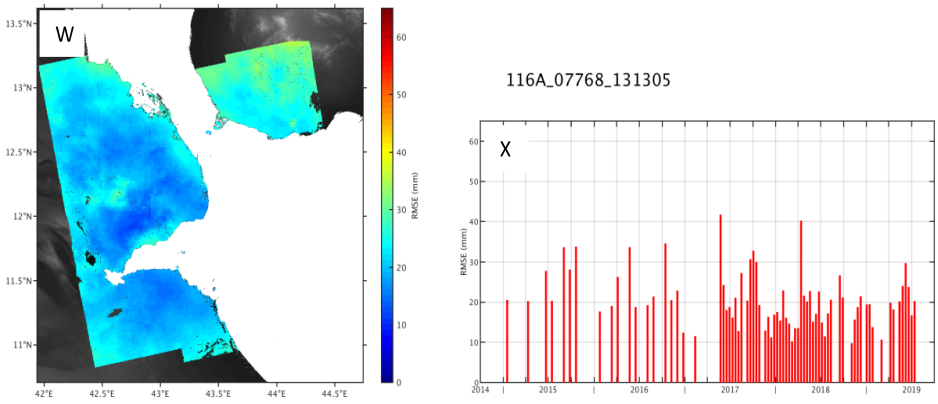
W
116A_07768_131305
X
RMSE (mm)

Figure B.2: Frame root-mean-square error (RMSE) in space for each pixel (A,C,E,G,I,K,M,O,Q,S,U,W) and time for each epoch (B,D,F,H,J,L,N,P,R,T,V,X). Frames: (A,B) 006D-07728-131313, (C,D) 006D-07929-131313, (E,F) 014A-07524-101303, (G,H) 014A-07688-131313, (I,J) 014A-07885-131313, (K,L) 079D-07503-061113, (M,N) 079D-07694-131313, (O,P) 079D-07894-131313, (Q,R) 087A-07674-131313, (S,T) 087A-07889-131313, (U,V) 116A-07590-071313, (W,X) 116A-07768-131305.

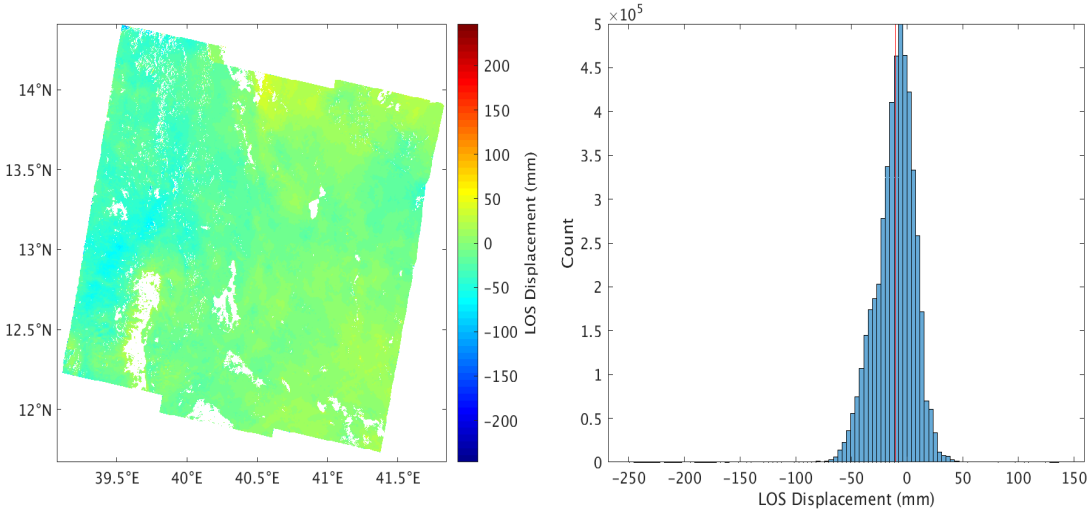

Figure B.3: Demonstrating line of sight (LOS) displacement bias ('phase bias') from the difference between 12 and 24 day interferogram 'daisy-chain' stacks for frame 079D-07694-131313 between 06 December 2017 and 11 February 2019. Residuals shown in map view and as a histogram with the mean value indicated by a vertical red line.

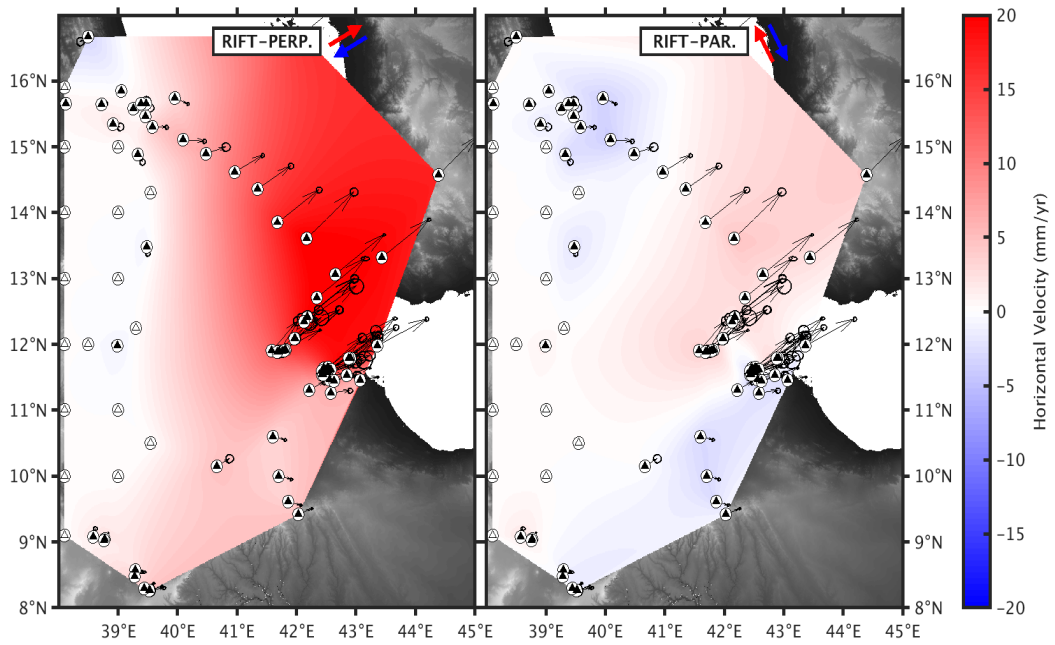

Figure B.4: GNSS derived rift-perpendicular (positive towards 61°N) and rift-parallel (positive towards -29°N) horizontal velocity fields. Black triangles indicate the subset of GNSS stations used from (King et al., 2019) with velocity vectors and error ellipses White triangles indicate the synthetic stations with zero velocity on the stable Nubian plate used to help constrain the velocity fields.

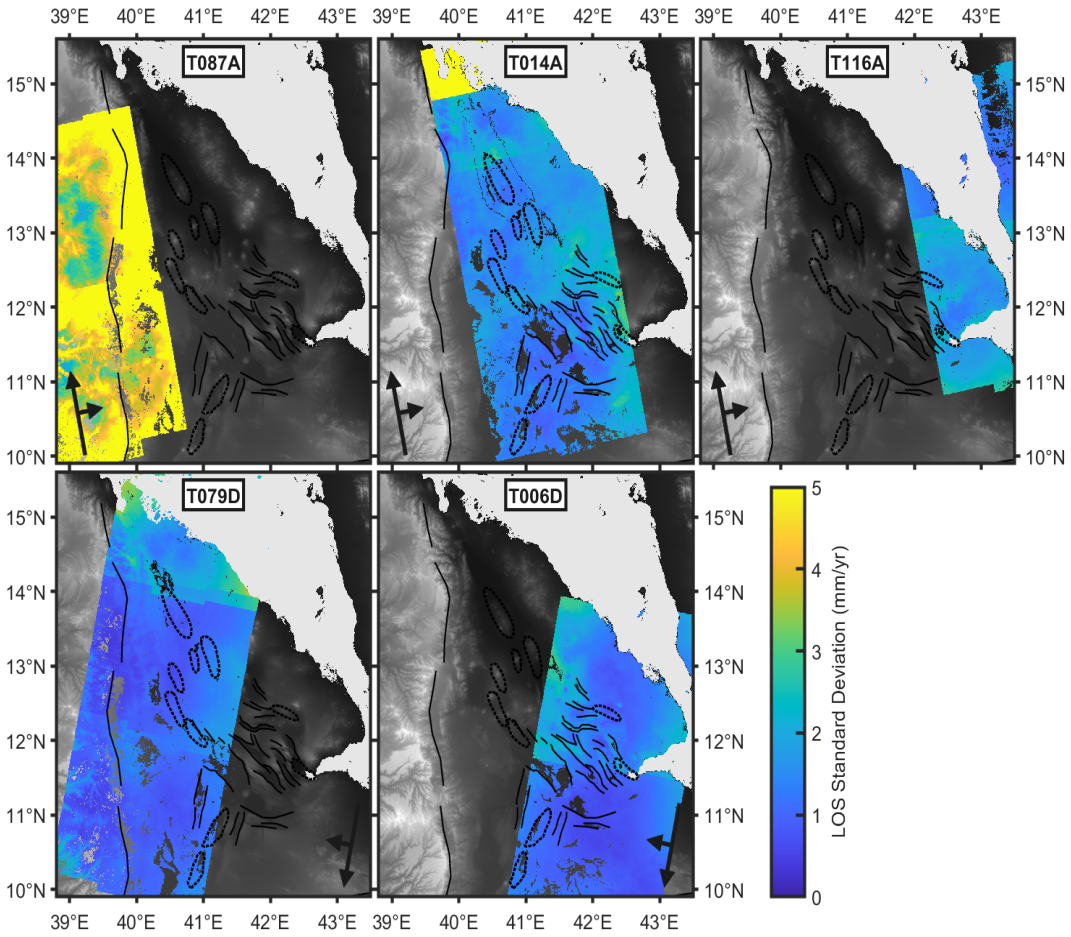

Figure B.5: LOS standard deviation over the Afar region between November 2014 and August 2019 from Sentinel-1 tracks T087A, T014A, T116A, T079D, and T006D. Colour scale is limited to 5 mm to highlight variation in regions of low variance. Maximum standard deviation for each track is (2 s.f.): 15 mm/yr (T087A), 13 mm/yr (T014A), 3.2 mm/yr (T116A), 3.8 mm/yr (T079D), 3.1 mm/yr (T006D). Volcanic segments and key faults are shown as black dashed outlines and black solid lines respectively.

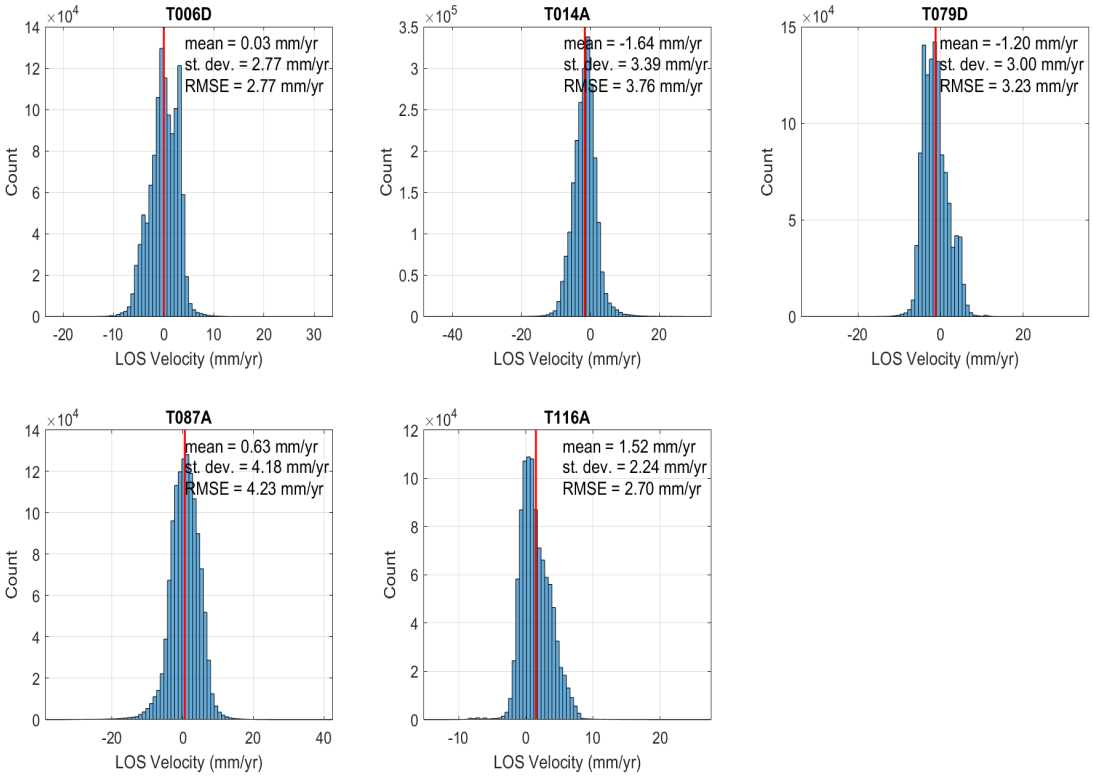

Figure B.6: Histograms of line of sight (LOS) velocity misfits for all points in the overlap region of each track. Misfits are calculated by excluding each track in turn from the 3D inversion, then projecting the resulting 3D velocity field in the track overlap region into the track LOS, and differencing from the original LOS observation. The mean (red lines), standard deviation, and RMSE of each set of misfits are displayed.

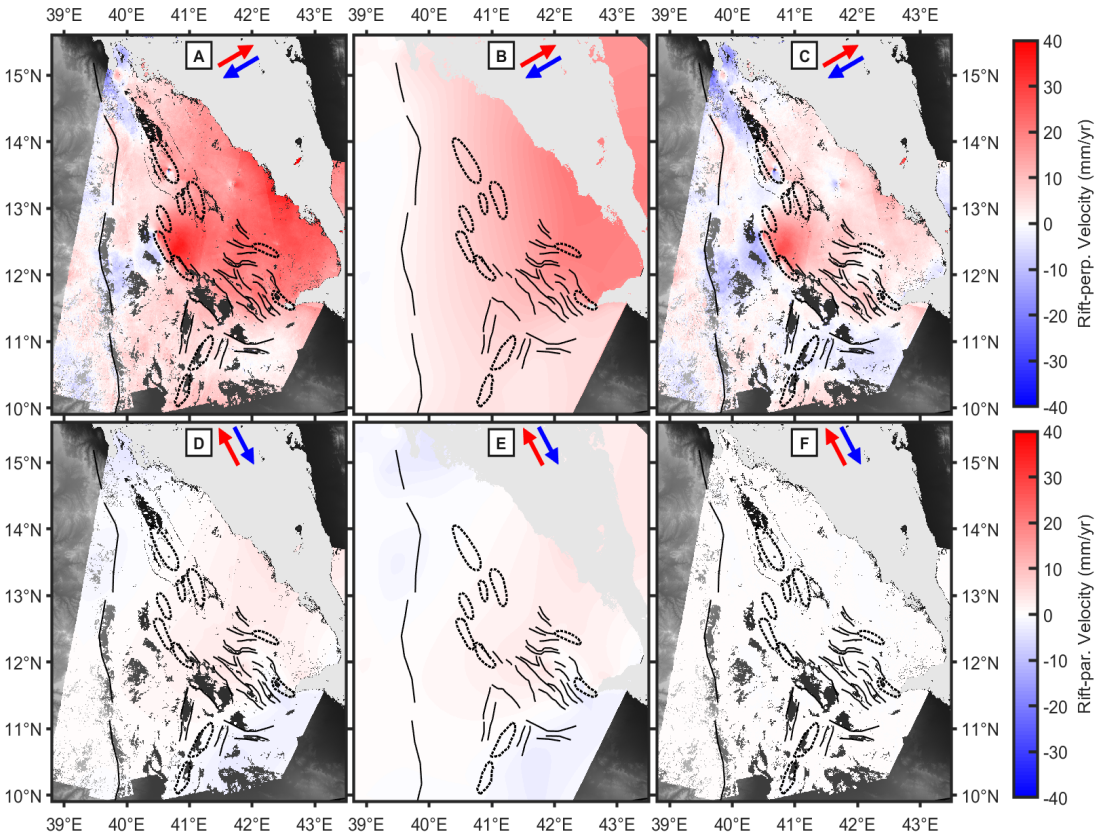

Figure B.7: The contributions to the rift-perpendicular (A, B, C) and rift-parallel (D, E, F) velocity maps (see Figure 3.3) from interpolated GNSS velocities (see Figure B.4) and Sentinel-1 InSAR. The isolated contribution of InSAR here (C, F) is the total velocity field (A, D) minus the interpolated GNSS velocity field (B, E).

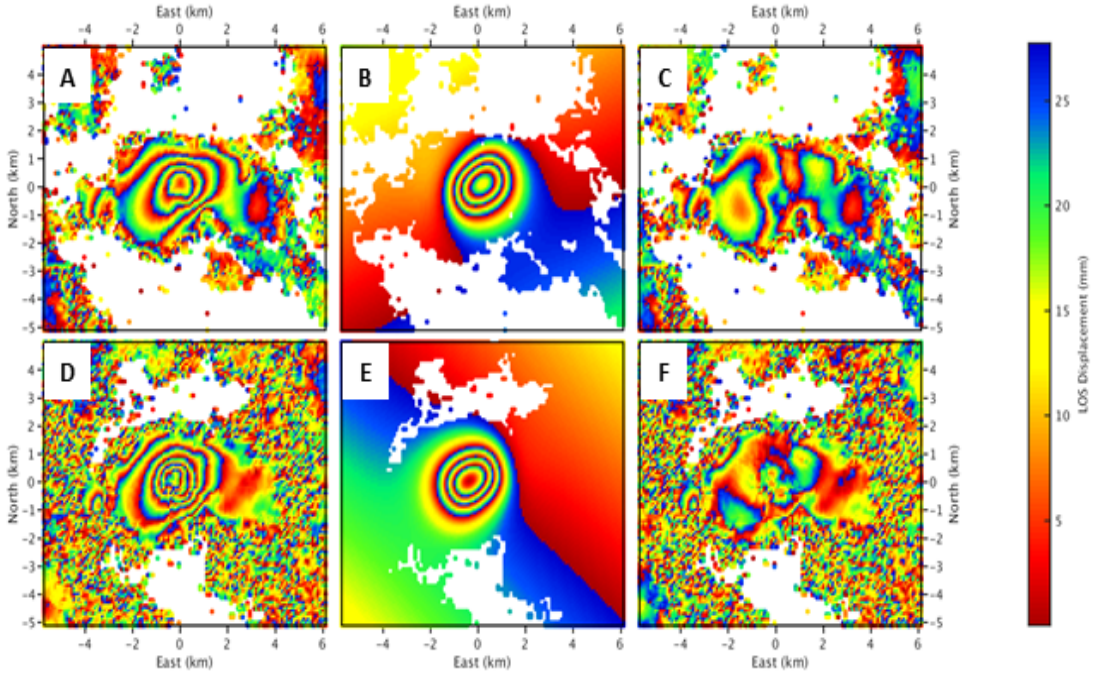

Figure B.8: Sentinel-1 data (A,D), GBIS (Bagnardi and Hooper, 2018) model (B,E), and residual (C,F), for 2015-19 surface deformation observed using tracks T079D (A,B,C), and T014A (D,E,F) at Dallol volcano. Surface displacements are shown wrapped where each fringe (red-blue) represents 26 mm of motion towards the satellite in the line of sight. The model consists of a $\sim$ 1×2 km horizontal sill (Okada, 1985) at 0.9-1.3 km depth with $\sim$ 0.27 m of contraction. The coordinate system is relative to the centre of the Dallol edifice.

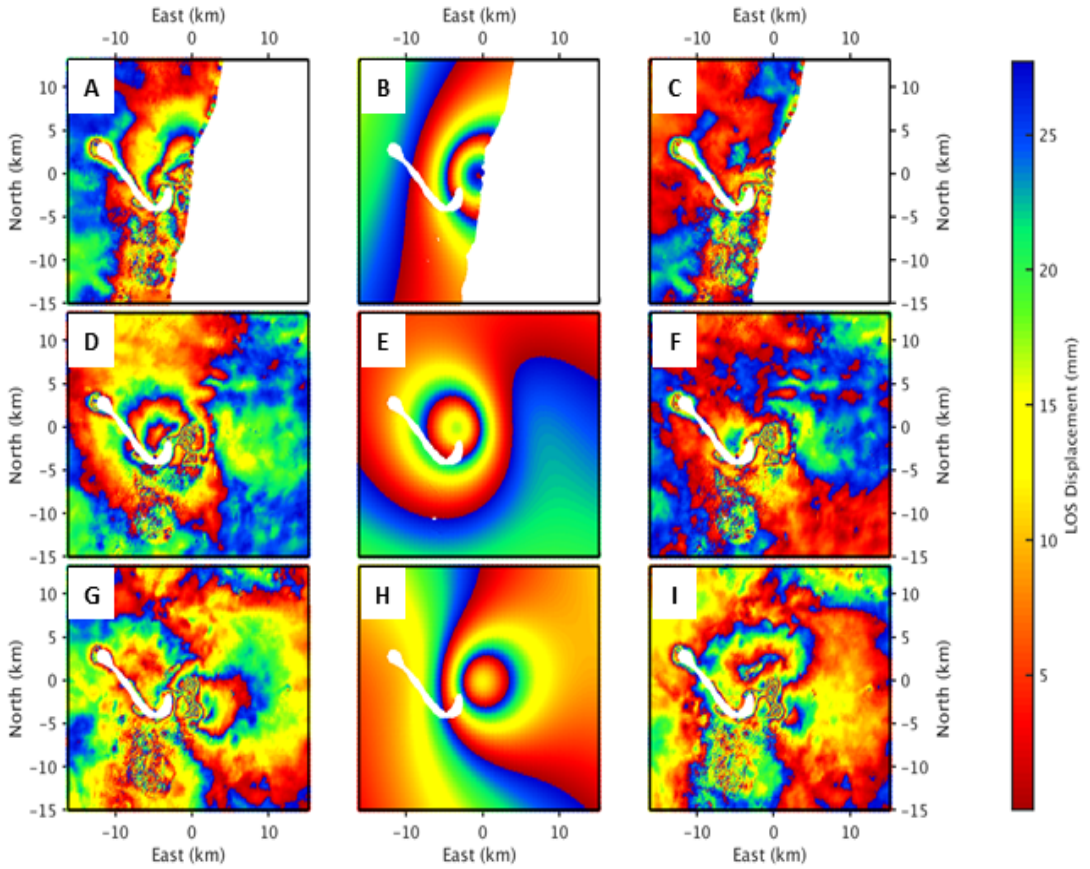

Figure B.9: Sentinel-1 data (A,D,G), GBIS (Bagnardi and Hooper, 2018) model (B,E,H), and residual (C,F,I), for 2014-19 surface deformation observed using tracks T079D (A,B,C), T014A (D,E,F), and T006D (G,H,I) at Nabro volcano. Surface displacements are shown wrapped where each fringe (red-blue) represents 26 mm of motion towards the satellite in the line of sight. The model consists of a point source (Mogi, 1958) at 5.5-6.8 km depth with an equivalent volume change of 7-11$\times 10^6$ m^3. The coordinate system is relative to the centre of the Nabro edifice.

References

Bagnardi, M. and Hooper, A. (2018). Inversion of Surface Deformation Data for Rapid Estimates of Source Parameters and Uncertainties: A Bayesian Approach. *Geochemistry, Geophysics, Geosystems*, **19**. doi:10.1029/2018GC007585. B.8, B.9

Cleveland, W. S. and Devlin, S. J. (1988). Locally weighted regression: an approach to regression analysis by local fitting. *Journal of the American statistical association*, **83**(403), pp. 596–610. 3a

King, R., Floyd, M., Reilinger, R. and Bendick, R. (2019). GPS velocity field (MIT 2019.0) for the East African Rift System generated by King et al.. Interdisciplinary Earth Data Alliance (IEDA). *Accessed on 20 Sep 2019.* doi:10.1594/IEDA/324785. B.4

Mogi, K. (1958). Relations between the Eruptions of Various Volcanoes and the Defomormations of the Ground Surfaces around them. *Bulletin of the Earthquake Research Institute*, **36**, pp. 99–134. B.9

Okada, Y. (1985). Surface deformation due to shear and tensile faults in a half-space. *Bulletin of the seismological society of America*, **75**(4), pp. 1135–1154. B.8

Weiss, J. R., Walters, R. J., Morishita, Y., Wright, T. J., Lazecky, M., Wang, H., Hussain, E., Hooper, A. J., Elliott, J. R., Rollins, C. et al. (2020). High-resolution surface velocities and strain for Anatolia from Sentinel-1 InSAR and GNSS data. *Geophysical Research Letters*, **47**(17), p. e2020GL087376. 7

Yu, C., Li, Z. and Penna, N. T. (2018). Interferometric synthetic aperture radar atmospheric correction using a GPS-based iterative tropospheric decomposition model. *Remote Sensing of Environment*, **204**, pp. 109–121. doi:10.1016/j.rse.2017.10.038. B.1

Yu, C., Penna, N. T. and Li, Z. (2017). Generation of real-time mode high-resolution water vapor fields from GPS observations. *Journal of Geophysical Research*, **122**(3), pp. 2008–2025. doi:10.1002/2016JD025753. B.1

Appendix C

Supplementary Materials for Chapter 4

Supplementary Table C.1 and Supplementary Figures C.1-C.4.

h	η	Dabbahu		Gabho		Ado Ale		Southern	
(km)	(Pa s)	06-10	14-19	06-10	14-19	06-10	14-19	06-10	14-19
14	10^{17}	+0.0	+0.2	+0.1	+0.3	+0.0	+1.2	-0.6	+0.2
14	10^{18}	+0.5	+0.0	+0.4	+0.1	+2.4	+0.6	-0.7	+0.2
14	10^{19}	+0.4	+0.0	+0.4	+0.0	+2.4	+0.5	-1.2	+0.8
16	$10^{17.5}$	+0.1	+0.1	+0.0	+0.2	+0.1	+0.8	-0.8	+0.3
16	10^{18}	+0.2	+0.0	+0.1	+0.1	+0.7	+0.4	-0.9	+0.2
16	$10^{18.5}$	+0.3	-0.1	+0.2	-0.1	+1.4	-0.2	-1.1	+0.4
18	10^{17}	-0.2	+0.2	-0.1	+0.3	+0.2	+0.6	-2.3	+0.5
18	10^{18}	+0.2	+0.0	+0.0	+0.1	+0.3	+0.3	-2.0	+0.3
18	10^{19}	+0.2	-0.1	+0.1	-0.2	+0.9	-0.6	-1.6	+0.3
20	$10^{17.5}$	-0.1	+0.1	-0.1	+0.2	+0.1	+0.5	-5.7	+0.5
20	10^{18}	+0.0	+0.0	-0.1	+0.1	+0.2	+0.2	-3.4	-0.4
20	$10^{18.5}$	+0.2	-0.1	+0.0	-0.1	+0.4	-0.3	-2.3	-0.5
22	10^{17}	-0.2	+0.2	+0.0	+0.2	+0.1	+0.6	-7.1	+1.0
22	10^{18}	+0.0	+0.0	-0.1	+0.1	+0.2	+0.2	-3.6	-0.3
22	10^{19}	+0.2	-0.2	+0.0	-0.2	+0.5	-0.7	-2.1	-0.4
24	$10^{17.5}$	+0.0	+0.1	+0.0	+0.2	+0.2	+0.5	-4.7	+0.6
24	10^{18}	+0.0	+0.0	+0.0	+0.0	+0.2	+0.2	-3.5	-0.2
24	$10^{18.5}$	+0.0	-0.1	+0.0	+0.0	+0.3	-0.3	-2.6	-0.7
26	10^{17}	+0.0	+0.0	+0.0	+0.2	+0.3	+0.6	-4.9	+0.8
26	10^{18}	+0.0	+0.0	+0.0	+0.1	+0.2	+0.3	-3.5	+0.0
26	10^{19}	+0.1	-0.2	+0.0	+0.2	+0.4	-0.7	-2.4	-0.6
28	$10^{17.5}$	-0.2	+0.2	-0.1	+0.2	+0.3	+0.5	-4.1	+0.7
28	10^{18}	+0.0	+0.0	+0.0	+0.1	+0.3	+0.3	-3.4	+0.0
28	$10^{18.5}$	+0.0	-0.1	+0.0	-0.1	+0.3	-0.2	-2.8	-0.7
30	10^{17}	-0.1	+0.1	+0.0	+0.2	+0.5	+0.6	-4.2	+0.5
30	10^{18}	-0.1	+0.0	+0.0	+0.1	+0.3	+0.3	-3.4	+0.1
30	10^{19}	+0.0	-0.2	+0.0	+0.2	+0.4	-0.7	-2.6	-0.7

Table C.1: Sill source time series volume changes for all model rheologies to 1 d.p. with units of 10^8 m^3. h represents the thickness of the elastic lid, with η showing the viscosity of the homogeneous layer beneath the elastic lid. Values show the cumulative volume change within the 2006-10 and 2014-19 time periods for sills below the Dabbahu, Gabho, Ado 'Ale, and Southern sources, and are coloured (green for positive, red for negative volume change) with the transparency of the colour directly related to the cell values. Sills are 1×1 km planar openings (Okada, 1985) at depths of 4, 4, 10, 17 km respectively.

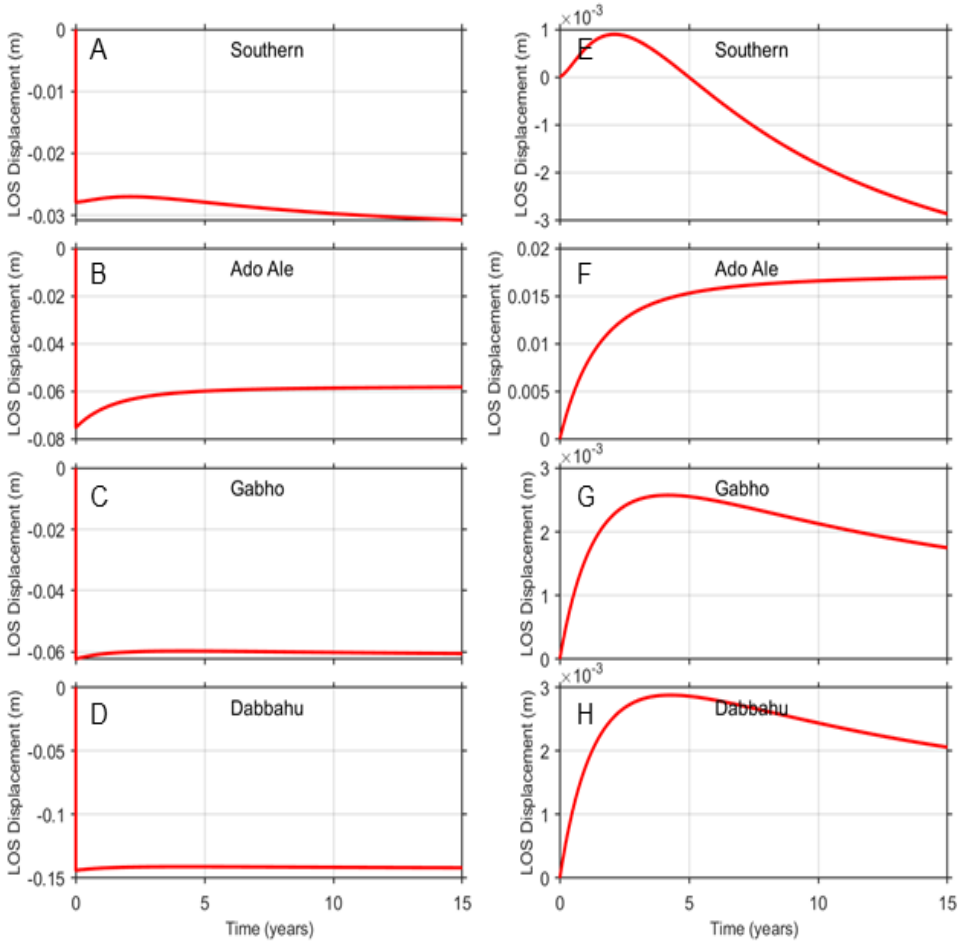

Figure C.1: Green's function responses of surface deformation for 1 m opening for each of the sill sources over 15 years. (A-D) shows the total deformation response, with (E-F) showing just the viscous response for sills below Dabbahu (D, H), Gabho (C, G), Ado 'Ale (B, F), and the Southern source (A, E). These time series apply to the rheology of an 18 km elastic lid thickness, and 10^{18} Pa s viscosity. Sills are 1×1 km planar openings (Okada, 1985) at depths of 4, 4, 10, 17 km respectively.

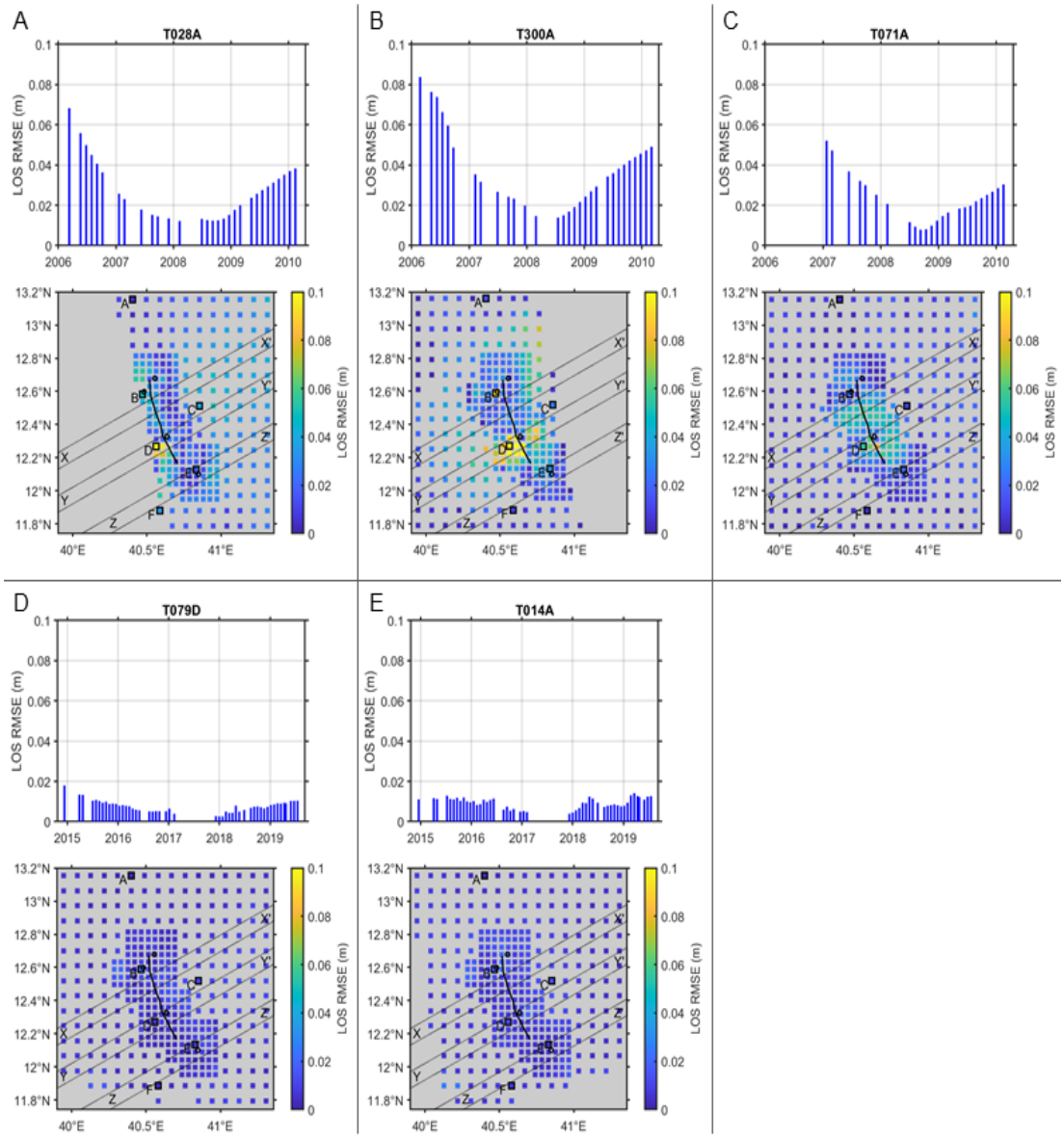

Figure C.2: Temporal and spatial variation in RMSE for the model residuals shown in Figure 4.3. RMSE values are calculated from the map of residuals at each epoch, and the time series of residuals at each spatial point. Values are shown in the LOS of each track, for the time period covered by each track. Points A-E in map view relate to the time series shown in Figure 4.3, with profiles X-Z shown in Figure 4.4.

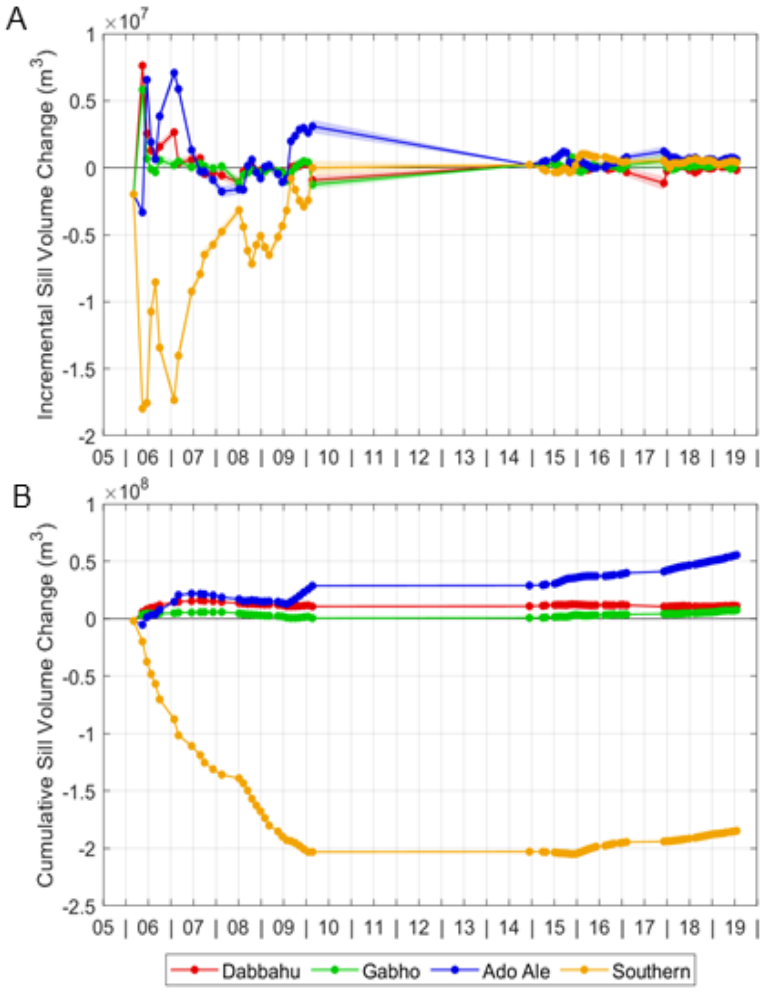

Figure C.3: Sill source time series for 2006-19 showing incremental (A) and cumulative (B) volume change for each of the sills below Dabbahu (red), Gabho (green), Ado 'Ale (blue), and the Southern source (yellow). Sills are 1×1 km planar openings (Okada, 1985) at depths of 4, 4, 10, 17 km respectively.

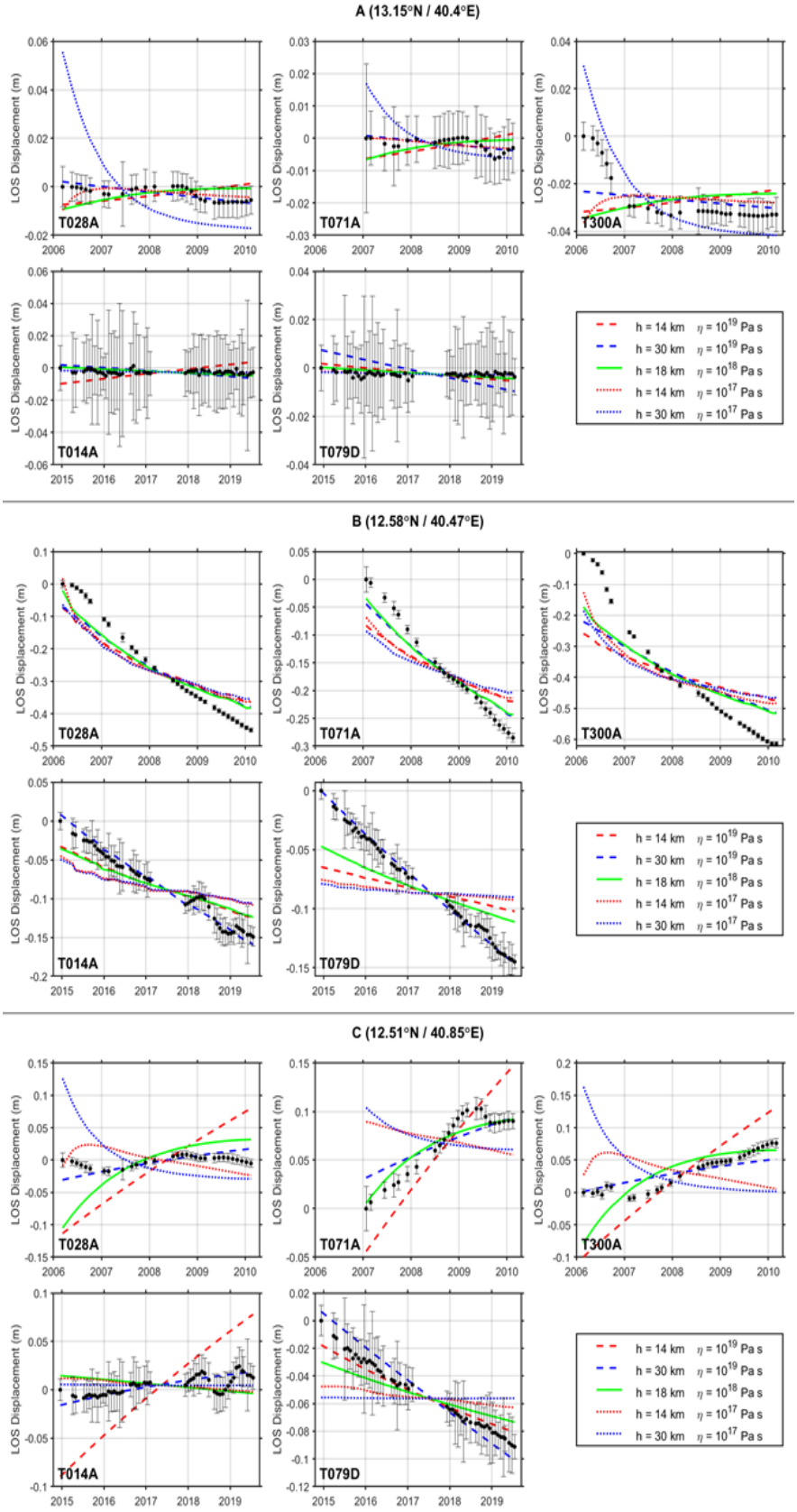
A (13.15°N / 40.4°E)
B (12.58°N / 40.47°E)
C (12.51°N / 40.85°E)
LOS Displacement (m)
T028A
T071A
T300A
T014A
T079D
h = 14 km η = 10^19 Pa s
h = 30 km η = 10^19 Pa s
h = 18 km η = 10^18 Pa s
h = 14 km η = 10^17 Pa s
h = 30 km η = 10^17 Pa s

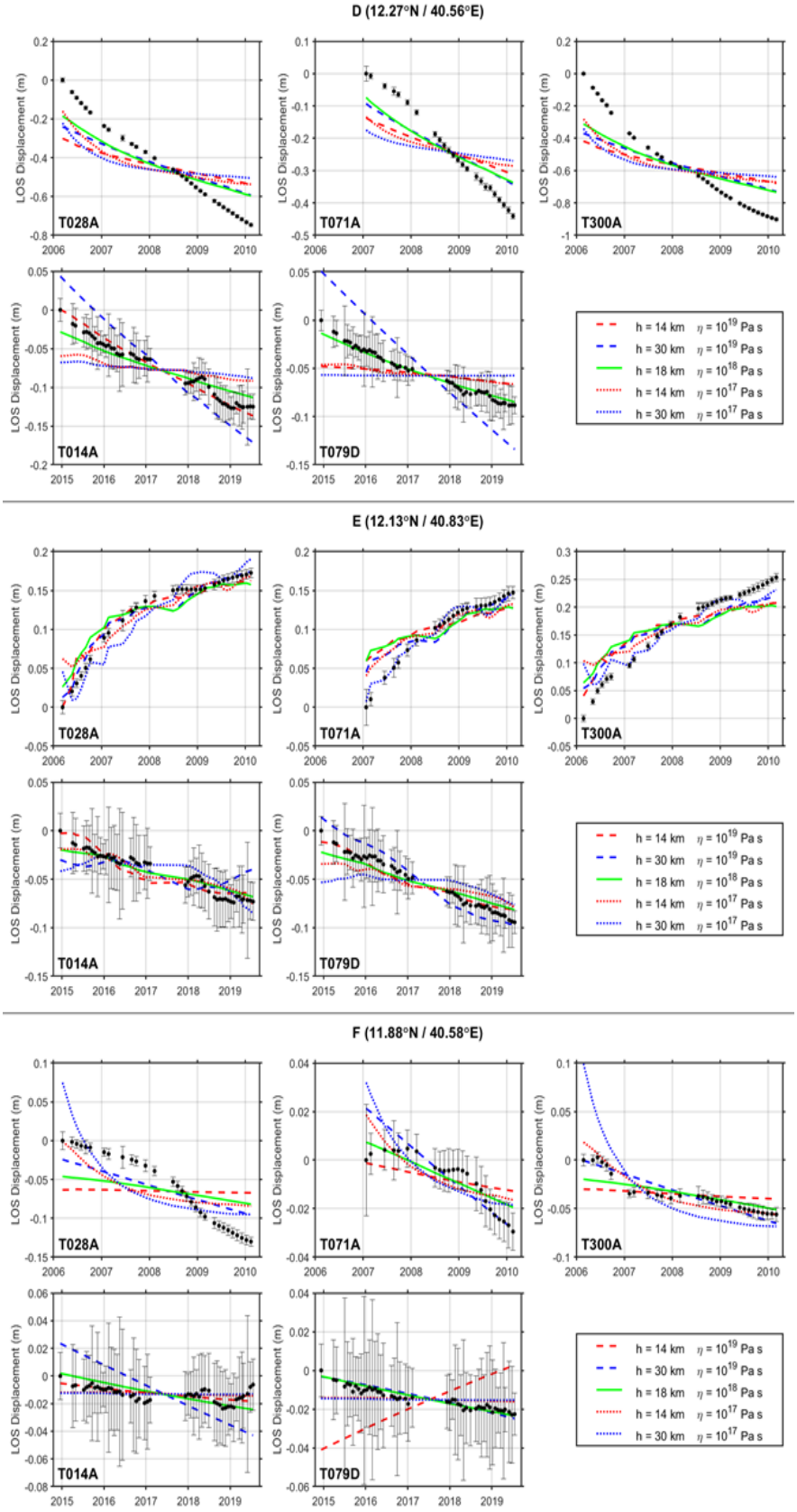

Figure C.4: LOS displacement time series for all time series points (A-F) as shown in Figure 4.3, with the variety of model fits (elastic thickness h = 14-30 km, viscosity $\eta = 10^{17-19}$ Pa s), and the overall best-fit model (h = 18 km, $\eta = 10^{18}$ Pa s).

References

Okada, Y. (1985). Surface deformation due to shear and tensile faults in a half-space. *Bulletin of the seismological society of America*, **75**(4), pp. 1135–1154. C.1, C.1, C.3